Rare Earth Metal Boryl and Gallyl Compounds: Synthesis and Reactivity

Liban Mohamoud Ali Saleh MChem

Thesis submitted to the University of Oxford for the degree of

Doctor of Philosophy.

The work described in this Thesis was carried out in the Chemistry Research Laboratory, University of Oxford from October 2009 to August 2014 under the supervision of Professor Philip Mountford. All work is my own unless stated to the contrary, and has not previously been submitted for any degree at this or any other university.

Liban Mohamoud Ali Saleh

August 2014

Abstract

Liban Mohamoud Ali Saleh Trinity 2014

New College D.Phil. Thesis

This Thesis describes the syntheses, characterisation and reactivity of rare earth metal boryl and gallyl compounds. Experimental and computational studies were performed to investigate the structure and bonding in these compounds.

Chapter 1 introduces key metal–boryl and metal–gallyl compounds of the *s*, *p*, *d* and *f*-blocks *via* literature review.

Chapter 2 describes the syntheses, structures and bonding analyses of rare earth metal boryl compounds. A short introduction to rare earth metal cations is given.

Chapter 3 describes the syntheses, structures and bonding analyses of rare earth metal gallyl compounds. The preparation of a new class of rare earth metal cations will also be reported. A short introduction to rare earth metal amidinates is given.

Chapter 4 presents reactivity studies of the rare earth metal gallyl compounds described in Chapter 3. To facilitate a direct structure and reactivity comparison, the corresponding boryl compounds were also synthesised. The results of a comprehensive DFT computational study to investigate the structure and bonding in these compounds are also presented. A short introduction to metal–element and metal–metal bond reactivity is given.

Chapter 5 presents full experimental procedures and characterising data for the new compounds reported.

Appendix

CD Appendix contains .cif files for all new crystallographically characterised compounds described.

Contents

Acknowledgements

بِسْمِ اللَّهِ الرَّحْمَٰنِ الرَّحِيمِ

Completing a D.Phil is a challenging task. Each Thesis produced is unique to the person that prepared it, and takes on their personality as much as that of the person who supervised the work. However, it is also true that the environment that the person finds themselves in also influences the final outcome. It is here, in the Acknowledgments, that those who provided that influence are recognised.

First, I would like to express my sincerest gratitude to Professor Philip Mountford. On three occasions he took a risk: once, when he accepted my application to work in his group; again, when he trusted me with the challenging chemistry that became the work presented in this Thesis; and finally, when he had the opportunity to give up on this wonderful project, he instead kept the faith and ensured that it would be completed. With Prof. Mountford's influence, I am well prepared for life after a D.Phil.

Working in a laboratory is a difficult, full time job, and so I would like to thank my lab mates over the years. I was extremely lucky that the atmosphere has always been light-hearted, accommodating and warm. I would like to thank Dr Andrew Schwarz, Dr Andrey Protchenko and Dr Matthew Blake for tirelessly listening to my rambling (and sometimes witless) soliloquies on lab life, and Andrey in particular for teaching me the dark arts of organometallic chemistry. I would also like to thank Dr Laura Groom and Junjuda Unruangsri for being there at the start and being great people to work with, and Dr Adam Russell for lightening the mood on many occasions with a well-placed inappropriate joke. I would also like to thank Dr Jonathan Selby, Dr Alex Heath, Dr Michael Cushion, Dr Daniel Schofield, Dr Pei Jen Tiong, Dr Richard Scott, George Hilton, Hannah Morgan, Richard Collins, Lee Collins, Chee Onn, Bryony Core, Laura Stevenson and Helen Yin for their contribution to making the Mountford group a wonderful place to work. Their influence is apparent in my continued good mental health!

I am grateful to Prof. Philip Mountford, Dr Andrew Schwarz and Dr Matthew Blake for their contribution to the collection and solving of X-ray crystallographic data. I am also grateful to the extremely talented Abigail Mountain and Dr Krishna Birjkumar

who, under the supervision of our collaborator Prof. Nikolas Kaltsoyannis at University College London, carried out DFT calculations on the compounds presented in this Thesis. I would also like to express my thanks to Dr Nick Rees for the training and assistance I have received in NMR spectroscopy. Their influence anchors the results presented in this Thesis.

Finally, I would like to thank my friends and family. The friends that I have made in Oxford are truly friends for life, and I am grateful for the opportunity to have met them and to get to know them. Amongst many others, I would like to thank in particular Oussama Mezoui, Abdulrahman El-Sayed, Adam Ali, Amir Rahim and Mohammad Arslan Ali for the time and effort they put in to our friendships.

A very special thank you goes to my family: my aunts and uncles, my brothers Hamza and Ali, my sisters Deqa, Zeynab and Sophia, and my father Mohamoud whose encouragement and support never wavered, and finally, my grandmother, Halima Ibrahim Abdalla, my late grandfather, Ali Saleh Esa, and my mother Mariame, who have always been my biggest supporters and made me who I am today. For this, I am always humbled and grateful.

Abbreviations

General

Å	Ångstrom
ca.	*circa*, about
cf.	*confer*, compared to
CSD	Cambridge Structural Database
°	degrees
°C	degrees Celsius
g	gram(s)
h	hour(s)
K	Kelvin
mg	milligram(s)
min	minute(s)
mL	millilitre(s)
mmol	millimole(s)
RT	room temperature
s	second(s)
vs.	versus

Chemical

Ae	alkaline earth metal
An	actinide
Ar	2,6-diisopropylphenyl
Ar'	2,4,6-trimethylphenyl
Ar"	2,3,5,6-C_6HMe_4
Ar*	2,6-$(Ph_2CH)_2$-4-C_6H_2Me
bian	bis[(2,6-diisopropylphenyl)imino]acenaphthene
^{n}Bu	*n*-butyl
COD	cyclooctadiene
COE	cyclooctene
Cp	C_5H_5
Cp'	C_5H_4Me
Cp"	C_5Me_4Et

Cp*	C_5Me_5
Cy	cyclohexyl
DME	1,2-dimethoxyethane
DMPE	$Me_2PCH_2CH_2PMe_2$
DPPE	$Ph_2PCH_2CH_2PPh_2$
Et	ethyl
Fc	ferrocenyl
Fp^-	$[CpFe(CO)_2]^-$
HMPA	$P(O)(NMe_2)_3$
^iPr	*iso*-propyl
IPr	$C(NArCH)_2$
L	a supporting ligand (set)
Ln	lanthanide
M	metal
Me	methyl
Mes	mesityl (2,4,6-$C_6H_2Me_3$)
^{Mes}NacNac	$[\{Ar'NC(Me)\}_2CH]^-$
NacNac	$[\{ArNC(Me)\}_2CH]^-$
NHC	n-heterocyclic carbene
Ph	phenyl
priso	$[(Ar)NC(NR_2)N(Ar)]^-$
py	pyridine
R	generic aryl or alkyl
Rp^-	$[CpRu(CO)_2]^-$
^tBu	*tert*-butyl
^{tBu}py	4-$^tBu(C_5H_4N)$
THF	tetrahydrofuran
TM	transition metal
TMEDA	tetramethylethylenediamine
Tol	4-C_6H_4Me
tren	$N(CH_2CH_2NSiMe_3)_3$
X	Generic halide
Xyl	2,6-$C_6H_3Me_2$

Calculations

AIM	atoms-in-molecules
BCP	bond critical point
BDE	bond dissociation energy
DFT	density functional theory
H	energy density
HOLO	highest occupied localized orbital
HOMO	highest occupied molecular orbital
LO	localized orbital
MO	molecular orbital
ρ	electron density
$\nabla^2\rho$	Laplacian of the electron density

Nuclear Magnetic Resonance Spectroscopy

$^{13}C\{^1H\}$	proton-decoupled ^{13}C
$^{11}B\{^1H\}$	proton-decoupled ^{11}B
br	broad
d	doublet
Hz	Hertz
i	*ipso*
J	coupling constant
m	*meta*
m	multiplet
MHz	Megahertz
NMR	nuclear magnetic resonance
o	*ortho*
p	*para*
ppm	parts per million
q	quartet
s	singlet
sept	septet
t	triplet
VT	variable temperature
δ	chemical shift in ppm

Infrared Spectroscopy

FT-IR	Fourier transform infrared red
IR	infrared
cm^{-1}	wavenumber
m	medium
s	strong
w	weak
ν	frequency

Notes

Literature compounds described in this Thesis are numbered **1.x**, **2.x**, **3.x**, **4.x** according to the Chapter in which they first occur. The new compounds described in this Thesis are numbered **1** – **xx**. Ionic compounds are numbered as an ion pair, *e.g.* **9-BPh$_4$**, or as **9**$^+$ if referring to the cation alone. Full model systems used in calculations are denoted by **#C**, whilst simpler model systems used in calculations are denoted by **#SC**. Hypothetical THF-containing or THF-free model systems have an additional subscript label, *e.g.* **22C$_{THF}$** or **14C$_{–THF}$**.

When quoting respective covalent radii, the values reported by Alvarez and co-workers are used (see page 39, reference 12).

X-ray crystallography data was collected, solved and refined by Drs Andrew D. Schwarz (compounds **1–4**, **9**$^+$ and **20**) and Matthew P. Blake (compounds **14**, **18**–**19** and **22–24**). Molecular drawings were produced by Prof. Philip Mountford.

DFT calculations were performed by Dr Krishna H. Birjkumar (Chapter 2) and Ms. Abigail R. E. Mountain (Chapters 3 and 4) under the supervision of Prof. Nikolas Kaltsoyannis at University College London.

Chapter One

Introduction

1.1 General Introduction

The unique properties of rare earth metals[1, 2] have made possible the huge technological advances that have been seen over the last decade. Technologies in which rare earth metals play a critical role include: wind turbines, electric vehicles, solar cells, energy-efficient lighting, flat screen displays, smartphones, medical imaging, and fibre optics. Their heavy use in clean energy applications has led the US Department of Energy to develop a "Critical Materials Strategy" to safeguard supply of rare earth metals for the immediate future.[3] Despite this explosion in interest, fundamental research and industrial processes involving rare earth metals continues to lag behind the more traditional transition metals. Any new advances in the understanding of rare earth metals and their physical and chemical properties are of paramount importance. Due to their high Lewis acidity, rare earth metals prefer ligands that contain hard Lewis bases as donors, which has led to the coordination chemistry of rare earth metals being dominated by oxygen and nitrogen based ligand sets.

This Thesis describes efforts to go beyond these limitations, involving the synthesis of novel rare earth metal-element bonds between the metals and non-conventional elements (*i.e.* not C, N or O). The investigation focuses on bonds between rare earth metals and the elements of Group 13, in particular boron and gallium of the type (L)M–EX_2 (where E = B or Ga). To probe their structure and reactivity it was necessary during this investigation to synthesise several new rare earth metal starting compounds, and these are also reported. Parts of this work have been published.[4]

This Chapter introduces the chemistry of compounds featuring bonds between the transition, alkaline earth and rare earth metals and boron and gallium. Due to the vast number of existing metal-element bonds, only those bonds involving a boron or gallium heterocycle are included, save for exceptional examples. The metals of Group 3 will be included with the *f*-block metals, as they have similar chemical and physical properties.

1.2 Metal-Boron Bond Types

Compounds featuring bonds between a metal and boron generally fall under one of five coordination modes according to the number of bonds between the metal and boron, and the coordination number of the boron atom (Figure 1.1).

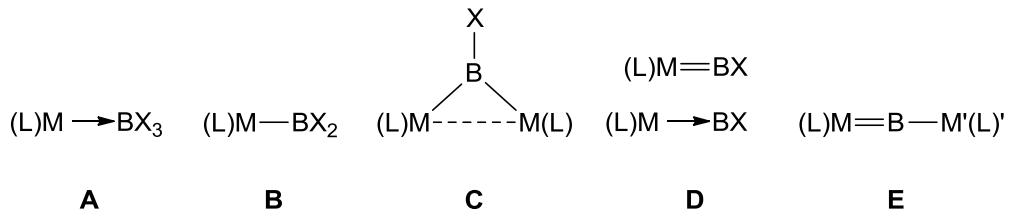

Figure 1.1. Metal-boron coordination modes.

Borane-type compounds (**A**, Figure 1.1) comprise of a dative bond from a metal to a BX_3 molecule to form Lewis base/Lewis acid adducts featuring four-coordinate boron atoms. Boryl-type compounds (**B**) comprise of a single bond between a metal and BX_2 fragment, featuring a three-coordinate boron atom. Borylene-type compounds can comprise of two subsets: bridging (**C**) or terminal (**D**). Here, a BX fragment can bridge between two metal fragments, or form a two-coordinate boron centre by being terminally bound to one metal fragment, featuring either a formal double bond or a dative bond between the metal and boron. Finally, metallaborylene-type compounds (**E**) feature a 'naked' boron atom between two metal centres. This review will concern itself with type **B** compounds, featuring metals singly bonded to three-coordinate boron atoms, and their gallium analogues (*i.e.* gallyl compounds).

1.3 *s*-block

1.3.1 Group 1

The lithium salts of the second row p-block elements are well established anionic nucleophiles in organic and inorganic syntheses. However, the corresponding lithium salt of boron had remained an elusive species despite decades of research.

There have been three examples of alkali metal salts of boron being proposed as an intermediate (Scheme 1.1). In 1952, Auten and Kraus reported the reduction of $^{n}Bu_2BCl$ using a Na/K alloy to generate the corresponding boryl salt **1.1**, which could be trapped with MeI to form $^{n}Bu_2BMe$.[5] In 1976, Smith and Swaminathan showed that the boryl anion in fact rearranges to form a boron-stabilised carbanion (**1.2**),

followed by aggregation to form a cyclic trimer, as characterised by IR spectroscopy.[6] In 1967, Williams and co-workers proposed the formation of a diphenylboryl anion (**1.3**) from the photolysis of sodium tetraphenylborate, based on the formation of biphenyl.[7] However, it was shown by Schuster that irraditation of tetraphenylborate produces a biradical species, which rearranged to a cyclic borate possessing a three-membered ring (**1.4**).[8] Most recently in 2001, Weber and co-workers proposed that the intermediate of the reduction of bromodihydrodiazaborole would either be a boryl radical (**1.5**) or a boryl anion (**1.6**).[9]

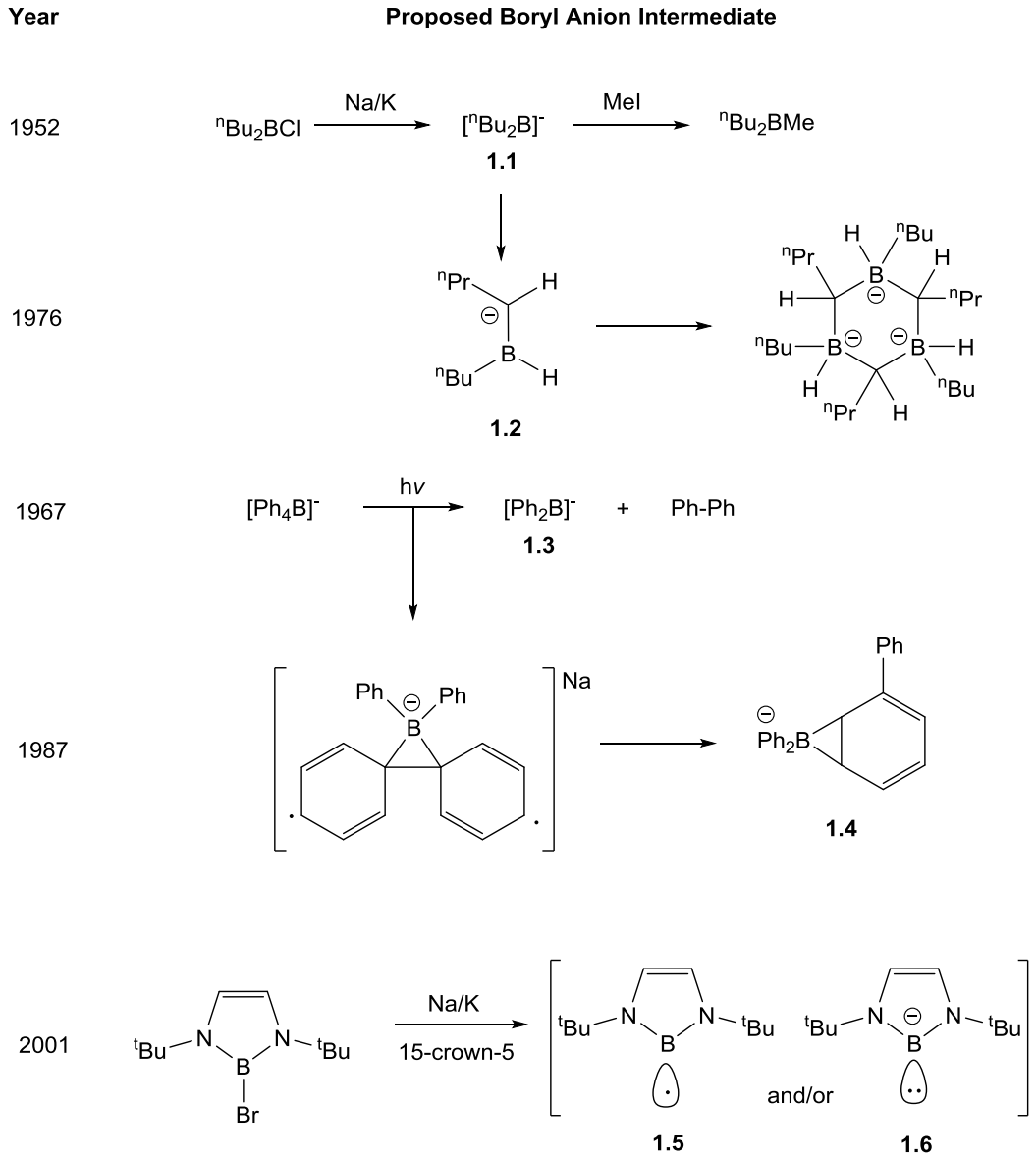

Scheme 1.1[10] Time-line of reported attempts at the isolation of a boryl anion. Metal counterions omitted for clarity.

The conventional methods of generating organolithium compounds *via* reductive dehalogenation and deprotonation of C–X or C–H, respectively, are difficult with boron. Deprotonation of B–H with a base is difficult as the lower electronegativity of boron compared to hydrogen confers hydridic character upon hydrogen. In addition to that, the boron centre, with its vacant 2*p*-orbital, favours formation of a Lewis acid-base adduct over deprotonation. One-electron reduction of a B–X bond (X = halogen) generates a boryl radical, which rapidly dimerises to form the diborane(4) species before any second electron transfer can occur to form the boryl lithium.

In 2006, Yamashita, Nozaki and co-workers isolated the first structurally characterised lithium salt of boron, Li{B(NArCH)$_2$}(THF)$_2$ (**1.7**), a boron containing NHC analogue (Scheme 1.2).[11] In this molecule, the B–Li bond is highly polarised, with the boron centre having anionic character. The use of the N-heterocyclic framework provided key structural and electronic features that helped aid isolation. The nitrogens in the heterocycle help to stabilise the vacant 2*p*-orbital in **1.7** and inductively withdraw the negative charge, whilst the *N*-bound aryl substituents provide steric protection from potential formation of the diborane(4) dimer.

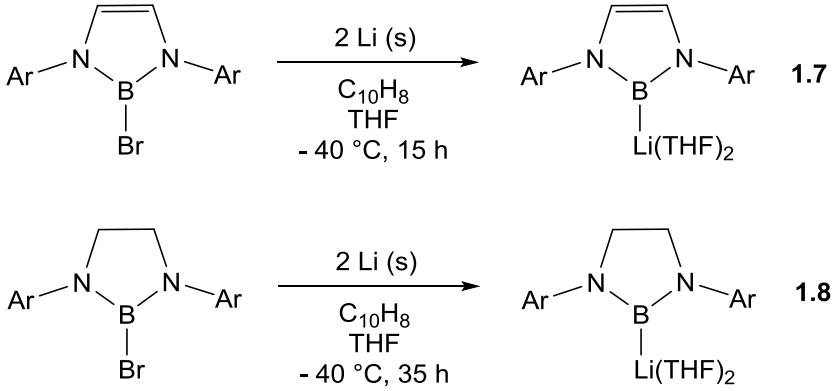

Scheme 1.2. By-products omitted for clarity. Ar = 2,6-$C_6H_3{}^iPr_2$.

The saturated version of **1.7**, Li{B(NArCH$_2$)$_2$}(THF)$_2$ (**1.8**), was also eventually synthesised, but required a considerably longer reaction time for complete reduction (Scheme 1.2).[10] The structure of **1.7** revealed a lithium-boron bond length of 2.276(5) Å, longer than the sum of the respective covalent radii (2.12 Å).[12] A full discussion of the structural features of the heterocycle will be presented in Chapter 4. The ^{11}B NMR spectrum of **1.7** shows a downfield shifted signal at 45 ppm in THF-d_8, typical of metal-coordinated boryls, and ^{1}H NMR studies show that the molecules of THF coordinated to lithium remain coordinated in solution.

Reactions with organic electrophiles were carried out, producing **1.9**–**1.22** (Scheme 1.3), confirming the nucleophilic nature of **1.7**.[10, 11]

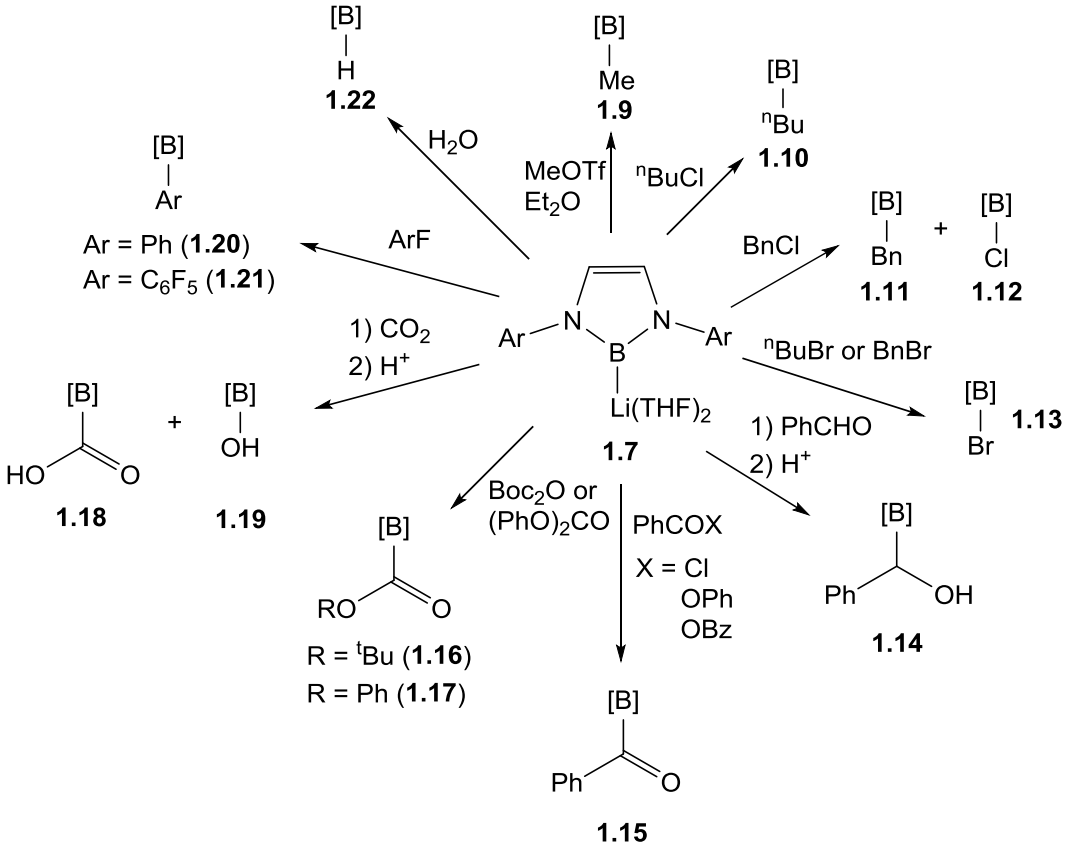

Scheme 1.3. See ref for details. [B] = $B(NArCH)_2$.

Liddle and co-workers reported the lithium boryl $Li\{B(PDA)\}(THF)_2$ (PDA = phenylenediamine), featuring bulky 2,4,6-triisopropylphenyl groups coordinated to the ring nitrogens.[13] Use of high-sodium content lithium powder (0.5 % Na) was essential to avoid formation of borylated naphthalene by-products.

The isolation of the corresponding gallyl anion had preceded that of **1.7** by nearly a decade. Schmidbaur and co-workers synthesised and structurally characterised the potassium salt of the gallium heterocycle (**1.24**, Scheme 1.4), featuring *tert*-butyl groups coordinated to nitrogen.[14] Reduction of the digallane(4) precursor (**1.23**) led to low yields of **1.24**. Jones and co-workers then produced a high yielding route to their gallyl anion (**1.26**), featuring diisopropylphenyl groups coordinated to nitrogen, by reduction of the heterocyclic gallium diiodide precursor **1.25** (Scheme 1.4).[15]

Fedushkin and co-workers later isolated a series of Group 1 metal salts of their gallyl compound featuring an acenaphthene backbone *via* reductive cleavage of the gallyl

dimer **1.27** with a variety of metals to produce the compounds $M\{Ga(NArC_6H_3)_2\}_2(L)_n$ (M = Li (**1.28**), L = Et_2O, n = 3; Na (**1.29**), L = Et_2O, n = 3; K (**1.30**), L = THF, n = 5).[16, 17]

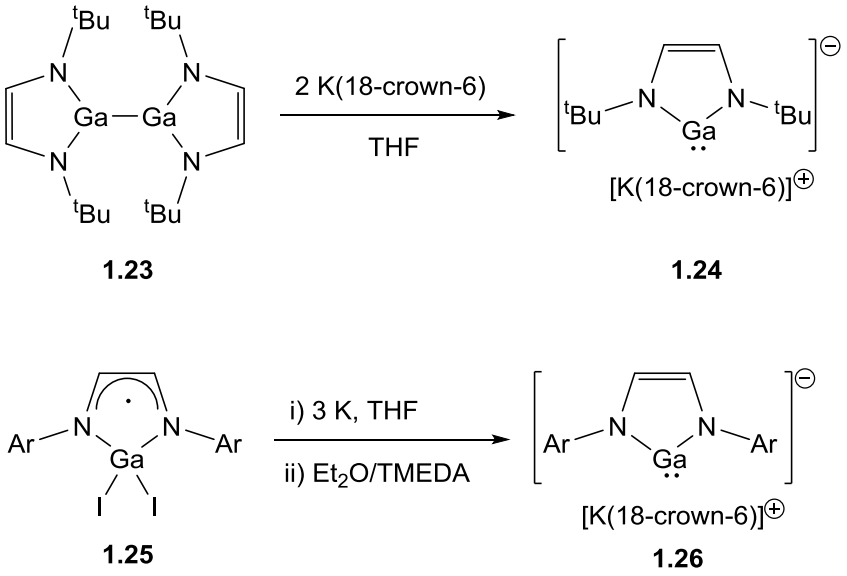

Scheme 1.4. By-products omitted for clarity. Ar = 2,6-$C_6H_3{}^iPr_2$.

1.3.2 Group 2

Reaction of one or two equivalents of **1.7** with $MgBr_2(Et_2O)$ produced the magnesium mono- (**1.31**) and bis(boryl) (**1.32**) compounds in poor isolated yields (17 % and 19 %, respectively).[18] **1.31** crystallised along with the "ate"-complex $Mg\{B(NArCH)_2\}(THF)(\mu\text{-}Br)_2Li(THF)_2$ (**1.33**), but could be manually separated, allowing **1.31**, **1.32** and **1.33** to all be crystallographically characterised (Scheme 1.5). The Mg–B bond lengths of **1.31** and **1.33** are identical within standard uncertainty, whilst there are significantly longer Mg–B bonds in **1.32**. When **1.31** and **1.33** are dissolved in THF-d_8, they produce the same ^1H and ^{11}B NMR spectra, indicating that in solution LiBr is non-coordinating. Compound **1.31** can be also be thought of as a boron analogue of a Grignard reagent; reaction with varying equivalents of benzaldehyde led to a number of products, but the authors noted that no borylbenzylalcohol was produced. In contrast, reaction of **1.7** with one equivalent of benzaldehyde produced borylbenzylalcohol in good yields. Compound **1.31** did produce the first fully characterised acylborane (**1.15**) *via* reaction with 1-3 equivalents of benzaldehyde, but in low yields (18-34 %). Reaction of **1.7** with

benzoyl chloride produced **1.15** in better yield (74 %, Scheme 1.3). The authors conclude that the change in metal results in a significant change in reactivity.[18]

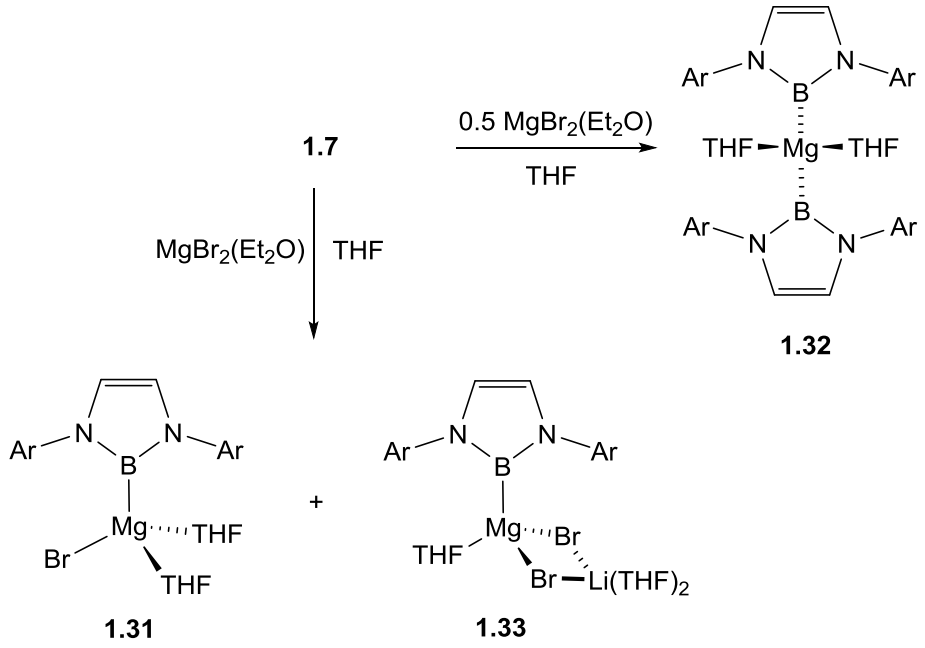

Scheme 1.5. By-products omitted for clarity. Ar = 2,6-$C_6H_3{}^iPr_2$.

A series of Group 2 metal bis(gallyl) compounds were synthesised by Jones and co-workers Addition of **1.26** to MI_2 (M = Mg or Ca) did not produce the corresponding bis(gallyl) compound, only intractable mixtures. $M\{Ga(NArCH)_2\}_2(THF)_n$ (M = Mg, n = 3 (**1.34**); M = Ca, n = 4 (**1.35**)) was eventually isolated *via* reaction of **1.25** with a large excess of the corresponding metal amalgam.[19] It is believed that the reaction proceeds *via* reduction of **1.25** by the amalgam to form the digallane(4) $\{Ga(NArCH)_2\}_2$ (**1.36**) *in situ*, followed by oxidative insertion of the metal into the Ga–Ga bond of **1.36** to form the final products. $Ca\{Ga(NArCMe)_2\}_2(THF)_4$ (**1.38**) was also isolated from the reaction of $GaI_2(NArCMe)_2$ (**1.37**) and calcium amalgam and structural analyses of **1.34**, **1.35** and **1.38** were carried out. The magnesium centre in **1.34** was found to have a distorted trigonal bipyramidal geometry, with both gallyls and one THF in the equatorial plane, and two THF molecules in the axial positions. Both **1.35** and **1.38** had similar structures in which the calcium centres possessed octahedral geometry, where both gallyls occupy the axial positions and the four THF molecules occupy the equatorial positions. The M–Ga bond lengths for **1.34**, **1.35** and **1.38** (2.7174(15), 3.1587(6) and 3.1988(12) Å, respectively) are all slightly longer than the sum of the respective covalent radii. In a later report,[20] Jones and co-workers

showed that bis(gallyl) compounds of Group 2 were indeed accessible from reaction of **1.26** and the corresponding metal diiodides. Addition of an excess of TMEDA to the reactions of **1.26** and MI_2 (M = Ca, Sr, Ba) allowed isolation of the bis(gallyl) compounds $M\{Ga(NArCH)_2\}_2(TMEDA)_2$ (M = Ca (**1.39**), Sr (**1.40**) and Ba (**1.41**)) in low to good yields. It was found that as the size of the metal increased, the yield of the bis(gallyl) compounds decreased. This was attributed to the increasing weakness of the M–Ga bond with the larger metals. Attempts at synthesising the heteroleptic $MI\{Ga(NArCH)_2\}$ compounds did not succeed, producing only 50:50 mixtures of **1.39**–**1.41** and unreacted MI_2. This was a rather unsurprising result, as heteroleptic compounds of the larger Group 2 metals are known to readily undergo redistribution reactions to form more stable homoleptic compounds. Use of the magnesium compound $Mg(NacNac)I(Et_2O)$, which features the bulky NacNac ligand, in a reaction with **1.26** resulted in the heteroleptic magnesium gallyl compound $Mg(NacNac)\{Ga(NArCH)_2\}(\eta^1\text{-TMEDA})$ (**1.42**) in low yield, featuring an η^1-coordinated molecule of TMEDA (Scheme 1.6).[20]

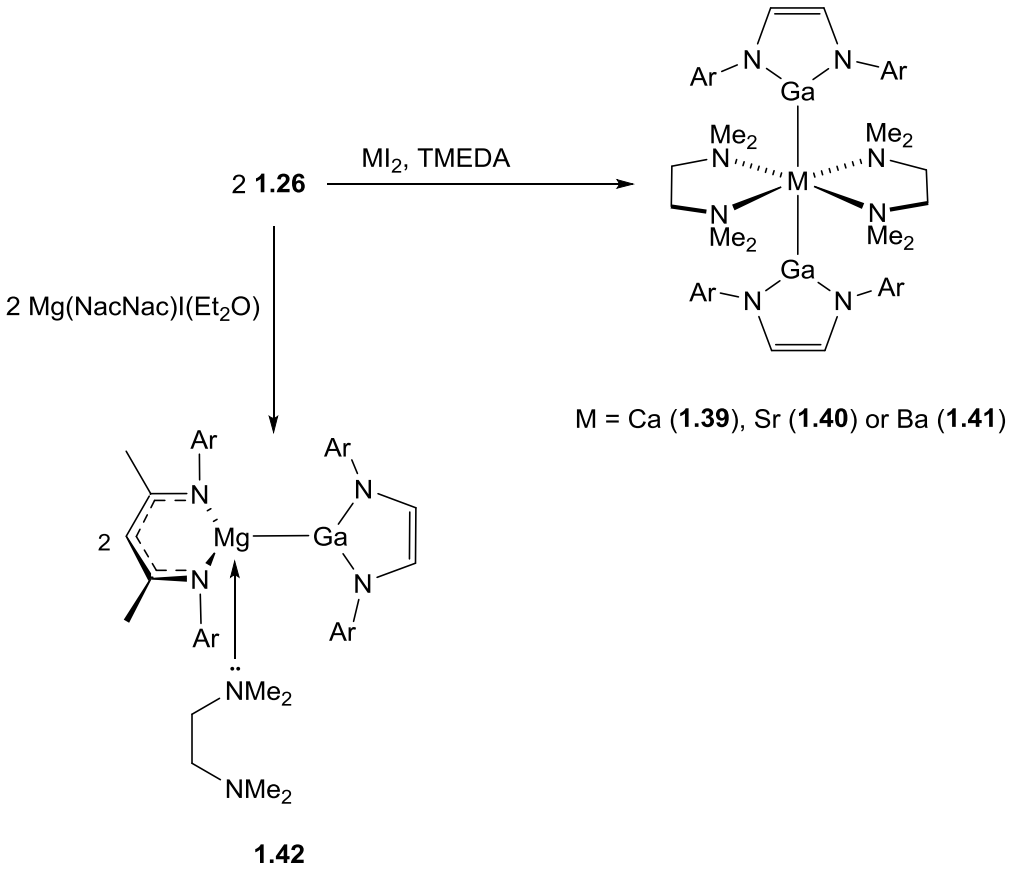

Scheme 1.6. By-products omitted for clarity. Ar = 2,6-$C_6H_3{}^iPr_2$.

Fedushkin and co-workers also reported a series of Group 2 metal gallyl compounds, but featuring a gallyl heterocycle with an acenaphthene backbone. Reductive cleavage of the gallyl dimer **1.27** with a Group 2 metal led to the synthesis of the Group 2 bis(gallyl) compounds $M\{Ga(NArC_6H_3)_2\}_2(THF)_n$ (M = Mg (**1.43**), n = 3; Ca (**1.44**), n = 4; Sr (**1.45**), n = 4; Ba (**1.46**), n = 5) (Equation 1.1).[17]

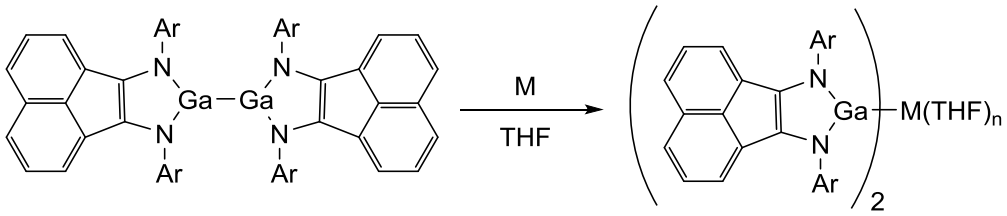

1.27

Ar = 2,6-$C_6H_3{}^iPr_2$

M = Mg, n = 3 (**1.43**)
Ca, n = 4 (**1.44**)
Sr, n = 4 (**1.45**)
Ba, n = 5 (**1.46**)

Equation 1.1

1.4 *d*-block

1.4.1 Group 4

The report in 2009 by Yamashita and Nozaki represents the first structurally authenticated Group 4 metal boryl compounds containing a two-centre, two-electron σ-bond between a Group 4 metal and boron (Scheme 1.7).[21] Reaction of the commercially available $Ti(O^iPr)_4$ with one equivalent of the boryl anion $Li\{B(NArCH)_2\}(THF)_2$ (**1.7**) resulted in the titanium boryl compound $Ti\{B(NArCH)_2\}(O^iPr)_3$ (**1.47**). It has been shown elsewhere that **1.47** can also be accessed from reaction of **1.7** and $TiCl(O^iPr)_3$.[22] Reaction of Cp^*HfCl_3 with one equivalent of **1.7**, followed by two equivalents of KCH_2Ph resulted in the corresponding hafnium boryl compound $Cp^*Hf\{B(NArCH)_2\}(CH_2Ph)_2$ (**1.48**).

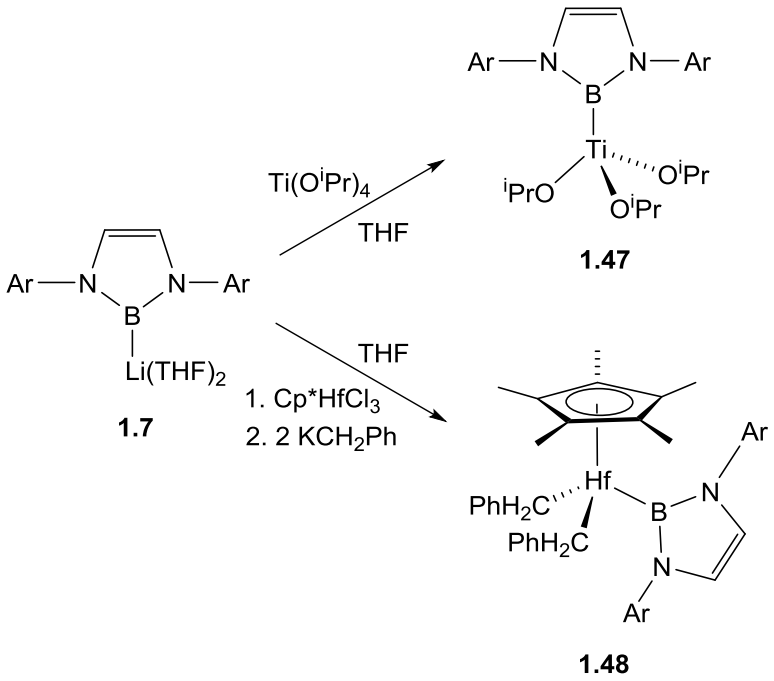

Scheme 1.7

Treatment of the titanium imido compound Cp*Ti(N^{t}Bu)Cl(py) (**1.49**) with 0.5 equivalent of [K{Ga(NArCH)$_2$}(TMEDA)]$_2$ (**1.26**) produced the titanium gallyl compound Cp*Ti{Ga(NArCH)$_2$}(N^{t}Bu)(py) (**1.50**) in 74% yield. The corresponding reaction with **1.7** resulted only in the dearomatization of pyridine to form a pyridyl borane ligand, which then went on to form Cp*Ti(NC$_5$H$_5${B(NArCH)$_2$})(N^{t}Bu)(py) (**1.51**, Scheme 1.8).[22]

With **1.36**, Jones and co-workers were able to successfully synthesise a zirconium gallyl compound *via* oxidative insertion of "Cp$_2$Zr" (made *in situ* from a mixture of Cp$_2$ZrCl$_2$ and an excess of ^{n}BuLi) into **1.36**, forming the ion pair [Li(THF)$_4$][Cp$_2$Zr{Ga(NArCH)$_2$}$_2$] (**1.52**, Equation 1.1).[23] The Zr–Ga bonds are appreciably longer (average length 2.738 Å) than in Cp$_2$Zr{Ga(C$_6$H$_3$-2,6-(2,4,6-C$_6$H$_2$ ^{i}Pr$_3$)$_2$)} (2.6350(8) Å), where the formally Ga(I) species forms a dative bond to zirconium.

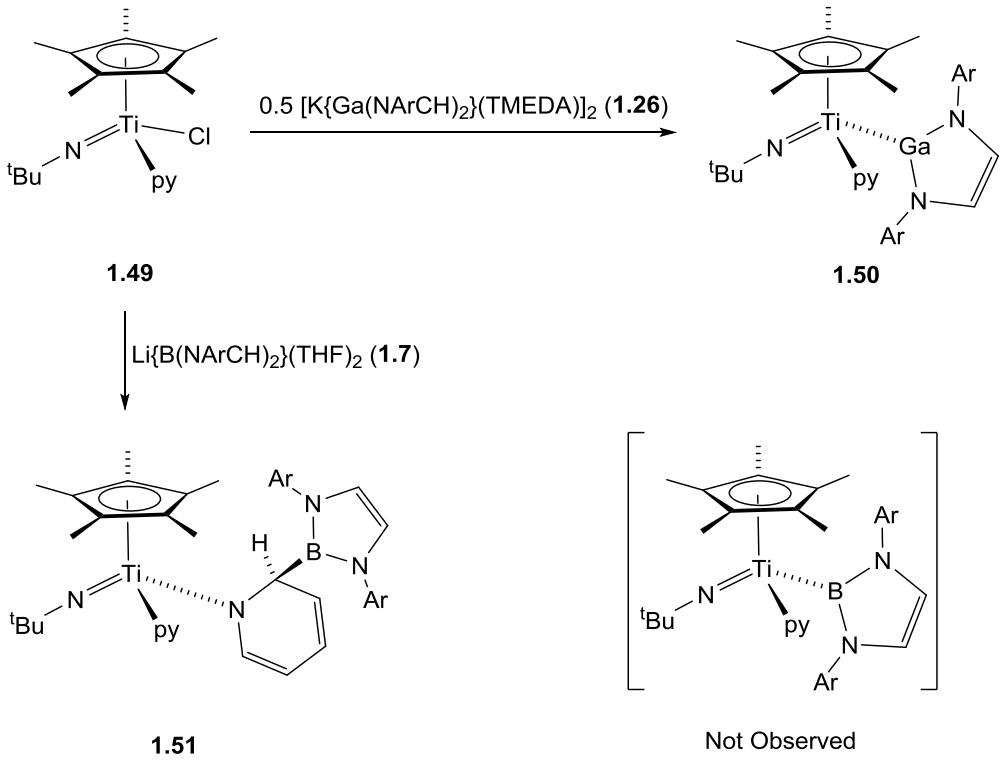

1.49 **1.50** **1.51**

Scheme 1.8. Ar = 2,6-$C_6H_3{}^iPr_2$

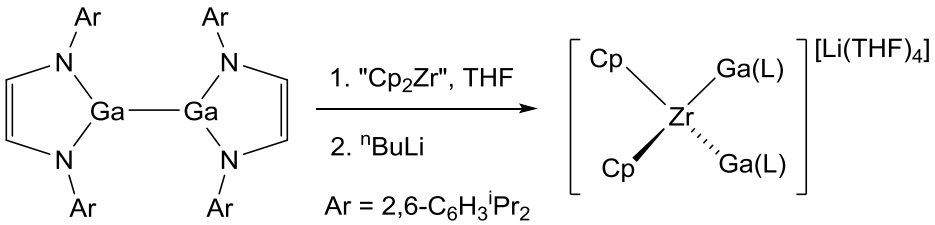

1.36 **1.52**

Equation 1.2

1.4.2 Group 5

In a report by Hartwig and co-workers, Cp_2NbH_3 was reacted with catecholborane, $HB(O_2C_6H_4)$, at 55 °C for two hours to produce, upon elimination of dihydrogen, the boryl compound $Cp_2NbH_2\{B(O_2C_6H_4)\}$ (**1.53a**). X-ray structural and spectroscopic analysis, however, reveal that although the compound remains predominantly in its boryl form, the presence of the hydrides allow for the formation of the bridging hydridoborate compound $Cp_2Nb\{(\mu\text{-}H_2)B(O_2C_6H_4)\}$ (**1.53b**, Equation 1.3).[24]

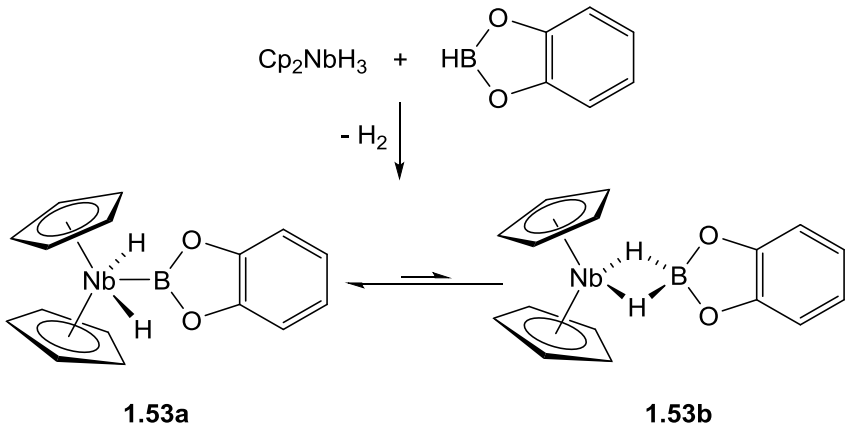

1.53a **1.53b**

Equation 1.3

The tantalocene dihydride boryl $Cp_2TaH_2\{B(O_2C_6H_4)\}$ was prepared by Smith and co-workers *via* another route (Equation 1.4). Reaction of the anionic tantalum compound $Li[Cp_2TaH_2]$ with chlorocatecholborane produced $Cp_2TaH_2\{B(O_2C_6H_4)\}$ in both *endo* (**1.54a**) (isostructural to the niobium boryl) and *exo* (**1.54b**) forms, both of which were crystallographically characterised.[25]

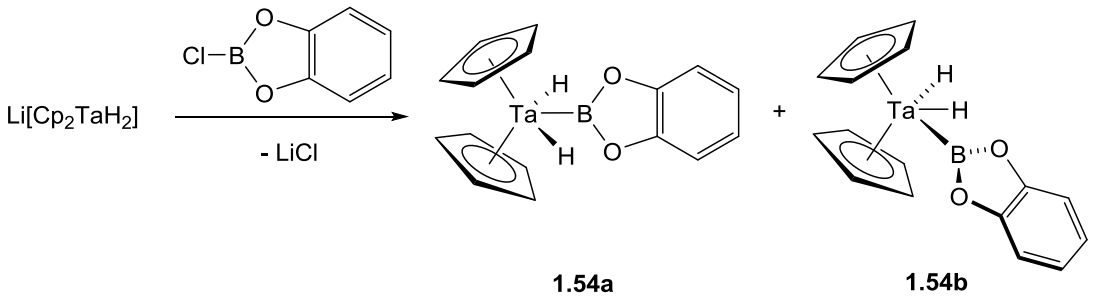

1.54a **1.54b**

Equation 1.4

A trio of neutral and ionic vanadium gallyl compounds were synthesised by Jones and co-workers (Scheme 1.9).[26] Reaction of $CpV(CO)_4$ with 0.5 eq of **1.26** produced the vanadium gallyl salt $[K(TMEDA)][CpV(CO)_3\{Ga(NArCH)_2\}]$ (**1.55**) with elimination of one equivalent of CO. Repeating the reaction with an excess of **1.26** produced only **1.55**, with the extra equivalents of **1.26** remaining unreacted. Oxidative insertion of Cp'_2V into the Ga–Ga bond of **1.36** resulted in low yields of the neutral gallyl compound $Cp'_2V\{Ga(NArCH)_2\}$ (**1.56**). It was postulated that the initial oxidative insertion resulted in a bis(gallyl) compound, which then comproportionates with Cp'_2V to produce **1.56**. In line with this hypothesis, when reactions were repeated with a 1:0.5 ratio of metal to **1.36**, good yields of **1.56** were obtained. Finally, reaction of **1.56** with 1 equivalent of **1.26** produced the vanadium bis(gallyl)

salt [K(TMEDA)(Et_2O)][Cp'_2V{$Ga(NArCH)_2$}$_2$] (**1.57**), which is closely related to the zirconium compound, **1.52**.

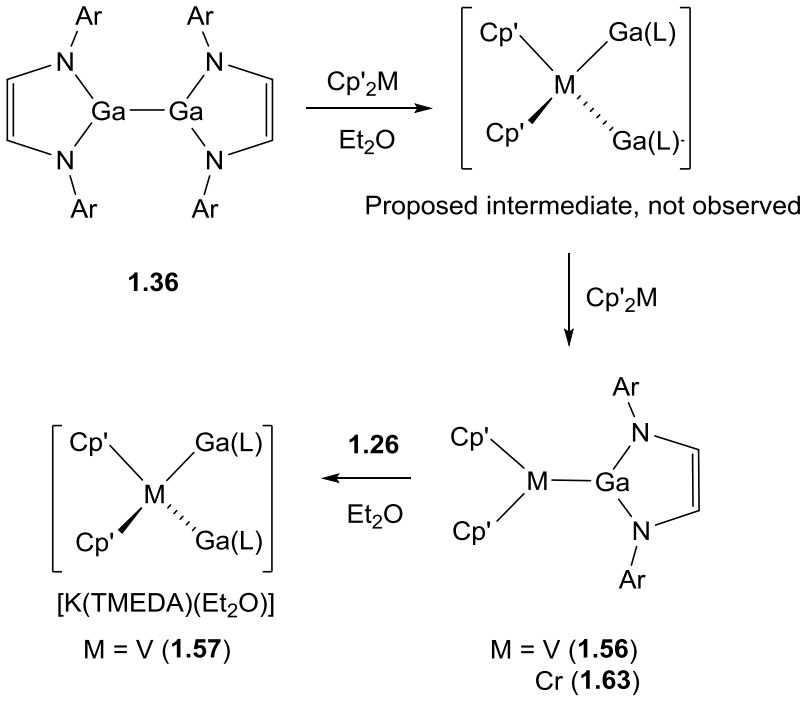

Scheme 1.9. Cp' = C_5H_4Me; Ar = 2,6-$C_6H_3{}^iPr_2$; L = $(NArCH)_2$.

1.4.3 Group 6

There are no reported chromium boryl compounds. Braunschweig and co-workers isolated and structurally authenticated the first base-free, three-coordinate molybdenum boryl compound **1.59** via an unprecedented rearrangement of the pre-formed dinuclear boryloxycarbyne **1.58** (Equation 1.5).[27] Formation of **1.58** was kinetically favourable, but rearrangement to **1.59** was possible as it is thermodynamically more favourable.

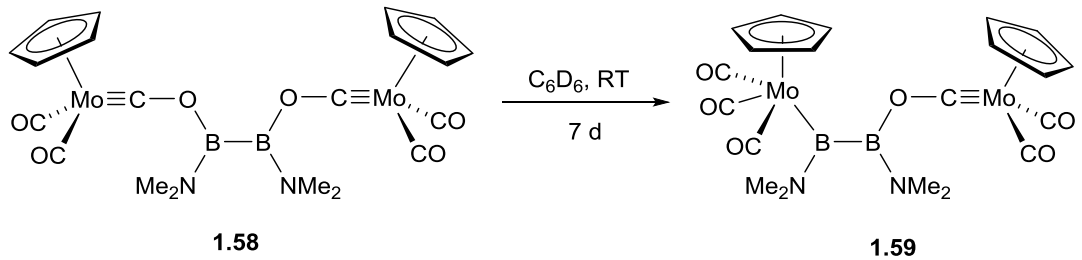

Equation 1.5

The salt metathesis reaction of the tungstenocene hydride salt {Li[Cp_2WH]}$_4$ with chlorocatecholborane produces the tungstenocene boryl hydride Cp_2WH{$B(O_2C_6H_4)$} (**1.60**, Equation 1.6).[28]

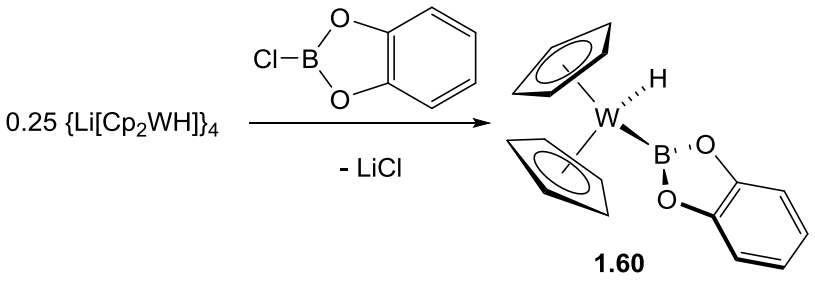

1.60

Equation 1.6

Irradiation of the tungstenocene dihydride Cp_2WH_2 delivers the highly reactive intermediate $[Cp_2W]$, which is known to oxidatively add C–H bonds of arenes. Generation of this intermediate in the presence of $B_2(4\text{-}C_6H_3O_2{}^tBu)_2$ produces the bisboryl tungstenocene $Cp_2W\{B(4\text{-}C_6H_3O_2{}^tBu)\}_2$ (**1.61**, Scheme 1.10). The W–B bond lengths in **1.60** (2.190(7) Å) and **1.61** (2.19(19) and 2.23(1) Å) were found to be similar.[29]

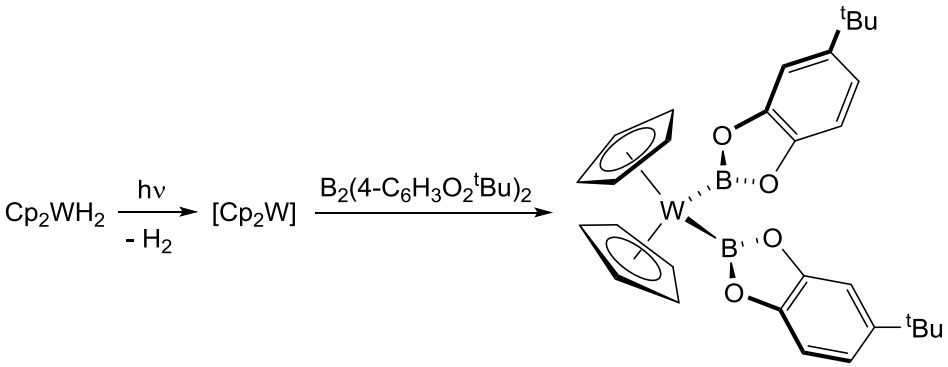

1.61

Scheme 1.10

The tungsten boryl compound $Cp^*W(CO)_3\{B(3,5\text{-}C_6H_2O_2Me_2)\}$ (**1.62**, Scheme 1.11) has been shown to engage in the remarkable selective functionalization of alkanes at the terminal position. Irradiation of solutions of **1.62** in the presence of alkanes produces the corresponding terminally borylated alkanes in moderate to excellent yields.[30]

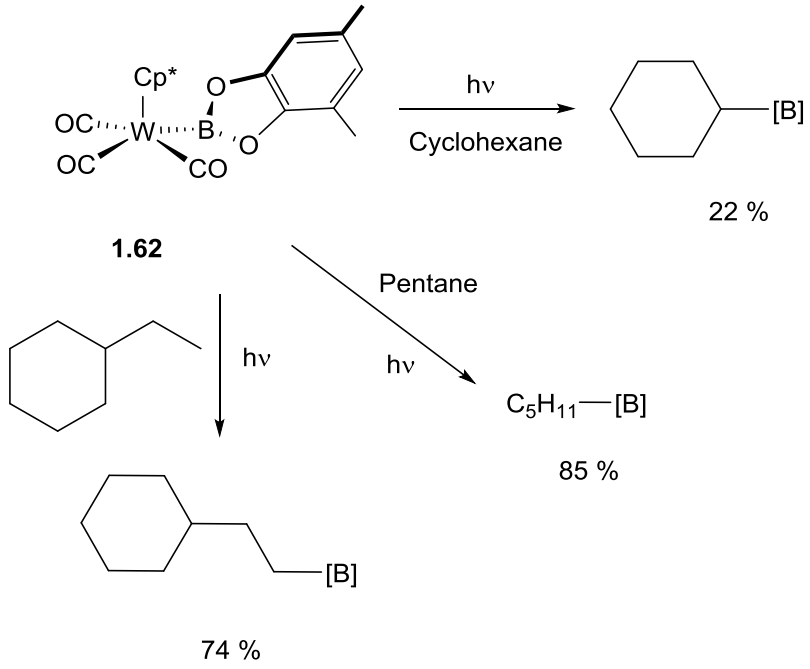

Scheme 1.11. Compound **1.62** and selected products of alkane activation with yields. [B] = B(3,5-$C_6H_2O_2Me_2$).

The only known Group 6 metal gallyl compound was produced in a reaction identical to that which produced **1.56**. Oxidative insertion of Cp'$_2$Cr into the Ga–Ga bond of **1.36** resulted in the formation of Cp'$_2$Cr{Ga(NArCH)$_2$} (**1.63**, Scheme 1.9).[26]

1.4.4 Group 7

Salt metathesis was again employed to synthesise the Group 7 boryls M(CO)$_5${B($O_2C_6H_4$)} (M = Mn (**1.64**) or Re (**1.65**)).[31] Thus, reaction of the carbonylate salt Na[M(CO)$_5$] with chlorocatecholborane resulted in the formation of **1.64** and **1.65** in moderate to good yields. These compounds were also shown to activate arene and alkene C–H bonds, producing the boryl alkanes in good yields.

Irradiation and subsequent reaction of a mixture of Cp'Mn(CO)$_3$ and **1.26** in THF resulted in the half-sandwich manganese gallyl compound [K(TMEDA)][Cp'Mn(CO)$_2${Ga(NArCH)$_2$}] (**1.66**, Equation 1.7), with the reaction stoichiometry mirroring that of the synthesis of **1.55**.[26] The solid state structure revealed a cyclic dimer, featuring isocarbonyl bridging from the carbonyl groups to a potassium that is η^2-coordinated to the arene of the heterocycle.

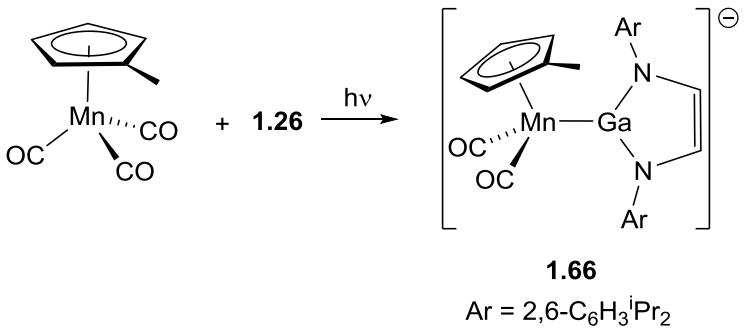

1.66

Ar = 2,6-$C_6H_3{}^iPr_2$

Equation 1.7

Reactions of Cp'_2Mn with **1.26** failed to produce gallyl compounds in the manner of **1.56** and **1.63**. However, use of the manganese dialkyl compound $Mn\{CH(SiMe_3)_2\}_2$ produced the corresponding manganese gallyl compound $[K(TMEDA)][Mn\{CH(SiMe_3)_2\}_2\{Ga(NArCH)_2\}]$ (**1.67**) in moderate yields. The molecular structure revealed an additional η^5-interaction between the TMEDA-chelated potassium cation and the anionic gallyl heterocycle.[26]

1.4.5 Group 8

Due to the vast number of known Group 8 metal boryl compounds, only leading examples will be discussed. More detailed accounts are provided in several excellent reviews in the area.[32-34]

The first structurally characterised examples of compounds featuring an Fe–B bond were isolated by Hartwig and Huber. The iron boryls $CpFe(CO)_2\{B(O_2C_6H_4)\}$ (**1.68**) and $CpFe(CO)_2(BPh_2)$ (**1.69**) were the products of salt metathesis reactions between NaFp (Fp = $CpFe(CO)_2$) and $ClB(O_2C_6H_4)$ and Ph_2BBr, respectively (Scheme 1.12).[35]

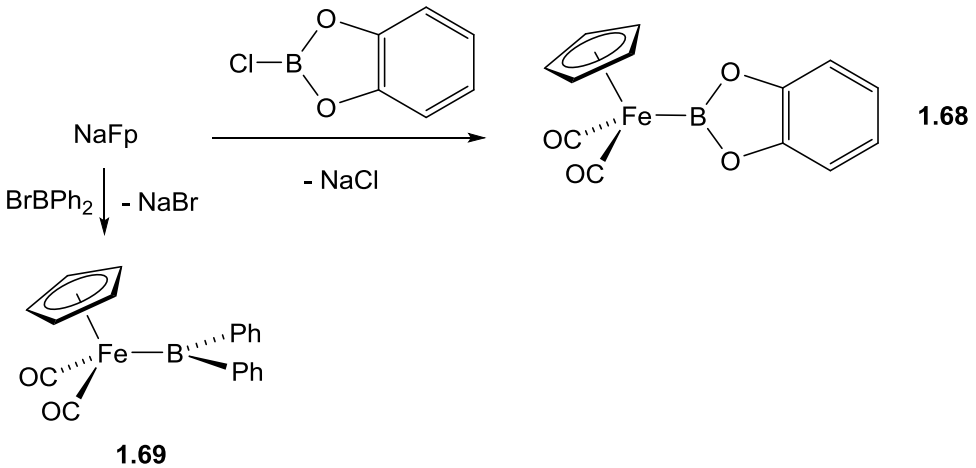

Scheme 1.12

It was noted that the ^{11}B NMR chemical shift for **1.69** (δ 121 ppm) did not correspond to that which had been reported by Nöth and Schmid (δ 37 ppm) for a compound assigned a similar structure. In their review of transition metal boryl compounds,[33] Marder and co-workers concluded that, due to the weight of evidence of recent results, many of the compounds formulated by Nöth and Schmid based on spectroscopic studies alone should be treated with caution.

Of particular interest was the difference in Fe–B bond lengths in **1.68** and **1.69**, which are 1.959(6) Å and 2.034(3) Å respectively. A combined crystallographic, spectroscopic and chemical investigation led to the conclusion that **1.68** had a weak (but significant) π-bond which was a result of the boryl ligand being orientated in such a way as to allow overlap of the HOMO of Fp^- and the boron 2*p*-orbital.[35] This π-interaction geometry is typical for Fp and metal fragments isoelectronic with Fp,[36, 37] and results in a shorter than expected Fe–B bond length for **1.68**. However, for **1.69** the steric effect of the bulky phenyl groups overcomes the preference for the usual geometry, resulting in the absence of an interaction with the Fp-HOMO, producing a longer bond length. Subsequent theoretical studies by Braunschweig and Aldridge and Willock have shown that such π-interactions only occur weakly in very specific cases where conditions are favourable (such as in **1.68**).[38] Due to the vacant boryl-centred π-orbital being high in energy, boryl ligands are strong σ-donors, but weak π-acceptors.

Whilst Roper and Wright synthesised the first ruthenium boryl compounds,[39] Braunschweig and co-workers reported the first crystallographically characterised example, $CpRu(CO)_2\{B(NMe_2)\{B(NMe_2)Br\}\}$ (**1.70**, Equation 1.8) which features a diborane(4)yl ligand.[40]

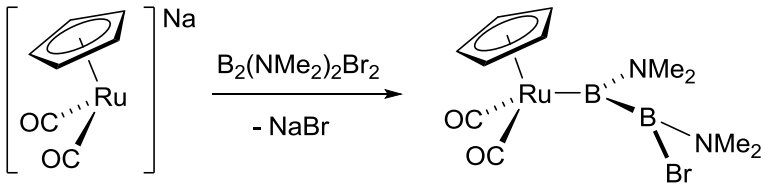

1.70

Equation 1.8

As with **1.69**, it was noted that the non-conventional geometry of the ligand coordinated to the Rp fragment (Rp = $CpRu(CO)_2$) indicated the absence of a Ru–B

π-interaction. Compound **1.70** shows remarkable stability, with solutions in hexane and benzene showing no decomposition after several days under ambient conditions, and can even be handled in air for short periods of time.

Roper and Wright reported the first crystallographically characterised osmium boryl compounds,[41] two of which will be described. The previously reported[39] compound $OsCl(CO)\{B(O_2C_6H_4)\}(PPh_3)_2$ (**1.71**) was found to have a square-based pyramidal geometry, with the boryl ligand in the apical position.

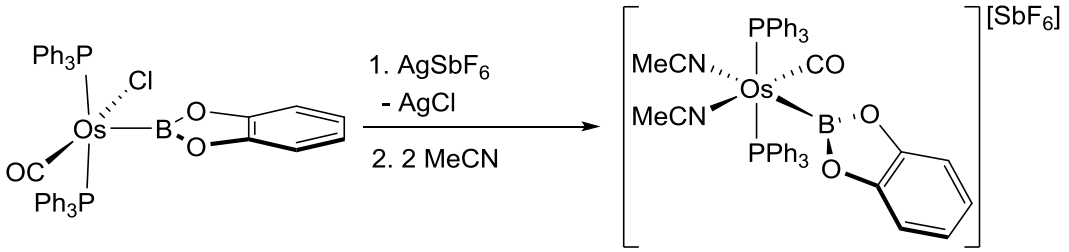

1.71 **1.72**

Equation 1.9

Chloride abstraction, followed by addition of acetonitrile produced the six-coordinate cationic compound $[Os(CO)\{B(O_2C_6H_4)\}(PPh_3)_2(MeCN)_2][SbF_6]$ (**1.72**, Equation 1.9), with a molecule of acetonitrile coordinated *trans* to the boryl ligand. This, along with possible effects of the overall positive charge on the complex, was the proposed by the authors as a reason for the observed increase in the Os–B bond length in **1.72** (2.094(5) Å) compared to **1.71** (2.019(3) Å).

Whilst it was shown that **1.68** could react under photolytic conditions with arenes and alkenes to produce their borylated counterparts, it remained unreactive towards alkanes. It was proposed by Hartwig that the lack of reactivity of **1.68** towards alkanes was due to irradiated **1.68** preferentially reacting with another molecule of **1.68** at its sp^2-hybridized positions. Therefore, replacing Cp and $B(O_2C_6H_4)$ with Cp* and $B(3,5\text{-}O_2C_6H_2Me_2)$ to produce $Cp^*Fe(CO)_2\{B(3,5\text{-}O_2C_6H_2Me_2)\}$ (**1.73**) ensured methyl groups were positioned on the sp^2-hybridized carbon atoms in place of hydrogen, and allowed the selective functionalisation of alkanes in a manner similar to that of **1.62**, albeit with significantly reduced yields.[30]

Power and co-workers synthesised an iron gallyl compound $Fe(CO)_4\{Ga(NacNac)\}$ (**1.74**, Fig. 1.2) by reacting a neutral, six-membered gallium(I) heterocycle with $Fe(CO)_5$ at room temperature.[42] In the same year, Jones and co-workers reported the

synthesis of the iron gallyl salt [K(TMEDA)][Fe(CO)$_4${Ga(NArCH)$_2$}] (**1.75**).[43] Compound **1.75** forms a polymeric structure in the solid state, with isocarbonyl bridging to a potassium that is coordinated to a molecule of TMEDA and to one of the arenes of the heterocycle through an η^2-interaction. In both **1.74** and **1.75**, the authors conclude that there is very little iron to gallium back-bonding involved.

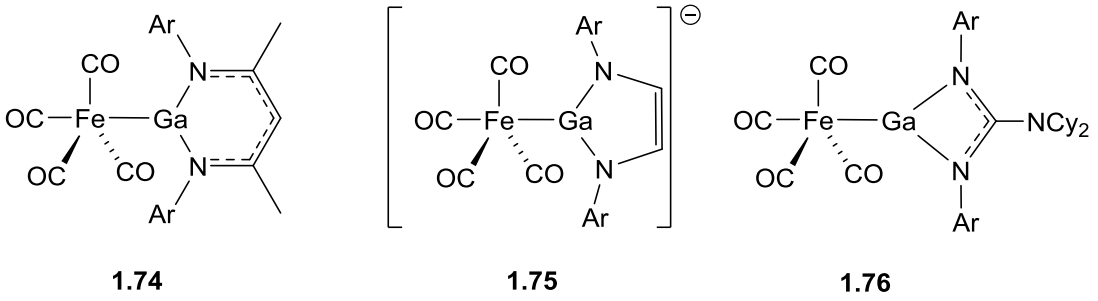

Figure 1.2. Iron gallyl compounds (Ar = 2,6-$C_6H_3{}^iPr_2$). $[K(TMEDA)]^+$ for **1.75** omitted for clarity

Jones and co-workers have also isolated an iron gallyl derivative similar to **1.74**, replacing the six-membered gallium heterocycle with a four-membered gallium heterocycle to form Fe(CO)$_4${Ga(NAr)$_2$C(NCy$_2$)} (**1.76**).[44] The compound is neutral as the four-membered gallium heterocycle is not anionic, forming a dative bond between iron and gallium.

1.4.6 Group 9

The first cobalt boryl compound to be structurally authenticated was reported by Marder and Norman. Oxidative addition of {B(O$_2$C$_6$H$_4$)}$_2$ to the Co(0) compound Co(PMe$_3$)$_4$ results in the cobalt(II) bis(boryl) species Co(PMe$_3$)$_3${B(O$_2$C$_6$H$_4$)}$_2$ (**1.77**, Figure 1.3).[45]

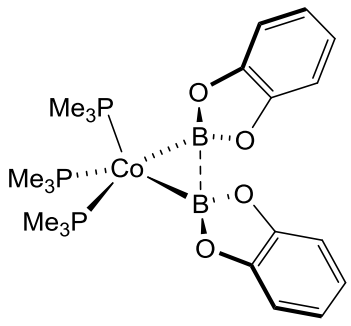

1.77

Figure 1.3

In their structural analysis, the authors argue that **1.77** could be described as either a distorted square-based pyramid, or, because of the close approach of the two boron atoms (B1−B2 (**1.77**) = 2.185 Å, *cf.* B1−B2 ({$B(O_2C_6H_4)$}$_2$) = 1.678(3) Å[46]), a distorted tetrahedron in which the two boryl ligands occupy one coordination site. The authors conclude that, due to the unknown degree of B–B interaction, **1.77** lies part way along an oxidative addition reaction pathway.[45]

The rhodium(III) boryl compound $RhHCl(P^iPr_3)_2\{B(O_2C_6H_4)\}$ (**1.78**) was isolated by Marder and Norman after reacting $RhCl(N_2)(P^iPr_3)_2$ and catecholborane (Equation 1.10).[47]

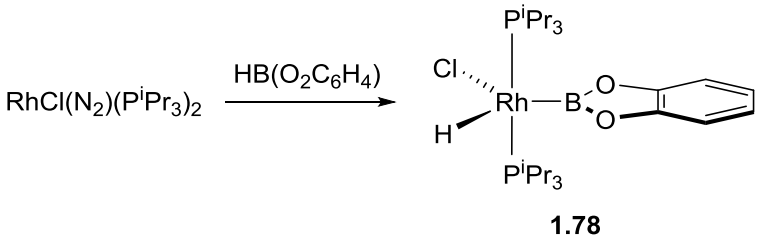

1.78

Equation 1.10

In attempting the synthesis of a rhodium(I) boryl compound, the reaction of $Rh\{(P^iPr_2CH_2)_2\}(\eta^3\text{-}2\text{-}C_3H_4Me)$ with catecholborane resulted in the formation of a $[B(O_2C_6H_4)_2]^-$ anion, which then coordinates in an η^6 fashion to the rhodium centre *via* one of the arene rings to form **1.79**.[48] In a later report by the same authors, oxidative addition of {$B(O_2C_6H_4)$}$_2$ to $RhMe(PMe_3)_4$ resulted, after rapid reductive elimination of $MeB(O_2C_6H_4)$, in the formation of the rhodium(I) boryl compound $Rh(PMe_3)_3\{B(O_2C_6H_4)\}$ (**1.80**, Figure 1.4).[47]

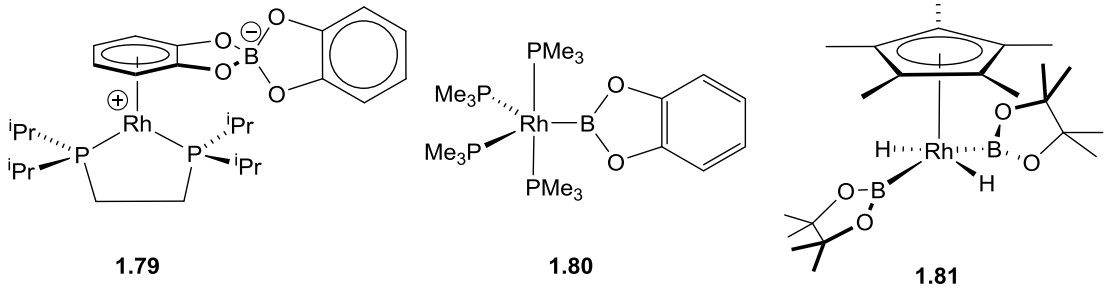

1.79 **1.80** **1.81**

Figure 1.4

Hartwig and co-workers reported an *in situ* generated rhodium bis(boryl) compound $Cp^*Rh(H)_2\{B(O_2C_2Me_4)\}_2$ (**1.81**, Figure 1.4) that behaves as a catalyst for the borylation of alkanes.[49] In a later report, they were able to structurally characterise

this species, finding it adopts a *trans*, four-legged piano stool structure in the solid state, matching that deduced from multinuclear NMR spectroscopy. A number of structural and spectroscopic features led to the conclusion that **1.81** contains significant B-H bonding.[50]

The first structurally authenticated transition metal-boron bonds were those featuring iridium-boron interactions. Merola reported the oxidative addition reaction of $HB(O_2C_6H_4)$ to $IrCl(COE)(PMe_3)_3$ to produce $IrHCl(PMe_3)_3\{B(O_2C_6H_4)\}$ (**1.82**),[51] whilst Baker and Marder prepared $Ir(H)_2(PMe_3)_3\{B(C_8H_{14})\}$ (**1.83**) from $IrH(PMe_3)_4$ and 9-BBN dimer, eliminating $Me_3P–BC_8H_{14}$ in the process (Figure 1.5).[52]

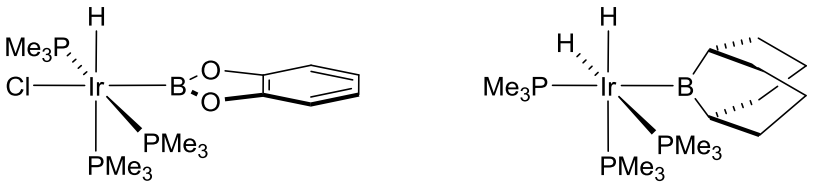

1.82 **1.83**

Figure 1.5

The difference in Ir–B bond length between **1.82** (2.023(10) Å) and **1.83** (2.500(2) Å) can be explained by analysing the structural features of both. Compounds **1.82** and **1.83** both adopt distorted octahedral arrangements in the solid state, with the trimethylphosphines arranged meridionally and facially in **1.82** and **1.83** respectively. For **1.82**, this means that a chloride lies *trans* to the boryl, whereas a trimethylphosphine lies *trans* to the boryl in **1.83**. The greater *trans* influence of PMe_3 results in bond lengthening in **1.83**.

The cobalt gallyl compound $[K(TMEDA)][CpCo(CO)\{Ga(NArCH)_2\}]$ (**1.84**, Figure 1.6) was prepared in a similar fashion to **1.55** and **1.66**. Figure 1.6 shows **1.84** as a monomer with the metal counterion omitted, but the solid state structure of **1.84** is a cyclic dimer, featuring a η^2-interaction between potassium and a carbonyl coordinated to cobalt.[26]

Jones and co-workers isolated the Group 9 gallyl compounds $M(COD)\{C(NAr'CH)_2\}\{Ga(NArCH)_2\}$ (M = Rh (**1.85**) or Ir (**1.86**), Figure 1.6) in moderate to good yields from the reaction of **1.26** with $MCl(COD)\{C(NAr'CH)_2\}$. Compounds **1.85** and **1.86** are monomeric and isostructural, each having a distorted square planar metal centre.[53]

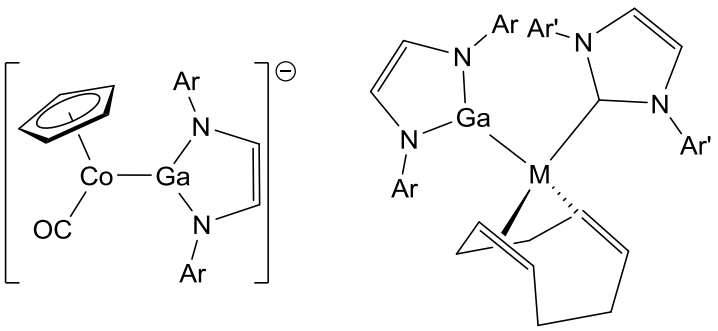

1.84 M = Rh (**1.85**) or Ir (**1.86**)

Figure 1.6. Ar = 2,6-$C_6H_3{}^iPr_2$ and Ar' = 2,4,6-$C_6H_2Me_3$. $[K(TMEDA)]^+$ omitted for clarity.

1.4.7 Group 10

The outstanding significance of the Suzuki coupling in organic synthesis has led to an explosion of interest in the boryls of Group 10. The first structurally authenticated nickel boryl compound was synthesised by Mindiola and co-workers in 2007. Reaction of the 'PNP' supported nickel hydride $NiH\{N(ArP^iPr_2)_2\}$ with catecholborane resulted in the elimination of H_2 and the formation of the nickel boryl compound $Ni\{N(ArP^iPr_2)_2\}\{B(O_2C_6H_4)\}$ (**1.87**, Ar = 4-C_6H_3Me, Scheme 1.13).[54]

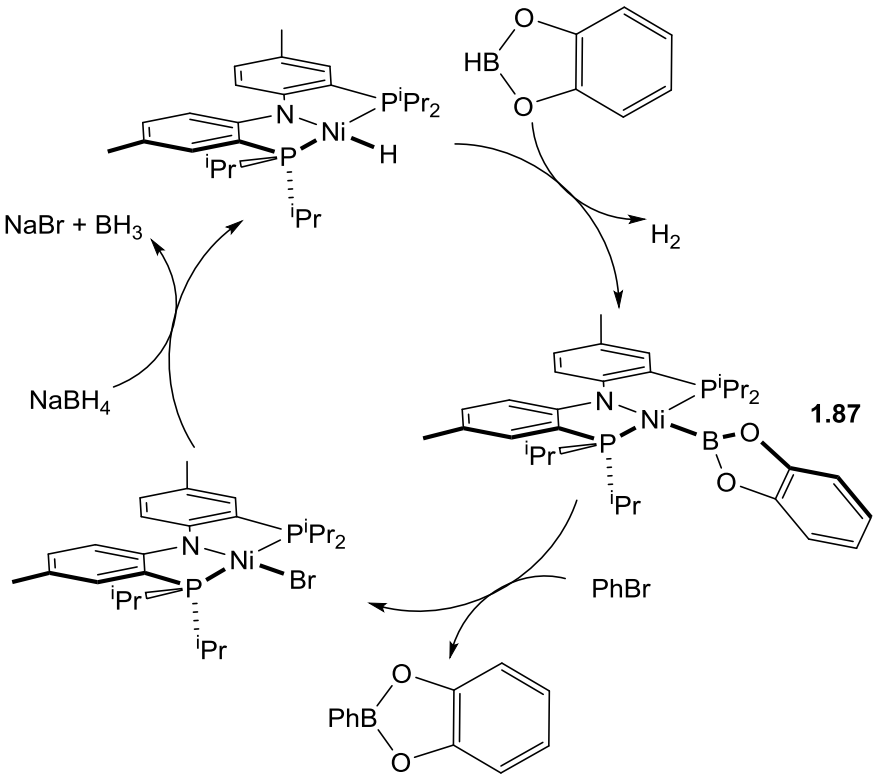

Scheme 1.13

Compound **1.87** was then shown to engage in the borylation of bromobenzene, with the resultant $NiBr\{N(ArP^iPr_2)_2\}$ reacting with $NaBH_4$ to regenerate $NiH\{N(ArP^iPr_2)_2\}$, formally completing the cycle. However, the process was found not to be catalytic, as the addition of 10-20 mol% $NiBr\{N(ArP^iPr_2)_2\}$, catecholborane and $NaBH_4$ in the presence of bromobenzene did not produce the borylated product $PhB(O_2C_6H_4)$ and $NiH\{N(ArP^iPr_2)_2\}$, but instead reformed $NiBr\{N(ArP^iPr_2)_2\}$ and benzene. It was proposed that the rate of reaction of $NiH\{N(ArP^iPr_2)_2\}$ with bromobenzene is comparable with that of the borylation reaction to form **1.87** (Scheme 1.13).[54]

The palladium boryl $Pd(DMPE)_2(SnMe_3)\{B(NMeCH_2)_2\}$ (**1.88**, Equation 1.12) was prepared by adding multiple equivalents of the tin(IV) boryl compound $SnMe_3\{B(NMeCH_2)_2\}$ to $Pd(DMPE)_2Me_2$ under forcing conditions.[55] The compound served as a model for the suspected intermediate in the catalytic synthesis of (stannylalkenyl)boranes from a mixture of a Pd(0) pre-catalyst, the tin(IV) boryl and an alkyne. It was found that use of **1.88** as a catalyst does indeed form the desired (stannylalkenyl)boranes in good yields.[55]

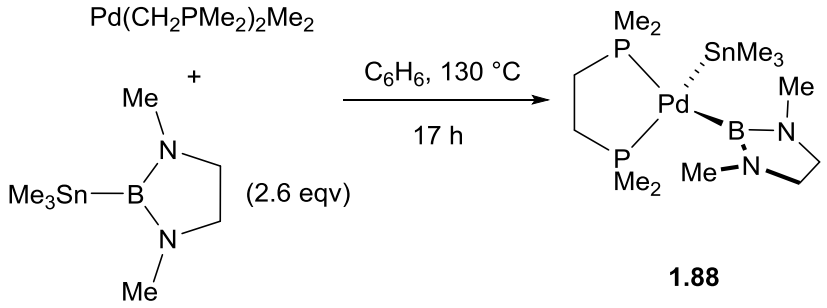

Equation 1.12. By-products omitted for clarity.

The most extensively studied boryl compounds of Group 10 involve platinum, with the method of choice in preparing these compounds involving oxidative addition of a B–X bond into a low oxidation state platinum compound. The first structurally authenticated platinum bis(boryl) was $Pt(PPh_3)_2\{B(O_2C_6H_4)\}_2$ (**1.89**, Equation 1.13) synthesised by Iverson and Smith, *via* the oxidative addition of $\{B(O_2C_6H_4)\}_2$ to the 'masked' platinum(0) compound $Pt(PPh_3)_2(\eta^2\text{-}C_2H_4)$ and concomitant release of ethylene.[56] Care had to be taken in the choice of olefin used in the platinum precursor as some coordinated olefins were found to be non-innocent and reacted with $\{B(O_2C_6H_4)\}_2$ rather than behaving as innocent leaving groups.

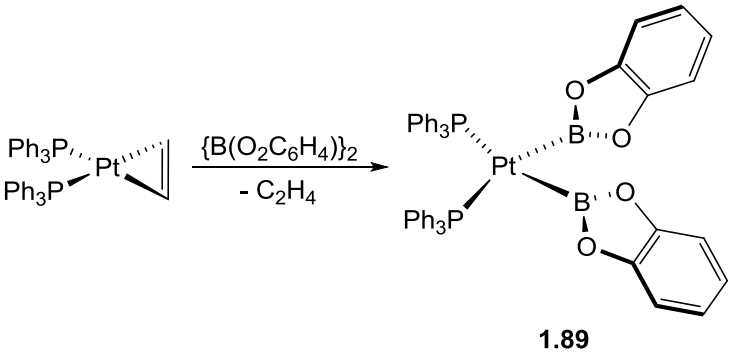

1.89

Equation 1.13

The group of Braunschweig has, in particular, advanced the chemistry of platinum boryl compounds. Amongst many remarkable compounds, the synthesis of a cationic three-coordinate platinum boryl compound, $[Pt(PCy_3)_2\{BBr(Fc)\}][B(C_6F_5)_4]$ (**1.90**, Equation 1.14) was particularly impressive as the low-coordinate platinum centre did not require any additional solvent or anion coordination to stabilise it, either in the solution or solid states. Upon addition of the neutral base 4-methylpyridine to **1.90**, transfer of the bromide from the boryl moiety to the platinum metal centre occurred, with 4-methylpyridine coordinating to boron to produce the base-stabilised borylene **1.91** (Equation 1.14).[57]

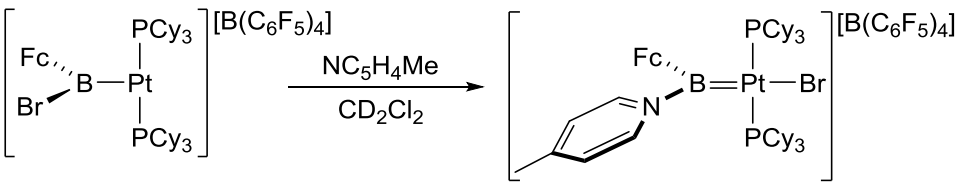

1.90 **1.91**

Equation 1.14

A series of Group 10 metal gallyl compounds have been synthesised by Jones and co-workers, some of which will be described here. The salt metathesis reactions of **1.26** with $MCl_2(PEt_3)_2$ produced the corresponding gallyl compounds $M(PEt_3)_2\{Ga(NArCH_2)_2\}_2$ (M = Ni (**1.92**), Pd (**1.93**) or Pt (**1.94**), Equation 1.15). All of the compounds are isostructural, and have the gallyl ligands *trans* to each other in a slightly distorted square planar arrangement.[58]

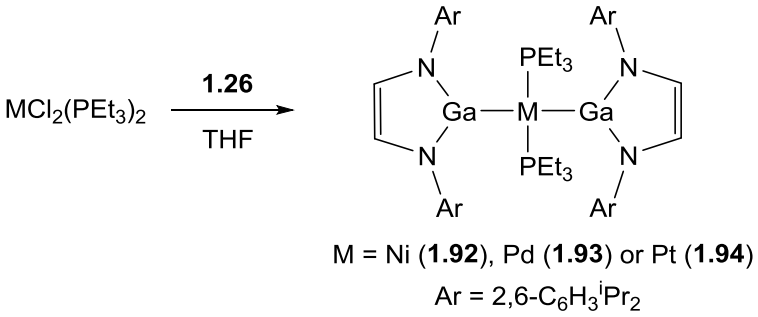

Equation 1.15

Fischer and co-workers isolated a series of Group 10 gallyl compounds featuring dative bonds between Group 10 metals and the neutral gallium(I) compound Ga(NacNac) and a variety of olefins as supporting ligands,[59, 60] whilst Jones and co-workers synthesised similar Group 10 compounds with the neutral gallium(I) guanidinate $Ga(NAr)_2C(NCy_2)$ species.[61]

1.4.8 Group 11

It was only within the last decade that the boryl chemistry of the Group 11 metals could be explored. The first structurally authenticated example of a Group 11 boryl compound was isolated by Sadighi and co-workers in 2005, with the use of an N-heterocyclic carbene (NHC) stabilised copper(I) alkoxide, $Cu(O^tBu)\{C(NArCH)_2\}$. Reaction with $\{B(O_2C_2Me_4)\}_2$ results in the formation of the copper(I) boryl compound $Cu\{C(NArCH)_2\}\{B(O_2C_2Me_4)\}$ (**1.95**) and $^tBuOB(O_2C_6H_4)$.[62] Subsequent studies showed remarkable reactivity. Addition of CO_2 at atmospheric pressure resulted in rapid oxygen abstraction and concomitant release of CO, as confirmed by ^{13}C labelling studies. The resultant copper compound was revealed to be the borate $Cu\{C(NArCH)_2\}\{OB(O_2C_2Me_4)\}$ (**1.96**, Equation 1.16). Addition of $\{B(O_2C_2Me_4)\}_2$ regenerates **1.95** and eliminates $O\{B(O_2C_2Me_4)\}_2$, closing the formal catalytic cycle.[62]

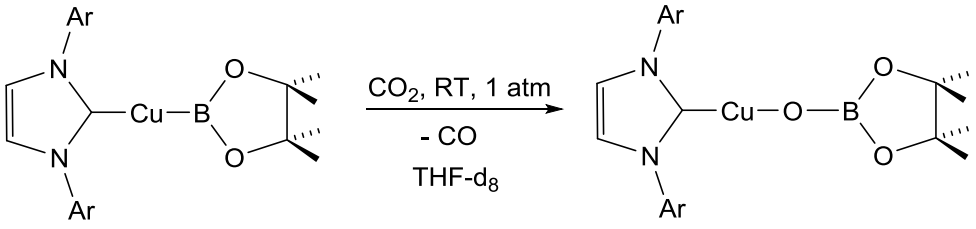

1.95 **1.96**

Equation 1.16

With the isolation of the boryl anion **1.7**,[10, 11] a new route to the synthesis of Group 11 boryls was available. Segawa, Yamashita and Nozaki showed that simple salt metathesis of the NHC or phosphine stabilised Group 11 metal(I) chlorides could produce the corresponding Group 11 metal(I) boryls M{C(NAr'CH)$_2$}{B(NArCH)$_2$} (M = Cu (**1.97**), Ag (**1.98**) or Au (**1.99**)) and Au(PPh$_3$){B(NArCH)$_2$} (**1.100**, Scheme 1.14).[63] In order to establish whether or not the σ-donor ability of the boryl would be affected by changing to a saturated version of **1.7**, **1.8** was also used with the same starting materials to produce the Group 11 metal(I) boryls M{C(NAr'CH)$_2$}{B(NArCH$_2$)$_2$} (M = Cu (**1.101**), Ag (**1.102**) or Au (**1.103**)) and Au(PPh$_3$){B(NArCH$_2$)$_2$} (**1.104**, Scheme 1.8). It was found that the σ-donor ability of the boryl did not change significantly.[63]

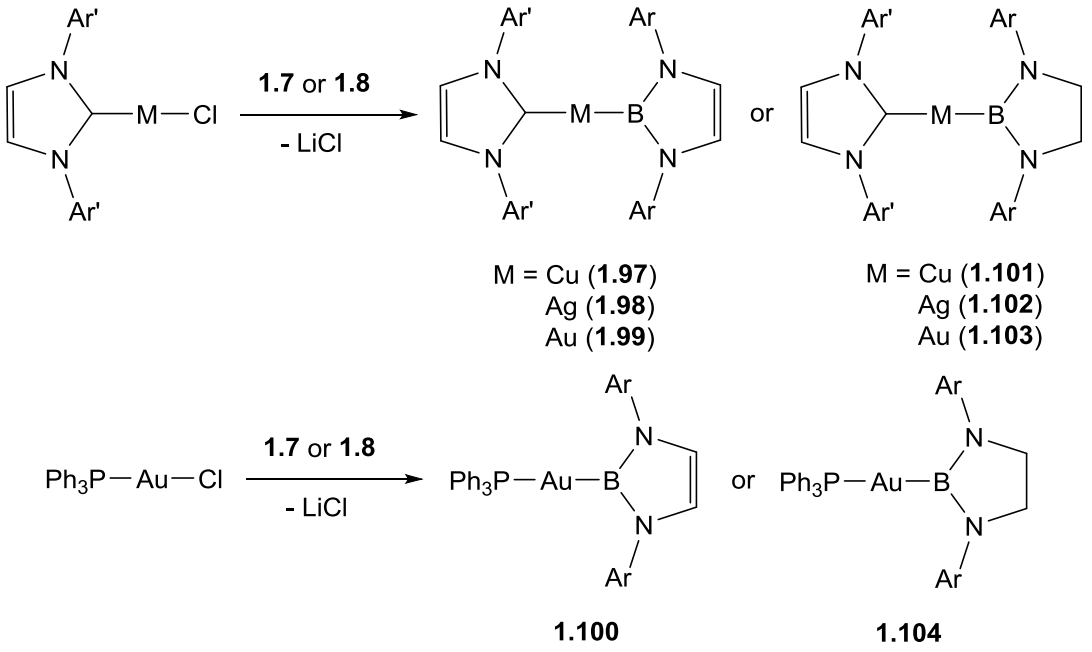

Scheme 1.14. Ar' = 2,4,6-C$_6$H$_2$Me$_3$ and Ar = 2,6-C$_6$H$_3$^{i}Pr$_2$.

In synthesising Group 11 metal gallyls, Jones and co-workers took a similar approach to the group of Yamashita and Nozaki and used the same starting compounds to effect a salt metathesis with **1.26** and produce the corresponding metal(I) gallyl compounds M{C(NAr'CH)$_2$}{Ga(NArCH)$_2$} (M = Cu (**1.105**), Ag (**1.106**) or Au (**1.107**), Equation 1.17).[53]

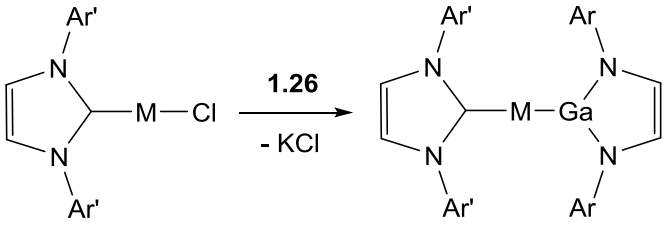

M = Cu (**1.105**), Ag (**1.106**) or Au (**1.106**)

Ar' = 2,4,6-$C_6H_2Me_3$ and Ar = 2,6-$C_6H_3{}^iPr_2$

Equation 1.17

1.4.9 Group 12

The first structurally authenticated Group 12 boryl compounds were zinc derivatives reported by Yamashita and Nozaki and co-workers, producing a mono(boryl) bromozincate Zn{B(NArCH$_2$)$_2$}(THF)(μ-Br)$_2$Li(THF)$_2$ (**1.108**) and the bis(boryl) zinc compounds Zn{B(NArCH)$_2$}$_2$ (**1.109**) and Zn{B(NArCH$_2$)$_2$}$_2$ (**1.110**) upon reaction of the appropriate equivalents of **1.7** and **1.8** with $ZnCl_2$ and $ZnBr_2$ (Scheme 1.15).[64]

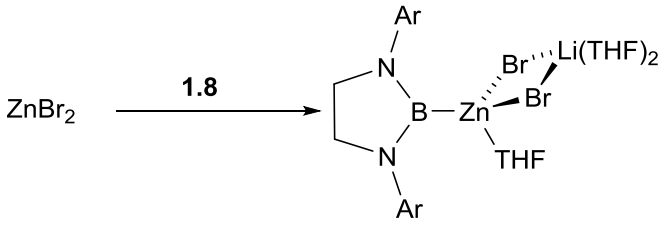

1.108

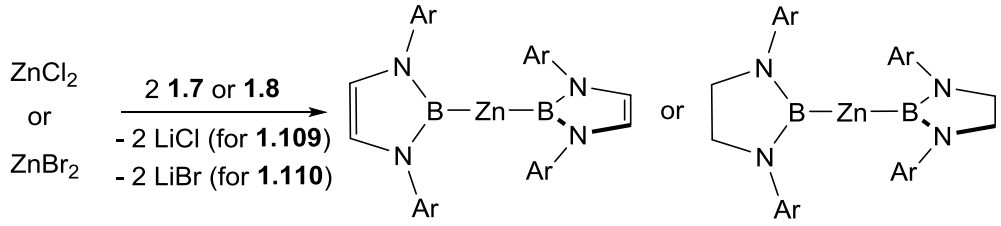

1.109 **1.110**

Scheme 1.15. Ar = 2,6-$C_6H_3{}^iPr_2$.

Aldridge, Jones and co-workers isolated the first cadmium and mercury boryl compounds (Scheme 1.16).[65] Reaction of varying equivalents of **1.7** resulted in either mono- or bis-boryl compounds of both metals, whilst addition of one equivalent of

1.26 to the mono-boryl compounds **1.112** and **1.115** resulted in the mixed boryl-gallyl compounds **1.113** and **1.116**.

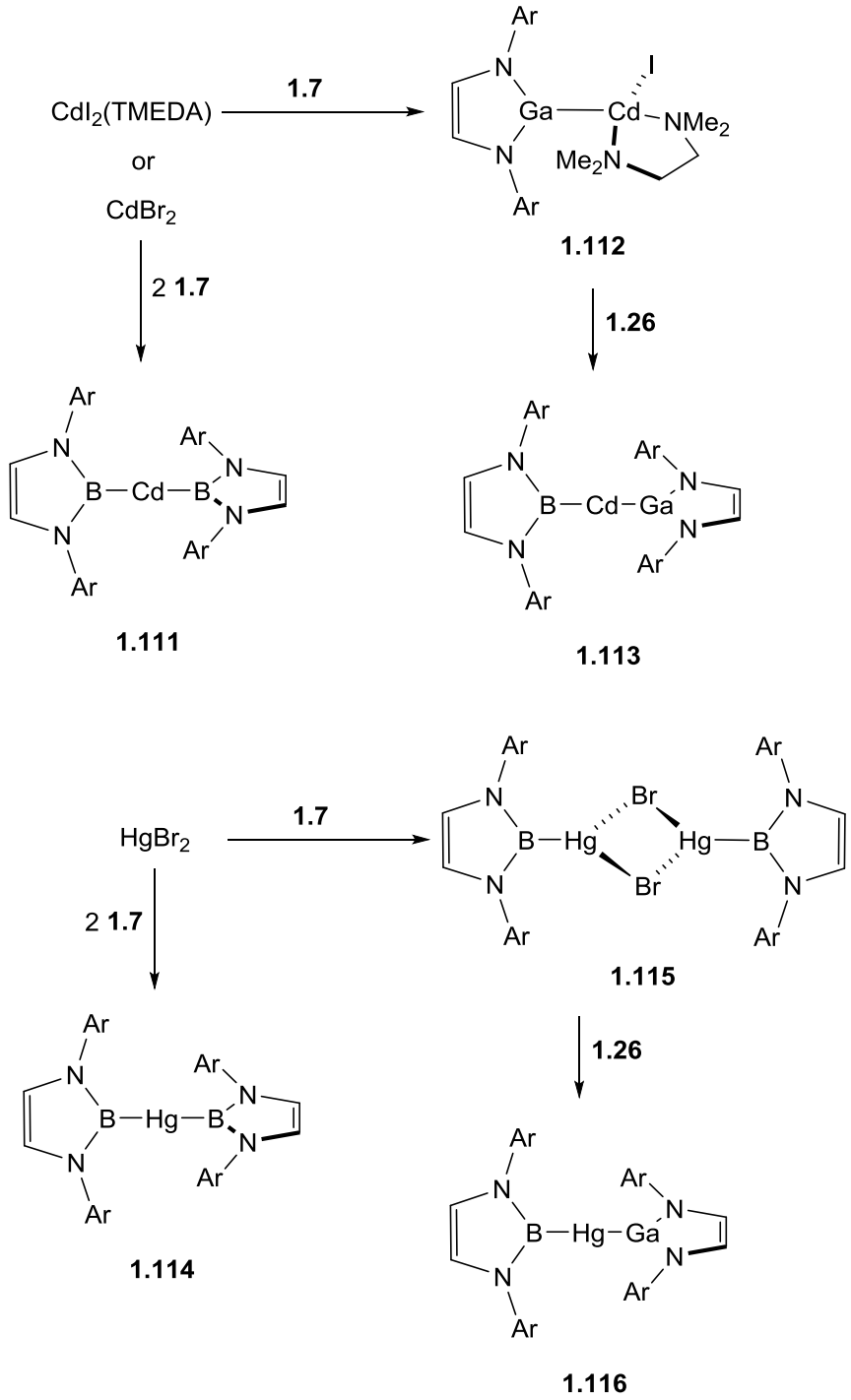

Scheme 1.16. Ar = 2,6-$C_6H_3{}^iPr_2$.

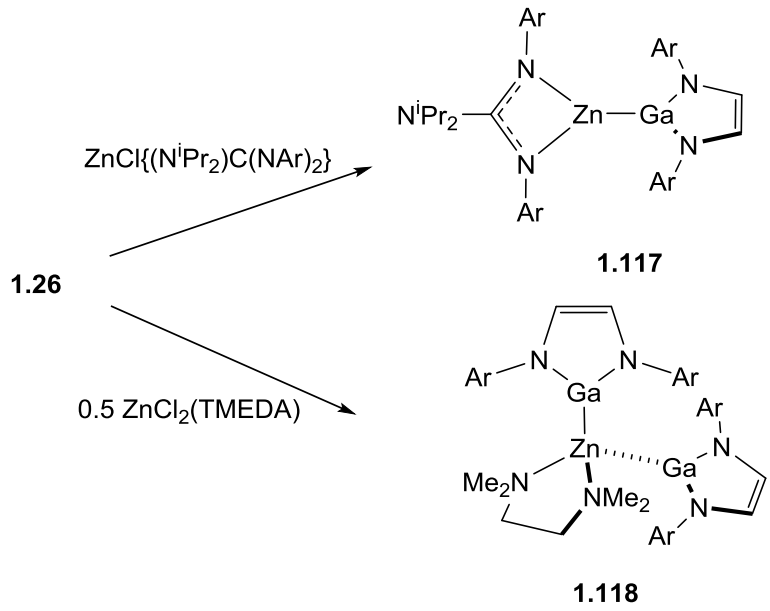

Scheme 1.17. By-products omitted for clarity. Ar = 2,6-$C_6H_3{}^iPr_2$.

In 2007, Jones and co-workers reported the isolation of the zinc gallyl compounds $Zn\{(N^iPr_2)C(NAr)_2\}\{Ga(NArCH)_2\}$ (**1.117**) and $Zn\{Ga(NArCH)_2\}_2(TMEDA)$ (**1.118**, Scheme 1.17).[66] In a later report, Jones and co-workers isolated two more zinc gallyl compounds, and a cadmium gallyl compound.[20]

1.5 *p*-block

1.5.1 Group 13

Anwander and co-workers isolated aluminium boryl compounds from the reaction of either excess $AlMe_3$ with **1.7** to produce the unsolvated dimer **1.119**, or a 4:1 mixture of $AlMe_3$ with **1.7** to produce the monomeric aluminium boryl $AlMe_2\{B(NArCH)_2\}(THF)$ (**1.120**).[67] Compound **1.119** was then used to synthesise the rare earth metal heteroaluminates **1.121** and **1.122**, which were not accessible from **1.120** (Scheme 1.18).[67] In a later report, the same authors isolated the corresponding gallium boryl compounds *via* reaction of either an excess or three equivalents of $GaMe_3$ with **1.7** to produce $GaMe_2\{B(NArCH)_2\}$ (**1.123**) or $GaMe_2\{B(NArCH)_2\}(THF)$ (**1.124**) respectively (Scheme 1.19).[68]

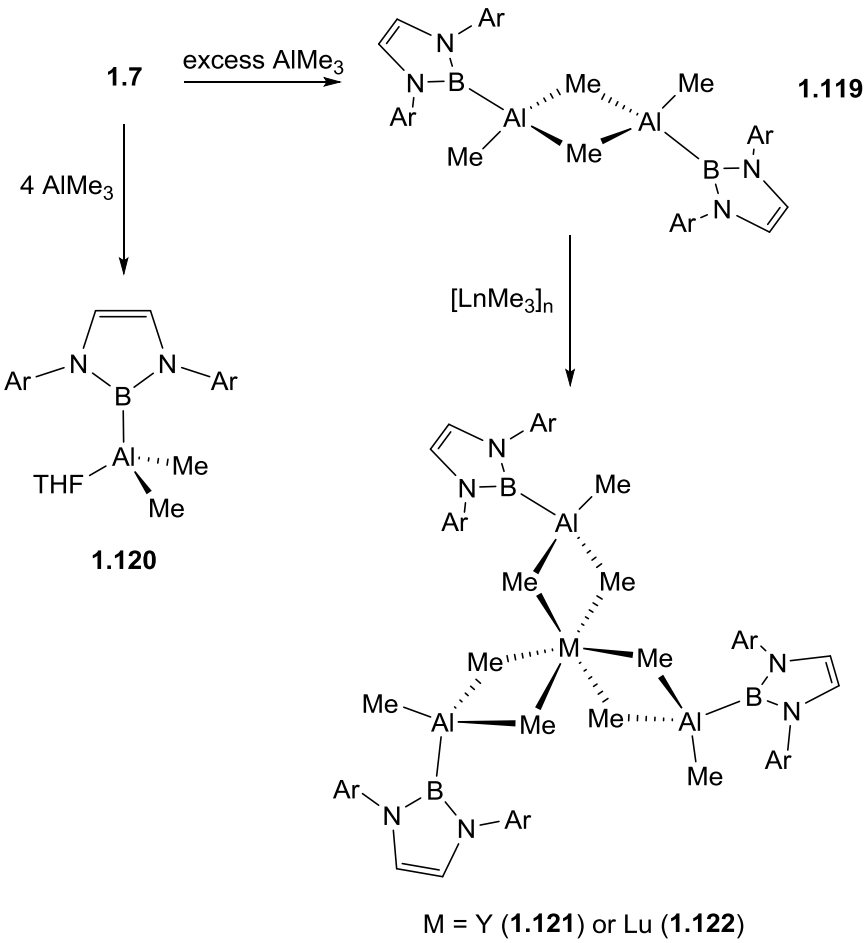

Scheme 1.18. By-products omitted for clarity. Ar = 2,6-$C_6H_3{}^iPr_2$.

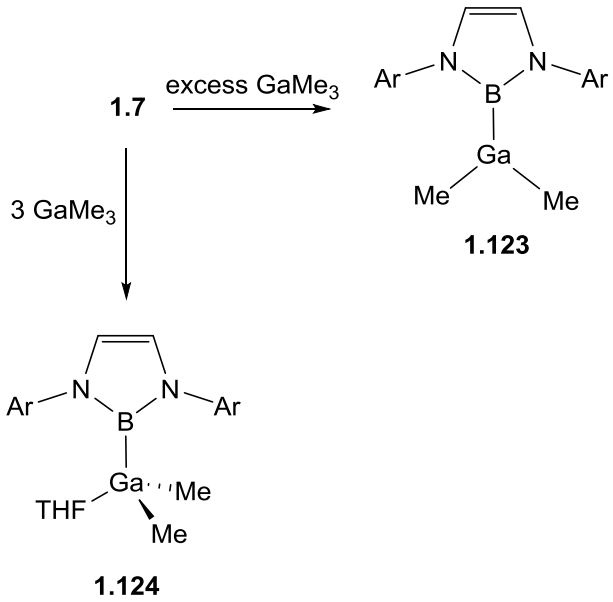

Scheme 1.19. By-products omitted for clarity. Ar = 2,6-$C_6H_3{}^iPr_2$.

Aldridge, Jones and co-workers synthesised a series of Group 13 metal bis(boryl) compounds of the type $M\{B(NArCH)_2\}_2$ (M = Ga (**1.125**), In (**1.126**) or Tl (**1.127**) Figure 1.7) from either M(I) or M(III) starting compounds.[69] The high steric loading and strong σ-donating properties of the boryl ligand allowed the isolation of these compounds as stable radicals, with the Group 13 metal having a formal oxidation state of II. Structural authentication of these compounds showed the size of the B–M–B angle changes with the metal, in the order Tl > Ga > In. DFT calculations replicated the trend, in which the B–M–B angle becomes more acute as the metal *s*-orbital contribution to the SOMO increases.

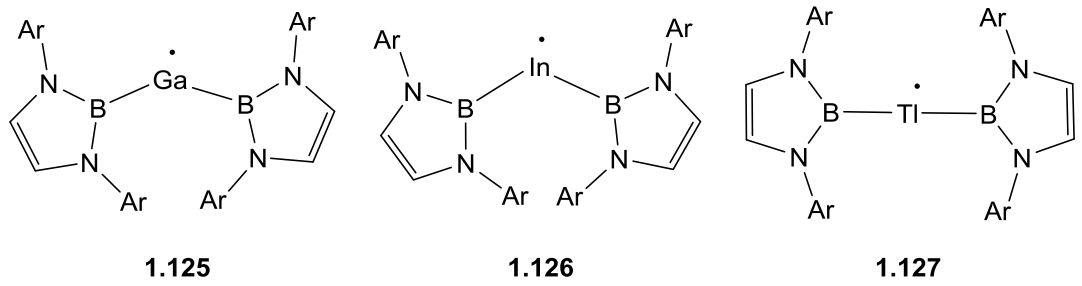

1.125 **1.126** **1.127**

Figure 1.7. Ar = 2,6-$C_6H_3{}^iPr_2$.

Reaction of two equivalents of **1.26** with either GaH_3(quinuclidine) or $InH_3(NMe_3)$ produced the anionic aluminium and gallium bis(gallyl) dihydrides $[K(TMEDA)_2][GaH_2\{Ga(NArCH)_2\}_2]$ (**1.128**) and $[Li(TMEDA)_2][InH_2\{Ga(NArCH)_2\}_2]$ (**1.129**).[70] The source of the lithium counter-ion in **1.129** was believed to have originated from the synthesis of $InH_3(NMe_3)$ where LiBr is an inseparable by-product. Structural analysis revealed that **1.128** forms a contact ion pair, with an interaction between the cation and the hydride ligands.[70]

1.5.2 Group 14

Aldridge, Jones and co-workers reported the remarkable ambient temperature isolation of a two coordinate acyclic silylene, $Si\{NAr(SiMe_3)\}\{B(NArCH)_2\}$ (**1.130**, Scheme 1.20).[71] The compound was arrived at by reaction of $SiBr_3\{NAr(SiMe_3)\}$ with two equivalents of **1.7**, in which the boryl anion behaves as both reducing agent and ligand. Unlike N-heterocyclic silylenes, **1.130** can activate dihydrogen, even at temperatures as low as 0 °C. DFT calculations suggested that dihydrogen approaches **1.130** in a side-on fashion, donating electron density from its HOMO into the LUMO of **1.130**, behaviour reminiscent of transition metal activation of dihydrogen. In the

same report, the germanium (**1.131**) and tin (**1.132**) analogues were isolated *via* reaction of the metal(II) precursors GeCl{NAr*(SiMe$_3$)} and SnCl{NAr(SiMe$_3$)} with one equivalent of **1.7** (Scheme 1.20). It was notable that the germanium boryl analogue could only be isolated with the very bulky Ar* silylamido substituent developed by Jones (Ar* = 2,6-(Ph$_2$CH)$_2$-4-C$_6$H$_2$Me).[71]

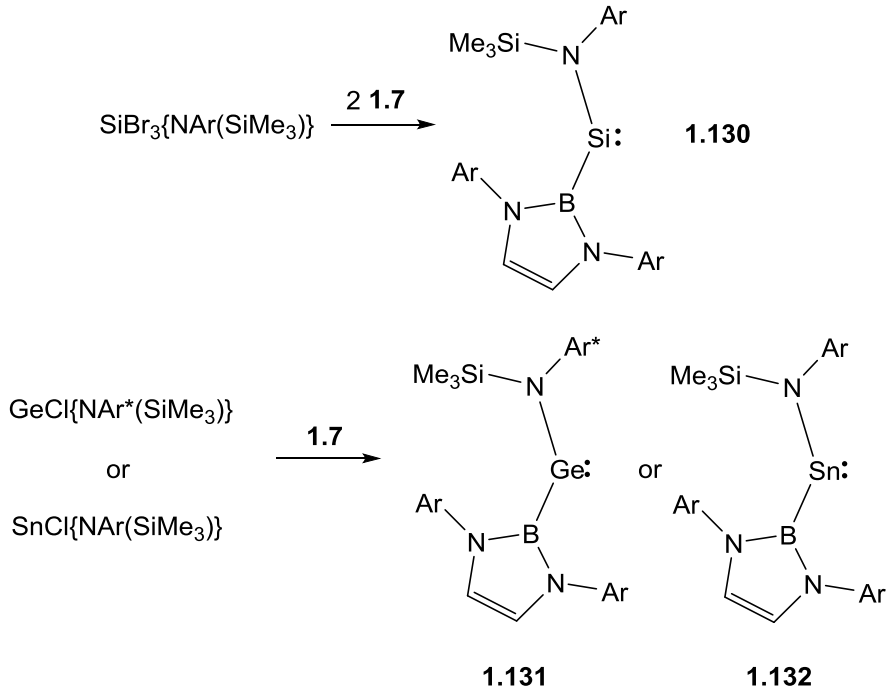

Scheme 1.20. By-products omitted for clarity. Ar = 2,6-C$_6$H$_3$^{i}Pr$_2$; Ar* = 2,6-(Ph$_2$CH)$_2$-4-C$_6$H$_2$Me.

Jones and co-workers also isolated a series of Group 14 metal gallyl compounds. 2:1 reactions of **1.26** with the heavy alkene analogues M$_2${CH(SiMe$_3$)$_2$}$_4$ (M = Ge or Sn) led to the anionic metal gallyl compounds [K(TMEDA)][M{CH(SiMe$_3$)$_2$}$_2${Ga(NArCH)$_2$}] (M = Ge (**1.133**) or Sn (**1.134**)) in moderate to good yields. Addition of another equivalent of **1.26** to **1.134** produces, after elimination of K{CH(SiMe$_3$)$_2$}, the tin bis(gallyl) salt [K(TMEDA)][Sn{CH(SiMe$_3$)$_2$}{Ga(NArCH)$_2$}$_2$] (**1.135**) in low yields. The reduced Lewis acidity and smaller ionic radius of germanium ensures the same reaction does not occur with **1.133**. Structural analyses of **1.133**–**1.135** found an η^6-interaction between a metal-bound potassium and one of the aryl groups of the gallyl in all cases (Scheme 1.21).[72]

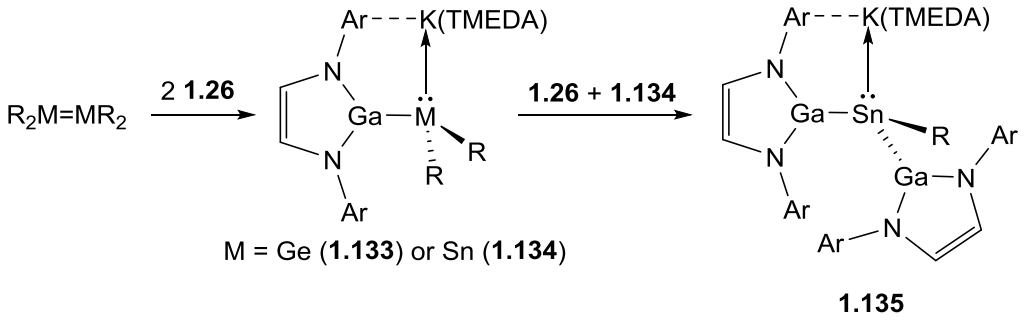

Scheme 1.21. By-products omitted for clarity. R = $CH(SiMe_3)_2$; Ar = 2,6-$C_6H_3{}^iPr_2$.

Replacing $M_2\{CH(SiMe_3)_2\}_4$ with $M_2Ar'_4$ (M = Sn or Pb, Ar' = 2,4,6-$C_6H_2{}^iPr_3$) and repeating the reaction with two equivalents of **1.26** results in the formation of [K(TMEDA)][$SnAr'_2\{Ga(NArCH)_2\}$] (**1.136**) or the precipitation of metallic lead and the gallium aryl compound $Ar'Ga(NArCH)_2$ (**1.137**). As with **1.133**–**1.135**, **1.136** exhibits an η^6-interaction between a metal-bound potassium and one of the aryl groups of the gallyl. In the same report, neutral Group 14 metal gallyl compounds were also accessed *via* reaction of the very bulky guanidinate metal precursors $MCl\{(N^iPr_2)C(NAr)_2\}$ (M = Ge or Sn) with one equivalent of **1.26**, producing $M\{(N^iPr_2)C(NAr)_2\}\{Ga(NArCH)_2\}$ (M = Ge (**1.138**) or Sn (**1.139**)) in good yields (Scheme 1.22).[72]

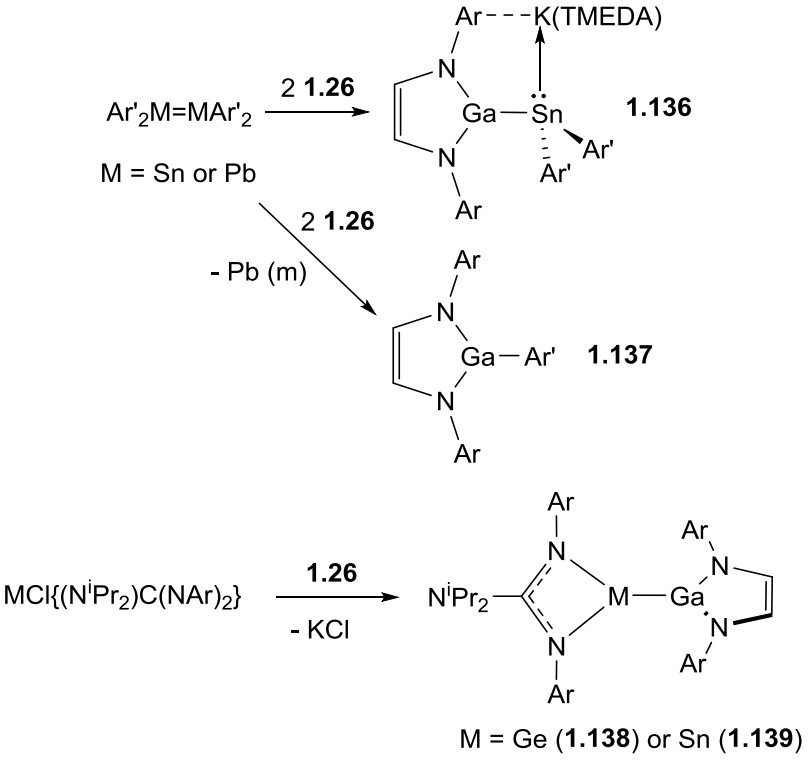

Scheme 1.22. Ar = 2,6-$C_6H_3{}^iPr_2$; Ar' = 2,4,6-$C_6H_2{}^iPr_3$.

1.6 Group 3 and *f*-block

Prior to the work reported in this Thesis, there were no known Group 3 or *f*-block boryl compounds. The synthesis and characterisation of metal boryl compounds featuring metals from Group 3 and the *f*-block will therefore be discussed in forthcoming Chapters. As such, this part of the introduction concerns itself only with metal gallyl compounds featuring those metals.

1.6.1 Group 3

The only known Group 3 gallyl compounds were synthesised by Jones and Liddle in 2009 and Fedushkin in 2011. Jones and Liddle isolated an yttrium gallyl compound $Y\{C(PPh_2NSiMe_3)_2\}\{Ga(NArCH)_2\}(THF)_2$ (**1.140**, Equation 1.18) featuring a carbene phosphinimine supporting ligand.[73] Simple salt metathesis of an *in situ* generated yttrium precursor with **1.26** produced **1.140** in low isolated yield. Crystallographic characterisation of **1.140** revealed an octahedral geometry, distorted by the bite angle of the supporting ligand. The Y–Ga bond length, at 3.1757(4) Å, is longer than the sum of the covalent radii (3.12 Å), and DFT calculations revealed that this linkage is best described as a highly polarised covalent bond.

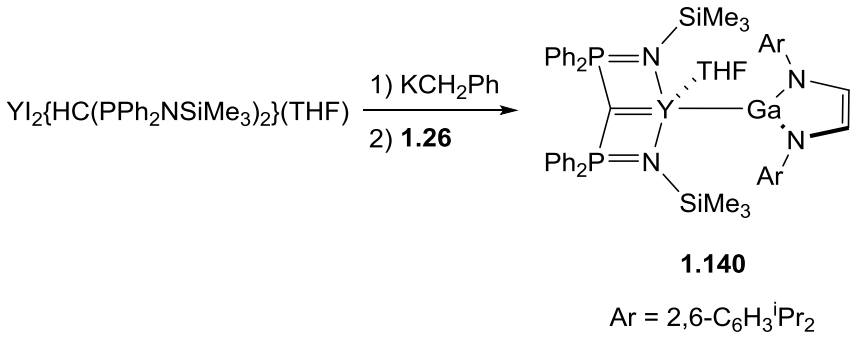

1.140

Ar = 2,6-$C_6H_3{}^iPr_2$

Equation 1.18

Fedushkin and co-workers utilised **1.27** and the metallocene "ate" compound $[K(THF)_2][Cp"_2LaCl_2]$ to produce $Cp"_2La\{Ga(NArC_6H_3)_2\}_2(THF)$ (**1.141**, Equation 1.19) in good isolated yield. **1.141** was structurally authenticated and showed a typical bent metallocene structure, with a La–Ga bond length of 3.0134(8) Å that is shorter than the sum of the respective covalent radii (3.29 Å), and is considerably shorter than the other known *f*-element gallium bonds.[74]

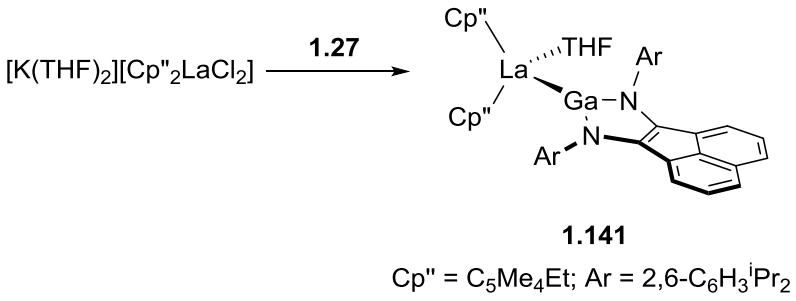

1.141

Cp" = C_5Me_4Et; Ar = 2,6-$C_6H_3{}^iPr_2$

Equation 1.19

1.6.2 *f*-block

The first *f*-element-gallium bonded compound to be structurally authenticated was isolated by Arnold and Jones and co-workers in 2007.[75] Reaction of $[NdI\{N(SiMe_3)_2\}\{C(N^tBu(CHCSiMe_3)N(CH_2)_2N^tBu\}]_2$ with **1.26** leads to the neodymium gallyl compound $Nd\{N(SiMe_3)_2\}\{C(N^tBu(CHCSiMe_3)N(CH_2)_2N^tBu\}$-$\{Ga(NArCH)_2\}(THF)$ (**1.142**, Equation 1.20). The Nd–Ga bond length (3.2199(3) Å) was found to be longer than the sum of the respective covalent radii (2.89 Å). **1.142** was also found to be stable in solution, in contrast to comparable lanthanide metal-Group 13 metal(I) adducts, which dissociated upon solvation. DFT studies revealed a bond energy that was an order of magnitude greater than that for the comparable adducts. The authors attribute the relative strength of the Nd–Ga bond to charge transfer from the more polarizable gallium(I) to the more polarizing neodymium(III) centre.[75]

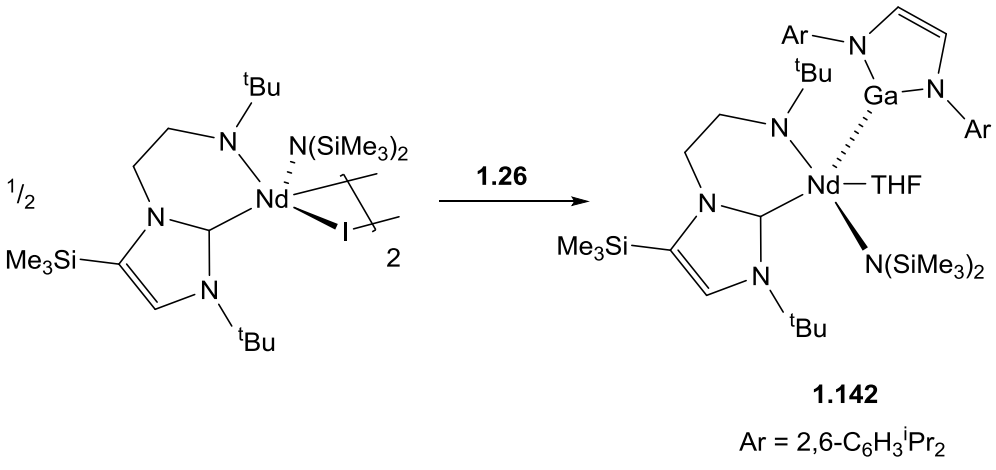

1.142

Ar = 2,6-$C_6H_3{}^iPr_2$

Equation 1.20

In 2009, Jones and co-workers isolated a series of divalent lanthanide gallyl compounds. Reaction of the divalent metal iodides MI_2 (M = Sm, Eu or Yb) with two

equivalents of **1.26** and an excess of TMEDA (*cf.* Group 2 gallyls, *vide supra*) led to low to moderate yields of the divalent lanthanide metal gallyl compounds $M\{Ga(NArCH)_2\}_2(TMEDA)_2$ (M = Sm (**1.143**), Eu (**1.144**) or Yb (**1.145**), Equation 1.21).[76] **1.143**-**1.145** were all crystallographically characterised and were found to be isostructural, with distorted octahedral geometry and the gallyl compounds *trans* to each other in the apical positions and the two TMEDA ligands occupying the equatorial coordination sites.

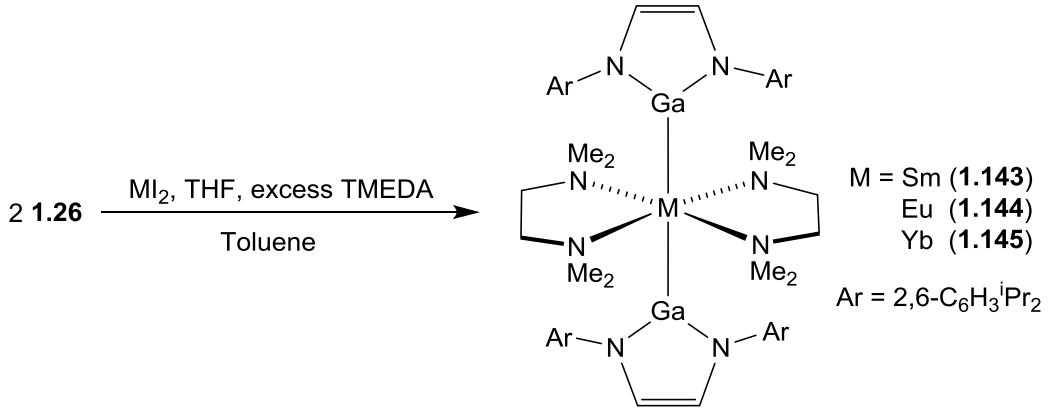

Equation 1.21

Attempting the same reaction with $TmI_2(THF)_5$ reproducibly resulted only in low yields of the thulium(III) gallyl compound **1.146** (Equation 1.22). An X-ray crystal structure revealed a Tm–Ga bond, with the rest of the metal coordination sphere being taken up by a molecule of TMEDA and a doubly reduced diazabutadiene ligand cooridinated in an η^4-fashion to the metal centre.[76]

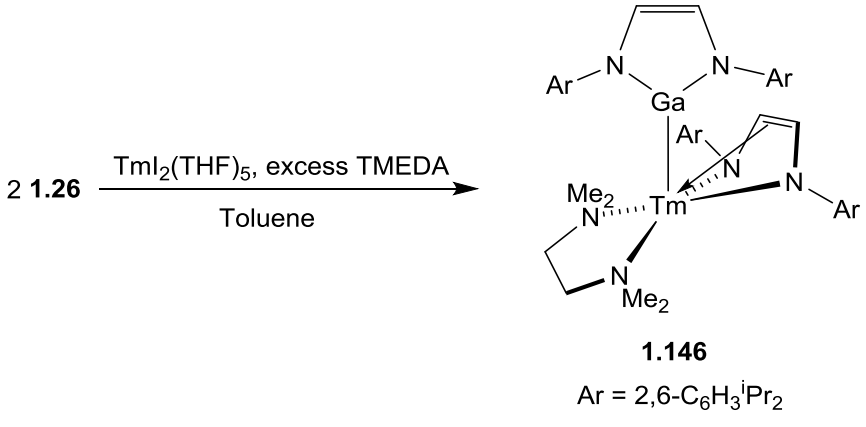

Equation 1.22

Finally, in 2009, reaction of the well-known uranium tren compound $UCl\{N((CH_2)_2NSiMe_3)_3\}(THF)$ with one equivalent of **1.26** produced the uranium

gallyl compound U{N((CH$_2$)$_2$NSiMe$_3$)$_3$}{Ga(NArCH)$_2$}(THF) (**1.147**, Equation 1.23) in high yields.[77] Compound **1.147** was structurally characterised, exhibiting a uranium metal centre in a distorted octahedral geometry. The authors report that the unit cell contained two crystallographically unique molecules that had very similar metric parameters. It was, however, noteworthy that whilst the molecules were very similar, the U–Ga bond lengths were significantly different (3.2115(8) Å *vs.* 3.2983(9) Å). The authors attributed this to crystal packing forces having a greater effect than normal on the mainly electrostatic (and therefore 'soft') U–Ga bond. DFT calculations revealed a remarkable instance of Group 13 metal/f-element π-donation, with π-donation from a filled π-orbital in the gallium heterocycle to the 5f orbital of uranium.[77]

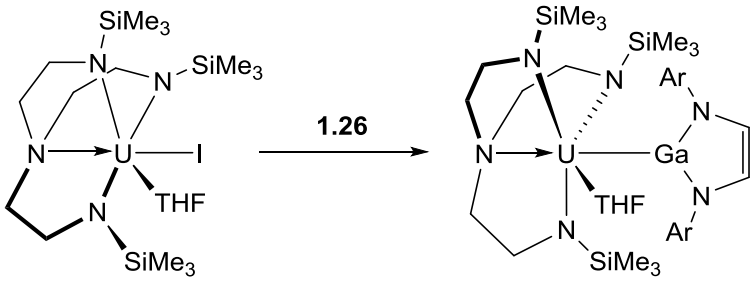

1.147

Ar = 2,6-C$_6$H$_3$^{i}Pr$_2$

Equation 1.23

1.7 Outlook

There is much work still to be done in the chemistry of metal boryl and gallyl compounds. The remarkable compounds that have been made have only scratched the surface of this chemistry; for example, the early transition and rare earth metal boryl and gallyl compounds have only very recently been isolated and their vast potential remains untapped. Of the compounds already made, some have shown astonishing reactivity, such as the compounds capable of selective alkane C–H activation pioneered by Hartwig. The rest of this Thesis is concerned with expanding this chemistry for the rare earth metals.

1.8 References

1. J.-C. Bünzli and V. Pecharsky, *Handbook on the Physics and Chemistry of Rare Earths*, Elsevier, North Holland, 2013.

2. F. A. Cotton, G. Wilkinson, C. A. Murillo and M. Bochmann, *Advanced Inorganic Chemistry*, 6th edn., Wiley, 1999.
3. U. S. D. o. Energy, 2010.
4. L. M. A. Saleh, K. H. Birjkumar, A. V. Protchenko, A. D. Schwarz, S. Aldridge, C. Jones, N. Kaltsoyannis and P. Mountford, *J. Am. Chem. Soc.*, 2011, **133**, 3836.
5. R. W. Auten and C. A. Kraus, *J. Am. Chem. Soc.*, 1952, **74**, 3398.
6. K. Smith and K. Swaminathan, *J. Chem. Soc., Dalton Trans.*, 1976, 2297.
7. J. L. Williams, J. C. Doty, P. J. Grisdale, R. Searle, T. H. Regan, G. P. Happ and D. P. Maier, *J. Am. Chem. Soc.*, 1967, **89**, 5153.
8. J. D. Wilkey and G. B. Schuster, *J. Org. Chem.*, 1987, **52**, 2117.
9. L. Weber, M. Schnieder and P. Lonnecke, *J. Chem. Soc., Dalton Trans.*, 2001, 3459.
10. Y. Segawa, Y. Suzuki, M. Yamashita and K. Nozaki, *J. Am. Chem. Soc.*, 2008, **130**, 16069.
11. Y. Segawa, M. Yamashita and K. Nozaki, *Science*, 2006, **314**, 113.
12. B. Cordero, V. Gomez, A. E. Platero-Prats, M. Reves, J. Echeverria, E. Cremades, F. Barragan and S. Alvarez, *Dalton Trans.*, 2008, 2832.
13. S. Robinson, J. McMaster, W. Lewis, A. J. Blake and S. T. Liddle, *Chem. Commun.*, 2012, **48**, 5769.
14. E. S. Schmidt, A. Jockisch and H. Schmidbaur, *J. Am. Chem. Soc.*, 1999, **121**, 9758.
15. R. J. Baker, R. D. Farley, C. Jones, M. Kloth and D. M. Murphy, *J. Chem. Soc., Dalton Trans.*, 2002, 3844.
16. I. L. Fedushkin, A. N. Lukoyanov, G. K. Fukin, S. Y. Ketkov, M. Hummert and H. Schumann, *Chem. Eur. J.*, 2008, **14**, 8465.
17. I. L. Fedushkin, A. N. Lukoyanov, A. N. Tishkina, G. K. Fukin, K. A. Lyssenko and M. Hummert, *Chem. Eur. J.*, 2010, **16**, 7563.
18. M. Yamashita, Y. Suzuki, Y. Segawa and K. Nozaki, *J. Am. Chem. Soc.*, 2007, **129**, 9570.
19. C. Jones, D. P. Mills, J. A. Platts and R. P. Rose, *Inorg. Chem.*, 2006, **45**, 3146.
20. O. Bonello, C. Jones, A. Stasch and W. D. Woodul, *Organometallics*, 2010, **29**, 4914.

21. T. Terabayashi, T. Kajiwara, M. Yamashita and K. Nozaki, *J. Am. Chem. Soc.*, 2009, **131**, 14162.
22. A. V. Protchenko, L. M. A. Saleh, D. Vidovic, D. Dange, C. Jones, P. Mountford and S. Aldridge, *Chem. Commun.*, 2010, **46**, 8546.
23. R. J. Baker, C. Jones and D. M. Murphy, *Chem. Commun.*, 2005, 1339.
24. J. F. Hartwig and S. R. Degala, *J. Am. Chem. Soc.*, 1994, **116**, 3661.
25. D. R. Lantero, D. H. Motry, D. L. Ward and M. R. Smith, *J. Am. Chem. Soc.*, 1994, **116**, 10811.
26. S. Aldridge, R. J. Baker, N. D. Coombs, C. Jones, R. P. Rose, A. Rossin and D. J. Willock, *Dalton Trans.*, 2006, 3313.
27. H. Braunschweig, K. W. Klinkhammer, M. Koster and K. Radacki, *Chem. Eur. J.*, 2003, **9**, 1303.
28. J. F. Hartwig and X. M. He, *Organometallics*, 1996, **15**, 5350.
29. J. F. Hartwig and X. M. He, *Angew. Chem. Int. Ed.*, 1996, **35**, 315.
30. K. M. Waltz and J. F. Hartwig, *Science*, 1997, **277**, 211.
31. K. M. Waltz, X. M. He, C. Muhoro and J. F. Hartwig, *J. Am. Chem. Soc.*, 1995, **117**, 11357.
32. H. Braunschweig, R. D. Dewhurst and A. Schneider, *Chem. Rev.*, 2010, **110**, 3924.
33. G. J. Irvine, M. J. G. Lesley, T. B. Marder, N. C. Norman, C. R. Rice, E. G. Robins, W. R. Roper, G. R. Whittell and L. J. Wright, *Chem. Rev.*, 1998, **98**, 2685.
34. S. Aldridge and D. L. Coombs, *Coord. Chem. Rev.*, 2004, **248**, 535.
35. J. F. Hartwig and S. Huber, *J. Am. Chem. Soc.*, 1993, **115**, 4908.
36. B. E. R. Schilling, R. Hoffmann and D. L. Lichtenberger, *J. Am. Chem. Soc.*, 1979, **101**, 585.
37. B. E. R. Schilling, R. Hoffmann and J. W. Faller, *J. Am. Chem. Soc.*, 1979, **101**, 592.
38. A. A. Dickinson, D. J. Willock, R. J. Calder and S. Aldridge, *Organometallics*, 2002, **21**, 1146.
39. G. J. Irvine, W. R. Roper and L. J. Wright, *Organometallics*, 1997, **16**, 2291.
40. H. Braunschweig, M. Koster and R. Wang, *Inorg. Chem.*, 1999, **38**, 415.
41. C. E. F. Rickard, W. R. Roper, A. Williamson and L. J. Wright, *Organometallics*, 1998, **17**, 4869.

42. N. J. Hardman, R. J. Wright, A. D. Phillips and P. P. Power, *J. Am. Chem. Soc.*, 2003, **125**, 2667.
43. R. J. Baker, C. Jones and J. A. Platts, *Dalton Trans.*, 2003, 3673.
44. C. Jones, A. Stasch, G. J. Moxey, P. C. Junk and G. B. Deacon, *Eur. J. Inorg. Chem.*, 2009, 3593.
45. C. Y. Dai, G. Stringer, J. F. Corrigan, N. J. Taylor, T. B. Marder and N. C. Norman, *J. Organomet. Chem.*, 1996, **513**, 273.
46. P. Nguyen, G. Lesley, N. J. Taylor, T. B. Marder, N. L. Pickett, W. Clegg, M. R. J. Elsegood and N. C. Norman, *Inorg. Chem.*, 1994, **33**, 4623.
47. C. Y. Dai, G. Stringer, T. B. Marder, A. J. Scott, W. Clegg and N. C. Norman, *Inorg. Chem.*, 1997, **36**, 272.
48. S. A. Westcott, N. J. Taylor, T. B. Marder, R. T. Baker, N. J. Jones and J. C. Calabrese, *J. Chem. Soc., Chem. Commun.*, 1991, 304.
49. H. Y. Chen, S. Schlecht, T. C. Semple and J. F. Hartwig, *Science*, 2000, **287**, 1995.
50. J. F. Hartwig, K. S. Cook, M. Hapke, C. D. Incarvito, Y. B. Fan, C. E. Webster and M. B. Hall, *J. Am. Chem. Soc.*, 2005, **127**, 2538.
51. J. R. Knorr and J. S. Merola, *Organometallics*, 1990, **9**, 3008.
52. R. T. Baker, D. W. Ovenall, J. C. Calabrese, S. A. Westcott, N. J. Taylor, I. D. Williams and T. B. Marder, *J. Am. Chem. Soc.*, 1990, **112**, 9399.
53. S. P. Green, C. Jones, D. P. Mills and A. Stasch, *Organometallics*, 2007, **26**, 3424.
54. D. Adhikari, J. C. Huffman and D. J. Mindiola, *Chem. Commun.*, 2007, 4489.
55. S. Onozawa, Y. Hatanaka, T. Sakakura, S. Shimada and M. Tanaka, *Organometallics*, 1996, **15**, 5450.
56. C. N. Iverson and M. R. Smith, *J. Am. Chem. Soc.*, 1995, **117**, 4403.
57. H. Braunschweig, K. Radacki, D. Rais and D. Scheschkewitz, *Angew. Chem. Int. Ed.*, 2005, **44**, 5651.
58. C. Jones, D. P. Mills, R. P. Rose and A. Stasch, *Dalton Trans.*, 2008, 4395.
59. A. Kempter, C. Gemel, T. Cadenbach and R. A. Fischer, *Organometallics*, 2007, **26**, 4257.
60. A. Kempter, C. Gemel and R. A. Fischer, *Chem. Eur. J.*, 2007, **13**, 2990.
61. G. J. Moxey, C. Jones, A. Stasch, P. C. Junk, G. B. Deacon, W. D. Woodul and P. R. Drago, *Dalton Trans.*, 2009, 2630.

62. D. S. Laitar, P. Muller and J. P. Sadighi, *J. Am. Chem. Soc.*, 2005, **127**, 17196.
63. Y. Segawa, M. Yamashita and K. Nozaki, *Angew. Chem. Int. Ed.*, 2007, **46**, 6710.
64. T. Kajiwara, T. Terabayashi, M. Yamashita and K. Nozaki, *Angew. Chem. Int. Ed.*, 2008, **47**, 6606.
65. A. V. Protchenko, D. Dange, A. D. Schwarz, C. Y. Tang, N. Phillips, P. Mountford, C. Jones and S. Aldridge, *Chem. Commun.*, 2014, **50**, 3841.
66. C. Jones, R. P. Rose and A. Stasch, *Dalton Trans.*, 2007, 2997.
67. N. Dettenrieder, H. M. Dietrich, C. Schadle, C. Maichle-Mossmer, K. W. Tornroos and R. Anwander, *Angew. Chem. Int. Ed.*, 2012, **51**, 4461.
68. N. Dettenrieder, C. Schädle, C. Maichle-Mössmer, P. Sirsch and R. Anwander, *J. Am. Chem. Soc.*, 2014, **136**, 886.
69. A. V. Protchenko, D. Dange, J. R. Harmer, C. Y. Tang, A. D. Schwarz, M. J. Kelly, N. Phillips, R. Tirfoin, K. H. Birjkumar, C. Jones, N. Kaltsoyannis, P. Mountford and S. Aldridge, *Nat. Chem.*, 2014, **6**, 315.
70. R. J. Baker, C. Jones, M. Kloth and J. A. Platts, *Angew. Chem. Int. Ed.*, 2003, **42**, 2660.
71. A. V. Protchenko, K. H. Birjkumar, D. Dange, A. D. Schwarz, D. Vidovic, C. Jones, N. Kaltsoyannis, P. Mountford and S. Aldridge, *J. Am. Chem. Soc.*, 2012, **134**, 6500.
72. S. P. Green, C. Jones, K. A. Lippert, D. P. Mills and A. Stasch, *Inorg. Chem.*, 2006, **45**, 7242.
73. S. T. Liddle, D. P. Mills, B. M. Gardner, J. McMaster, C. Jones and W. D. Woodul, *Inorg. Chem.*, 2009, **48**, 3520.
74. I. L. Fedushkin, A. N. Lukoyanov, A. N. Tishkina, M. O. Maslov, S. Y. Ketkov and M. Hummert, *Organometallics*, 2011, **30**, 3628.
75. P. L. Arnold, S. T. Liddle, J. McMaster, C. Jones and D. P. Mills, *J. Am. Chem. Soc.*, 2007, **129**, 5360.
76. C. Jones, A. Stasch and W. D. Woodul, *Chem. Commun.*, 2009, 113.
77. S. T. Liddle, J. McMaster, D. P. Mills, A. J. Blake, C. Jones and W. D. Woodul, *Angew. Chem. Int. Ed.*, 2009, **48**, 1077.

Chapter Two

Syntheses, Structures and Bonding Analyses of Rare Earth Metal Boryl Compounds

2.1 Overview

The traditional synthetic routes for constructing the vast majority of M–B bonds consist of oxidative addition or salt metathesis with an anionic metalate salt, and are not suitable for the synthesis of Ln–B bonds. Anionic metalate salts of the rare earths are not accessible, whilst the narrow range of oxidation states for the rare earths rules out oxidative addition as a synthetic tool. This Chapter describes the synthesis and isolation of rare earth metal boryl compounds, utilising cationic rare earth metal alkyl compounds and the salt of the boryl anion $Li\{B(NArCH)\}_2(THF)_2$ (**1.7**). The attempted synthesis of a uranium boryl compound will also be described. A short introduction on cationic rare earth metal compounds and their chemistry will precede the presentation of results, as will the Schlenk-based synthesis of the boryl anion, as, to date, this has not been reported. Parts of this work have been published.[1]

2.2 Introduction

Initial attempts at the synthesis of a rare earth metal boryl compound centred around the use of classical rare earth metal compounds as starting materials such as $LnCl_3$, LnI_3, Cp_2LnCl and $CpLnCl_2$, as the use of **1.7** opens up salt metathesis routes. However, all of these attempts ended in either decomposition of **1.7** to the corresponding borane $HB(NArCH)_2$ *via* some redox process (**1.22**, Figure 2.1), decomposition of any products or produced intractable mixtures. Rather than attempting to effect simple salt metathesis, "charge neutralisation", in which a cationic metal species is quenched by an anionic species to produce the final neutral product, was proposed as a more controlled route to the desired target compounds.

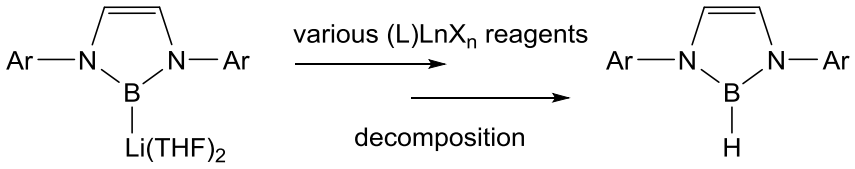

1.7 **1.22**

Figure 2.1

2.2.1 Rare Earth Metal Alkyl Compounds

Before discussing the chemistry of cationic alkyl compounds of the rare earths, it is important to discuss their neutral rare earth metal alkyl precursors. By way of context,

a series of lanthanide tris(cyclopentadienyl) compounds, $LnCp_3$ (Ln = Sc (**2.1**), Y (**2.2**), La (**2.3**), Ce (**2.4**), Pr (**2.5**), Nd (**2.6**), Sm (**2.7**) and Gd (**2.8**), Equation 2.1) were reported by Birmingham and Wilkinson in 1954.[2] These were the first rare earth metal organometallic compounds, isolated more than a century after Frankland's dialkyl zinc compounds.[3]

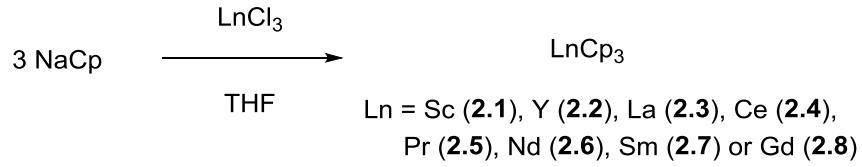

Equation 2.1

For this work, the compounds reported by Lappert more than 40 years ago were used as starting materials.[4] The synthesis of these compounds require tight control of the stoichiometry to avoid the formation of 'ate' compounds, and even tighter control of the thermal conditions to avoid decomposition of the final products. Reaction of the THF-solvated rare earth metal chlorides $LnCl_3(THF)_x$ (Ln = Sc, x = 3; Y, x = 3.5; Lu, x = 3) with three equivalents of $LiCH_2SiMe_3$ at 0 °C in pentane, followed by cold (0 °C) filtration and removal of volatiles under reduced pressure produces white powders of the desired tris(alkyl) compounds $Ln(CH_2SiMe_3)_3(THF)_2$ (Ln = Sc (**2.9**), Y (**2.10**) and Lu (**2.11**), Equation 2.2). Working up the reaction at 0 °C is critical to the successful isolation of these compounds.

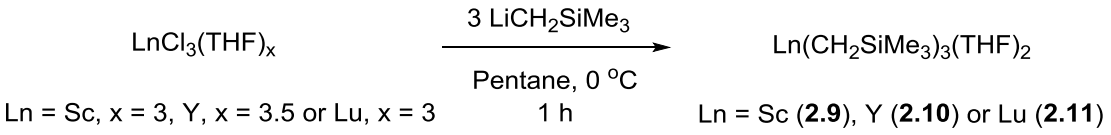

Equation 2.2

2.2.2 Rare Earth Metal Alkyl Cations

A review by Okuda *et al*. provides a comprehensive account of the chemistry of rare earth metal cations.[5] This introduction will provide information on pertinent examples relating to the chemistry that will be presented later in this Chapter.

The first example of a cationic lanthanide alkyl compound was reported by Schaverian in 1992.[6] Reaction of the lanthanum half-sandwich compound

$Cp^*La\{CH(SiMe_3)_2\}_2$ (**2.12**, Scheme 2.1) with one equivalent of $[PhMe_2NH][BPh_4]$ produced the cationic half-sandwich alkyl compound $Cp^*La\{CH(SiMe_3)_2\}\{(\mu\text{-}Ph)_2BPh_2)\}$ (**2.13-BPh_4**, Scheme 2.1). Elemental analysis and multinuclear NMR confirmed the composition of **2.13-BPh_4**, with the ^{13}C NMR shifts of the *ipso* carbons of the borate anion providing evidence of a weak π-interaction of the phenyl rings with the metal centre, as compared to the free borate anion. Addition of THF to **2.13-BPh_4** irreversibly produced the solvent-separated ion pair $[Cp^*La\{CH(SiMe_3)_2\}(THF)_3][BPh_4]$ (**2.14-BPh_4**, Scheme 2.1), with the ^{13}C shifts of the *ipso* carbons this time matching those of the free borate anion.

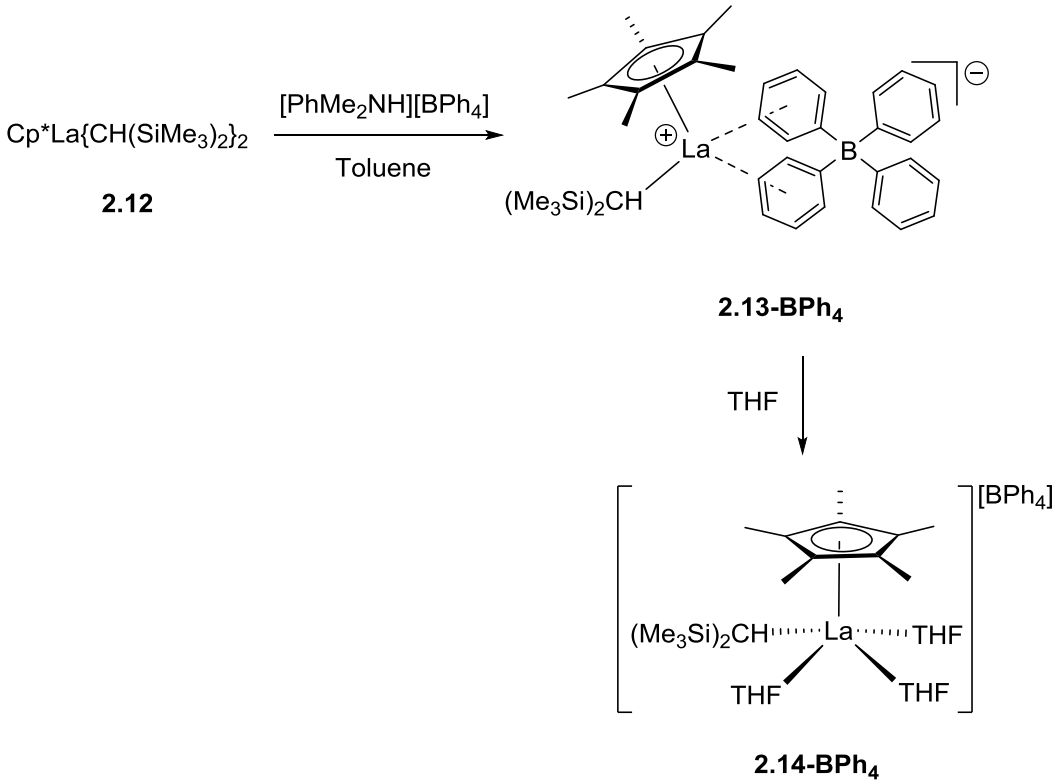

Scheme 2.1. By-products omitted for clarity.

Reaction of **2.13-BPh_4** with $LiCH(SiMe_3)_2$ regenerated **2.12**, whilst reaction with $Li(O\text{-}2,6\text{-}C_6H_3{}^tBu_2)(Et_2O)$ produced the mixed alkyl-alkoxide compound $Cp^*La\{CH(SiMe_3)_2\}(O\text{-}2,6\text{-}C_6H_3{}^tBu_2)$ (**2.15**, Equation 2.3).

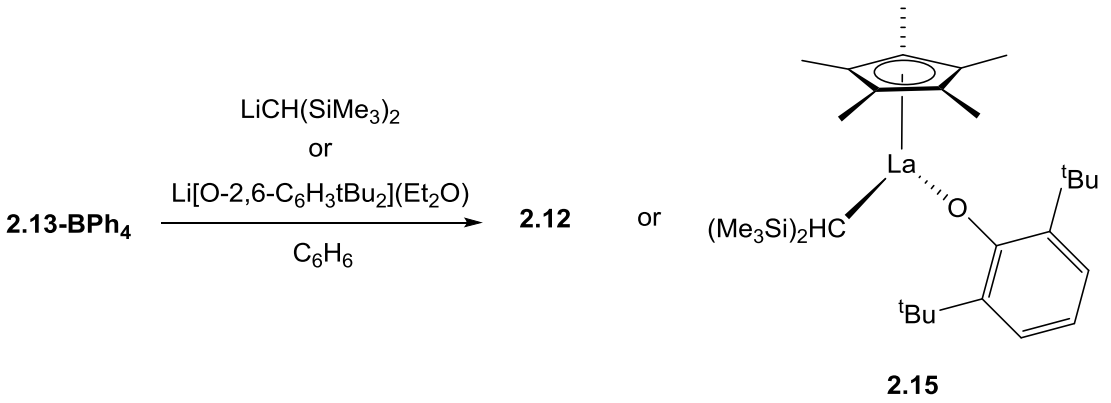

2.15

Equation 2.3

Okuda *et al*. isolated a series of di- and mono-alkyl mono- and di-cations featuring a variety of neutral ligands and non-coordinating anions.[7] Starting with **2.9**–**2.11**, addition of one equivalent of the desired Brønsted or Lewis acid produced the di-alkyl mono-cations **2.16**–**2.25** (Equation 2.4).

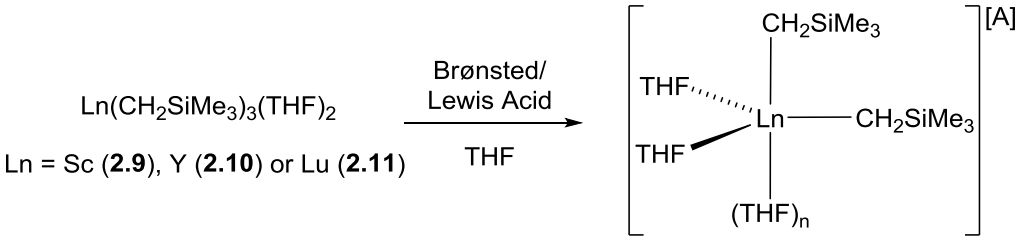

Ln = Sc, n = 1, A = BPh_4 (**2.16-BPh_4**)
Y, n = 1 or 2, A = BPh_4 (**2.17-BPh_4**)
A = $B(C_6F_5)_4$ (**2.18**)
A = $BPh_3CH_2SiMe_3$ (**2.19**)
A = $B(C_6F_5)_3CH_2SiMe_3$ (**2.20**)
A = $Al(CH_2SiMe_3)_4$ (**2.21**)
Lu, n = 1, A = BPh_4 (**2.22-BPh_4**)
A = $B(C_6F_5)_4$ (**2.23**)
A = $BPh_3CH_2SiMe_3$ (**2.24**)
A = $B(C_6F_5)_3CH_2SiMe_3$ (**2.25**)

Equation 2.4

Addition of 12-crown-4 to **2.9**-**2.11** to create **2.26**-**2.28**, followed by the addition of the same variety of Brønsted or Lewis acids produced the supported di-alkyl mono-cations **2.29**–**2.39** (Scheme 2.2).

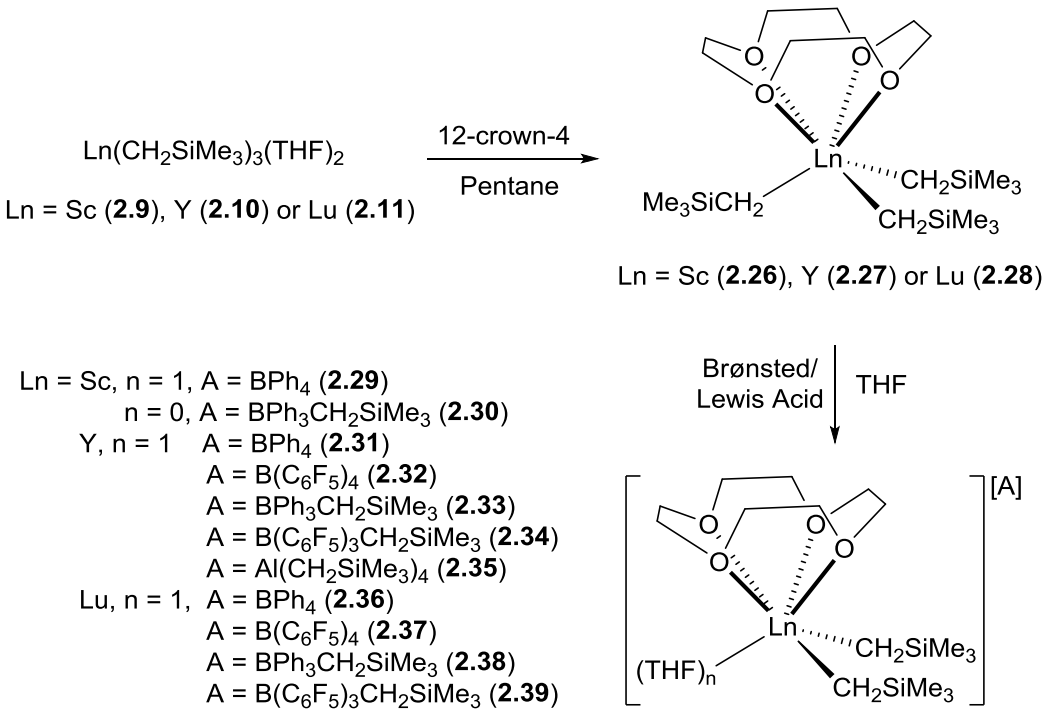

Scheme 2.2. By-products omitted for clarity.

Addition of 2.5 equivalents of $[PhMe_2NH][BPh_4]$ to **2.10** and **2.11** produced the mono-alkyl dications **2.40** and **2.41**, whilst starting from **2.27** and **2.28** and addition of two equivalents of Brønsted or Lewis acid produces the supported mono-alkyl dications **2.42**–**2.45** (Scheme 2.3).

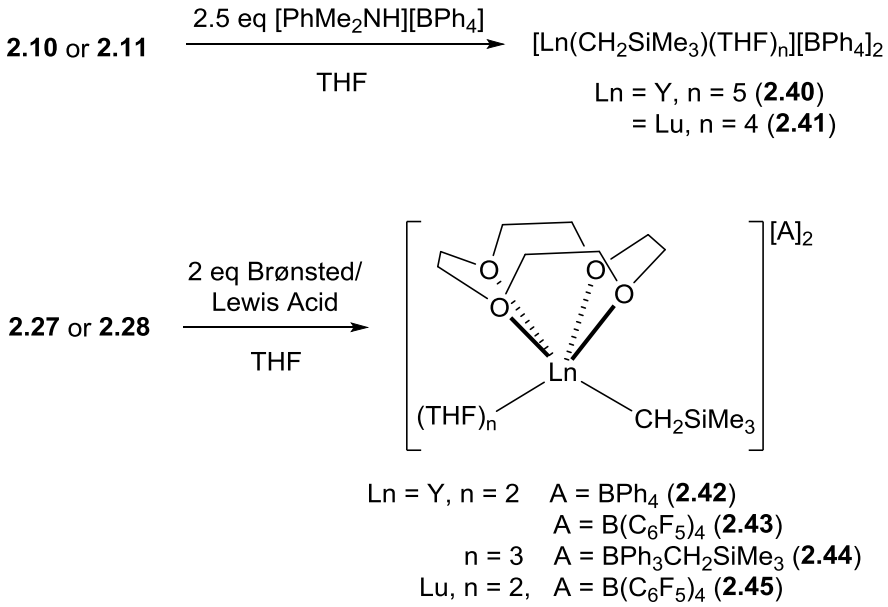

Scheme 2.3. By-products omitted for clarity.

Following the same procedure, but including addition of another equivalent of 12-crown-4 produced the THF-free mono-alkyl di-cations **2.46**–**2.49** (Equation 2.5). All of the alkyl cations synthesised show remarkable thermal stability, in contrast to the neutral starting compounds **2.9**-**2.11**.

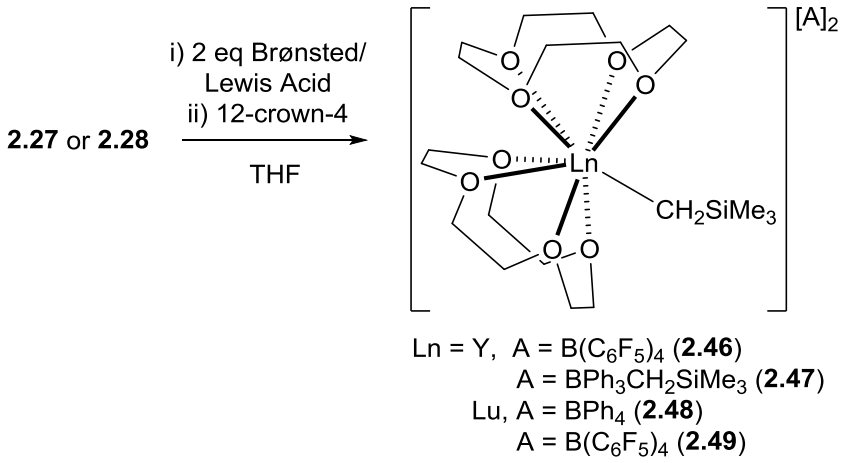

Equation 2.5

2.2.3 Schlenk-line Synthesis of Li{B(NArCH)$_2$}(THF)$_2$ (1.7)

The synthesis of Li{B(NArCH)$_2$}(THF)$_2$ (**1.7**) was originally reported by Yamashita and Nozaki in 2006,[8] with an improved preparation reported in 2008.[9] However, in both instances the final reductive dehalogenation of the bromoborane precursor **2.53** was carried out in a glovebox freezer under an argon atmosphere, and after filtration the resulting solution of **1.7** in THF was used without further purification as a stock solution for further reactivity. In order to control the reactivity of **1.7**, which is known to be strongly reducing and an extremely powerful nucleophile, an isolable crystalline starting compound of known purity and mass would be preferable to a stock solution. With that in mind, a reliable, Schlenk-line based synthesis of **1.7** was sought.

Reduction of the easily synthesised diazabutadiene **2.50** with pieces of lithium wire in Et_2O produced **2.51** as a light yellow-brown solution after two days. To the solution of **2.51** in Et_2O was added [Et_3NH]Cl, producing the protonated form of **2.51**, namely **2.52**, and concomitant precipitation of LiCl. Filtration and removal of volatiles from the filtrate under reduced pressure produced **2.52** as a light yellow powder. To a solution of **2.52** in CH_2Cl_2 cooled to 0 °C was added boron tribromide, immediately eliminating hydrogen bromide. After reacting overnight, the resulting dark brown

solution was cooled to 0 °C and Hünig's base (EtN^iPr_2) was slowly added to quench any remaining HBr. After removal of all volatiles under reduced pressure, the resulting brown solid was extracted into hexane. Upon reducing the volume of hexane, a light brown precipitate of the bromoborane heterocycle (**2.53**) formed. The supernatant was decanted and the solid dried *in vacuo* to yield pure **2.53** (Scheme 2.4).

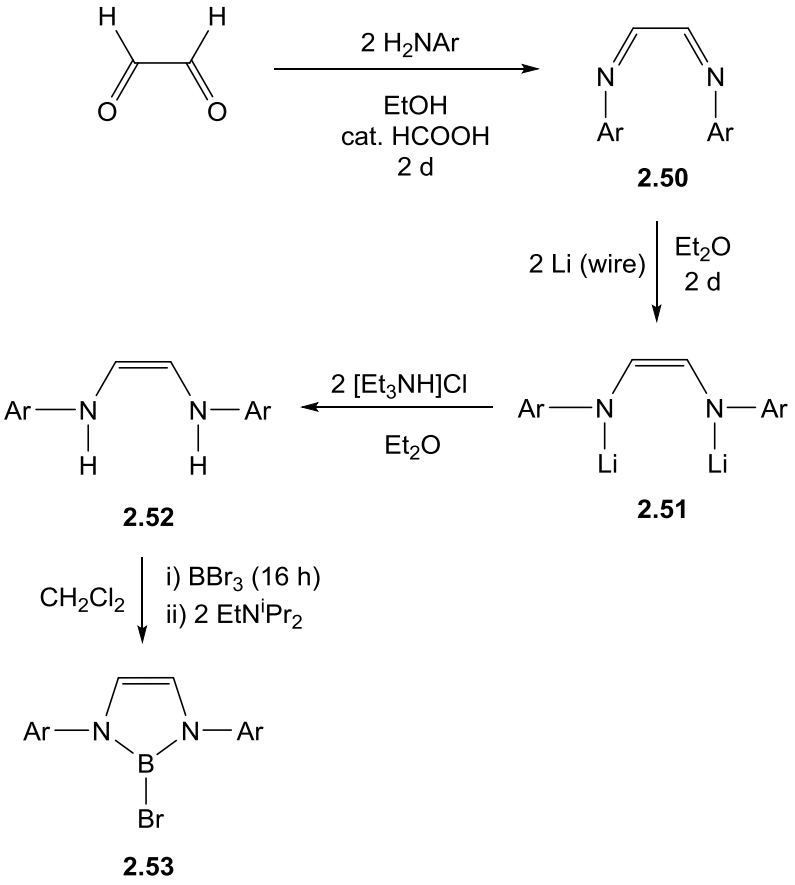

Scheme 2.4. By-products omitted for clarity. Ar = 2,6-$C_6H_3{}^iPr_2$.

In the original preparation, lithium dispersion is used to achieve the final reductive dehalogenation of **2.53** (Equation 2.6). Lithium dispersion is difficult to handle without access to gloveboxes operating with non-nitrogen inert atmosphere, and so lithium wire was employed instead. On the bench top, pieces of wire approximately 5 mm in length and coated in mineral oil were rolled out into a thin foil. These were placed directly into a pre-dried Schlenk flask under argon, and washed with anhydrous pentane and dried *in vacuo*. A catalytic amount of naphthalene was then added to the flask containing the freshly prepared lithium foil. The flask was then exposed to vacuum for a short period of time to remove any remaining air and

moisture from the lithium foil/naphthalene solid mixture. To this solid mixture was added THF, with the resulting green solution cooled to -40 °C, and to this stirring, cooled solution was added a THF solution of **2.53**. The resulting dark green solution was then allowed to react for 15 h at -40 °C, producing a dark brown solution and with the surface of the pieces of lithium foil taking on a shiny, clean look. All the volatiles were removed, leaving a dark brown solid which was extracted into pentane and filtered. The filtrate was cooled to -30 °C overnight to allow any excess lithium bromide to precipitate. After the dark brown solution was filtered away from lithium bromide, crystallisation was induced *via* multiple freezing and thawing of the solution, and cooled to -30 °C overnight. Dark yellow crystals of **1.7** were produced in 40 % yield, and repeating the above procedure with the mother liquor allowed isolation of a further crop of crystalline **1.7** for a total isolated crystalline yield of 60 %. Crystals of **1.7** can be stored for *ca*. 1 month under inert an atmosphere at -30 °C, and can also be handled at room temperature for considerable periods of time. Solutions of **1.7** have variable stability depending upon the type of solvent used and the thermal conditions. At room temperature in benzene, THF, hexane or pentane, **1.7** is stable for a few hours, and at -30 °C in THF, hexane and pentane is stable for weeks. However, at room temperature in toluene or Et_2O **1.7** is relatively unstable, forming $HB(NArCH)_2$ (**1.22**) within 0.5 h *via* a recently resolved redox process.[10]

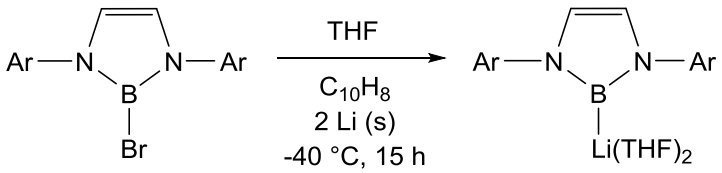

2.53 **1.7**

Equation 2.6

2.3 Rare Earth Metal Boryl Compounds[1]

2.3.1 Synthesis

As mentioned in the introduction to this Chapter, initial reactivity studies carried out by Dr Andrey Protchenko in the Aldridge and Mountford groups revolved around classical rare earth compounds featuring halide or cyclopentadienyl ligands. For the "charge neutralisation" approach, the cationic rare earth metal dialkyl compounds of the type $[Ln(CH_2SiMe_3)_2(THF)_3][BPh_4]$ (Ln = Sc (**2.16-BPh$_4$**), Y (**2.17-BPh$_4$**) or Lu (**2.22-BPh$_4$**) were believed to be suitable precursors to boryl compounds. **2.16-BPh$_4$**, **2.17-BPh$_4$** and **2.22-BPh$_4$** respectively were reacted with one equivalent of $Li\{B(NArCH)_2\}(THF)_2$ (**1.7**) in THF-d_8 on the NMR tube scale at -40 °C. Using the consumption of **1.7** as a guide, the reactions involving **2.16-BPh$_4$** and **2.22-BPh$_4$** required approximately 9 h to reach completion, whilst the reaction involving **2.17-BPh$_4$** required approximately 2 h. Approximately 10 % of **1.22** formed during the course of the reaction, indicating that the majority product was a metal boryl compound of some description. The $^{11}B\{^1H\}$ NMR showed a broad, downfield shifted resonance for each of the test reactions, which is a reliable indicator of a metal boryl compound. These promising early results led to attempting the reactions on a preparative scale. Addition of a cold (-40 °C) solution of **1.7** in THF to cold solutions of either **2.16-BPh$_4$**, **2.17-BPh$_4$** or **2.22-BPh$_4$** in THF led to the formation of a pale yellow solution, which was allowed to react overnight at -40 °C. Following this, the reaction mixture was allowed to warm to room temperature, and upon work up and isolation from either hexane or pentane led to the formation of $Ln(CH_2SiMe_3)_2\{B(NArCH)_2\}(THF)_n$ (Ln = Sc, n = 1 (**1**); Y, n = 2 (**2**); Lu, n = 2 (**3**), Equation 2.7) as extremely air and moisture sensitive compounds. Compounds **1**–**3** are the first rare earth metal boryl compounds featuring 2-centre, 2-electron Ln–B σ-bonds.

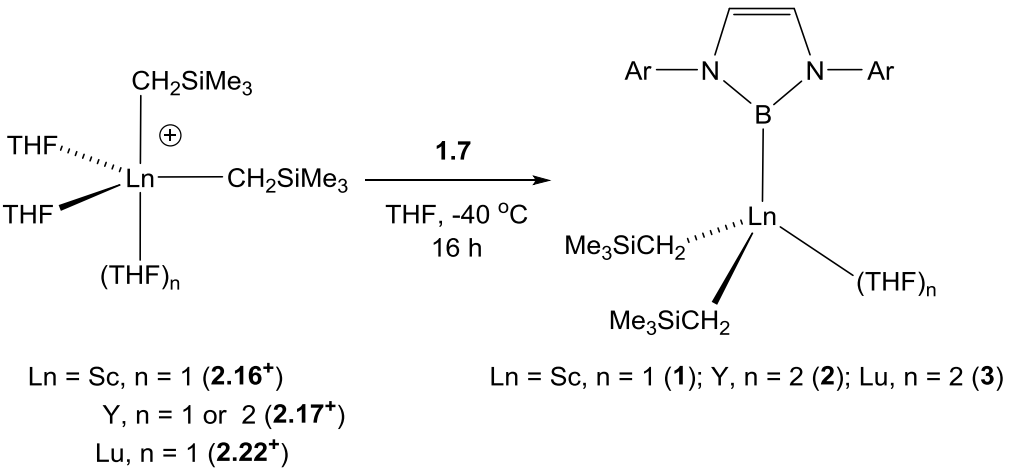

Equation 2.7. By-products omitted for clarity. Ar = 2,6-$C_6H_3{}^iPr_2$.

2.3.2 NMR Spectroscopy

Crystals of **1**–**3** were analysed by multinuclear NMR spectroscopy in C_6D_6. In the ^1H NMR of all three compounds, the vinyl backbone protons of the metal-coordinated boryl heterocycle produce a diagnostic sharp, downfield shifted resonance at 6.24 (**1**), 6.26 (**2**) and 6.33 (**3**) ppm, respectively. However even after crystallisation a small amount (*ca*. 5-10 %) of **1.22** was still present, producing a signal at 6.18 ppm. Residual **1.22** is seen in previously reported examples of metal boryl compounds derived from **1.7** and from the isolation of **1.7** itself.[9] The $^{11}B\{^1H\}$ NMR spectra of **1**–**3** featured broad, downfield-shifted peaks, with the presence of **1.22** producing a relatively sharp peak at 23 ppm. Compounds **1** and **2** have resonances at 38 and 45 ppm, respectively, whilst **3** shows a considerably more downfield-shifted peak at 62 ppm. These are consistent with a significantly deshielded three-coordinate boron atom, which is the most characteristic spectroscopic feature that all boryl compounds have in common.[11] They also compare well with their Group 4 counterparts, with the $^{11}B\{^1H\}$ NMR spectrum of **1** matching that of $Ti(O^iPr)_3\{B(NArCH)_2\}$ (**1.47**, 38 ppm)[12] and **3** closely matching that of $Cp^*Hf\{B(NArCH)_2\}(CH_2Ph)_2$ (**1.48**, 70 ppm).[12]

2.3.3 Solid State Structures

Cooled (-30 °C) saturated solutions of pentane (**1**) or hexane (**2** and **3**) produced diffraction quality crystals, enabling the elucidation of the solid state structures of **1**–**3**. These structures confirm that **1**–**3** are rare earth mixed boryl dialkyl compounds.

Compound **1** has a distorted tetrahedral structure, analogous to that of **1.47**, with one coordinated molecule of THF (Figure 2.2). The Sc–B bond distance in **1** was found to be 2.422(2) Å, within the sum of the respective covalent radii (2.54(10) Å).[13] The bond distance found in **1** is considerably longer than that found in the Ti–B bond of the similarly four-coordinate **1.47** (2.258(2) Å) and the Mg–B bond in $MgBr\{B(NArCH)_2\}(THF)_2$ (**1.31**) (2.281(6) Å),[14] but this can be rationalised by taking into account the differences in covalent radii for scandium, titanium and magnesium (Sc = 1.70 Å ; Ti = 1.60 Å; Mg = 1.41 Å). Interestingly, the four coordinate compound $Sc(CH_2SiMe_3)_3\{C(NArCH)_2\}$ (**2.54**, Figure 2.3), featuring a neutral N-heterocyclic carbene (NHC) analogous to **1.7**, has a Sc–C_{NHC} bond length of 2.412(5) Å, strikingly similar to that found in **1**.[15]

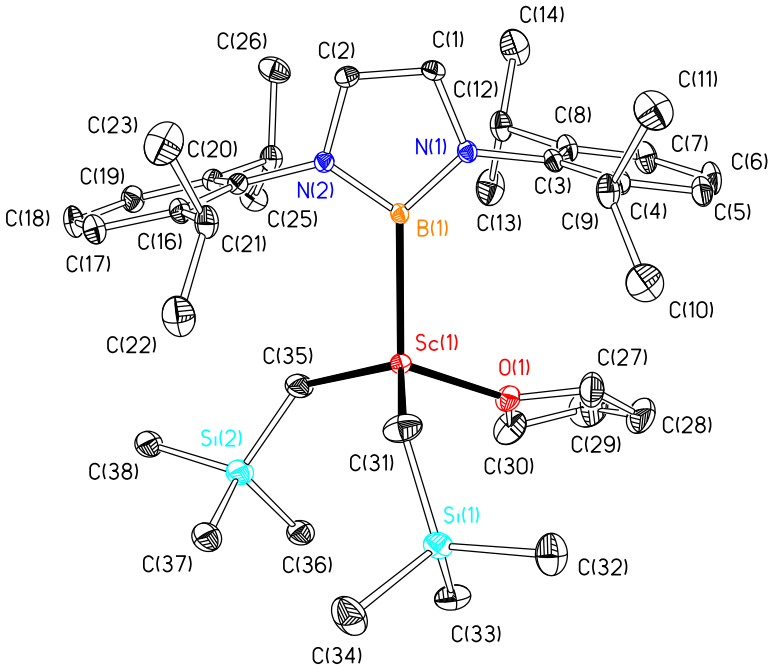

Figure 2.2. Displacement ellipsoid plot (20 % probability) of $Sc(CH_2SiMe_3)_2\{B(NArCH)_2\}(THF)$ (**1**). H atoms omitted for clarity.

Table 2.1. Selected distances (Å) and angles (°) for **1**.

Sc(1)-B(1)	2.422(2)	B(1)-N(2)	1.454(3)
Sc(1)-C(31)	2.171(3)	N(1)-C(1)	1.396(3)
Sc(1)-C(35)	2.174(2)	N(2)-C(2)	1.401(3)
Sc(1)-O(1)	2.1180(17)	C(1)-C(2)	1.342(3)
B(1)-N(1)	1.458(3)		
N(1)-B(1)-N(2)	101.18(18)	B(1)-Sc(1)-C(35)	106.30(9)
B(1)-Sc(1)-C(31)	105.21(10)	B(1)-Sc(1)-O(1)	111.49(8)

Compound **2** possesses a distorted trigonal-bipyramidal structure, in which the two coordinated THF molecules are in the axial position (Figure 2.4). The Y–B bond distance was found to be 2.696(4) Å, within the sum of the respective covalent radii (2.74(10) Å).[13] The Ln–B bond found in **2** is (as with **1** and **3**) without precedent, but a comparison may be made with the corresponding yttrium gallyl compound, $Y\{C(PPh_2NSiMe_3)_2\}\{Ga(NArCH)_2\}(THF)_2$ (**1.140**).[16] Compound **1.140** features a Y–Ga bond measuring 3.1757(4) Å, considerably longer than that found for **2**. However, this difference in bond length can almost entirely be explained by the difference in the respective covalent radii of boron and gallium (0.84(3) and 1.22(3) Å respectively), the difference in coordination number in **1.140** and **2**, and the lower nucleophilicity of the gallyl anion.[17]

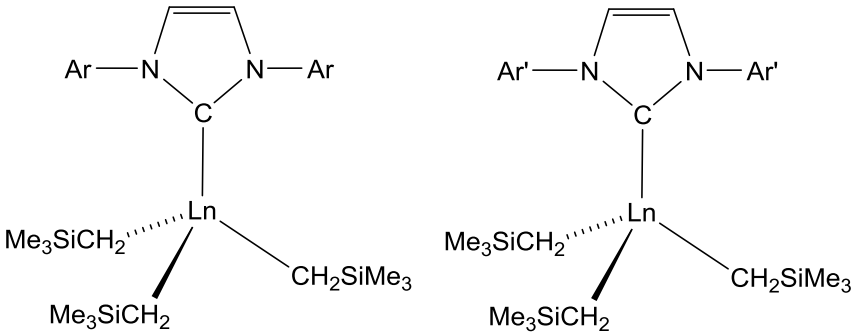

Ln (Ar) = Sc (**2.54**) or Y (**2.55**) Ln (Ar') = Lu (**2.56**)

Figure 2.3. Ar = 2,6-$C_6H_3{}^iPr_2$; Ar' = 2,4,6-$C_6H_3Me_3$.

Compound **2** also has a related NHC compound $Y(CH_2SiMe_3)_3\{C(NArCH)_2\}$ (**2.55**, Figure 2.3).[18] A $Y–C_{NHC}$ bond length of 2.555(2) Å was found, considerably shorter

than that found in **2**, which can be explained by the NHC being able to approach the less crowded metal centre more closely due to the lower coordination number of **2.55** compared to **2**.

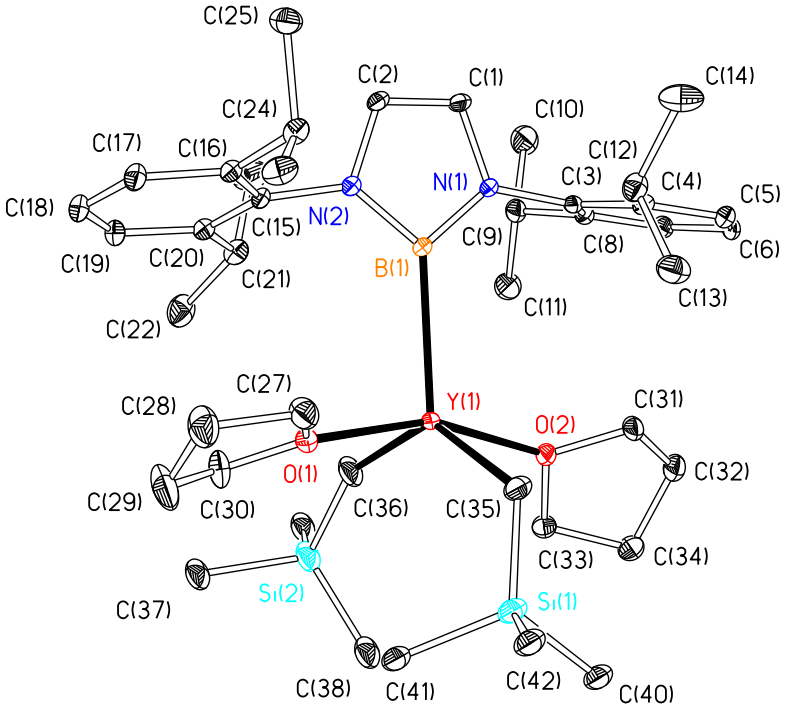

Figure 2.4. Displacement ellipsoid plot (20 % probability) of $Y(CH_2SiMe_3)_2\{B(NArCH)_2\}(THF)_2$ (**2**). H atoms omitted for clarity.

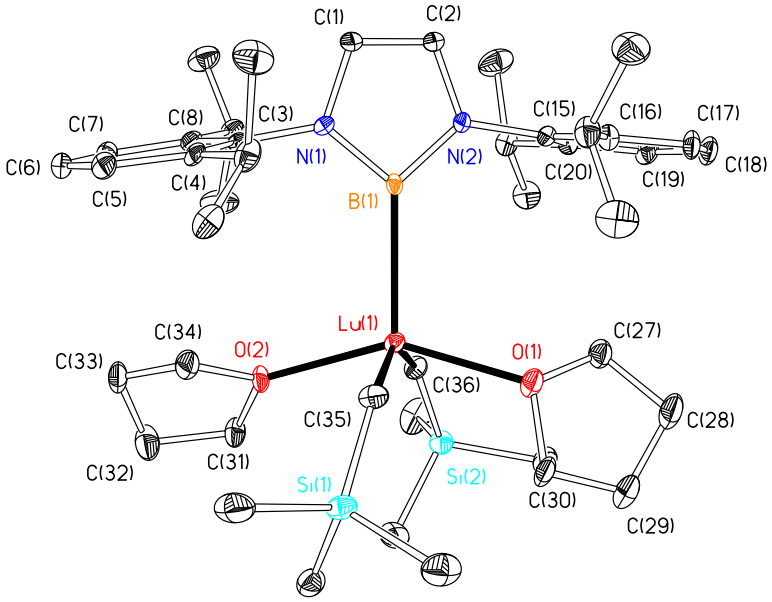

Figure 2.5. Displacement ellipsoid plot (20 % probability) of $Lu(CH_2SiMe_3)_2\{B(NArCH)_2\}(THF)_2$ (**3**). H atoms omitted for clarity.

Table 2.2. Selected distances (Å) and angles (°) for **2**.

Y(1)-B(1)	2.696(4)	B(1)-N(1)	1.456(6)
Y(1)-C(35)	2.424(4)	B(1)-N(2)	1.467(5)
Y(1)-C(36)	2.394(6)	N(1)-C(1)	1.401(5)
Y(1)-O(1)	2.350(3)	N(2)-N(2)	1.397(5)
Y(1)-O(2)	2.370(3)	C(1)-C(2)	1.335(6)
N(1)-B(1)-N(2)	100.3(3)	B(1)-Y(1)-O(1)	93.94(13)
B(1)-Y(1)-C(35)	114.26(15)	B(1)-Y(1)-O(2)	106.33(13)
B(1)-Y(1)-C(36)	109.8(2)	O(1)-Y(1)-O(2)	159.71(11)
C(35)-Y-C(36)	135.8(2)		

Table 2.3. Selected distances (Å) and angles (°) for **3**.

Lu(1)-B(1)	2.555(8)	B(1)-N(1)	1.490(9)
Lu(1)-C(35)	2.354(7)	B(1)-N(2)	1.487(9)
Lu(1)-C(36)	2.352(8)	N(1)-C(1)	1.399(9)
Lu(1)-O(1)	2.316(6)	N(2)-C(2)	1.371(10)
Lu(1)-O(2)	2.314(5)	C(1)-C(2)	1.339(11)
N(1)-B(1)-N(2)	98.3(6)	B(1)-Lu(1)-O(1)	105.3(2)
B(1)-Lu(1)-C(35)	104.5(3)	B(1)-Lu(1)-O(2)	105.9(2)
B(1)-Lu(1)-C(36)	106.3(3)	O(1)-Lu(1)-O(2)	148.9(2)
C(35)-Lu-C(36)	149.2(3)		

Compound **3** exhibits a more square-based pyramidal structure than that found for **2**, in which the boryl is in the axial position and the other ligands forming the base of the pyramid (Figure 2.5). The Lu–B bond length was found to be 2.555(8) Å, within the sum of the respective covalent radii (2.71(11) Å).[13] The related NHC compound $Lu(CH_2SiMe_3)_3\{C(NAr'CH)_2\}$ (**2.56**, Figure 2.3), featuring the less bulky 2,4,6-$Me_3C_6H_3$ as the flanking N-bound aryl groups on the NHC, is four coordinate and as with the yttrium example shows a shorter Lu–C_{NHC} bond length of 2.488(3) Å.[18]

2.3.4 Comparison of $Ln(CH_2SiMe_3)_2\{B(NArCH)_2\}(THF)_n$ Compounds

For **1**–**3**, the geometries and Ln–C and Ln–O bond lengths are unremarkable with respect to boryl compounds, as there is a precedent for four and five-coordinate boryl systems for *d*-block metals,[19] and the Ln–C and Ln–O bond lengths come within the expected ranges and are comparable to the corresponding homoleptic tris(alkyls) **2.9**–**2.11**. The square-based pyramidal geometry of **3** is unusual with respect to rare earth metals, as five-coordinate compounds of the small to mid-size rare earth metals commonly adopt trigonal bipyramidal geometries. Further discussion of this observation can be found in Chapter 4.

As expected,[20] all of the metal-ligand bond lengths follow the periodic trend Sc–X < Y–X > Lu–X, and it can be inferred that there is an appreciable covalent contribution to the Ln–B bond because the Ln–B bond lengths all lie within the sum of the respective covalent radii.[13]. The increased number of THF molecules going from **1** to **2** and **3** can be attributed to the larger covalent radii of yttrium and lutetium compared to scandium.[21]

In solution, **1**–**3** all follow a similar decomposition pathway. At first, all three compounds appear to form a new boryl compound, with new peaks being seen in the ^{1}H NMR spectra. There is no change in the ^{11}B{^{1}H} NMR spectra indicating that although the supporting ligand environment may have changed, the boron environment has essentially stayed the same. These unknown compounds then rapidly decompose to form **1.22** and several unidentifiable products. Further work to identify these intermediates is ongoing. In the solid state, **1**–**3** are stable under inert atmosphere at -30 °C for several weeks, and stable for days at a time in ambient conditions under inert atmosphere.

2.3.5 DFT Computational Analysis of $Ln(CH_2SiMe_3)_2\{B(NArCH)_2\}(THF)_n$

Scalar relativistic, gradient-corrected density functional theory calculations were carried out by Ms Krishna H. Birjkumar and Prof. Nikolas Kaltsoyannis at University College London to further investigate the structure and bonding in **1**–**3**. There is good agreement between the geometry-optimised computed structures (denoted **1C**–**3C**, Figure 2.6) and the solid state structures of **1**–**3**. Table 2.4 presents some selected results from these calculations. The Ln–B bond lengths were reproduced quite well compared to those derived from the solid state structures, with a slightly worse agreement with experiment with the Lu–B example, where the bond length was somewhat overestimated.

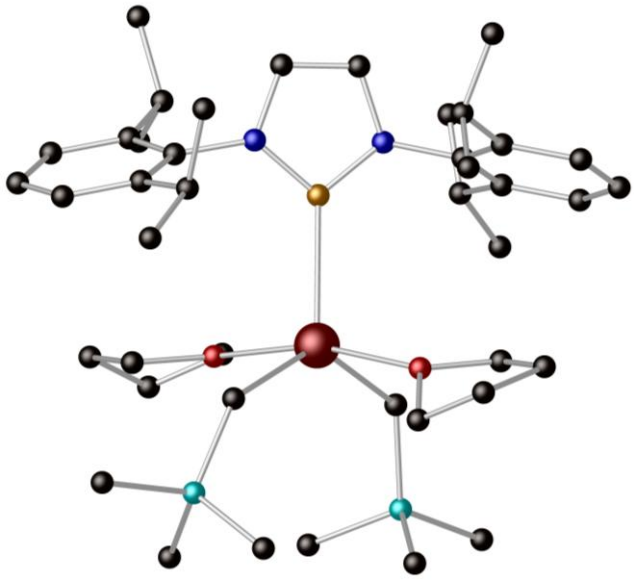

Figure 2.6. Ball and stick plot (arbitrary radius) of the calculated structure of $Lu(CH_2SiMe_3)_2\{B(NArCH)_2\}(THF)_2$ (**3C**). H atoms omitted for clarity.

The potential energy surface of the Ln–B bonds were probed by varying the Ln–B bond distances for **1C**–**3C** and calculating the energy at various points. The Ln–B bonds were shown to have very shallow potential energy surfaces, meaning that small shifts in bond length induce only a small energy change. For example, for Lu–B in **3C**, a 0.1 Å elongation about the equilibrium distance requires a 2.8 kJ mol^{-1}

Table 2.4. Selected DFT computational results for $Ln(CH_2SiMe_3)_2\{B(NArCH)_2\}(THF)_n$. Ln = Sc (**1C**), Y (**2C**) and Lu (**3C**).[a]

	1C	**2C**	**3C**
r(Ln–B) (Å)	2.458	2.692	2.633
r(Ln–C) (mean Å)	2.194	2.412	2.372
r(Ln–O) (mean for **2C** and **3C** Å)	2.193	2.439	2.404
N–B–N (°)	100.3	99.5	99.6
C–Ln–C (°)	117.2	130.2	130.9
O–Ln–O (°)	-	165.3	165.9
Ln–B interaction energy	-346.6	-359.4	-375.1
Pre-relaxation (“steric”) energy	316.4	352.2	386.0
orbital energy	-663.0	-711.6	-761.2
Δq (Ln–B) (Hirshfeld Charge Difference)	0.55	0.64	0.65
Δq (Ln–Boryl) (Hirshfeld Charge Difference)	0.69	0.82	0.82
ρ (electron density)	0.052	0.046	0.050
$\nabla^2\rho$ (electron density Laplacian)	-0.020	0.040	0.050
H (energy density)	-0.012	-0.009	-0.011
Normalised Ln/B Mulliken contributions to the HOMO (%)	38/62	30/70	34/66

a. All energies in kJ mol^{-1}. AIM data (atomic units) obtained at the Ln–B bond critical point

increase in energy, and shortening it by 0.1 Å costs only 3.8 kJ mol^{-1}, with the remaining Ln–B bonds behaving in a similar manner. These results indicate that the relatively soft nature of the bonds can account for the overestimation found for the Lu–B bond length in **3C**. The Ln–B interaction energies increase steadily from scandium to lutetium, and the Ziegler-Rauk breakdown indicates that this occurs because the increased stabilisation energy of the favourable orbital term outweighs that of the unfavourable pre-relaxation ("steric") term. However, the orbital term can involve electron-pair, charge-transfer and/or donor-acceptor interactions, with the orbital term arising from the relaxation of the molecular fragments (in this case the two neutral Ln- and B-containing units) due to the mixing of occupied and unoccupied orbitals. Therefore, the ionic/covalent nature of the Ln–B bond could not readily be inferred from the orbital term, so other analysis tools were used to probe the bonding further. The Hirshfeld charges were calculated for **1C**–**3C**. The positive charge on the metal increases from scandium to lutetium, whilst the boron maintains similar Hirshfeld charges throughout. The charge differences between Ln and B (Δq(Ln–B)) and Ln and the boryl molecule (Δq(Ln–Boryl)) were calculated, with the significant Δq(Ln–Boryl) indicating that the bond is significantly ionic. The Δq(Ln–Boryl) for **1C** was the smallest value for the three calculated compounds, indicating that the Sc–B bond is the least ionic.

The ^{11}B chemical shifts for **1C**–**3C** were also calculated. The calculations all underestimate the experimental values (31, 37 and 45 ppm *vs* 38, 45 and 62 ppm), with the maximum deviation being seen for lutetium. However, the downfield shift of the ^{11}B chemical shift going from Sc to Lu is reproduced by the calculations. It is believed that the significantly downfield shifted signal for lutetium is due to the filled 4*f* orbitals leading to poorer shielding of the outer valence electrons.

To assess the character of the Ln–B bond, the Kohn-Sham molecular orbital approach was applied. For the Ln–B bonds, the bonding orbital is the HOMO and is dominated by a σ-orbital. As expected, there is no evidence of any π-bonding. The normalised contributions (i.e. neglecting all contributions from atoms other than Ln or B) to the σ-bonding HOMO were also calculated. In all cases, boron is found to be the major

contributor, again indicating significantly ionic bonds. The Sc–B HOMO showed the largest degree of mixing between the two atoms, in agreement with the result from the Hirshfeld charge difference suggesting that the Sc–B bond is the least ionic of the three. At the same time, the Y–B HOMO showed the lowest degree of mixing, and it can be concluded that this is the most ionic bond.

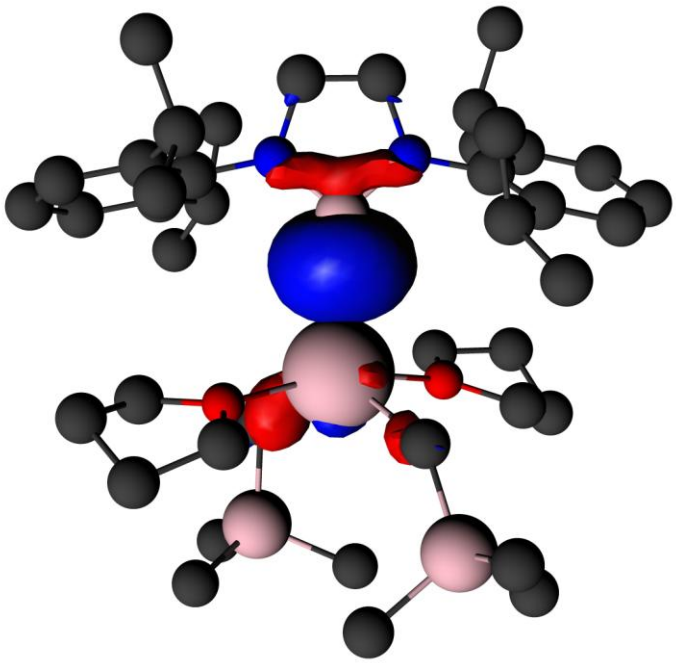

Figure 2.7. Three-dimensional representation of the HOMO of the calculated structure of $Y(CH_2SiMe_3)_2\{B(NArCH)_2\}(THF)_2$ (**2C**). H atoms omitted for clarity.

Atoms-in-Molecules (AIM) analysis was carried out and generated values for the electron density (ρ), the energy density (H) and the electron density Laplacian ($\nabla^2\rho$) at the Ln–B bond critical point. All the values support the conclusion inferred from the Hirshfeld charge calculations, that the bonds are predominantly ionic.[22] The Sc–B bond has the largest ρ, the most negative H and a $\nabla^2\rho < 0$, all indicating that of the three Ln–B bonds it is the least ionic, which is also supported by the relatively small Hirshfeld charge difference, whilst the Y–B bond was found to be the most ionic. With these analyses in hand, the most appropriate bonding description of Ln-B was found to be that of an ionic bond with a highly polarised covalent contribution concentrated in the HOMO.

2.3.6 Other Reported Compounds

After reporting **1**–**3**, a publication by Hou and co-workers detailed the independent isolation of **1**–**3**, as well as the gadolinium and erbium analogues, $Ln(CH_2SiMe_3)_2\{B(NArCH)_2\}(THF)_2$ (Ln = Gd (**2.57**) or Er (**2.58**)).[23] For the independently isolated versions of **1**–**3**, the characterising data and solid state structures matched what had been reported.[1]

2.4 Attempted Synthesis of a Uranium Boryl Compound

A natural progression after the isolation of lanthanide boryl compounds is to compare them to their actinide counterparts. The early metals of the actinide series are particularly interesting due to the extent to which the 5*f* orbitals radially extend, allowing them to potentially be involved in covalent bonding interactions. Of the early metals in the actinide series, only thorium and uranium occur naturally in any great quantity, and uranium has a greater number of available oxidation states and starting compounds reported in the literature. With that in mind, uranium was chosen as the actinide of choice to prepare an actinide boryl compound.

Due to security and environmental controls enforced by national and international authorities, uranium based compounds are not easily commercially available. Procurement of uranium as the metal and as the oxides (UO_3 or U_3O_8) can only realistically be achieved via national laboratories or organisations such as Springfields Fuels Ltd, with the resulting uranium compounds being logged and reported to various authorities, including the University safety office. In addition, the research teams and associated departments then become subject to audits administered by the Environment Agency, with stock, usage and waste disposal checks being carried out and safety protocols being tested.

2.4.1 Starting Materials

The ideal starting materials for the organometallic chemistry of uranium are the halides, which are available in multiple oxidation states. However, as stated earlier, **1.7** is extremely reducing and a powerful nucleophile. In order to avoid reduction of the metal centre, the higher oxidation states of uranium were avoided, and starting compounds with uranium in the 3+ and 4+ oxidation states were sought.

It has been known since the late 1950's that the radical initiated reaction of UO_3 with hexachloropropene at *ca* 220 °C produces, after work up, uranium tetrachloride (**2.59**, Scheme 2.5).[24] Improvements to the safety of the reaction were reported by Kiplinger *et al*., and a modified version of this preparation was used to synthesise **2.59**.[25] The reaction is carried out in a 2 L three-necked round-bottomed flask, with three stacked reflux condensers to control the large exotherm that occurs upon initiation. Slowly heating the reaction mixture to *ca* 200 °C with stirring allows the reaction to be controlled somewhat, until the initiation occurs. After initiation, the reaction is allowed to stir with heating overnight, producing emerald green **2.59** in good yields.

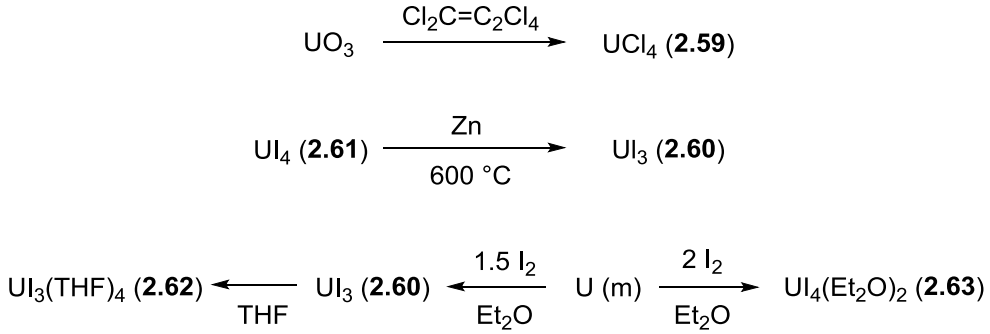

Scheme 2.5. By-products omitted for clarity.

Synthesis of uranium triiodide (**2.60**) and tetraiodide (**2.61**) is much simpler. Historically, the synthesis of **2.60** involved the reduction of **2.61** with zinc metal in sealed silica tubes at 600 °C, whilst the synthesis of **2.61** was laborious and readily decomposed to **2.60** and I_2. In 2008, Arnold *et al*. reported the solution based syntheses of **2.60** and the solvated version of **2.61**, $UI_4(Et_2O)_2$ (**2.63**), both from sonication and stirring of uranium metal and the appropriate quantity of I_2 in Et_2O.[26] For the purposes of reactivity, the THF-solvated version of **2.60**, $UI_3(THF)_4$ (**2.62**), was desirable and is easily accessed by repeated extraction of **2.60** into THF (Scheme 2.5). Test reactions of **2.62** and **2.63** with 1–4 equivalents of **1.7** led only to formation of **1.22** in all cases, consistent with results of other reactions with early transition and rare earth metal halides.

2.4.2 Permethylcyclopentadienyl (Cp*) Compounds

The Cp* ligand is ubiquitous in transition and rare earth metal chemistry as a supporting ligand due to its excellent steric and electronic properties. With that in mind, U^{3+} and U^{4+} Cp* compounds were targeted as precursors for reactions with **1.7**, in particular the landmark compounds reported by Marks *et al*. and Burns and Clark *et al*. $Cp^*_2UCl_2$ (**2.65**) can be isolated in good yields via reaction with **2.59** and Cp*MgCl(THF) (**2.64**).[27] Compound **2.64** is used in place of the usual LiCp* compounds as it was found to reproducibly achieve higher pure yields of **2.65.** The uranium (III) Cp* compounds, $Cp^*UI_2(THF)_3$ (**2.66**) and $Cp^*_2UI(THF)$ (**2.67**), were accessible by reaction of either one (**2.66**) or two (**2.67**) equivalents of KCp* and **2.62**, also in good yields (Scheme 2.6).[28] Reactions of **2.65**–**2.67** with **1.7** again produced only **1.22** and intractable mixtures.

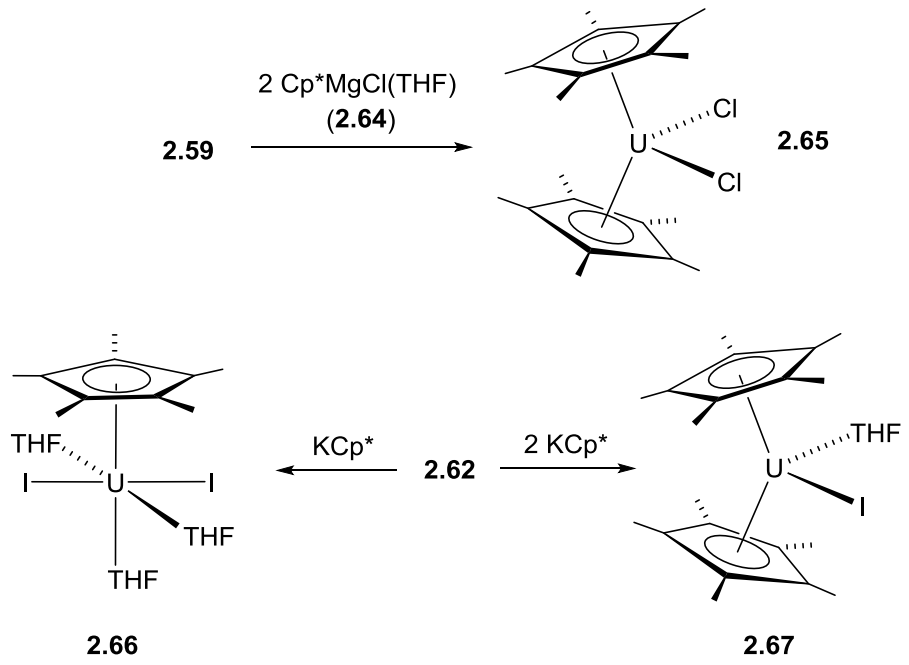

Scheme 2.6. By-products omitted for clarity.

Salt metathesis did not appear to be a good method of generating the desired uranium boryl compound, and so derivatives of **2.65**–**2.67** featuring alkyl and amide ligands were synthesised, and these are summarised in Scheme 2.7. Addition of two equivalents of MeLi to **2.65** yielded, after recrystallisation from toluene, $Cp^*_2UMe_2$ (**2.68**) as orange needles.[27] Reaction of one or two equivalents of $\{KN(SiMe_3)_2\}$ with either **2.66** or **2.67** produced $Cp^*U\{N(SiMe_3)_2\}_2$ (**2.69**) or $Cp^*_2U\{N(SiMe_3)_2\}$ (**2.70**).[28] In keeping with the recurring theme, addition of varying equivalents of **1.7** with **2.68**–**2.70** produced only **1.22**.

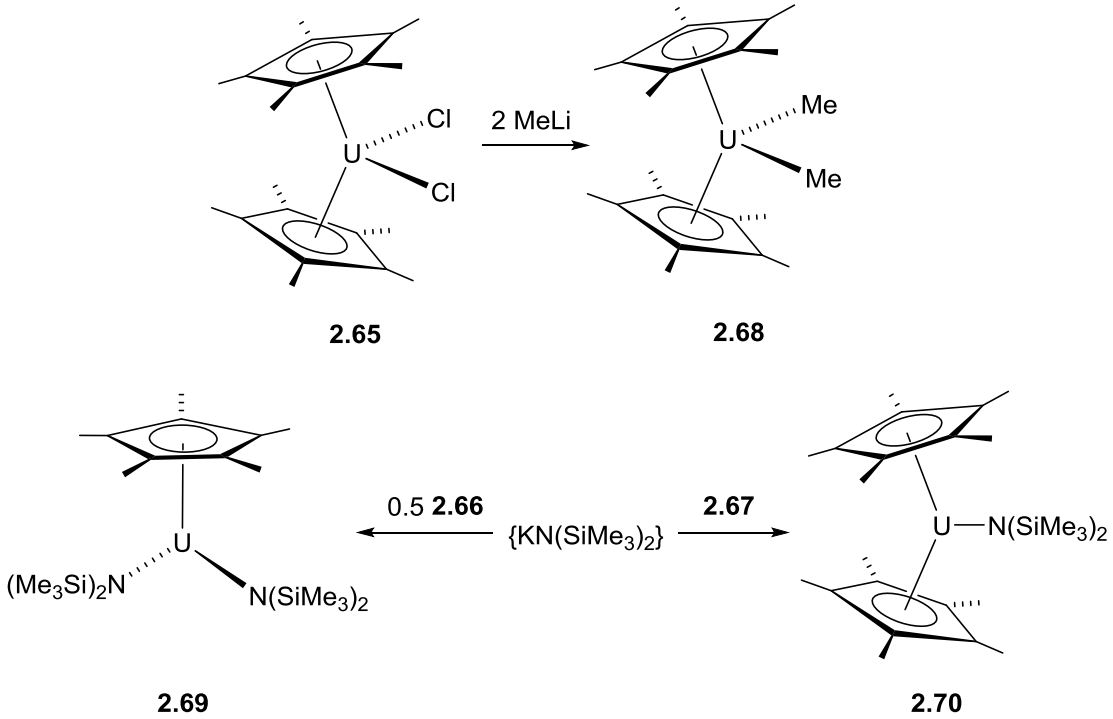

Scheme 2.7. By-products omitted for clarity.

2.4.3 Tripodal Ligands

The lack of success with the Cp*-based systems led to the use of the well know tren-based ligand types, featuring a tripodal N_3^- donor (Scheme 2.8). The uranium tren compound $UCl\{N((CH_2)_2N(SiMe_3))_3\}(THF)$ (**2.71**) was synthesised from **2.59** and $\{N((CH_2)_2N(SiMe_3))_3\}Li_3$, as reported by Scott[29] (structure elucidated later by Liddle *et al.*).[30] Reaction of **2.71** or its associated iodide, $UI\{N((CH_2)_2N(SiMe_3))_3\}(THF)$ (**2.72**),[31] with **1.7** produced only **1.22**.

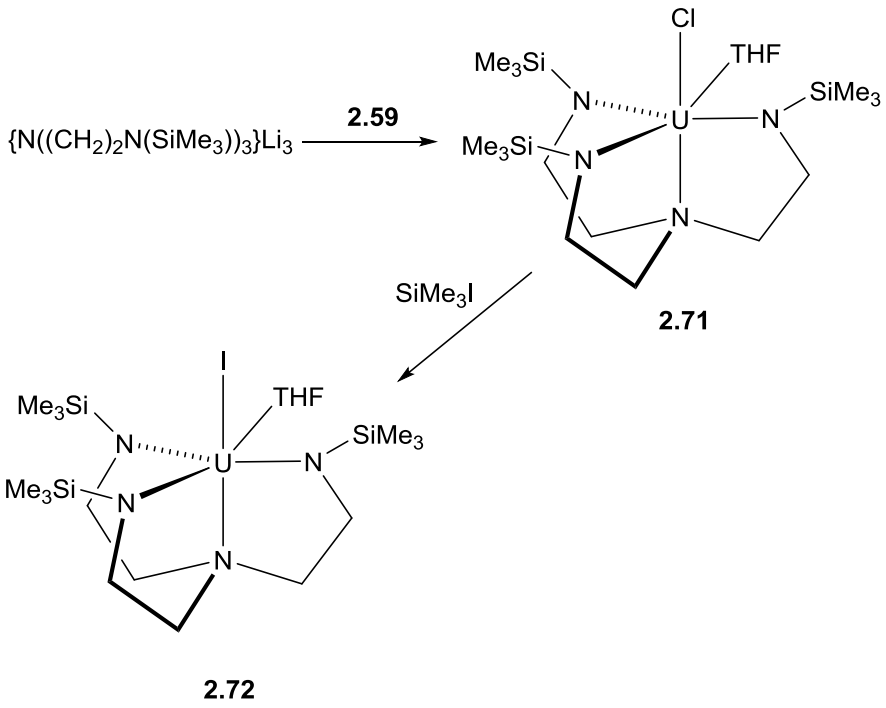

Scheme 2.8. By-products omitted for clarity.

2.4.4 Cationic Compounds and Transfer Agents

Returning to the previously successful synthetic methodology that led to **1**–**3**, cationic compounds of uranium in both the 3+ and 4+ oxidation states were employed. Addition of $[NH_4][BPh_4]$ to **2.70** produced the cationic sandwich compound $[Cp^*_2U(THF)_2][BPh_4]$ (**2.73-BPh$_4$**).[32] The uranium tetraamide, $U(NEt_2)_4$ (**2.74**), was synthesised from the reaction of **2.59** with four equivalents of $LiNEt_2$ and purification *via* high-vacuum sublimation.[33] Reaction of **2.74** with one equivalent of $[Et_3NH][BPh_4]$ led to the isolation of the cationic uranium (IV) compound, $[U(NEt_2)_3][BPh_4]$ (**2.75-BPh$_4$**, Scheme 2.9).[34] Unfortunately, reactions of **2.73-BPh$_4$** and **2.75-BPh$_4$** with **1.7** again produced **1.22**, as did a reaction with **2.74**.

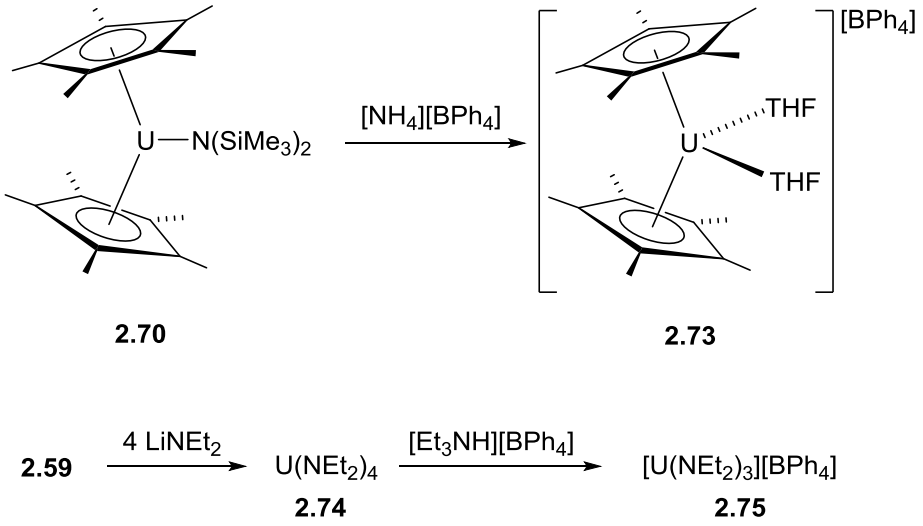

Scheme 2.9. By-products omitted for clarity.

With the failure of a series of starting compounds, **1.7** was deemed to be too reactive and a milder way of transferring the boryl anion was sought. There is precedent in rare earth metal chemistry of using mercury or tin compounds as mild transfer agents for ligands. Jones, Mountford and Aldridge *et al*. have reported the isolation of the tin(II) boryl compound Sn{NAr(SiMe$_3$)}{B(NArCH)$_2$} (**1.132**).[35] The bis(boryl) version of that compound, Sn{B(NArCH)$_2$}$_2$ (**2.76**), was also reported and it was this compound that was reacted with **2.59** to effect the transfer of two boryl ligands and form UCl$_2${B(NArCH)$_2$}$_2$. However, rather than form UCl$_2${B(NArCH)$_2$}$_2$, chloride transfer from **2.59** to, and oxidation of, **2.76** occurred, producing SnCl$_2${B(NArCH)$_2$}$_2$ (**4**, Figures 2.8 and 2.9).

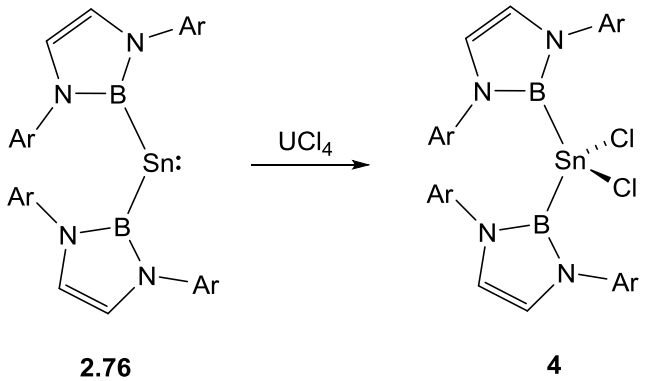

Figure 2.8

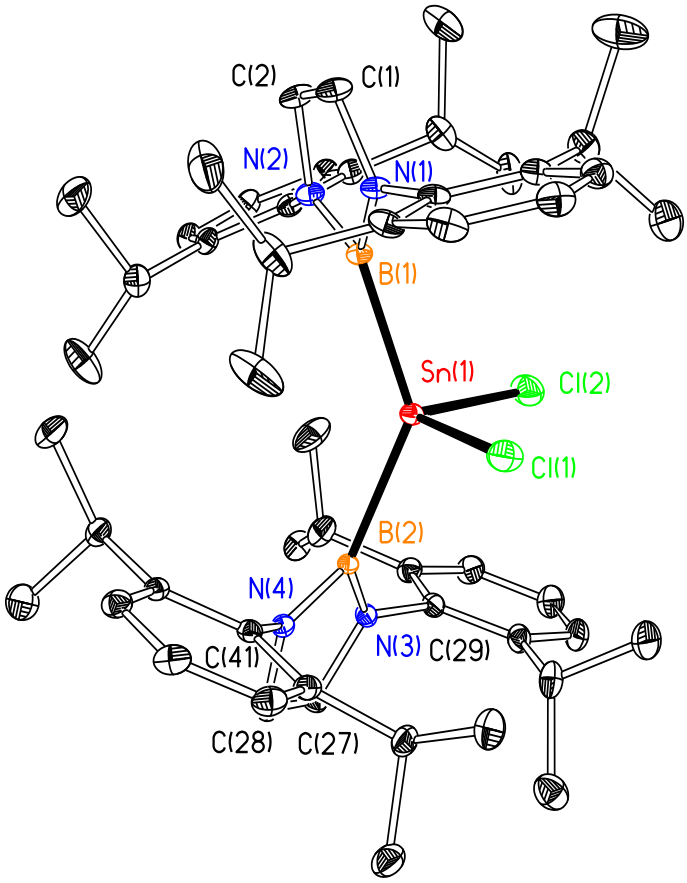

Figure 2.9. Displacement ellipsoid plot (20 % probability) of $SnCl_2\{B(NArCH)_2\}_2$ (**4**). H atoms and minor disorder omitted for clarity.

Table 2.5. Selected distances (Å) and angles (°) for **4**.

Sn(1)-B(1)	2.250(3)	B(1)-N(2)	1.426(3)
Sn(1)-B(2)	2.252(2)	B(2)-N(3)	1.435(3)
Sn(1)-Cl(1)	2.3531(7)	B(2)-N(4)	1.425(3)
Sn(1)-Cl(2)	2.3579(8)	C(1)-C(2)	1.329(4)
B(1)-N(1)	1.428(3)	C(27)-C(28)	1.346(4)
B(1)-Sn(1)-B(2)	136.28(10)	N(1)-B(1)-N(2)	105.7(2)
Cl(1)-Sn(1)-Cl(2)	100.93(4)	N(3)-B(2)-N(4)	106.01(19)

2.5 Conclusions

The work presented in this Chapter has introduced the Schlenk-line synthesis of the boryl anion, **1.7**. Rare earth metal alkyls and their cationic counterparts were also introduced. The synthesis of the first rare earth metal boryl compounds of the type $Ln(CH_2SiMe_3)_2\{B(NArCH)_2\}(THF)_n$, featuring a 2-centre, 2-electron σ-bond between a rare earth metal and boron was then reported, with the "charge neutralisation" approach providing a way to control reactivity of the strongly reducing and nucleophilic boryl anion. Their solid state structures were established, and their structure and bonding were probed by DFT studies. The scandium dialkyl boryl compound, **1**, was found to form a four-coordinate compound, not unlike that of $Ti(O^iPr)_3\{B(NArCH)_2\}$ (**1.47**), and was found to have the least ionic Ln–B bond. The yttrium (**2**) and lutetium (**3**) analogues formed five-coordinate compounds, each with two molecules of THF, and form the more ionic Ln–B bonds. It was concluded that the most appropriate bonding description of the Ln–B bond was found to be that of an ionic bond with a highly polarised covalent contribution concentrated in the HOMO. Attempts at synthesising a uranium boryl compound were also reported, with all attempts ending in failure. It is believed that the choice of a suitable supporting ligand set and suitable form of the boryl anion will enable the isolation of these species in the future.

2.6 References

1 L. M. A. Saleh, K. H. Birjkumar, A. V. Protchenko, A. D. Schwarz, S. Aldridge, C. Jones, N. Kaltsoyannis and P. Mountford, *J. Am. Chem. Soc.*, 2011, **133**, 3836.

2 G. Wilkinson and J. M. Birmingham, *J. Am. Chem. Soc.*, 1954, **76**, 6210.

3 E. Frankland, *Quarterly Journal of the Chemical Society of London*, 1850, **2**, 263.

4 M. F. Lappert and R. Pearce, *J. Chem. Soc., Chem. Commun.*, 1973, 126.

5 P. M. Zeimentz, S. Arndt, B. R. Elvidge and J. Okuda, *Chem. Rev.*, 2006, **106**, 2404.

6 C. J. Schaverien, *Organometallics*, 1992, **11**, 3476.

7 B. R. Elvidge, S. Arndt, P. M. Zeimentz, T. P. Spaniol and J. Okuda, *Inorg. Chem.*, 2005, **44**, 6777.

8 Y. Segawa, M. Yamashita and K. Nozaki, *Science*, 2006, **314**, 113.

9 Y. Segawa, Y. Suzuki, M. Yamashita and K. Nozaki, *J. Am. Chem. Soc.*, 2008, **130**, 16069.

10 N. Dettenrieder, Y. Aramaki, B. M. Wolf, C. Maichle-Mossmer, X. X. Zhao, M. Yamashita, K. Nozaki and R. Anwander, *Angew. Chem. Int. Ed.*, 2014, **53**, 6259.

11 H. Braunschweig and M. Colling, *Coord. Chem. Rev.*, 2001, **223**, 1.

12 T. Terabayashi, T. Kajiwara, M. Yamashita and K. Nozaki, *J. Am. Chem. Soc.*, 2009, **131**, 14162.

13 B. Cordero, V. Gomez, A. E. Platero-Prats, M. Reves, J. Echeverria, E. Cremades, F. Barragan and S. Alvarez, *Dalton Trans.*, 2008, 2832.

14 M. Yamashita, Y. Suzuki, Y. Segawa and K. Nozaki, *J. Am. Chem. Soc.*, 2007, **129**, 9570.

15 Y. Pan, T. Q. Xu, Y. S. Ge and X. B. Lu, *Organometallics*, 2011, **30**, 5687.

16 S. T. Liddle, D. P. Mills, B. M. Gardner, J. McMaster, C. Jones and W. D. Woodul, *Inorg. Chem.*, 2009, **48**, 3520.

17 A. V. Protchenko, L. M. A. Saleh, D. Vidovic, D. Dange, C. Jones, P. Mountford and S. Aldridge, *Chem. Commun.*, 2010, **46**, 8546.

18 W. Fegler, T. P. Spaniol and J. Okuda, *Dalton Trans.*, 2010, **39**, 6774.

19 (a) R. T. Baker, J. C. Calabrese, S. A. Westcott, P. Nguyen and T. B. Marder, *J. Am. Chem. Soc.*, 1993, **115**, 4367; (b) C. Y. Dai, G. Stringer, T. B. Marder, A. J. Scott, W. Clegg and N. C. Norman, *Inorg. Chem.*, 1997, **36**, 272.

20 D. M. P. Mingos, *Essential Trends in Inorganic Chemistry*, Oxford University Press, 1998.

21 R. D. Shannon, *Acta Crystallogr. Sect. A*, 1976, **32**, 751.

22 M. J. Tassell and N. Kaltsoyannis, *Dalton Trans.*, 2010, **39**, 6719.

23 S. H. Li, J. H. Cheng, Y. H. Chen, M. Nishiura and Z. M. Hou, *Angew. Chem. Int. Ed.*, 2011, **50**, 6360.

24 J. A. Hermann and J. F. Suttle, *Inorganic Syntheses*, 1957, **5**, 143.

25 J. L. Kiplinger, D. E. Morris, B. L. Scott and C. J. Burns, *Organometallics*, 2002, **21**, 5978.

26 C. D. Carmichael, N. A. Jones and P. L. Arnold, *Inorg. Chem.*, 2008, **47**, 8577.

27 P. J. Fagan, J. M. Manriquez, E. A. Maatta, A. M. Seyam and T. J. Marks, *J. Am. Chem. Soc.*, 1981, **103**, 6650.

28 L. R. Avens, C. J. Burns, R. J. Butcher, D. L. Clark, J. C. Gordon, A. R. Schake, B. L. Scott, J. G. Watkin and B. D. Zwick, *Organometallics*, 2000, **19**, 451.

29 P. Scott and P. B. Hitchcock, *Polyhedron*, 1994, **13**, 1651.

30 S. T. Liddle, J. McMaster, D. P. Mills, A. J. Blake, C. Jones and W. D. Woodul, *Angew. Chem. Int. Ed.*, 2009, **48**, 1077.

31 B. M. Gardner, J. McMaster, W. Lewis and S. T. Liddle, *Chem. Commun.*, 2009, 2851.

32 C. Boisson, J. C. Berthet, M. Ephritikhine, M. Lance and M. Nierlich, *J. Organomet. Chem.*, 1997, **533**, 7.

33 J. G. Reynolds, A. Zalkin, D. H. Templeton, N. M. Edelstein and L. K. Templeton, *Inorg. Chem.*, 1976, **15**, 2498.

34 J. C. Berthet, C. Boisson, M. Lance, J. Vigner, M. Nierlich and M. Ephritikhine, *J. Chem. Soc., Dalton Trans.*, 1995, 3019.

35 A. V. Protchenko, K. H. Birjkumar, D. Dange, A. D. Schwarz, D. Vidovic, C. Jones, N. Kaltsoyannis, P. Mountford and S. Aldridge, *J. Am. Chem. Soc.*, 2012, **134**, 6500.

Chapter Three

Syntheses, Structures and Bonding Analyses of Rare Earth Metal Gallyl Compounds

3.1 Overview

This Chapter describes the synthesis and isolation of cationic rare earth metal bis(amidinate) compounds and their use in the synthesis of rare earth metal gallyl compounds. A short introduction to the amidinate ligand and its suitability as a stable, generally innocent supporting ligand set for rare earth metals, as well as providing pertinent examples, will precede the presentation of results.

3.2 Rare Earth Metal Amidinates

3.2.1 Introduction

Rare earth metal *N*,*N*′-disubstituted amidinates (and the closely related *N*,*N*′-disubstituted guanidinates) are a relatively new class of compounds, coming into existence in the early 1990's. The increased use of the amidinate ligand coincided with the need to diversify the well-known rare earth metal cyclopendienyl compounds and their chemistry, with the amidinate ligand being regarded as "steric cyclopentadienyl equivalents", a concept developed by Wolczanski and co-workers in connection with a series of tri-*tert*-butylmethoxide (tritox) compounds[1] and associated with amidinates by Edelmann and co-workers.[2] This steric equivalency is especially important when considering reactivity with rare earth metals, as steric saturation of the coordination sphere is more important than the number of valence electrons. In general, metal amidinates are accessible *via* several synthetic routes, the most important of which for rare earth metals include:

i) Insertion of carbodiimides (RNCNR') into a metal-carbon bond

ii) Deprotonation of an amidine using a metal alkyl compound

iii) Salt metathesis reactions between a metal halide and alkali metal amidinate

Metal guanidinates are accessible *via* analogous routes, with insertion of carbodiimides into metal-nitrogen bonds being used for (i) and guanidines and alkali metal guanidinates being used for (ii) and (iii), respectively.

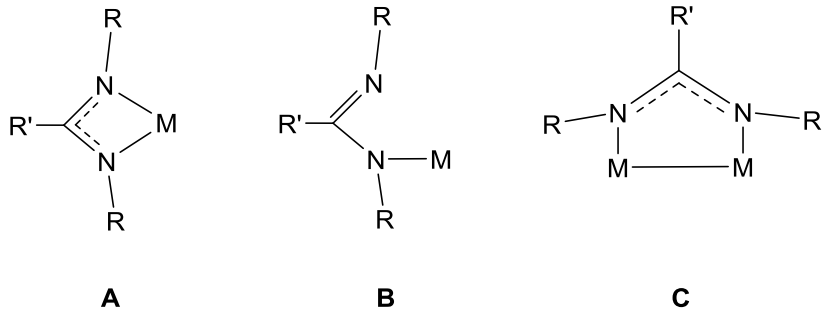

Figure 3.1 The most common *N,N'*-disubstituted amidinate coordination modes.

The coordination chemistry of these ligands is varied, with monodentate, chelating and bridging coordination modes possible. The most common coordination mode is the chelating type (**A**, Figure 3.1). The monodentate coordination mode (**B**) is rare, with only a few examples known. The bridging coordination mode (**C**) is well known for transition metals, often forming dinuclear compounds featuring short metal-metal distances, the sort that are completely unknown for rare earth metals. The ease with which the substituents at carbon and nitrogen can be varied to tune the steric and (to a lesser extent) electronic properties of the ligands allows these ligands to fit across the entire size range of the rare earth metals, from the smaller scandium to the very large lanthanum.

A series of reviews by Edelmann provide a comprehensive account of the chemistry of rare earth metal amidinates.[3-6] The rest of this introduction will provide information on key compounds relevant to the chemistry that will be presented later in this Chapter.

3.2.2 Neutral Compounds

The first lanthanide metal amidinates were isolated by Edelmann and co-workers in 1990.[7] Addition of two equivalents of the sodium amidinates Na[ArC(NSiMe$_3$)$_2$] (Ar = C_6H_5, 4-C_6H_4OMe or 4-C_6H_4Ph) to $YbI_2(THF)_2$ produced the dark red divalent ytterbium bisamidinates Yb{ArC(NSiMe$_3$)$_2$}$_2$(THF)$_2$ (Ar = C_6H_5 (**3.1**), 4-C_6H_4OMe (**3.2**) or 4-C_6H_4Ph (**3.3**), Equation 3.1). An X-ray diffraction study of **3.1** showed a distorted octahedral structure with the two amidinate ligands coordinated in a chelating fashion *trans* to each other. Compound **3.1** also showcases the classic "cone-like" shape of the amidinate ligands when featuring these subsituents. This is

due to the large dihedral angle between the phenyl ring and the amidinate NCN unit, which precludes any conjugation between the two π-systems.

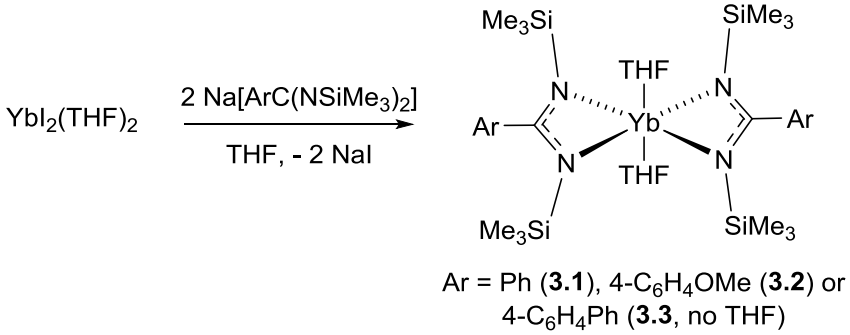

Ar = Ph (**3.1**), 4-C_6H_4OMe (**3.2**) or 4-C_6H_4Ph (**3.3**, no THF)

Equation 3.1

Edelmann and co-workers then reported the synthesis of the first trivalent lanthanide amidinates, synthesising a series of homoleptic tris(amidinates) with different aryl groups on the carbon atom.[2] These are outlined in Equation 3.2, with those containing Ar = Ph (**3.4**–**3.12**) being presented as typical examples.

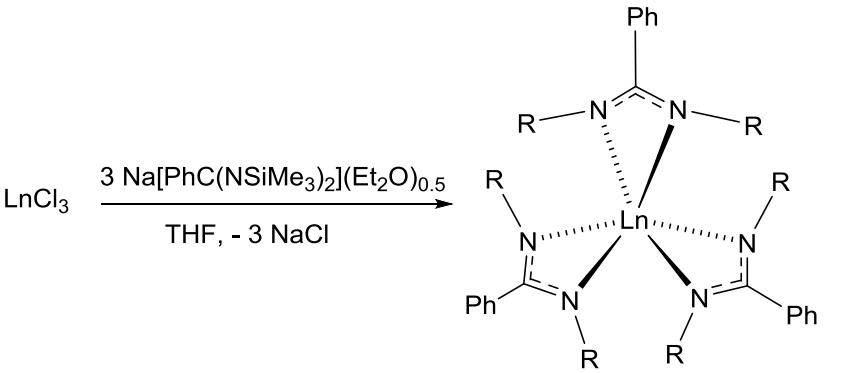

Ln = Sc (**3.4**), Ce (**3.5**), Pr (**3.6**), Nd (**3.7**), Sm (**3.8**), Eu (**3.9**), Gd (**3.10**), Yb (**3.11**), Lu (**3.12**),

R = $SiMe_3$

Equation 3.2

Trivalent rare earth metal bis(amidinates) were attractive targets as they could be compared to the analogous rare earth metal metallocene compounds. Amongst the first to be isolated was the neodymium bis(amidinate) "ate" compound $Nd\{ArC(NSiMe_3)_2\}_2(\mu\text{-}Cl)_2Li(THF)_2$ (Ar = 2,4,6-$C_6H_2(CF_3)_3$ (**3.13**), Scheme 3.1), with the very bulky amidinate ligand required to stabilise the large Nd metal centre.[8] This compared favourably with the well-known metallocene equivalent, $Cp^*_2Nd(\mu$-

$Cl)_2Li(THF)_2$. Teuben and co-workers showed that for the smaller yttrium, salt-free compounds of rare earth bis(amidinates) could be accessed. Reaction of $YCl_3(THF)_{3.5}$ with two equivalents of the less sterically demanding amidinate, $Li[PhC(NSiMe_3)_2]$, leads to excellent yields of the yttrium bis(amidinate) compound $YCl\{PhC(NSiMe_3)_2\}_2(THF)$ (**3.14**, Scheme 3.1).[9]

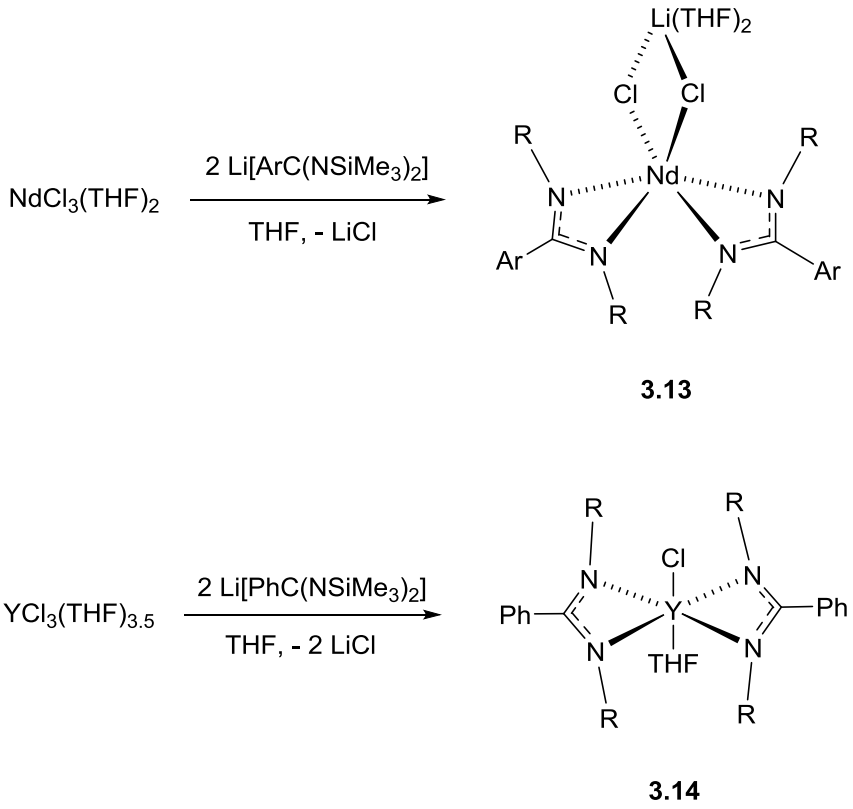

3.13

3.14

Scheme 3.1. Ar = 2,4,6-$C_6H_2(CF_3)_3$. R = $SiMe_3$.

Having demonstrated that rare earth metal bis(amidinate) and bis(guanidinate) compounds could be isolated in a similar manner to the rare earth metal metallocenes, it was further demonstrated that bis(amidinate) and bis(guanidinate) alkyl, amide and hydride species could be isolated using techniques analogous to those used for metallocene compounds. Trifonov and co-workers isolated a lutetium bis(guanidinate) chloride "ate" compound, $Lu\{(N(SiMe_3)_2)C(N^iPr)_2\}_2(\mu\text{-}Cl)_2Li(THF)_2$ (**3.15**, Scheme 3.2), and subsequently reacted it with one equivalent of $LiCH_2SiMe_3$ to produce the alkyl compound $Lu\{(N(SiMe_3)_2)C(N^iPr)_2\}_2(CH_2SiMe_3)$ (**3.16**). Reaction of **3.16** with $PhSiH_3$ produced the bridging hydride compound, $[Lu\{(N(SiMe_3)_2)C(N^iPr)_2\}_2(\mu\text{-}H)]_2$ (**3.17**).[10]

In keeping with the metallocene analogy, **3.17** was found to have an $Lu_2(\mu\text{-}H)_2$ core featuring similar Lu–H and Lu–Lu distances to those containing cyclopentadienyl supporting ligands.[11]

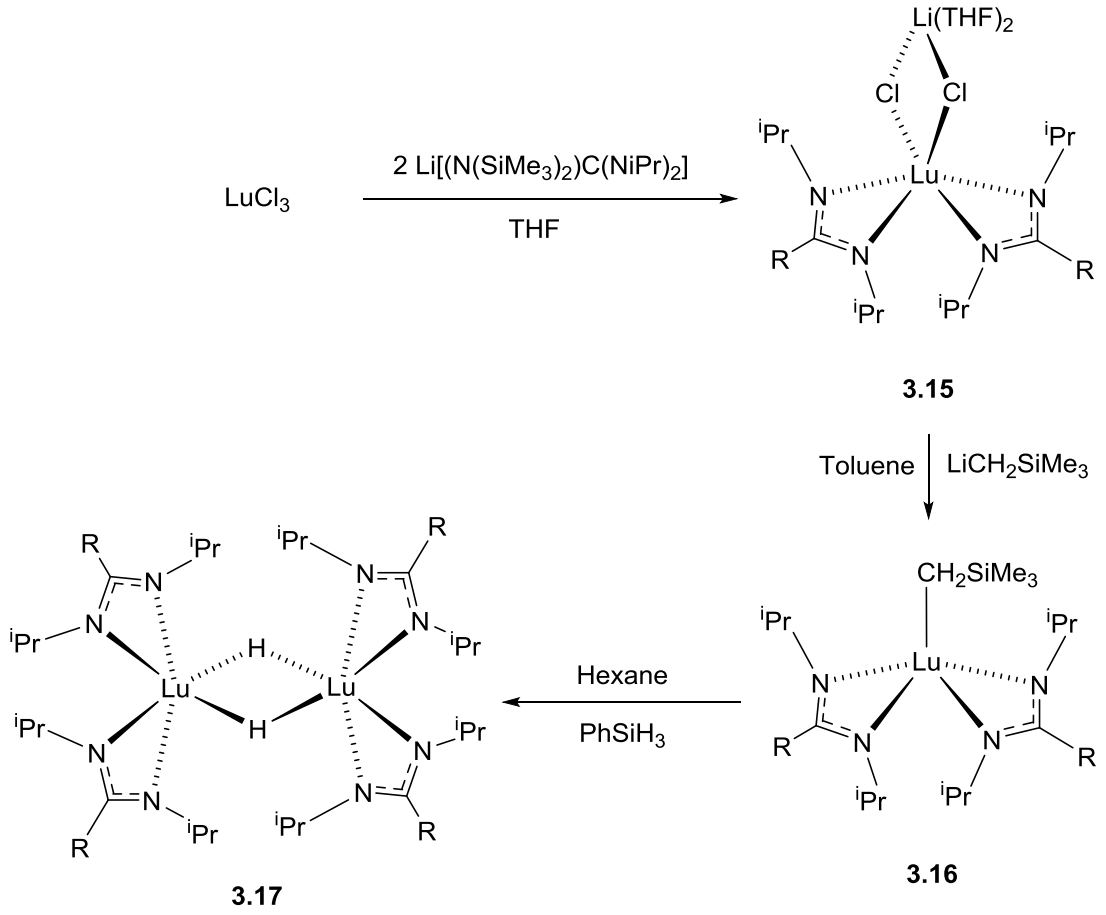

Scheme 3.2. By-products omitted for clarity. R = $N(SiMe_3)_2$.

The last group of rare earth metal amidinate and guanidinates to be synthesised were the singly substituted compounds. In a landmark report by Hessen, a specially designed bulky amidine was used to isolate rare earth metal mono(amidinate) dialkyl compounds across the entire size range of the rare earths, from scandium to lanthanum.[12, 13] Reaction of $Ln(CH_2SiMe_3)_3(THF)_n$, either generated *in situ* (Sc, Nd, Gd and La) or from isolated examples (Sc, Y and Lu), with the amidine PhC(NHAr)(NAr) (Ar = 2,6-$C_6H_3{}^iPr_2$) produced, upon elimination of tetramethylsilane, the rare earth metal mono(amidinate) dialkyls, $Ln\{PhC(NAr)_2\}(CH_2SiMe_3)_2(THF)_n$ (Ln = Sc, n = 1 (**3.18**); Y, n = 2 (**3.19**); Gd, n = 2 (**3.20**); Lu, n = 1 (**3.21**); La, n = 2 (**3.22**); Nd, n = 2 (**3.23**), Scheme 3.3). An X-ray

diffraction study of **3.23** revealed a structure that is essentially isostructural to the previously reported **3.19**,[12] with the alkyl groups axial to the amidinate ligand.

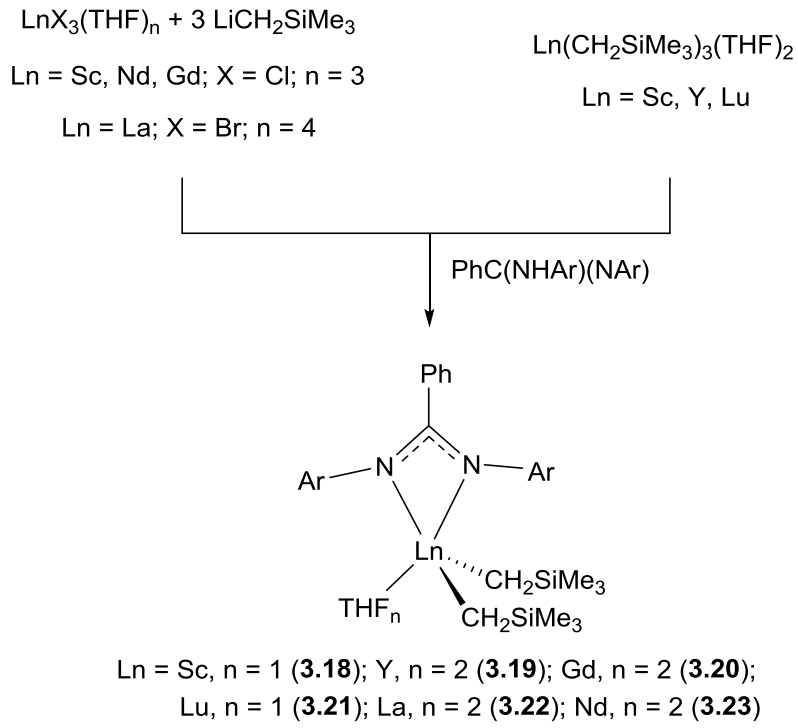

Scheme 3.3. By-products omitted for clarity. Ar = 2,6-$^{i}Pr_2C_6H_3$.

3.2.3 Cationic Compounds

In the same communication that reported the isolation of **3.18**–**3.23**, Hessen and co-workers also reported the synthesis and isolation of their cationic counterparts, **3.24**–**3.29-BPh$_4$**.[13] Reaction of one equivalent of [PhMe$_2$NH][BPh$_4$] with **3.18**–**3.23** produces the cationic rare earth metal mono(amidinate) alkyl compounds, [Ln{PhC(NAr)$_2$}(CH$_2$SiMe$_3$)(THF)$_n$][BPh$_4$] (Ln = Sc, n = 2 (**3.24-BPh$_4$**); Y, n = 3 (**3.25-BPh$_4$**); Gd, n = 3 (**3.26-BPh$_4$**); Lu, n = 3 (**3.27-BPh$_4$**); La, n = 4 (**3.28-BPh$_4$**); Nd, n = 4 (**3.29-BPh$_4$**), Equation 3.3). Compounds **3.24**–**3.29-BPh$_4$** were tested for their catalytic activity in the polymerisation of ethane. It was found that catalytic activity was strongly dependent on metal ionic radius, with the smallest and largest metals, scandium and lanthanum, showing very low activity, and the intermediate metals, yttrium and gadolinium, showing the highest activity.

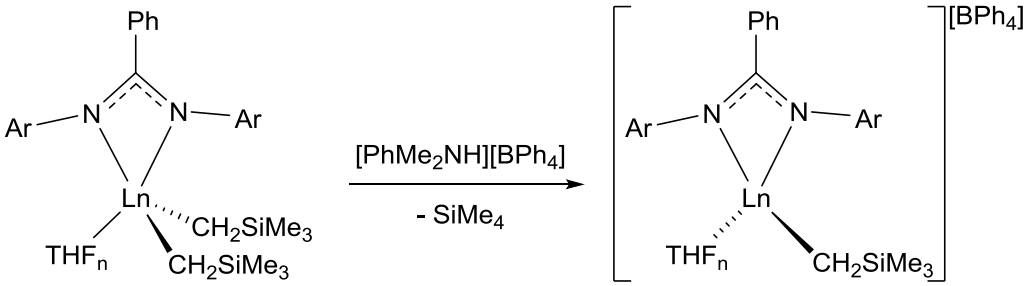

Ln = Sc, n = 1 (**3.18**); Y, n = 2 (**3.19**); Gd, n = 2 (**3.20**); Lu, n = 1 (**3.21**); La, n = 2 (**3.22**); Nd, n = 2 (**3.23**)

Ln = Sc, n = 2 (**3.24-BPh$_4$**); Y, n = 3 (**3.25-BPh$_4$**); Gd, n = 3 (**3.26-BPh$_4$**); Lu, n = 3 (**3.27-BPh$_4$**); La, n = 4 (**3.28-BPh$_4$**); Nd, n = 4 (**3.29-BPh$_4$**)

Equation 3.3

3.3 Rare Earth Metal Bis(amidinate) Cations

3.3.1 Introduction

The synthesis of the rare earth metal boryl compounds $Ln(CH_2SiMe_3)_2\{B(NArCH)_2\}(THF)_n$ (**1**–**3**) prompted an attempt at extending the "charge neutralisation" approach towards synthesising the analogous gallyl compounds. If the gallyl compounds could be isolated, unprecedented structural and reactivity comparisons between the rare earth metal boryl and gallyl compounds could be made, and would, in fact, constitute the first direct comparison of metal boryl and metal gallyl compounds featuring identical supporting ligand sets. However, use of the cationic rare earth metal compounds $[Ln(CH_2SiMe_3)_2(THF)_3][BPh_4]$ (**2.16–2.17-BPh$_4$** and **2.22-BPh$_4$**) with the salt of the gallyl anion $[K\{Ga(NArCH)_2\}(Et_2O)]_2$ (**3.30**), where the cation is solvated by diethyl ether, did not result in the expected rare earth metal gallyl compounds, with decomposition of the cation and formation of the known digallane(4) $[Ga(NArCH_2)_2]_2$ (**1.36**) being observed. It was hypothesised that the dialkyl ligands could not offer sufficient steric protection for any corresponding gallyl compound, and a more sterically encumbered supporting ligand set that could provide access to both stable cationic precursors and stabilise the desired gallyl compound was required. Additionally, it was highly desirable that the ligands selected could provide a platform for isolating the resulting Ln–Ga bond for reactivity. With those criteria in mind, bis(amidinate) cationic compounds of the rare earth metals were targeted.

3.3.2 Synthesis

As mentioned in section 3.2.1, there are three important synthetic routes to metal amidinate compounds, all of which could be employed in the synthesis of cationic rare earth metal bis(amidinate) compounds. The only known rare earth metal cationic compounds with an amidinate ligand, **3.24**–**3.29-BPh$_4$** (Scheme 3.3 and Equation 3.3), employed route (ii) (see page 74 and Figure 3.2) to ligate the amidinate prior to deprotonation with [PhMe$_2$NH][BPh$_4$] to form the separated ion pair.[13] Use of route (iii) could be envisaged, reacting an alkali metal amidinate of choice with a rare earth metal halide, followed by alkylation and deprotonation. However, these routes were deemed to be circuitous, and it was concluded that route (i), insertion of a carbodiimide into a metal-carbon bond, would provide the best access to cationic rare earth metal bis(amidinate) compounds (Figure 3.2).

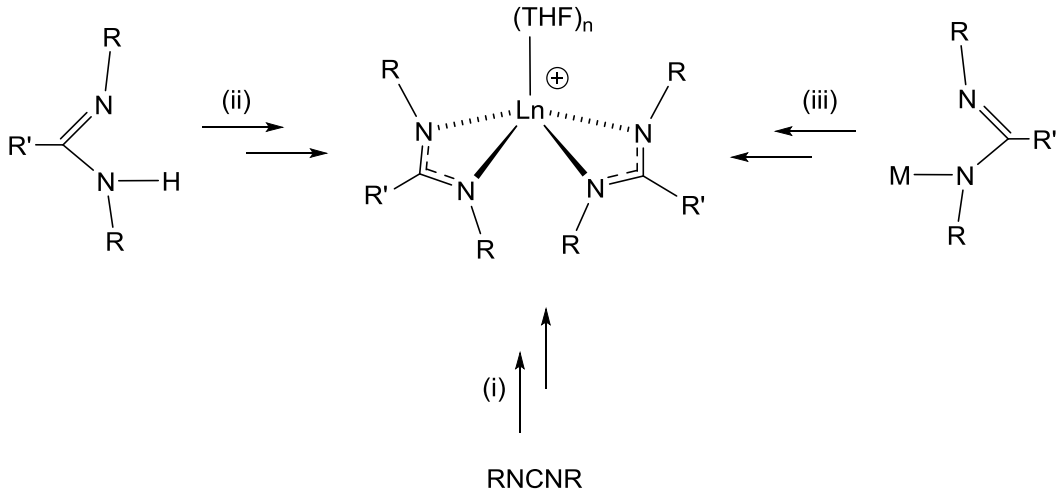

Figure 3.2. Routes to bis(amidinate) cations.

Addition of two equivalents of carbodiimide, RNCNR (R = ^{i}Pr, Cy or Tol), to the cationic rare earth metal dialkyls [Ln(CH$_2$SiMe$_3$)$_2$(THF)$_3$][BPh$_4$] (**2.16**–**2.17-BPh$_4$** and **2.22-BPh$_4$**), produced the cationic rare earth metal bis(amidinate) compounds [Ln{(Me$_3$SiCH$_2$)C(NR)$_2$}$_2$(THF)$_n$][BPh$_4$] (**5**–**13-BPh$_4$**, Scheme 3.4) in yields from 55-62%. Starting from the rare earth metal trialkyls **2.9**–**2.11**, and carrying out the subsequent deprotonation and addition of carbodiimide in a "one-pot" fashion, produced **5**–**13-BPh$_4$** in significantly higher yields, 80-87%. Compounds **5**–**13-BPh$_4$** constitute the first cationic rare earth metal bis(amidinate) compounds, and are stable in the solid state at room temperature, as well as stable in solutions of THF and

dichloromethane for extended periods of time under an inert atmosphere. As with most cationic rare earth metal compounds, **5**–**13-BPh$_4$** are completely insoluble in hydrocarbons, and sparingly soluble in arene solvents. The cyclohexyl derivatives **6-BPh$_4$**, **9-BPh$_4$** and **12-BPh$_4$** showed lower solubilities in THF and CH_2Cl_2 than their *iso*-propyl and tolyl counterparts.

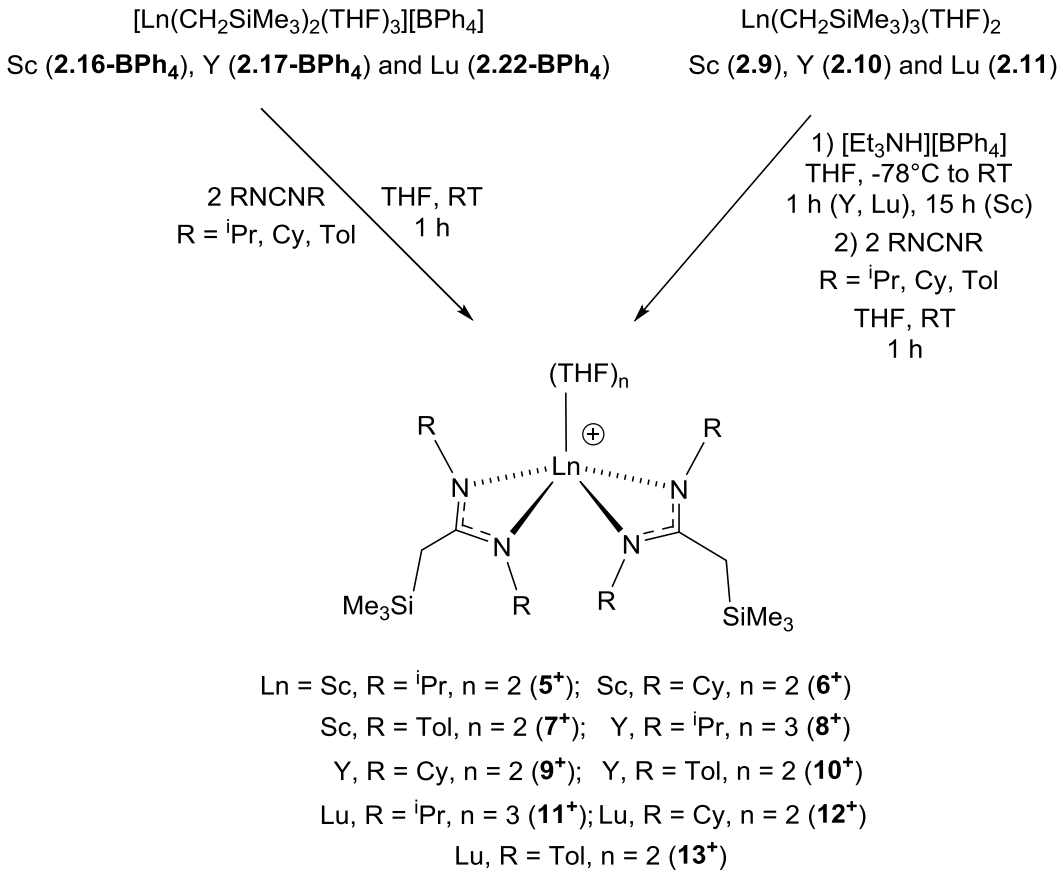

Scheme 3.4. Synthesis of bis(amidinate) cations. $[BPh_4]^-$ anion omitted for clarity.

Compounds **5**–**13-BPh$_4$** show similar ^{1}H NMR spectroscopic features in CD_2Cl_2. A sharp singlet resonance for the $SiMe_3$ group is found in the range -0.40 and +0.20 ppm, whilst a singlet resonance for the CH_2 group is found at approximately 2 ppm, considerably shifted from the related alkyl cations **2.16**$^+$, **2.17**$^+$ and **2.22**$^+$ as the carbon atom changes coordination from the metal to an *sp*^{2}-hybridised carbon. The three multiplets associated with the non-coordinated $[BPh_4]^-$ anion are also found in the expected range for these anions in ^{1}H NMR spectra. Compounds **8-BPh$_4$** and **11-BPh$_4$** diverge from the other cationic compounds as they show two, broad resonances for inequivalent α-protons of THF. The reduced steric bulk of the *N*-bound ^{i}Pr groups, when compared to Cy and Tol, allows for an extra molecule of coordinated THF for

8-BPh$_4$ and **11-BPh$_4$**, although not for the smaller scandium in **5-BPh$_4$**. The $^{11}B\{^1H\}$ NMR resonances for **5**–**13-BPh$_4$** were also in the expected range, with sharp resonances at approximately -6 ppm indicating the presence of four-coordinate boron. This data supports the expected structure for the cationic rare earth bis(amidinate) compounds depicted in Scheme 3.4.

3.3.3 Solid State Structure

A cooled (-30 °C) saturated solution of **9-BPh$_4$** in THF produced diffraction-quality crystals, enabling the elucidation of the solid state structure of **9-BPh$_4$** (Figure 3.2). The structure confirms that **9-BPh$_4$** is a cationic rare earth metal bis(amidinate) with a non-coordinating tetraphenylborate anion, which matches its ^1H NMR resonances and other characterising data (see Chapter 5), and, by analogy, it can be assumed that **5–8-BPh$_4$** and **10–13-BPh$_4$** contain cationic rare earth metal bis(amidinate) compounds.

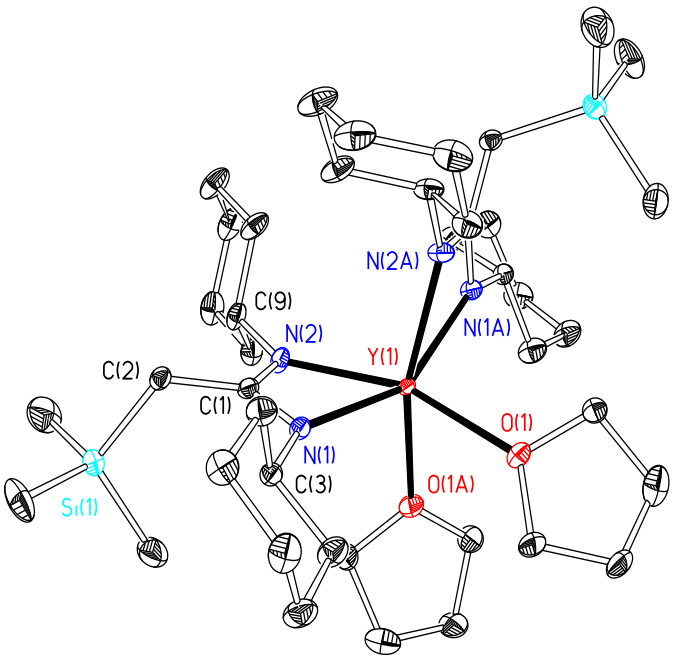

Figure 3.2. Displacement ellipsoid plot (20 % probability) of $[Y\{(Me_3SiCH_2)C(NCy)_2\}_2(THF)_2]^+$ (**9$^+$**). H atoms, minor disorder and $[BPh_4]^-$ omitted for clarity. Atoms carrying the suffix 'A' are related to their counterparts by the symmetry operator 1-*x*, *y*, $^3/_2$-*z*.

Table 3.1 lists selected important bond lengths and angles. Compound **9$^+$** has a distorted six-coordinate octahedral structure, with two molecules of coordinated THF. The THF molecules occupy one equatorial and one axial position, with the remaining

positions occupied by the amidinate nitrogens. The N–Y–N bite angle of 57.9° is close to the range of bite angles (51.2–65.3 °) seen for yttrium *N,N'*-disubstituted amidinates and guanidinates,[14] and contribute to the distortion of the octahedron. The Y–N bond distances are also within the range for yttrium *N,N'*-disubstituted amidinates and guanidinates (2.28–2.60 Å),[14] but the bond lengths appear to be affected by a small but significant *trans* influence. The Y–N(1) bond found *trans* to an amidinate nitrogen has a longer bond distance than Y–N(2) bond, which is found *trans* to the neutral THF. This observation for rare earth metals is not unknown, and has been noted in compounds reported by Deacon,[15] Rabe[16] and Brennan,[17-19] but is unusual as the electronic properties of the metal are independent of the coordination sphere.

Table 3.1. Selected distances (Å) and angles (°) for $[Y\{(Me_3SiCH_2)C(NCy)_2\}_2(THF)_2]^+$ (**9**$^+$).

Y(1)-N(1)	2.3432(19)	Y(1)-O(1)	2.3444(18)
Y(1)-N(2)	2.310(2)	N(1)-Y(1)-N(2)	57.94(7)
N(1)-C(1)-N(2)	114.5(2)	O(1)-Y(1)-O(1A)	79.90(10)

3.4 Rare Earth Metal Gallyl Compounds

3.4.1 Synthesis

With the isolation of cationic rare earth metal bis(amidinate) compounds, the "charge neutralisation" approach utilised for the synthesis of the boryl compounds $Ln(CH_2SiMe_3)_2\{B(NArCH)_2\}(THF)_n$ (**1**–**3**) could be extended to the synthesis of rare earth metal gallyl compounds. The conditions that were successful for the synthesis of the rare earth metal boryl compounds **1**–**3** were therefore employed.[20] Having elucidated the molecular structure of **9-BPh$_4$**, initial attempts at isolating rare earth gallyl compounds began with this compound. It was hoped that the lower solubility of the cyclohexyl derivatives would also aid crystallisation of the final gallyl compounds, since the 2,6-$C_6H_3{}^iPr_2$ groups on the gallyl are very lipophilic. Addition of a cooled (-40 °C) solution of 0.5 eq of $[K\{Ga(NArCH)_2\}(Et_2O)]_2$ (**3.30**) in THF to a cooled, stirring solution of **9-BPh$_4$** in THF resulted in an orange solution that was

allowed to react overnight at -40 °C. After work-up, a ^{1}H NMR spectrum of the crude product revealed that only a small amount of a new compound had formed, with starting materials and formation of the known digallane(4) (**1.36**) making up the rest of the sample. The low temperature had appeared to slow the formation of the purported product, and so the reaction was repeated under ambient conditions. The ^{1}H NMR spectrum of the crude product after workup showed only formation of **1.36**, from which it was concluded that allowing the reaction to run for a lengthy period of time gives decomposition of the desired product to the more favourable **1.36**. Reduction of the reaction time to 2 h resulted in the formation of what appeared to be the desired product, but with concomitant formation of **1.36**, unreacted **3.30** and unknown by-products. The use of THF as the reaction solvent appeared to have an adverse effect on the reaction. It was noted that there had been some success in the literature in using aromatic solvents where potassium salts had been involved.[21] Addition of toluene to a cooled (-78 °C) solid mixture of **9-BPh$_4$** and 0.5 eq of **3.30** resulted in a bright orange solution which was allowed to warm to room temperature and react for 2 h. The resulting red solution was filtered, and all the volatiles removed under reduced pressure leaving a bright orange solid. The solid was extracted into pentane and filtered, with all the volatiles being removed from the filtrate. The ^{1}H NMR spectrum of this sample showed the formation of what appeared to be the desired yttrium gallyl compound (**15**, Equation 3.4), with a singlet resonance for the vinyl protons seen upfield shifted from where **3.30** is found (6.30 ppm for **15** *vs* 6.48 ppm for **3.30**).[22]

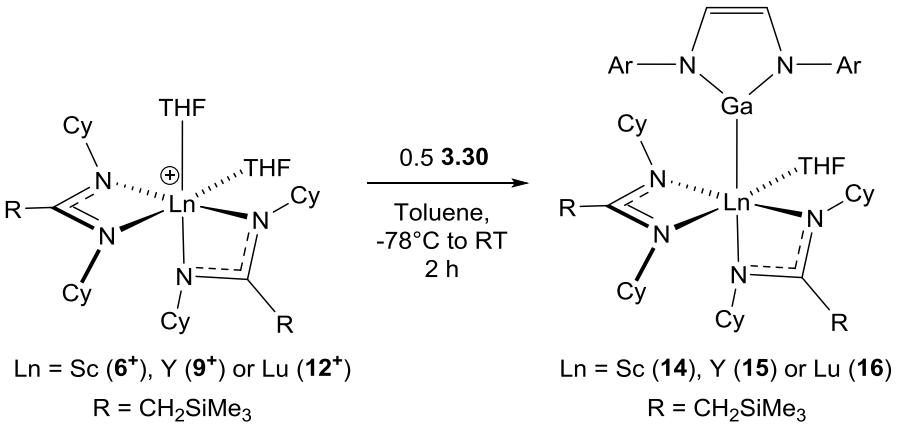

Equation 3.4

The reaction was repeated with the scandium and lutetium analogues (**6-BPh$_4$** and **12-BPh$_4$** respectively), each producing an analagous bright orange powder, but, as with the boryl examples, differing singlet resonances for the vinyl protons of the gallyl corresponding to the desired scandium and lutetium gallyl compounds Ln{(Me$_3$SiCH$_2$)C(NCy)$_2$}$_2${Ga(NArCH)$_2$}(THF) (Ln = Sc (**14)** and Lu (**16**)). In each case, a small impurity in the form of **1.36** would always be present (*c.a.* 10 %), with an additional unknown impurity found in **15**. The scale of these impurities is dependent upon the amount of time spent in solution during the reaction and during work-up. Therefore reaction conditions must be strictly adhered to so that the reaction time and time taken during work-up is limited so as to avoid the undesirable formation of **1.36** and other unknown impurities. A reaction time of two hours was sufficient to produce, after work up, analytically pure **14**–**16** (see Chapter 5 for details). Allowing NMR tube scale solutions of **14**–**16** in C_6D_6 to stand for several days resulted in decomposition, with the main decomposition products being **1.36**, gallium metal and diazabutadiene (NArCH)$_2$ from the gallyl ligand.

The ^{1}H NMR spectra of **14**–**16** in C_6D_6 showed diagnostic singlet resonances of the vinyl protons at 6.27 (**14**), 6.30 (**15**) and 6.32 (**16**) ppm respectively, mirroring the increasing downfield shift as the metal changes from scandium to yttrium to lutetium. By way of comparison, the only previously isolated example of an yttrium gallyl compound, **1.140** (page 35, Chapter 1), was reported to have a resonance at 6.53 ppm for the gallyl vinyl protons.[23] In all examples, resonances corresponding to one molecule of bound THF are seen, as well as broad resonances ranging from 1.20 to 1.90 ppm corresponding to the cyclohexyl protons overlapping with the resonances associated with *iso*-propyl methyl protons and the methylene protons of the alkyl. Compounds **14** and **16** show similar resonances for the α-proton of THF (3.97 ppm), and are found downfield shifted from the resonance corresponding to the methine proton of the *iso*-propyl groups on the gallyl. The resonance for the α-proton of THF in compound **15** is upfield shifted from the resonance corresponding to the methine proton of the *iso*-propyl groups on the gallyl, which is observed in the reported ^{1}H NMR of compound **1.140**.[23] The resonances for the β-protons of THF for **14**–**16** are within 0.07 ppm of each other and overlap with the resonances for the cyclohexyl protons of the amidinate. This data supports the expected structure for the bis(amidinate) gallyl compounds depicted in Equation 3.4.

3.4.2 Solid State Structure

Crystallisation of **14**–**16** was difficult due to the high solubility of all three compounds in all solvents and the instability in solution of **15** and **16** over the time periods required for crystallisation. However, slow evaporation of a hexane solution of the most stable of the gallyl compounds, **14**, resulted in diffraction-quality crystals, enabling the elucidation of its solid state structure. This structure confirms that **14** is a bis(amidinate) supported scandium gallyl compound, and completes the Group 3 triad for structurally authenticated Ln–Ga bonds.[23, 24] Compound **14** has a six-coordinate distorted octahedral structure, comparable to that of the cation $[Y\{(Me_3SiCH_2)C(NCy)_2\}_2(THF)_2]^+$ (**9**$^+$), with one coordinated molecule of THF (Figure 3.3). The Sc–Ga bond length was found to be 3.0365(3) Å, which lies outside the sum of the respective covalent radii (2.92(10) Å).[25] The Sc–Ga bond is unprecedented, but it is noteworthy that while it is significantly shorter than the Y–Ga bond in $Y\{C(PPh_2NSiMe_3)_2\}\{Ga(NArCH)_2\}(THF)_2$ (**1.140**, 3.1757(4) Å), it is slightly longer than the La–Ga bond in $Cp''_2La\{Ga(NArC_6H_3)_2\}_2(THF)$ (**1.141**, 3.0134(8) Å), featuring the larger, four coordinate lanthanum metal ion.[23, 24] Whilst the lower coordination number of lanthanum in **1.141** may be expected to furnish a shorter Ln–Ga bond, it has been observed in other metal-gallyl compounds that changes in coordination number do not follow the expected changes in bond distance, *i.e.* lower coordination number, shorter bond distance. For example, five-coordinate $Mg\{Ga(NArCH)_2\}_2(THF)_3$ (**1.34**) has shorter Mg–Ga bond distances (2.722 Å (mean)) than four-coordinate $Mg(NacNac)\{Ga(NArCH)_2\}(\eta^1\text{-TMEDA})$ (**1.42**) (2.7470(7) Å).

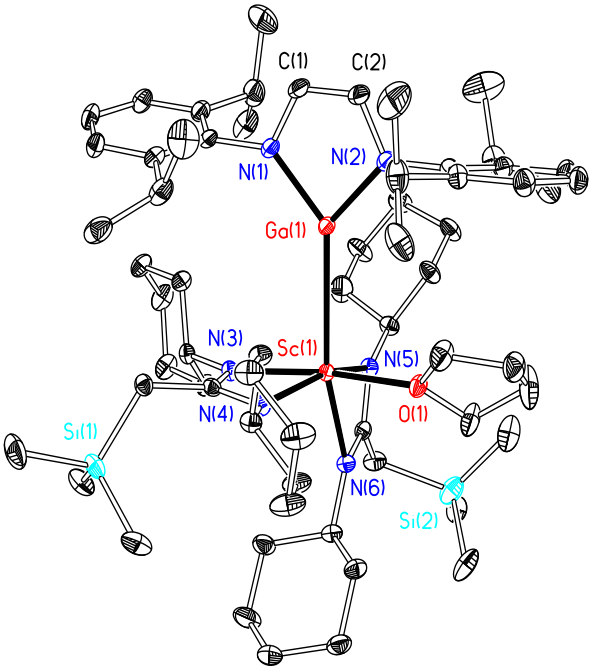

Figure 3.2. Displacement ellipsoid plot (20 % probability) of $Sc\{(Me_3SiCH_2)C(NCy)_2\}_2\{Ga(NArCH)_2\}(THF)$ (**14**). H atoms and hexane of crystallisation omitted for clarity.

The bite angle of the amidinate ligands is more obtuse than those of the yttrium cation $\mathbf{9}^+$, but falls in line with the average bite angle (61.2 °) for scandium metal coordinated *N,N'*-disubstituted amidinates and guanidinates.[14] One of the amidinate ligands occupies two equatorial sites of the octahedron, whilst the other occupies one equatorial and one axial site. As with $\mathbf{9}^+$, there is an apparent *trans* influence affecting the metal-amidinate bond lengths. Table 3.2 highlights selected bond distances and angles for **14**, and it can be seen that the amidinate nitrogen N(3) *trans* to the THF oxygen O(1) has a shorter Sc–N bond length when compared to those *trans* to either another amidinate nitrogen (*i.e.* N(4) or N(5)) or *trans* to the gallyl anion (*i.e.* N(6)). The gallyl ligand itself has been shown to have a significant *trans* influence,[26] but in **14** the Sc–N(6) bond maintains the same bond distance as Sc–N(5) despite being positioned *trans* to the gallyl. This indicates that for this system the *trans* influence of the gallyl ligand compares favourably with the *trans* influence of the amidinate. It is important to note at this point that this influence can have a 'structural effect', *i.e.* affect the bond length of the *trans* substituent, or a 'kinetic effect', *i.e.* affect the lability of the *trans* substituent.[27] The structural effect can be seen with the relatively

short Sc–N(3) bond distance, as the neutral THF has a weaker *trans* influence than the amidinate, but the labilising effect is not clear.

Table 3.2. Selected distances (Å) and angles (°) for **14**.

Sc(1)-Ga(1)	3.0365(3)	Ga(1)-N(1)	1.9419(12)
Sc(1)-N(3)	2.1554(11)	Ga(1)-N(2)	1.9569(12)
Sc(1)-N(4)	2.1815(11)	N(1)-C(1)	1.397(2)
Sc(1)-N(5)	2.1976(11)	N(2)-C(2)	1.3951(19)
Sc(1)-N(6)	2.1910(11)	C(1)-C(2)	1.341(2)
Sc(1)-O(1)	2.2442(10)		
N(1)-Ga(1)-N(2)	83.66(5)	N(5)-Sc(1)-N(6)	61.16(4)
N(3)-Sc(1)-N(4)	62.23(4)	Ga(1)-Sc(1)-O(1)	87.31(3)

There are also structural changes observed in the gallyl heterocycle upon change in coordination from potassium to scandium. The potassium gallyl precursor $[K\{Ga(NArCH)_2\}(Et_2O)]_2$ (**3.30**) features an ionic K–Ga bond,[22] and it has been observed that upon coordination to atoms where a more covalent bond is formed, the Ga–N bond distances in the heterocycle become shorter and the N–Ga–N angle becomes more obtuse.[28] In **14**, the scandium bound gallyl heterocycle shows a more obtuse N–Ga–N angle (83.7 ° *vs* 81.9 ° for **3.30**)[22] and shorter Ga–N bonds (1.949 Å (mean) vs 2.007 Å (mean) for **3.30**),[22] suggesting some covalency in the Sc–Ga bond. A useful way of rationalising the changes in the heterocycle would be to invoke Bent's rule. Bent's rule is predicated on highly electronegative substituents "attracting" *p*-character. As the electronegativity of the atom coordinated to gallium increases (from potassium to scandium), the ionic nature of the interaction decreases. As a result of this, less 4*s* character on the gallium atom will be directed towards the newly formed Sc–Ga bond, resulting in the Ga–N bonds shortening. With the remaining bonds in the heterocycle largely unchanged, the N–Ga–N angle becomes more obtuse to accommodate the change in Ga–N bond distance. Evidence for M–Ga covalency and change in electronegativity of metals affecting the bond distances and angles in the gallyl heterocycle can be found in surveying the Cambridge Structural Database.[14]

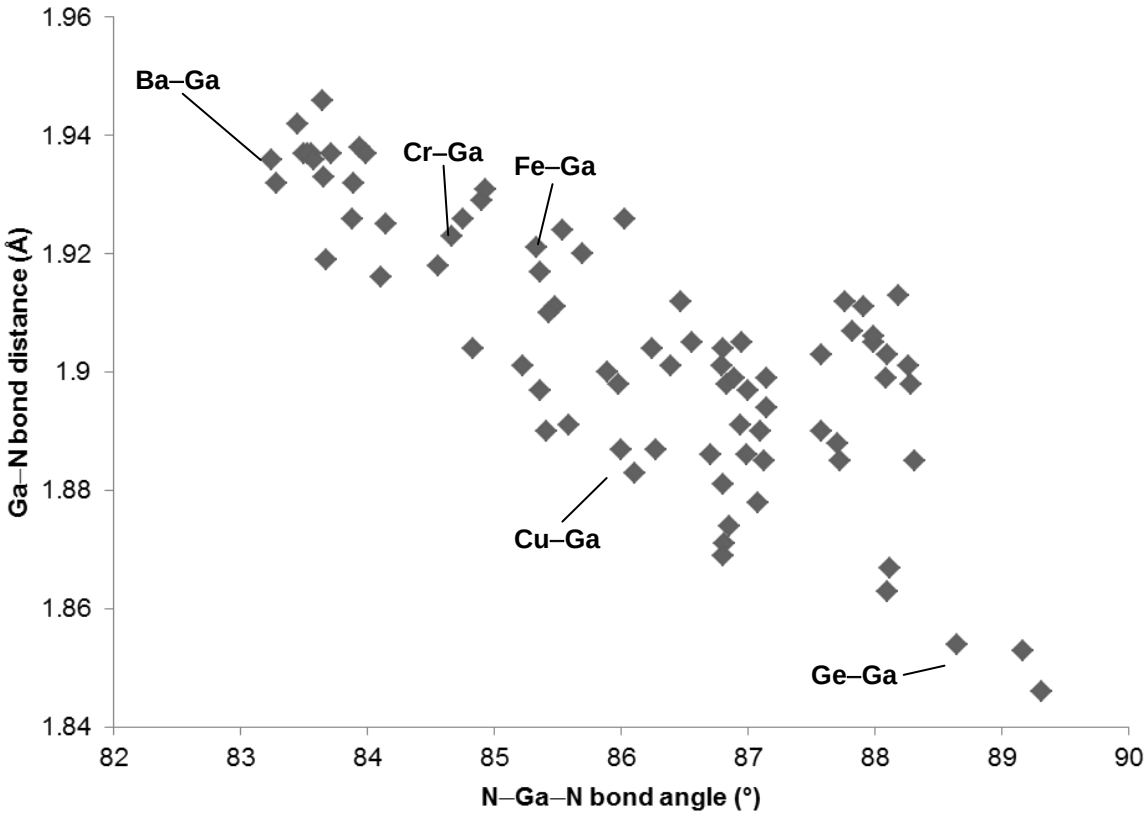

Figure 3.3. Ga–N bond distance *vs* N–Ga–N bond angle for compounds with M–Ga(NArCH)$_2$ bonds.

Figure 3.3 shows a plot of Ga–N bond distances against the N–Ga–N bond angle for all compounds featuring an unsupported metal-gallium bond, with the source of gallium coming from the gallyl anion. There is a clear relationship where the bond distances become progressively shorter as the bond angles become progressively more obtuse, and they do so as the metals bound to the heterocycle form progressively more covalent bonds, with some examples highlighted. In order to further elucidate the bonding and structure of **14**–**16**, computational analyses of these compounds were sought.

3.5 DFT Computational Analysis of Ln{(Me$_3$SiCH$_2$)C(NCy)$_2$}$_2${Ga(NArCH)$_2$}THF

Scalar relativistic, gradient corrected density functional theory calculations using the PBE functional were carried out by Ms Abigail Mountain and Prof. Nikolas Kaltsoyannis at University College London to further investigate the bonding and structure of **14**–**16**. The geometry optimised structures for

Ln{$(Me_3SiCH_2)C(NCy)_2$}$_2${$Ga(NArCH)_2$}(THF) (Ln = Sc (**14C**), Y (**15C**) or Lu (**16C**), Figure 3.4) were calculated with dispersion corrections applied. Table 3.3 shows selected calculated bond distances and angles, with the calculated structures showing the expected periodic trend Sc–Ga < Y–Ga > Lu–Ga in Ln–Ga bond distance. The Sc–N amidinate bond lengths were reproduced well in **14C**, showing excellent agreement with **14**. The *trans* influence affecting bond distances in **14** is replicated in **14C**, with the Sc–N bond *trans* to THF approximately 0.05 Å shorter than those of the Sc–N bonds *trans* to an amidinate nitrogen (2.153 Å *vs* 2.201 Å (mean)), approximating the difference seen in **14** (2.1154(11) Å *vs* 2.1896(16) Å (mean)). The calculated values for Ln–N *trans* to THF in both **15C** and **16C** are consistently around 0.05 Å shorter than those found for Ln–N *trans* to another amidinate nitrogen in those optimised structures. Whilst the solid state structure of **14** suggested a roughly equal *trans* influence for the gallyl ligand and the amidinate nitrogen *trans* to it, the calculated structure **14C** suggests that the amidinate nitrogen may have a slightly stronger *trans* influence than expected, greater than that of the gallyl ligand, as a shorter Sc–N bond distance *trans* to the gallyl is seen. The Sc–Ga bond distance of 2.886 Å for **14C** underestimates by 0.152 Å the bond distance found for **14**. As with the boryl examples **1C**–**3C**, the potential energy surface of the Ln–Ga bonds were probed by incrementally varying the Ln–Ga bond distances of **14C**–**16C** about their equilibrium values and optimising all other geometric parameters.

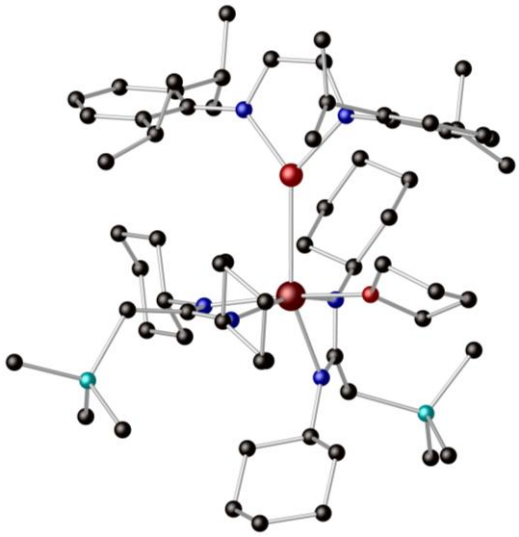

Figure 3.4. Ball and stick plot (arbitrary radius) of the calculated structure of Sc{$(Me_3SiCH_2)C(NCy)_2$}$_2${$Ga(NArCH)_2$}THF (**14C**). H atoms omitted for clarity.

During initial calculations, unfavourable steric interactions between the aryl rings of the gallyl heterocycle and the amidinate cyclohexyl and trimethylsilyl groups played a significant role in the overall geometry and energy of the system, such that information about the Ln–Ga interaction was masked. In order to eliminate these undesirable steric effects and focus more on the Ln–Ga interaction, the calculations were repeated on models of **14C**–**16C**, Ln{MeC(NMe)$_2$}$_2${Ga(NXylCH)$_2$}(THF) (Ln = Sc (**14SC**) or Lu (**16SC**)) where the cyclohexyl and trimethylsilyl groups on the amidinate were replaced with methyl groups, and the di-*iso*-propylphenyl groups on the gallyl were replaced with *ortho*-xylyl groups. The calculated models of **14SC** (2.770 Å) and **16SC** (2.839 Å) display shortened Ln–Ga bonds compared to the optimised full structures, but adopt the same distorted octahedral geometry and bond distances that are affected by a *trans* influence, and so offer good approximations of the optimised full structures. The results visualised in Figure 3.5 show the Sc–Ga bond as an example, and, as with the Ln–B bonds described in Chapter 2, the Ln–Ga bonds in general have very shallow potential energy surfaces, with significant changes in bond length inducing only small energy changes. For example, displacing the scandium-gallium bond in **14SC** by ±0.1 Å from its equilibrium value destabilises the molecule by only 3.8 kJ mol^{-1} (Figure 3.5). The results of the potential energy surface calculations on the model system **14SC** suggest that the Sc–Ga bond distance in **14C** offers a reasonable approximation of the Sc–Ga bond distance in **14**.

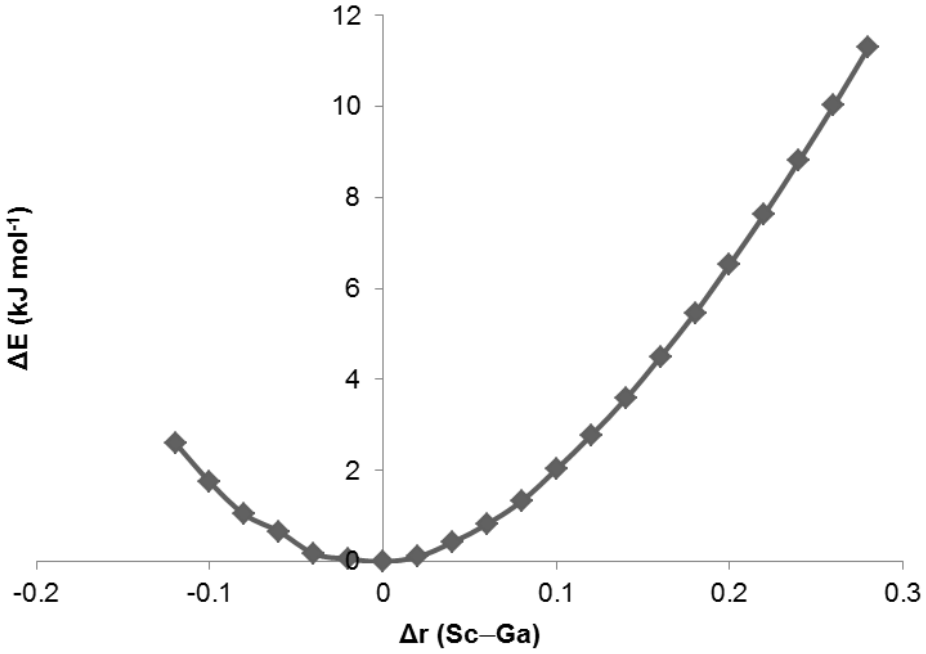

Figure 3.5. Relative change in energy with respect to change in Sc–Ga bond distance from the optimised value in Sc{MeC(NMe)$_2$}$_2${Ga(NXylCH)$_2$}(THF) (**14SC**).

Returning to the geometry optimised full structures **14C**–**16C**, the Hirshfeld charge differences between the metals and the gallyl fragment Δ*q*(Ln–Gallyl) were calculated and the results presented in Table 3.3. In all cases, the charge differences were large, indicating that all of the Ln–Ga bonds are predominantly ionic. Compound **14C** possesses the smallest charge difference, indicating that the scandium-gallium bond is the least ionic of the three rare earth metal-gallium bonds, whilst **15C** and **16C** had significantly larger charge differences. To further probe the nature of the bonding, the canonical Kohn-Sham molecular orbitals were analysed. However, this method could not clearly identify the Ln–Ga σ-bonding orbital due to significant delocalization, and so the Boys-Foster localized orbitals (LO), which are found by unitary transformations of the canonical functions in order to minimize the spatial extent of the resultant orbitals, were calculated. With this method, the Ln–Ga bonding orbital was identified as the highest occupied localized orbital (HOLO), as visualised in Figure 3.6, and is a predominantly σ-orbital. Four gallyl-based LOs were also identified, and these are visualised in Figure 3.7.

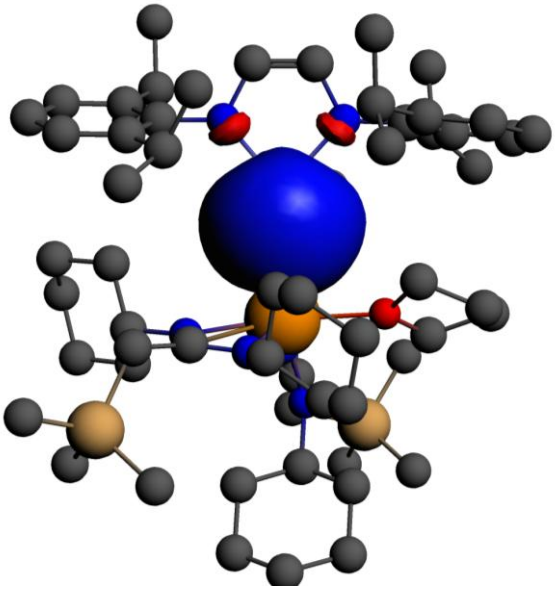

Figure 3.6. Three-dimensional representation of the HOLO for the calculated structure of Sc{(Me_3SiCH_2)C($NCy)_2$}$_2${Ga($NArCH)_2$}(THF) (**14C**). H atoms omitted for clarity.

The normalised contributions to the σ-bonding HOLO were calculated, with the results shown in Table 3.3. In all cases, the gallyl anion is found to be the major contributor, again indicating predominantly ionic bonds. The Sc–Ga and Lu–Ga HOLOs showed the largest degree of mixing between the two atoms, whilst the Y–Ga HOLO showed the lowest degree of mixing. Taking into account the conclusion reached with the Hirshfeld charge difference analysis, the Sc–Ga bond can be considered the least ionic of the three, whilst the Y–Ga bond is the most ionic. Atoms-in-Molecules (AIM) analysis was carried out and generated values for the electron density (ρ), the energy density (H) and the electron density Laplacian ($\nabla^2\rho$) at the Ln–Ga bond critical point. The small values for ρ and H, coupled with the small, positive $\nabla^2\rho$ reinforce the conclusions reached from analysis of the Hirshfeld charge differences and the Boys-Foster Localized orbitals, that the Ln–Ga bond is predominantly ionic. The Lu–Ga bond has marginally the largest ρ and H values suggesting that it is the least ionic of the three bonds, in agreement with the HOLO data though not with the Hirshfeld Δq. Overall, however, the AIM, HOLO composition and Hirshfeld data are in agreement in suggesting that the Y–Ga bond is the most ionic.

Table 3.3. Selected DFT computational results for Ln{$(Me_3SiCH_2)C(NCy)_2$}$_2${$Ga(NArCH)_2$}(THF) (Ln = Sc (**14C**), Y (**15C**) or Lu (**16C**)).[a]

	14C	**15C**	**16C**
r(Ln–Ga) (Å)	2.886	3.036	2.974
Ln–N *trans* to THF (Å)	2.153	2.311	2.268
Ln–N *trans* to Ga (Å)	2.189	2.340	2.296
Ln–N *trans* to N (mean (Å))	2.201	2.365	2.322
N–Ga–N angle (°)	82.8	82.8	83.0
Ln–Ga interaction energy	-479.7	-492.1	-505.2
Pre-relaxation (“steric”) energy	332.2	421.0	487.8
orbital energy	-688.9	-795.6	-873.5
Δq (Ln–Gallyl) (Hirshfeld Charge Difference)	1.27	1.42	1.42
ρ (electron density)	0.033	0.030	0.034
$\nabla^2\rho$ (electron density Laplacian)	0.027	0.031	0.028
H (energy density)	-0.006	-0.005	-0.007
Normalised Ln/Ga Mulliken contributions to the highest occupied localized orbital (HOLO) (%)	19/81	11/89	19/81

a. All energies in kJ mol^{-1}. AIM data (atomic units) obtained at the Ln–Ga bond critical point.

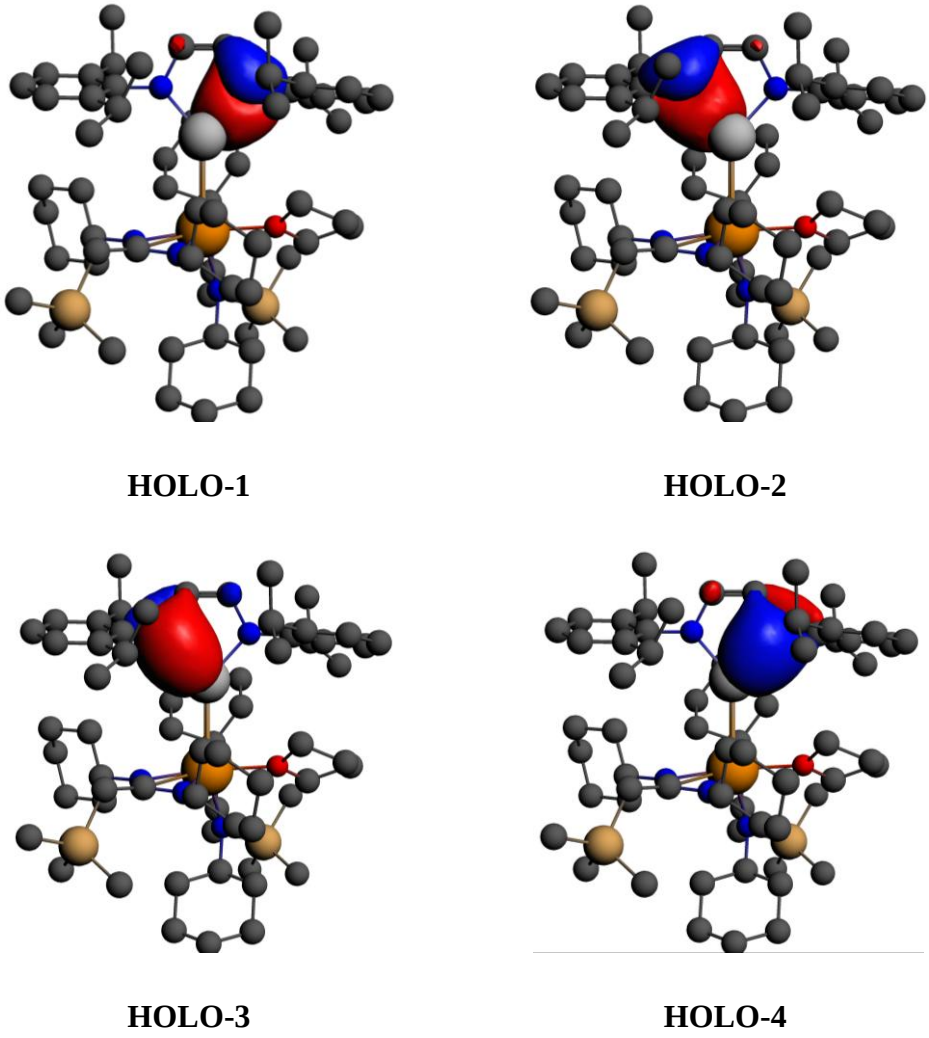

Figure 3.7. Three-dimensional representations of gallyl-based LOs of $Sc\{(Me_3SiCH_2)C(NCy)_2\}_2\{Ga(NArCH)_2\}(THF)$ (**14C**). H atoms omitted for clarity.

3.6 Conclusions

In this Chapter, the *N,N'*-disubstituted amidinate ligand was introduced as a "steric cyclopentadienyl equivalent", imparting a high level of stability through steric bulk and the ability to tune the steric and electronic properties *via* changes to the *ipso C*-bound and *N*-bound substituents. The facile and high-yielding syntheses and characterisation of a series of novel cationic rare earth metal bis(amidinate) compounds were described, and the molecular structure of $[Y\{(Me_3SiCH_2)C(NCy)_2\}_2(THF)_2][BPh_4]$ (**9-BPh$_4$**) confirmed the proposed structural composition of these compounds. The molecular structure of the cation **9**$^+$ reveals the adoption of a distorted octahedral geometry, with the Y–N and N–Y–N bond distances and angles corresponding to those normally found for yttrium *N,N'*-

disubstituted amidinates.[14] Upon closer inspection of the molecular structure of $\mathbf{9}^{+}$, a small, but significant *trans* influence can be seen affecting the metal-nitrogen bond distances. This is an unusual observation for rare earth metals, but is not unknown.[17-19]

In an extension of the successful synthetic approach that resulted in the boryl compounds **1**–**3**, reaction of $[Ln\{(Me_3SiCH_2)C(NCy)_2\}_2(THF)_2][BPh_4]$ (Ln = Sc (**6-BPh$_4$**), Y (**9-BPh$_4$**) or Lu (**12-BPh$_4$**)) with 0.5 eq. of **3.30** resulted in the isolation and characterisation of the rare earth metal gallyl compounds $Ln\{(Me_3SiCH_2)C(NCy)_2\}_2\{Ga(NArCH)_2\}(THF)$ (Ln = Sc (**14**), Y (**15**) and Lu (**16**)), with the molecular structure of **14** also detailed. Compound **14** is the first structurally authenticated compound featuring a direct Sc–Ga bond, and completes the Group 3 triad for structurally authenticated compounds with Ln–Ga bonds.[23, 24] The molecular structure of **14** matches its characterising data (see Chapter 5 for details), and those of the analogous yttrium and lutetium compounds, and it can be assumed that they too adopt similar structures in the solid state. Compound **14**, like the cation $\mathbf{9}^{+}$, adopts a distorted octahedral geometry, with the Sc–N and N–Sc–N bond distances and angles now corresponding to those normally found for scandium *N*,*N*′-disubstituted amidinates.[14] As with $\mathbf{9}^{+}$, the molecular structure of **14** also reveals a small, but significant, *trans* influence affecting the metal-nitrogen bond distances. Evidence of some covalency in the Sc–Ga bond can be found in inspecting the Ga–N and N–Ga–N bond distances and angles of the gallyl heterocycle. There is excellent evidence to suggest that as covalency of the M-Ga bond increases, the Ga–N bonds shorten, which then leads to the N–Ga–N angle becoming more obtuse in response (Figure 3.3). The gallyl heterocycle in **14** has both shorter Ga–N bond distances and a more obtuse N–Ga–N angle than the heterocycle in the potassium bound heterocycle **3.30**. DFT computational analysis of **14-16** were then carried out to further elucidate their structure and bonding. The majority of calculations were carried out on the full geometry optimised structures **14C-16C**, with the exception being the potential energy surface calculations, which were carried out on models of the full structures $Ln\{MeC(NMe)_2\}_2\{Ga(NArCH)_2\}(THF)$ **14SC-16SC**. The optimised full structure **14C** matched the experimentally observed structure of **14**, with the bond distances showing the same *trans* influenced differences. Potential energy surface calculations

showed that the Ln–Ga bond is 'soft', with a displacement of the Sc–Ga bond by ±0.1 Å from its equilibrium value destabilises the molecule by only 3.8 kJ mol^{-1}. Hirshfeld charge difference calculations suggest that the Ln–Ga bonds are predominantly ionic, with the Sc–Ga bond being the least ionic and the Y–Ga bond the most ionic. Boys-Foster localized orbital (LO) analysis identified the Ln–Ga bonding orbital as the highest occupied localized orbital (HOLO), which is a σ-bonding orbital. The normalised contributions to the σ-bonding HOLO were also calculated, and these show the gallyl anion to be the major contributor in all cases, again indicating a predominantly ionic interaction. Finally, Atoms-in-Molecules (AIM) analysis found that the Lu–Ga bond was the least ionic, in agreement with the HOLO data though not with the Hirshfeld, whilst the Y–Ga bond was found to be the most ionic, in agreement with both the Hirshfeld and HOLO data.

3.7 References

1. T. V. Lubben, P. T. Wolczanski and G. D. Vanduyne, *Organometallics*, 1984, 3, 977.
2. M. Wedler, F. Knosel, U. Pieper, D. Stalke, F. T. Edelmann and H. D. Amberger, *Chem. Ber. Recl.*, 1992, 125, 2171.
3. F. T. Edelmann, *Coord. Chem. Rev.*, 1994, 137, 403.
4. F. T. Edelmann, *Advances in the Coordination Chemistry of Amidinate and Guanidinate Ligands*, Elsevier Inc., 2008.
5. F. T. Edelmann, *Chem. Soc. Rev.*, 2009, 38, 2253.
6. F. T. Edelmann, *Chem. Soc. Rev.*, 2012, 41, 7657.
7. M. Wedler, M. Noltemeyer, U. Pieper, H. G. Schmidt, D. Stalke and F. T. Edelmann, *Angew. Chem. Int. Ed.*, 1990, 29, 894.
8. A. Recknagel, F. Knosel, H. Gornitzka, M. Noltemeyer, F. T. Edelmann and U. Behrens, *J. Organomet. Chem.*, 1991, 417, 363.
9. R. Duchateau, C. T. Vanwee, A. Meetsma and J. H. Teuben, *J. Am. Chem. Soc.*, 1993, 115, 4931.
10. A. A. Trifonov, E. A. Fedorova, G. K. Fukin and M. N. Bochkarev, *Eur. J. Inorg. Chem.*, 2004, 4396.
11. H. Schumann, W. Genthe, E. Hahn, M. B. Hossain and D. Vanderhelm, *J. Organomet. Chem.*, 1986, 299, 67.

12. S. Bambirra, D. van Leusen, A. Meetsma, B. Hessen and J. H. Teuben, *Chem. Commun.*, 2003, 522.
13. S. Bambirra, M. W. Bouwkamp, A. Meetsma and B. Hessen, *J. Am. Chem. Soc.*, 2004, 126, 9182.
14. D. A. Fletcher, R. F. McMeeking and D. Parkin, *J. Chem. Inf. Comput. Sci.*, 1996, 36, 746.
15. G. B. Deacon, B. M. Gatehouse, Q. Shen and G. N. Ward, *Polyhedron*, 1993, 12, 1289.
16. G. W. Rabe, C. D. Berube, G. P. A. Yap, K. C. Lam, T. E. Concolino and A. L. Rheingold, *Inorg. Chem.*, 2002, 41, 1446.
17. J. Lee, M. Brewer, M. Berardini and J. G. Brennan, *Inorg. Chem.*, 1995, 34, 3215.
18. K. Norton, G. A. Kumar, J. L. Dilks, T. J. Emge, R. E. Riman, M. G. Brik and J. G. Brennan, *Inorg. Chem.*, 2009, 48, 3573.
19. K. Krogh-Jespersen, M. D. Romanelli, J. H. Melman, T. J. Emge and J. G. Brennan, *Inorg. Chem.*, 2010, 49, 552.
20. L. M. A. Saleh, K. H. Birjkumar, A. V. Protchenko, A. D. Schwarz, S. Aldridge, C. Jones, N. Kaltsoyannis and P. Mountford, *J. Am. Chem. Soc.*, 2011, 133, 3836.
21. W. J. Evans, G. W. Nyce, K. J. Forrestal and J. W. Ziller, *Organometallics*, 2002, 21, 1050.
22. R. J. Baker, R. D. Farley, C. Jones, M. Kloth and D. M. Murphy, *J. Chem. Soc., Dalton Trans.*, 2002, 3844.
23. S. T. Liddle, D. P. Mills, B. M. Gardner, J. McMaster, C. Jones and W. D. Woodul, *Inorg. Chem.*, 2009, 48, 3520.
24. I. L. Fedushkin, A. N. Lukoyanov, A. N. Tishkina, M. O. Maslov, S. Y. Ketkov and M. Hummert, *Organometallics*, 2011, 30, 3628.
25. B. Cordero, V. Gomez, A. E. Platero-Prats, M. Reves, J. Echeverria, E. Cremades, F. Barragan and S. Alvarez, *Dalton Trans.*, 2008, 2832.
26. S. P. Green, C. Jones, D. P. Mills and A. Stasch, *Organometallics*, 2007, 26, 3424.
27. B. J. Coe and S. J. Glenwright, *Coord. Chem. Rev.*, 2000, 203, 5.
28. I. L. Fedushkin, A. N. Lukoyanov, A. N. Tishkina, G. K. Fukin, K. A. Lyssenko and M. Hummert, *Chem. Eur. J.*, 2010, 16, 7563.

Chapter Four

Structure and Reactivity Comparisons of Rare Earth Metal Boryl and Gallyl Compounds

4.1 Overview

This Chapter describes reactivity studies of the rare earth metal bis(amidinate) gallyls Ln{(Me_3SiCH_2)C($NCy)_2$}$_2${$Ga(NArCH)_2$}(THF) (Ln = Sc (**14**), Y (**15**) or Lu (**16**)) with unsaturated molecules, and the synthesis of rare earth metal bis(amidinate) boryl compounds featuring the same ligand set. A full structure and reactivity comparison between the rare earth metal gallyl and boryl compounds will be described. A short introduction on the reactivity of compounds featuring M–E (E = B or Ga) and Ae/Ln–M (Ae = Alkaline earth metal; Ln = Group 3 or lanthanide metal) bonds will precede the presentation of results.

4.2 M–E Bond Reactivity (E = B or Ga)

Reactivity studies of Group 13 elements coordinated to metals are dominated by compounds featuring metal-boron bonds. When compared to traditional elements involved in bonding with metals, the relatively high electropositivity of boron and the existence of an empty p-orbital for three-coordinate boron indicates the potential for metal-boryl compounds to undergo new transformations with small molecules or undergo existing transformations by new mechanisms.[1] In addition, metal-boryl compounds have outstanding significance in a variety of catalytic and stoichiometric transformations, including the hydroboration and diboration of C–C π bonds and the functionalization of alkane and arene C–H bonds.[2]

4.2.1 Transition Metal Catalysed Hydroboration

The formation of a transition metal-boryl as the key intermediate in the transition metal-catalysed hydroboration of alkenes was invoked early on in catalysis involving Wilkinson's catalyst, $RhCl(PPh_3)_3$.[3] The favoured mechanism begins with the loss of a molecule of PPh_3, followed by oxidative addition of a borane to form the putative metal-boryl intermediate. Insertion of an alkene into the Rh–H bond is then followed by reductive elimination to form the desired alkylborane. Subsequent transition metal-catalysed hydroboration studies featuring iridium,[4] palladium[5] and nickel[6] are believed to proceed via similar mechanisms. The advantages of metal-mediated processes such as these are that they are tolerant of boranes that are, for example, generally unreactive or have poor thermal stability and are otherwise unsuitable for non-catalysed hydroborations.[7]

4.2.2 Transition Metal Boryl Reactivity

The availability of transition metal boryl compounds has allowed the probing of the metal-boron bond directly, and the potential for these compounds to act as "drop in" stoichiometric or catalytic borylating reagents. The metals of Group 10 in particular are important due to their implication in Suzuki couplings in organic synthesis. Chapter 1 highlighted some of the more important examples, which can be briefly touched on here. The nickel boryl compound Ni{N(ArP^{i}Pr$_2$)$_2$}{B(O$_2$C$_6$H$_4$)} (**1.87**) can borylate bromobenzene, with the resultant nickel bromide compound NiBr{N(ArP^{i}Pr$_2$)$_2$} able to react with $NaBH_4$ to regenerate NiH{N(ArP^{i}Pr$_2$)$_2$}, completing a potential catalytic cycle (Scheme 4.1). However, addition of 10-20 mol% NiBr{N(ArP^{i}Pr$_2$)$_2$}, catecholborane and $NaBH_4$ in the presence of bromobenzene did not produce the borylated product and NiH{N(ArP^{i}Pr$_2$)$_2$}, instead producing NiBr{N(ArP^{i}Pr$_2$)$_2$} and benzene.[8]

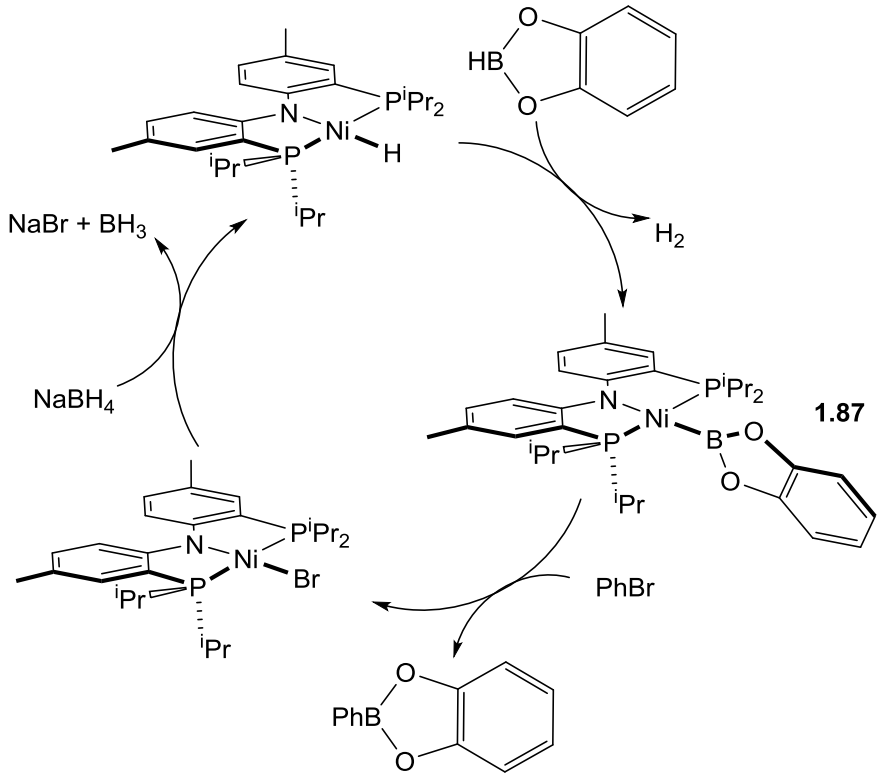

Scheme 4.1

The palladium boryl Pd(CH$_2$PMe$_2$)$_2$(SnMe$_3$){B(NMeCH$_2$)$_2$} (**1.88**) was synthesised as a model for the suspected intermediate in the catalytic synthesis of (stannylalkenyl)boranes from a mixture of a Pd(0) pre-catalyst, a tin(IV) boryl and an

alkyne. It was found that use of **1.88** as a catalyst does indeed form the desired (stannylalkenyl)boranes in good yields (Scheme 4.2).

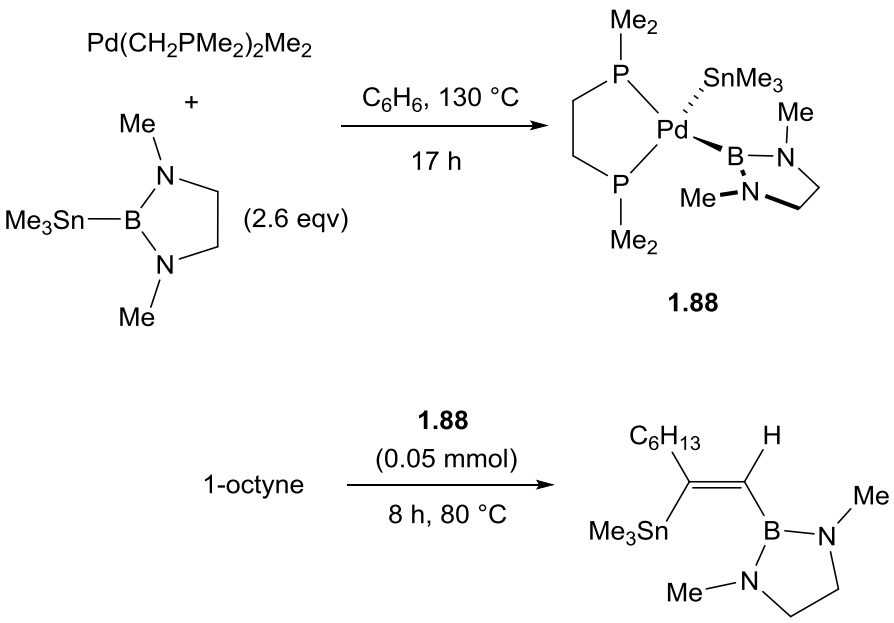

Scheme 4.2. By-products omitted for clarity.

Platinum tends to form more robust metal-boron bonds than the other metals of Group 10, the result being the number of compounds featuring platinum-boron bonds and their reactivity far outweighing those of palladium and nickel.[2c] Oxidative addition is the preferred method of preparing platinum-boron bonds, with a huge variety of boron-element bonds available, including B–H, B–X (X = halide) or B–E bonds (E = B, C, Si, Ge and Sn). Ozawa and co-workers showed that oxidative addition of B–Si bonds into Pt(0) compounds can produce the corresponding platinum boryl compounds in a facile manner.[9] The silylborane $Me_2PhSi–BO_2C_2Me_4$ (**4.1**) was reacted with $Pt(COD)_2$ and two equivalents of an appropriate phosphine to produce the platinum boryl compounds **4.2**–**4.4**. In all cases, the boryl ligand was coordinated *cis* to its silyl counterpart. Compounds **4.2**–**4.4** were then tested for their reactivity towards phenylacetylene, as they are believed to be key intermediates in the silylborylation of alkynes and alkenes. Compounds **4.2**–**4.4** reacted smoothly, producing the insertion compounds **4.5**–**4.7**. It was noteworthy that the insertions selectively occurred at the Pt–B bond, and not the Pt–Si bond. Heating **4.5** and **4.6** led to the reductive elimination of the desired silylborylated products, whilst reductive elimination of the silylborylated product from **4.7** occurred at room temperature (Scheme 4.3).

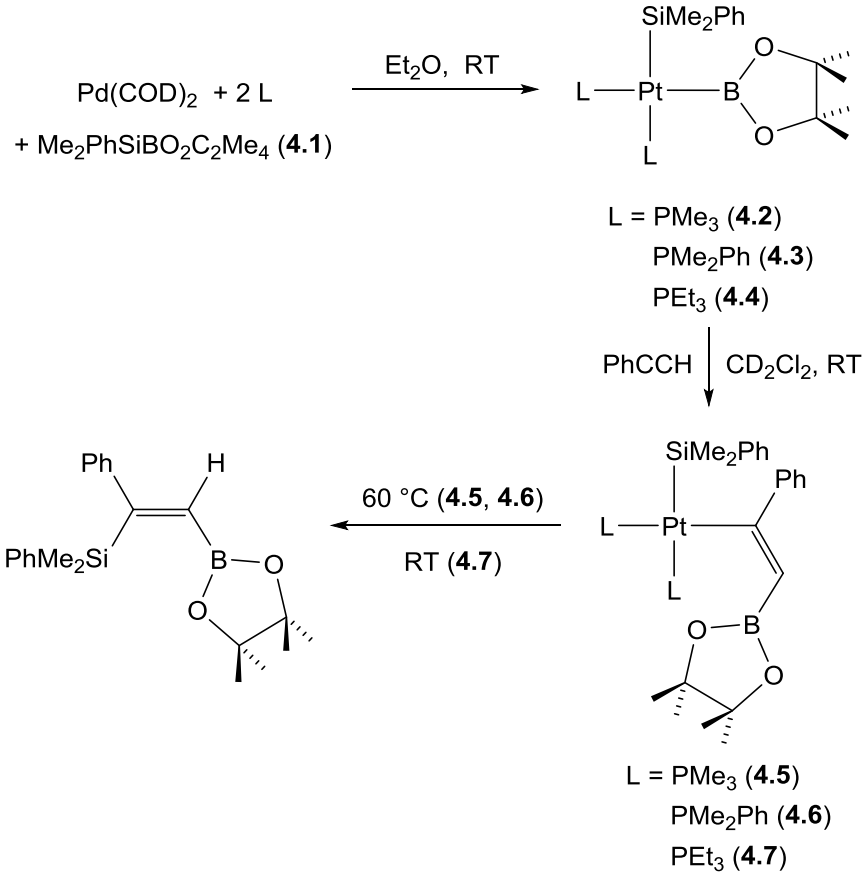

Scheme 4.3. By-products omitted for clarity.

Whilst Group 10 metal-boryl reactivity has received the most attention during the past decade, there have been notable examples of Group 11 metal-boryl compounds engaging in striking reactivity. As mentioned in Chapter 1, Sadighi and co-workers isolated the first Group 11 metal-boryl compound, the copper(I) boryl Cu{C(NArCH)$_2$}{B(O$_2$C$_2$Me$_4$)} (**1.95**).[10] Addition of CO_2 at atmospheric pressure to **1.95** resulted in rapid oxygen abstraction and concomitant release of CO, as confirmed by ^{13}C labelled studies. The resultant copper compound was revealed to be the borate Cu{C(NArCH)$_2$}{OB(O$_2$C$_2$Me$_4$)} (**1.96**). Addition of B$_2$(O$_2$C$_2$Me$_4$)$_2$ regenerates **1.95** and eliminates OB$_2$(O$_2$C$_2$Me$_4$)$_2$, closing the catalytic cycle. In two subsequent publications,[11] Sadighi and co-workers also show that alkenes and aldehydes can insert into the Cu–B bond in **1.95**, forming metal-carbon bonds in each case to produce the corresponding β-borylalkyl compound **4.8** and (α-boroxy)benzylcopper compound **4.9** respectively (Scheme 4.4). It was further shown that by reducing the steric bulk of the nitrogen bound substituents on the n-heterocyclic carbene in **1.95** from 2,6-C$_6$H$_3$^{i}Pr$_2$ to cyclohexyl groups, catalytic 1,2-diboration of aldehydes could be achieved.

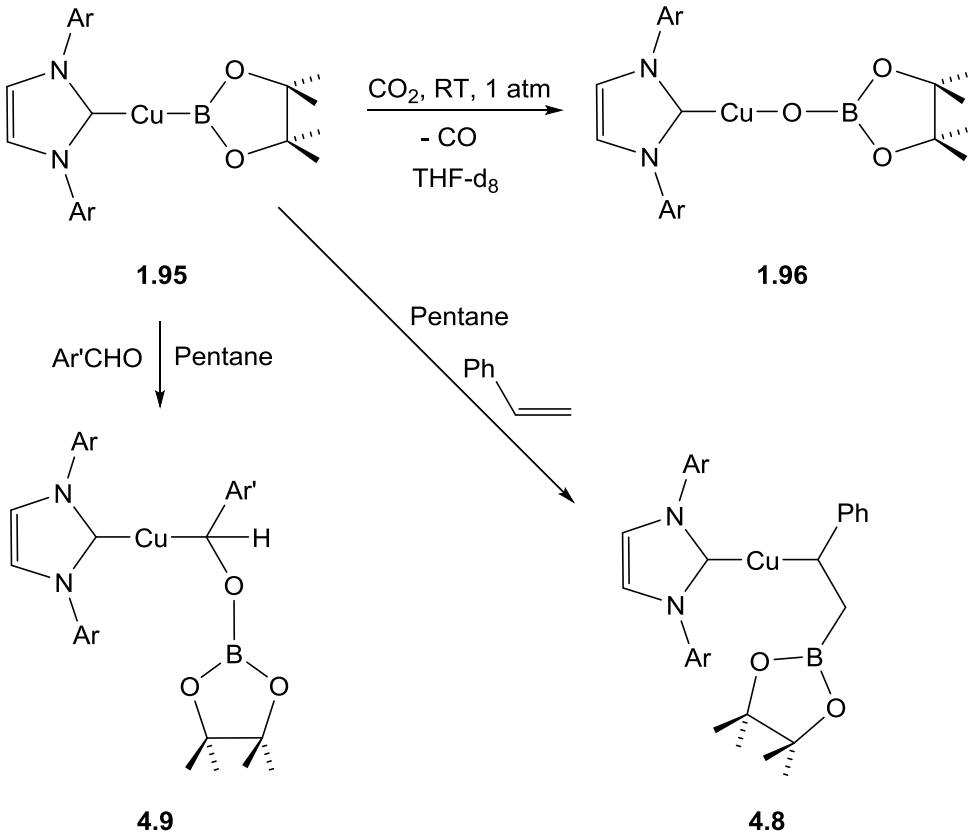

Scheme 4.4. Ar = 2,6-$C_6H_3{}^iPr_2$; Ar' = 2,4,6-$C_6H_2Me_3$.

4.2.3 Transition Metal Gallyl Reactivity

Jones *et al*. carried out reactivity studies on the platinum bis(gallyl) compound $Pt(PPh_2CH_2)_2\{Ga(NArCH)_2\}_2$ (**4.10**) and the copper gallyl compound $Cu\{C(NArCH)_2\}\{Ga(NArCH)_2\}$ (**4.11**).[12] Reactions of both compounds with a series of alkenes and alkynes led to no clean reaction at the M–Ga bond, with either intractable mixtures or compounds with substrates coordinated to the metals being formed. The reaction of **4.10** with the phosphaalkyne ^{t}BuCP to produce compound **4.12** (Scheme 4.5) is noteworthy due to the fact that rapid insertion of ^{t}BuCP into one of the gallium heterocycles occurs with no cleavage of the Pt–Ga bond. Furthermore, it was found that the insertion is reversible, with addition of ^{t}BuNC rapidly regenerating the phosphaalkyne and produces the platinum bis(gallyl) compound $Pt(^tBuNC)_2\{Ga(NArCH)_2\}_2$ (**4.13**, Scheme 4.5).

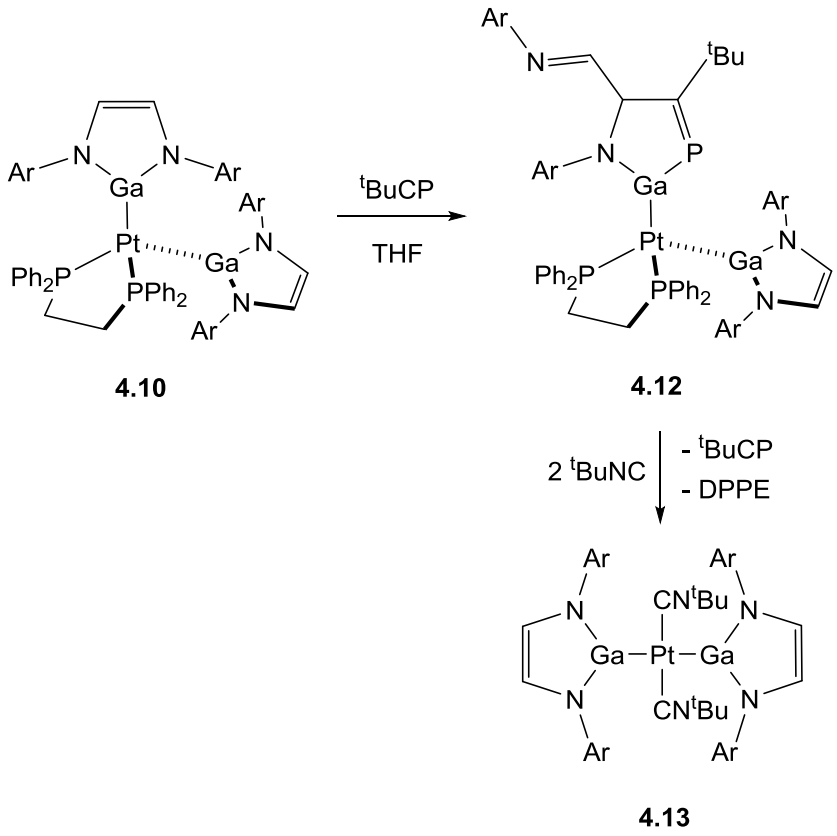

Scheme 4.5. Ar = 2,6-$C_6H_3{}^iPr_2$.

4.3 Ae/Ln–M Bond Reactivity

Reactivity studies on compounds featuring alkaline earth or Group 3 and lanthanide metals bonded to other metals are scarce due to the paucity of compounds of this type, with no examples known in the literature for Ln–M bonded compounds. Mountford *et al*. reported the isolation of a compound featuring an unsupported Mg–Fe bond. Addition of KFp to Mg(NacNac)I(THF) in THF produced Mg(NacNac)Fp(THF) (**4.14**) in 78 % yield. Reaction of **4.14** with 1,3-di-*p*-tolylcarbodiimide produced Mg(NacNac){FpC(NTol)$_2$} (**4.15**) *via* net insertion into the Mg–Fe bond, and is the first example of an insertion of an unsaturated substrate into an Ae–M bond (Scheme 4.6). Compound **4.14** was also shown to react with iodomethane to quantitatively produce Mg(NacNac)I(THF) and FpMe.

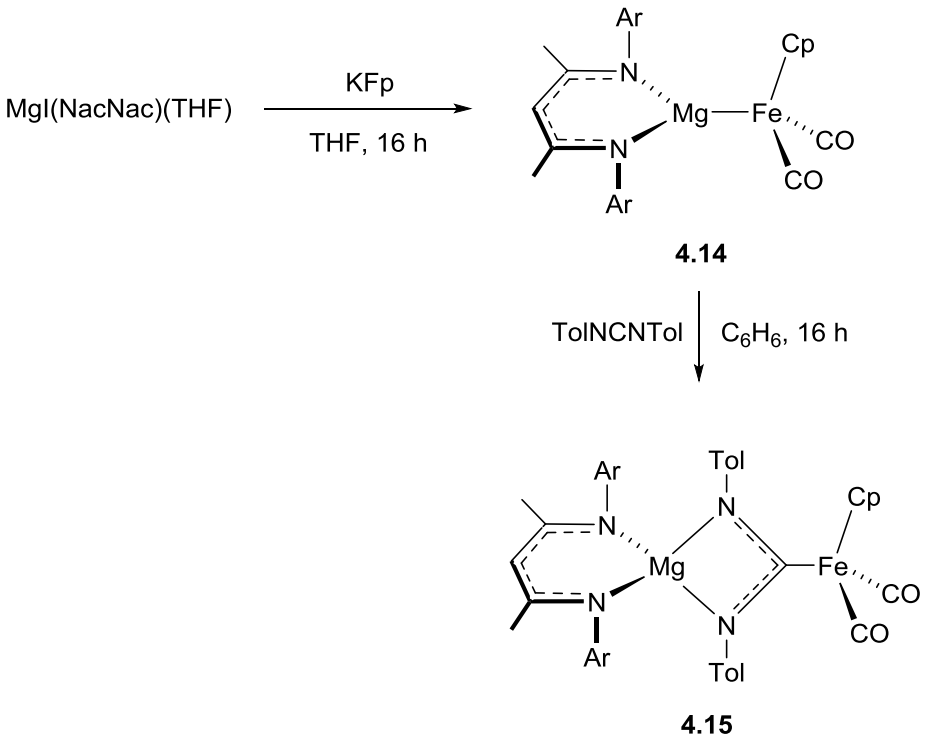

Scheme 4.6. Ar = 2,6-$C_6H_3{}^iPr_2$.

Jones *et al*. prepared a magnesium compound featuring an unprecedented Mg–Mg bond, with both magnesium atoms having a formal oxidation state of +1.[13] The compound is prepared in a facile manner, *via* reduction of MgI(NacNac)(Et_2O) with potassium, forming $[Mg(NacNac)]_2$ (**4.16**). Reaction of **4.16** with N,N'-dicyclohexylcarbodiimide resulted in the double reduction of the carbodiimide and the formation of Mg(NacNac){(MgNacNac)$C(NCy)_2$} (**4.17**, Scheme 4.7). In addition, the strongly reducing nature of compound **4.16** and its less bulky analogue $[Mg(^{Mes}NacNac)]_2$ (**4.18**), as well as their high solubility in organic solvents, has led to these magnesium dimers being employed as bespoke reducing agents in the synthesis of unusual main group and transition metal compounds. Power *et al*. employed **4.18** for the reduction of the dibromosilane precursor **4.19** to prepare a stable acyclic silylene (**4.20**, Scheme 4.8),[14] whilst Braunschweig *et al*. used **4.18** to effect the reduction of the platinum compound $PtBr(PEt_3)_2\{B_2Br(Ar'')_2\}$ (**4.21**) to produce the first example of a metal diborene compound, $Pt(PEt_3)_2\{B(Ar'')\}_2$ (**4.22**, Scheme 4.8).[15] In each case, two equivalents of $MgBr(^{Mes}NacNac)$ were eliminated.

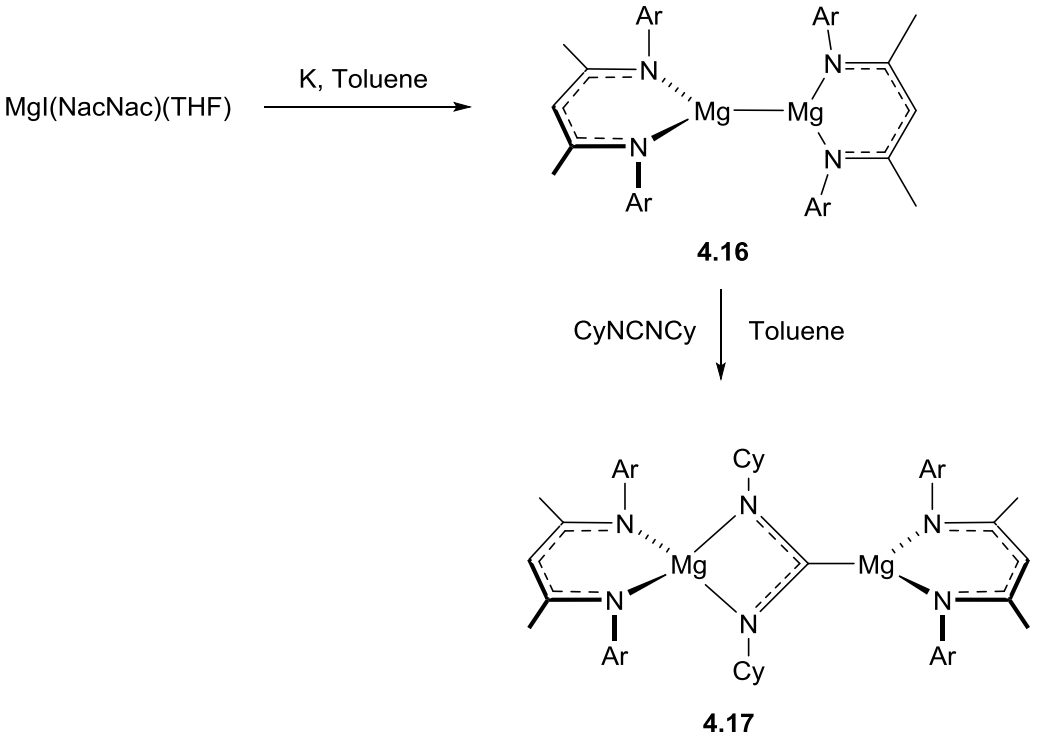

Scheme 4.7. Ar = 2,6-$C_6H_3{}^iPr_2$.

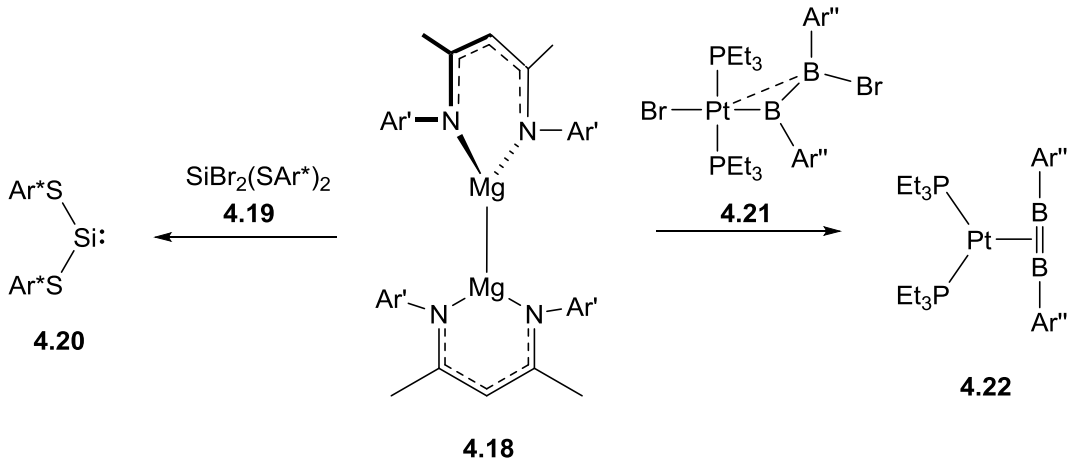

Scheme 4.8. Ar' = 2,4,6-$C_6H_2Me_3$; Ar'' = 2,3,5,6-C_6HMe_4;
Ar* = 2,6-C_6H_3(2,4,6-$C_6H_2Me_3$)$_2$.

4.4 Ln–E Bond Reactivity (E = B or Ga)

4.4.1 Introduction

The chemistry of rare earth metal boryl and gallyl compounds remains almost entirely unexplored due to the dearth of compounds featuring these bonds. Of the compounds that are available, few have the suitable supporting ligand platforms required to investigate the Ln–E bond. In Chapter 3, rare earth metal gallyl compounds featuring the amidinate moiety as innocent supporting ligands were introduced, with the intention of investigating their reactivity with small molecules.

4.4.2 Ln–Ga Bond Reactivity

4.4.2.1 Reactions with Carbodiimides

Studies involving compounds **14–16** (Figure 4.1) began by investigating their reactivity with carbodiimides, as they have been extensively used as CO_2 surrogates.[16] NMR tube scale reactions of **14** with one equivalent of RN=C=NR (R = Cy, ^{i}Pr or Tol) in C_6D_6 led to a rapid change in colour from the bright orange-red of **14** to an orange-yellow of the putative products of insertion into the Sc–Ga bond, Sc{$(Me_3SiCH_2)C(NCy)_2$}$_2${$(Ga(NArCH)_2)C(NR)_2$} (R = Cy (**17**), ^{i}Pr (**18**) or Tol (**19**), Equation 4.1).

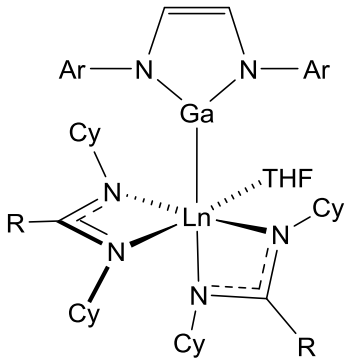

Ln = Sc (**14**), Y (**15**) or Lu (**16**)

R = CH_2SiMe_3; Ar = 2,6-$C_6H_3{}^{i}Pr_2$

Figure 4.1

The ^{1}H NMR spectrum of the NMR tube scale reaction in C_6D_6 showed quantitative conversion of **14** to **17**–**19**, with an upfield shift from the resonance found in **14** for the singlet resonance associated with the vinyl protons of the gallyl heterocycle indicating a change in gallium coordination from metal to sp^2-carbon. As an example,

the singlet resonance for **17** comes at 6.13 ppm, closely matching that of the resonance for the sp^2-carbon bound gallyl heterocycle in {Ga(NArCH)$_2$}(2,4,6-$C_6H_2{}^iPr_3$), which appears at 6.14 ppm.[17] Also seen in the ^{1}H NMR spectrum was non-coordinated THF, consistent with the formation of a sterically saturated metal centre. The $^{13}C\{^1H\}$ NMR showed two peaks in the region associated with the quaternary carbon of the amidinate, with one corresponding to that of the ligand amidinates (175 ppm) and the more downfield shifted peak corresponding to that of the galla-amidinate (179 ppm). The reactions were repeated on the preparative scale in hexane, with similarly fast reaction times (*ca*. 5 minutes), and the products isolated in reasonable yields (60-62 %) as yellow-orange powders. Compounds **17**–**19** are all stable in solutions of C_6D_6 for days in ambient conditions without significant decomposition. These results constitute the first insertion reactions with Ln–Ga bonded compounds and unsaturated substrates, and indeed the first successful reactions of any type at an unsupported metal-gallium bond.

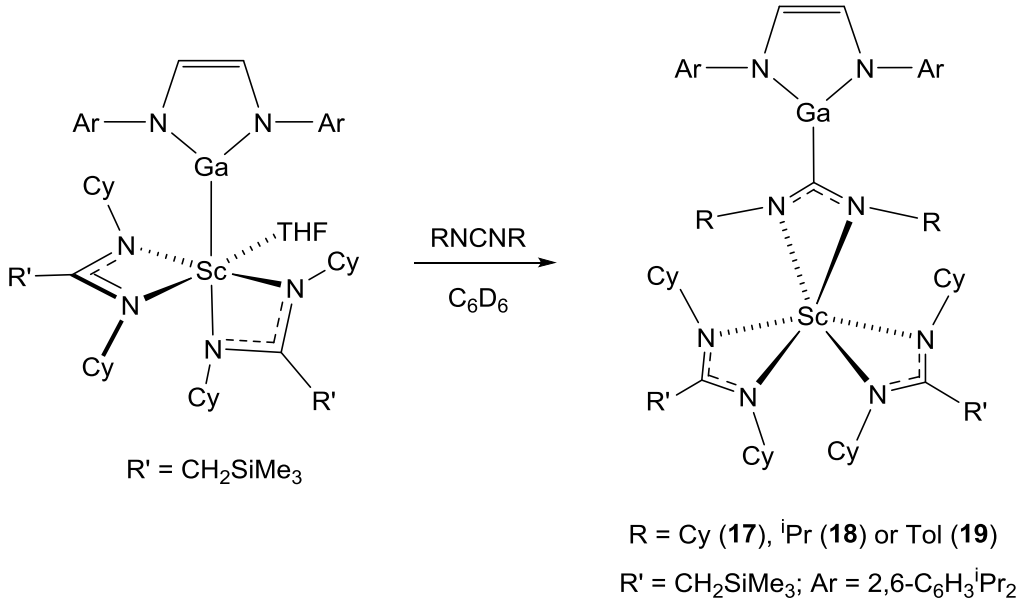

Equation 4.1

The yttrium (**15**) and lutetium (**16**) analogues of **14** exhibited similar reactivity. Addition of one equivalent of CyNCNCy to solutions of either **15** or **16** in C_6D_6 on the NMR tube scale resulted in rapid and quantitative conversion to the insertion products Ln{$(Me_3SiCH_2)C(NCy)_2$}$_2${$(Ga(NArCH)_2)C(NCy)_2$} (Ln = Y (**20**) or Lu (**21**), Equation 4.2), with the ^{1}H NMR spectra showing similar upfield shifted resonances for the vinyl protons of the heterocycle. It is noteworthy that the resonance

associated with **20** (6.18 ppm) matches that of an impurity found when synthesising **15**, indicating that some formation of **20**, *via* an as yet unknown mechanism, occurs during the reaction that produces **15**. Repeating the reactions on a preparative scale in hexane produced **20** and **21** as pale orange powders in 65 % and 72 % yields respectively.

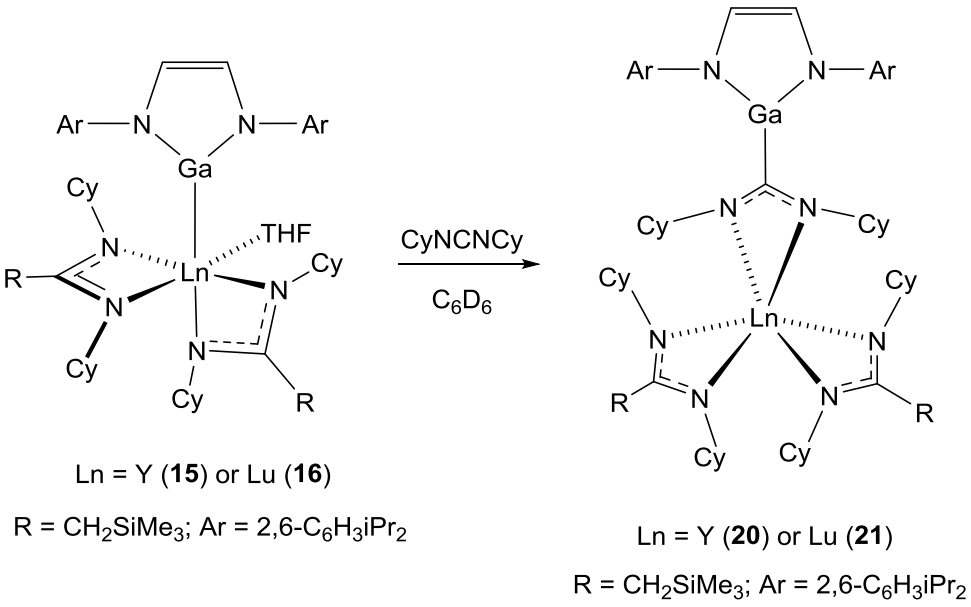

Equation 4.2

An attempt to slow the rapid rate of reaction to identify any reaction intermediates was unsuccessful. An NMR tube scale reaction of **14** and ^{i}PrNCN^{i}Pr in toluene-d_8 at -78 °C, and followed by ^{1}H NMR spectroscopy at that temperature saw formation of **18** during the time taken to go from mixing of reactants to viewing the resultant NMR spectrum (*ca*. 5 minutes). The rapid rate of reaction is quite surprising and will be investigated later in this Chapter.

4.4.2.2 Solid State Structures

Crystals of **18**–**20** suitable for X-ray diffraction were grown from either slow evaporation of a concentrated hexane solution (**18** and **19**) or cooling of a concentrated hexane solution to -30 °C (**20**). The structures confirm that **18** and **19** (Figures 4.2 and 4.3) are products of insertion of a carbodiimide into the Sc–Ga bond of **14**, whilst **20** (Figure 4.4) shows the product of insertion into the Y–Ga bond of **15**. Compounds **18**–**20** have distorted octahedral structures, with two amidinate ligands and a galla-amidinate bound through chelating nitrogens to the Ln metal centres.

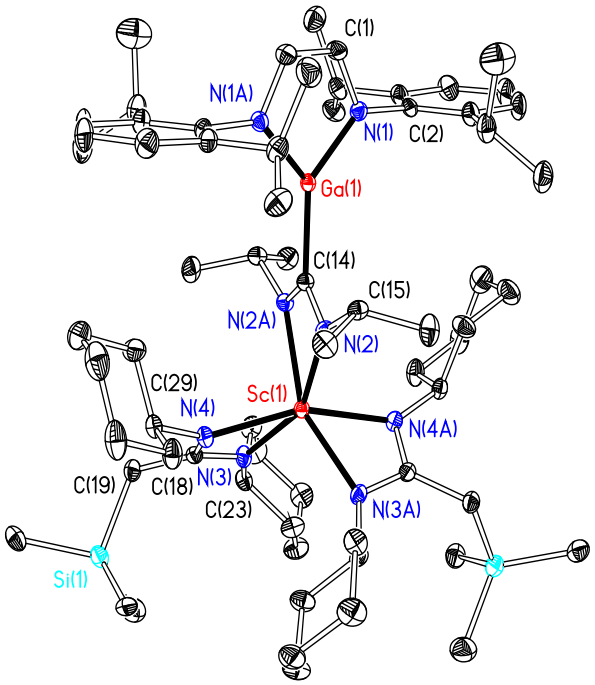

Figure 4.2. Displacement ellipsoid plot (20 % probability) of $Sc\{(Me_3SiCH_2)C(NCy)_2\}_2\{(Ga(NArCH)_2)C(N^iPr)_2\}$ (**18**). H atoms omitted for clarity. Atoms carrying the suffix 'A' are related to their counterparts by the symmetry operator 1-*x*, *y*, $^3/_2$-*z*.

Table 4.1. Selected distances (Å) and angles (°) for **18**.

Sc(1)-N(2)	2.2407(11)	Ga(1)-N(1)	1.8537(12)
Sc(1)-N(3)	2.1782(11)	Ga(1)-C(14)	1.9939(17)
Sc(1)-N(4)	2.2278(11)	N(1)-Ga(1)-N(1A)	89.72(7)
N(3)-Sc(1)-N(4)	60.87(4)	N(2)-Sc(1)-N(2A)	60.61(5)

Whilst the galla-amidinate Ln–N bond distances are slightly longer, the amidinate Ln–N bond distances fall in line with the averages found for scandium (2.203 Å) and yttrium (2.385 Å) bound *N*,*N*′-disubstituted amidinates and guanidinates. Compounds **18** and **19** have amidinate bite angles around the average for *N*,*N*′-disubstituted amidinates and guanidinates bound to scandium (61.2 °), whilst **20** exhibits N–Y–N bond angles expected for yttrium bound examples (56.5 °).[18] Compound **19** has a slightly more acute than average bite angle for the galla-amidinate (58.9 °), perhaps to better accommodate the bulkier *N*,*N*′-bound tolyl groups. For **18**, the Sc–N bonds of

the amidinates that are *trans* to the Sc–N bonds of the galla-amidinate are appreciably shorter than those *trans* to other amidinates. Although it is tempting to attribute this observation to evidence of *trans* influence producing a difference in bond lengths, it is not likely in this instance to be a factor as neither **19** or **20** show the same differences in bond length seen in **18**.

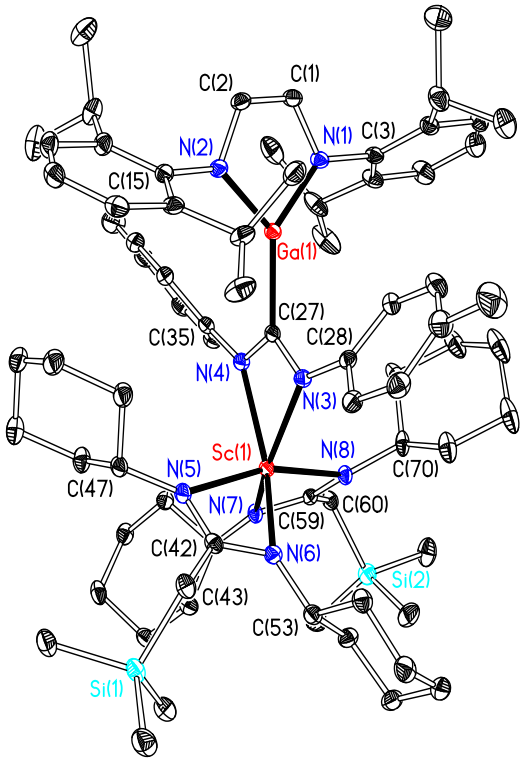

Figure 4.3. Displacement ellipsoid plot (20 % probability) of $Sc\{(Me_3SiCH_2)C(NCy)_2\}_2\{(Ga(NArCH)_2)C(NTol)_2\}$ (**19**). H atoms and other molecule in asymmetric unit omitted for clarity.

Table 4.2. Selected distances (Å) and angles (°) for **19**.

Sc(1)-N(3)	2.2595(12)	Sc(1)-N(8)	2.1782(12)
Sc(1)-N(4)	2.2662(13)	Ga(1)-N(1)	1.8590(12)
Sc(1)-N(5)	2.1972(12)	Ga(1)-N(2)	1.8648(12)
Sc(1)-N(6)	2.1693(13)	Ga(1)-C(27)	2.0088(14)
Sc(1)-N(7)	2.1759(12)		
N(1)-Ga(1)-N(2)	90.31(5)	N(5)-Sc(1)-N(6)	61.27(5)
N(3)-Sc(1)-N(4)	58.97(5)	N(7)-Sc(1)-N(8)	61.57(5)

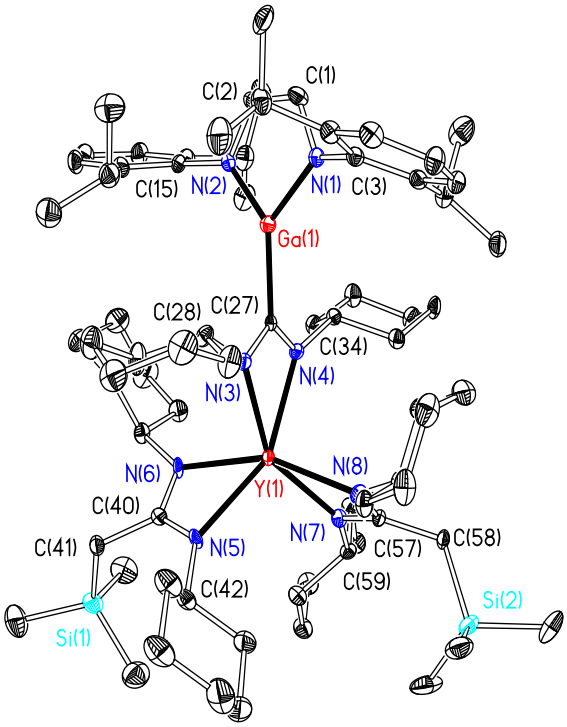

Figure 4.4. Displacement ellipsoid plot (20 % probability) of $Y\{(Me_3SiCH_2)C(NCy)_2\}_2\{(Ga(NArCH)_2)C(NCy)_2\}$ (**20**). H atoms and other molecule in asymmetric unit omitted for clarity.

Table 4.3. Selected distances (Å) and angles (°) for **20**.

Y(1)-N(3)	2.378(4)	Y(1)-N(8)	2.357(4)
Y(1)-N(4)	2.379(4)	Ga(1)-N(1)	1.863(4)
Y(1)-N(5)	2.351(4)	Ga(1)-N(2)	1.868(4)
Y(1)-N(6)	2.358(3)	Ga(1)-C(27)	1.997(5)
Y(1)-N(7)	2.329(4)		
N(1)-Ga(1)-N(2)	89.78(18)	N(5)-Y(1)-N(6)	56.61(13)
N(3)-Y(1)-N(4)	56.60(14)	N(7)-Y(1)-N(8)	57.14(15)

The change in *N*,*N'*-bound substituents from *iso*-propyl to *p*-tolyl from **18** to **19** results in a more obtuse angle between the supporting amidinate ligands in **19** compared to **18**, as the ligands rearrange to accommodate the bulkier *p*-tolyl substituents and their longer Sc–N bond distances (Figure 4.5).

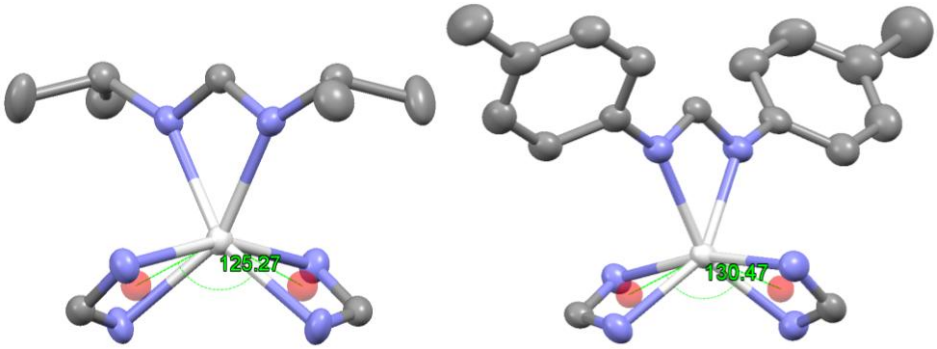

Figure 4.5. Amidinate core for **18** (left) and **19** (right).

Chapter 3 introduced Bent's rule as a way of rationalising the changes seen in the gallyl heterocycle when changing the atom the heterocycle is coordinated to. Upon change in coordination from potassium in $[(K\{Ga(NArCH)_2\}(Et_2O)]_2$ (**3.30**) to scandium in $Sc\{(Me_3SiCH_2)C(NCy)_2\}_2\{Ga(NArCH)_2\}THF$ (**14**), we see a shortening in the Ga–N bond distances, and a more obtuse N–Ga–N angle. Upon change in coordination from scandium to an sp^2-carbon atom in **18** and **19**, we see further shortening of the Ga–N bonds, and an even more obtuse N–Ga–N angle, reflecting the increased covalency of the Ga–C bond. These changes are summarised in Figure 4.6. The N–Ga–N angles for **18** (89.7 °) and **19** (90.3 °) correspond well to that found in $\{Ga(NArCH)_2\}(2,4,6\text{-}C_6H_2{}^iPr_3)$ (89.7 °).[17]

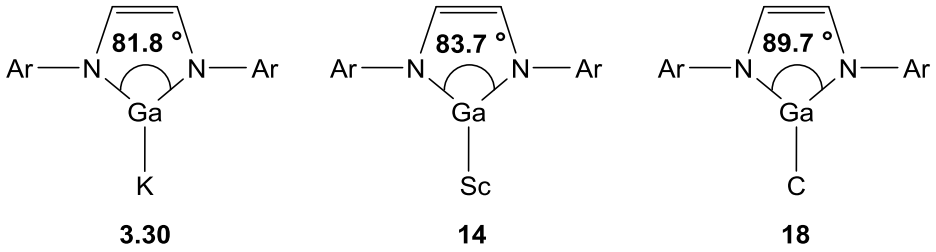

Figure 4.6

4.4.3 Ln–B Bond Reactivity

4.4.3.1 Literature Examples

Hou and co-workers reported the synthesis and isolation of a scandium boryl compound featuring a bis(amidinate) supporting ligand set, $Sc\{(Me_3SiCH_2)C(N^iPr)_2\}_2\{B(NArCH)_2\}$ (**4.23**), via addition of two equivalents of $^iPrNCN^iPr$ to the scandium boryl compound **1**.[19] The synthetic protocol utilised by Hou and co-workers presented in Scheme 4.9 is intriguing, as it implies the Sc–B bond is relatively unreactive under ambient conditions. Indeed, addition of one

equivalent of ^{i}PrNCN^{i}Pr to **4.23**, or three equivalents to **1**, required heating at 60 °C for five hours before insertion into the Sc–B bond occurred, forming Sc{(Me$_3$SiCH$_2$)C(N^{i}Pr)$_2$}$_2${(B(NArCH)$_2$)C(N^{i}Pr)$_2$} (**4.24**, Scheme 4.9). The contrast with the reactivity of **14** is striking, and prompted an investigation into the structure and bonding of the boryl analogues of **14**-**16**, featuring the same bis(amidinate) ligands. This would constitute the first full structure and bonding comparison of a metal-boryl and metal-gallyl compound with the same supporting ligand sets.

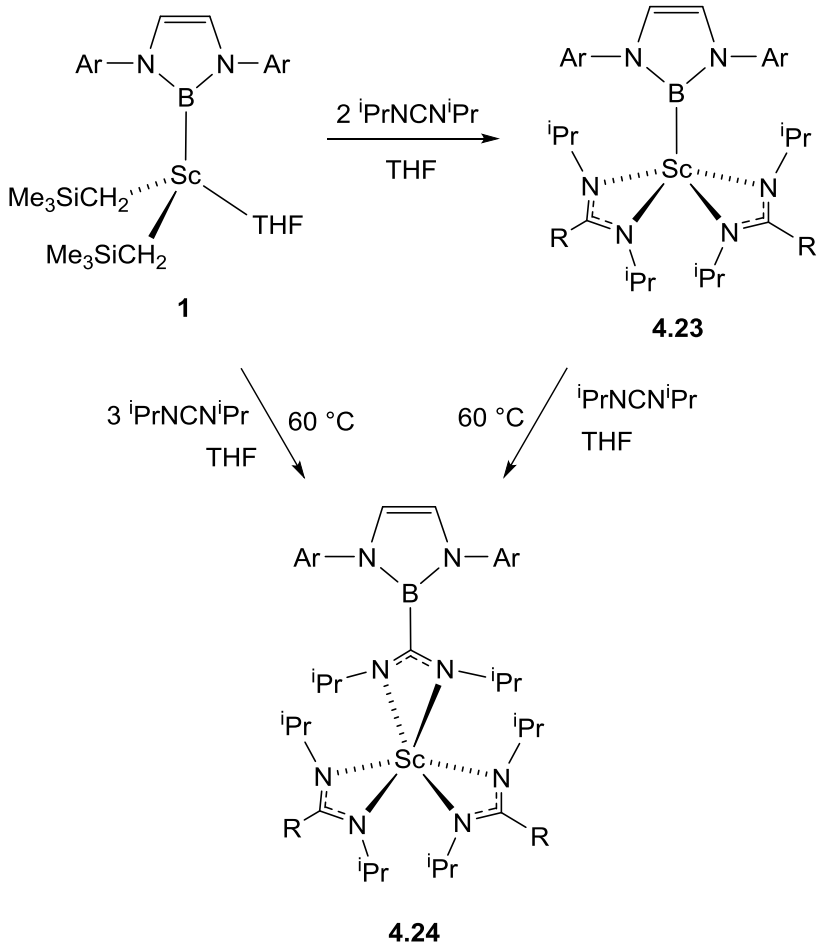

Scheme 4.9. R = CH$_2$SiMe$_3$; Ar = 2,6-C$_6$H$_3$^{i}Pr$_2$.

4.4.3.2 Ln–B bis(amidinate) Compounds

Initial attempts at synthesising Ln{(Me$_3$SiCH$_2$)C(NCy)$_2$}$_2${B(NArCH)$_2$} (Ln = Sc (**22**), Y (**23**) or Lu (**24**)) centred around the use of the cationic bis(amidinate) compounds [Ln{(Me$_3$SiCH$_2$)C(NCy)$_2$}$_2$(THF)$_2$][BPh$_4$] (Ln = Sc (**6-BPh$_4$**), Y (**9-BPh$_4$**) or Lu (**12-BPh$_4$**)). Reaction of **6-BPh$_4$** or **12-BPh$_4$** with one equivalent of

$Li\{B(NArCH)_2\}(THF)_2$ (**1.7**) failed to produce the desired boryl compounds, instead producing $HB(NArCH)_2$ (**1.22**). Employing a slightly modified version of the method of Hou and co-workers, a cooled (-30 °C) solution of two equivalents of CyNCNCy in THF were added to cooled (-30 °C) solutions of **1**–**3**, producing the desired rare earth metal bis(amidinate) boryl compounds **22**–**24** as white microcrystalline solids (Scheme 4.10). Cooling the reaction mixtures is important as it minimises the formation of **1.22**. Once isolated, **22**–**24** are insoluble in pentane and sparingly soluble in hexane and aromatic solvents.

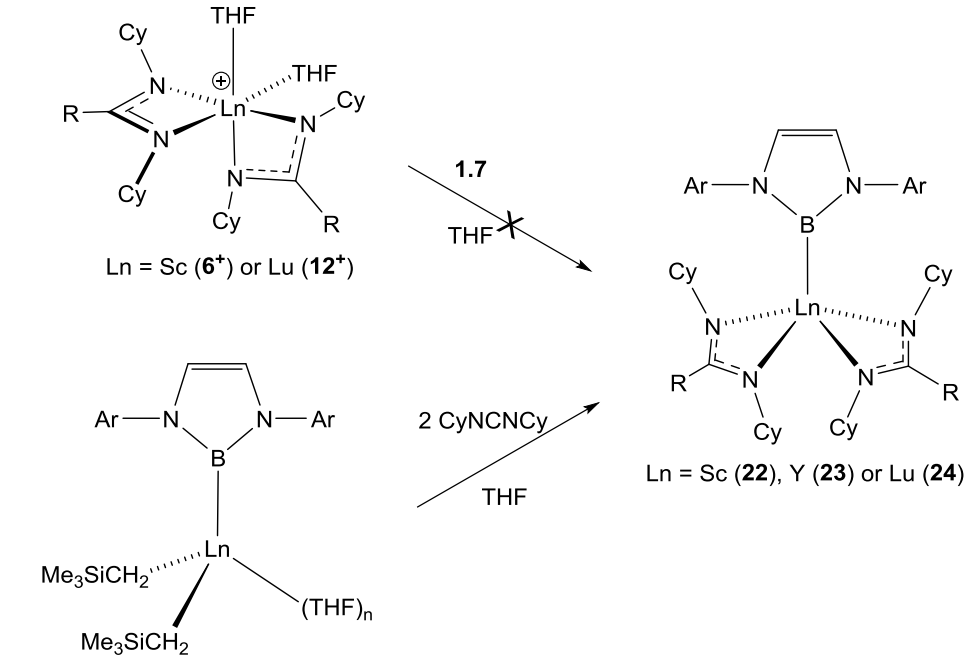

Scheme 4.10. R = CH_2SiMe_3; Ar = 2,6-$C_6H_3{}^iPr_2$.

The ^1H NMR spectra of **22**–**24** in C_6D_6 reveal an absence of coordinated THF, as in the case of compound **4.23**. The singlet resonance for the vinyl protons of the boryl heterocycle are slightly upfield shifted from where they are found for **1**–**3** (*e.g.* 6.24 ppm (**1**) *vs* 6.18 ppm (**22**)). The ^{11}B NMR resonances of **22**–**24**, however, closely match those found for **1**–**3**, and remain unaffected by the change in ligands around the metal centre. As with the bis(amidinate) compounds described in Chapter 3, the singlet resonance for the methylene protons of the CH_2SiMe_3 group in **22**–**24** are considerably downfield shifted from where they are found for **1**–**3** (*e.g.* 0.10 ppm (**1**) *vs* 1.88 ppm (**22**)).

Crystals of **22**–**24** suitable for X-ray diffraction were grown from either slow evaporation of a concentrated hexane solution (**22** and **23**) or cooling of a concentrated pentane solution to -30 °C (**24**). The structures are shown in Figures 4.7-4.9, and confirm that **22**–**24** are rare earth metal (bis)amidinate boryl compounds of the type $Ln\{(Me_3SiCH_2)C(NCy)_2\}_2\{B(NArCH)_2\}$. The Ln–B bond distances follow the expected periodic trend Sc < Y > Lu. The Sc–B (2.4981(9) Å) and Lu–B (2.620(5) Å) bond distances in **22** and **24** are longer than those found in **1** (2.422(2) Å) and **3** (2.555(8) Å), whereas the Y–B (2.6616(14) Å) bond distance in **23** is slightly shorter than that found for **2** (2.696(4) Å). The structures for **22** and **23** are isomorphous, and all three compounds adopt a distorted square-based pyramidal (SBP) geometry, with the amidinate ligands occupying the base of the pyramid, and the boryl occupying the apical position. The Ln–N bond distances in **22**–**24** follow a pattern in which the two Ln–N bond distances found on the same amidinate ligand (*e.g.* N(3) and N(4) in **22**) are not equal, with one being approximately 0.05 Å longer than the other in all cases. The origin of this difference is likely due to sterics, with the amidinate ligand adjusting to accommodate the sterically demanding boryl ligand, rather than electronics, as the C–N bond distances for the amidinate are nearly equal for **22**–**24**, indicating that the π-electrons are delocalised evenly across the N–C–N backbone.

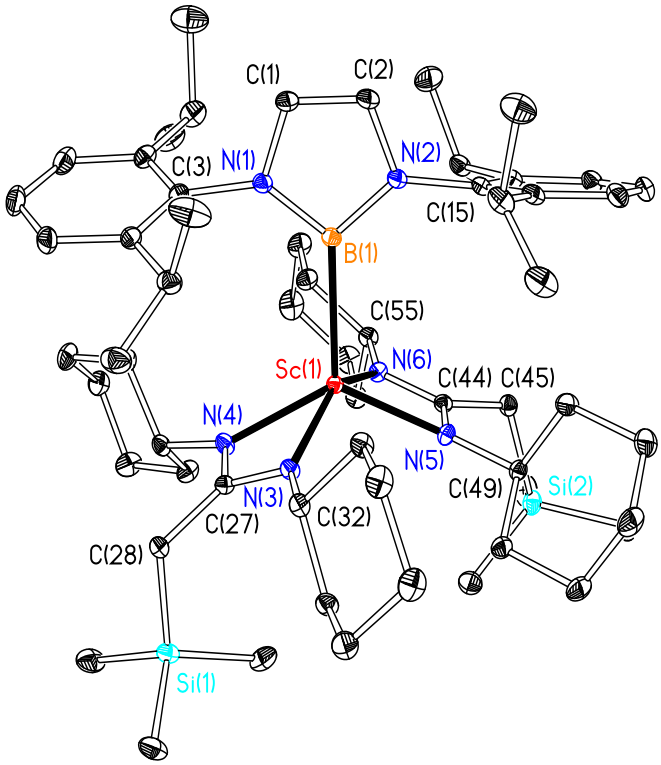

Figure 4.7. Displacement ellipsoid plot (20 % probability) of $Sc\{(Me_3SiCH_2)C(NCy)_2\}_2\{B(NArCH)_2\}$ (**22**). H atoms omitted for clarity.

Five-coordinate compounds of the small to mid-size rare earth metals commonly adopt trigonal bi-pyramidal (TBP) geometries, and so the observed SBP geometry for **22**–**24** is unusual. It is known that boryl ligands are powerful σ-donors and exhibit a very strong *trans* influence, with examples in the literature of this influence affecting the geometry adopted by transition metal complexes. Compound **14** (and other literature compounds)[20] has provided evidence that *trans* influence can have a small, but significant effect on the structure of rare earth metal compounds. The SBP geometry adopted by compounds **3** and **22**–**24**, as well as the compounds independently reported by Hou and co-workers, appears to suggest that this geometry is preferred for five-coordinate rare earth metal boryl compounds.

Table 4.4. Selected distances (Å) and angles (°) for **22**.

Sc(1)-B(1)	2.4981(9)	B(1)-N(1)	1.4713(11)
Sc(1)-N(3)	2.2127(7)	B(1)-N(2)	1.4751(11)
Sc(1)-N(4)	2.1616(7)	N(1)-C(1)	1.4018(11)
Sc(1)-N(5)	2.1648(7)	N(2)-C(2)	1.3991(11)
Sc(1)-N(6)	2.2216(7)	C(1)-C(2)	1.3356(14)
N(1)-B(1)-N(2)	100.05(7)	N(5)-Sc(1)-N(6)	61.40(3)
N(3)-Sc(1)-N(4)	61.46(3)		

As with the gallyl heterocycles described earlier in this Chapter and in Chapter 3, there are structural changes observed in the boryl heterocycle upon change in coordination from lithium to scandium. The lithium boryl starting material $Li\{B(NArCH)_2\}(THF)_2$ (**1.7**) features an ionic Li–B bond. Using the scandium compound **22** as an example, upon coordination to scandium, the boryl heterocycle shows a more obtuse N–B–N angle (*ca.* 100.1 ° *vs* 98.6 ° for **1.7**)[21] with roughly equal B–N bonds (1.473 Å (mean) vs 1.478 Å (mean) for **1.7**)[21], suggesting some covalency in the Sc–B bond.

Using Bent's rule,[22] as the electronegativity of the atom coordinated to boron increases (from lithium to scandium), the ionic nature of the interaction decreases. As a result of this, less 2*s* character on the boron atom will be directed towards the newly formed Sc–B bond, in principle resulting in the B–N bonds shortening. With the remaining bonds in the heterocycle largely unchanged, the N–B–N angle becomes more obtuse to accommodate the change in B–N bond distance. As with the gallyl examples in Chapter 3, evidence for M–B covalency and change in electropositivity of metals affecting the bond distances and angles in the gallyl heterocycle can be found in surveying the Cambridge Structural Database.[18]

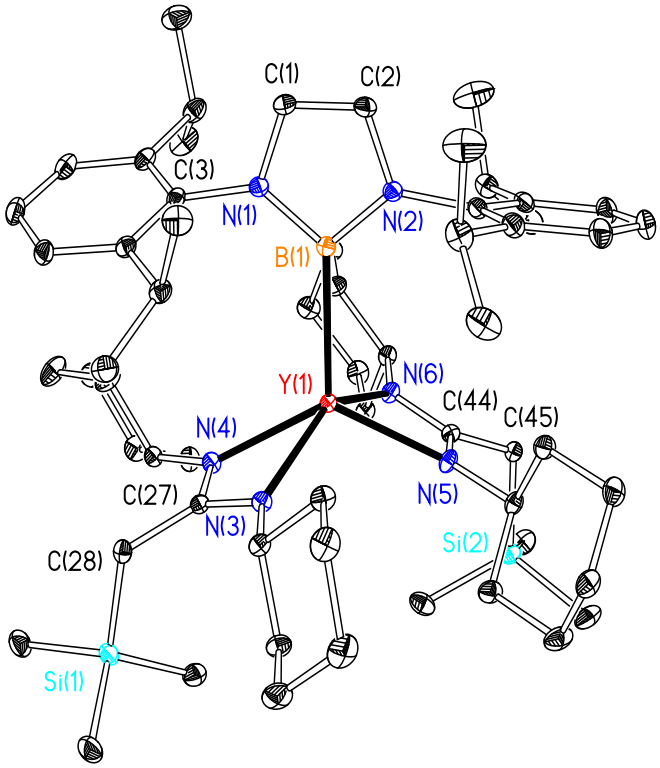

Figure 4.8. Displacement ellipsoid plot (20 % probability) of $Y\{(Me_3SiCH_2)C(NCy)_2\}_2\{B(NArCH)_2\}$ (**23**). H atoms omitted for clarity.

Table 4.5. Selected distances (Å) and angles (°) for **23**.

Y(1)-B(1)	2.6616(14)	B(1)-N(1)	1.4653(18)
Y(1)-N(3)	2.3638(11)	B(1)-N(2)	1.4660(18)
Y(1)-N(4)	2.3179(11)	N(1)-C(1)	1.3989(18)
Y(1)-N(5)	2.3125(11)	N(2)-C(2)	1.3986(17)
Y(1)-N(6)	2.3507(11)	C(1)-C(2)	1.339(2)
N(1)-B(1)-N(2)	100.43(11)	N(5)-Y(1)-N(6)	57.57(4)
N(3)-Y(1)-N(4)	57.41(4)		

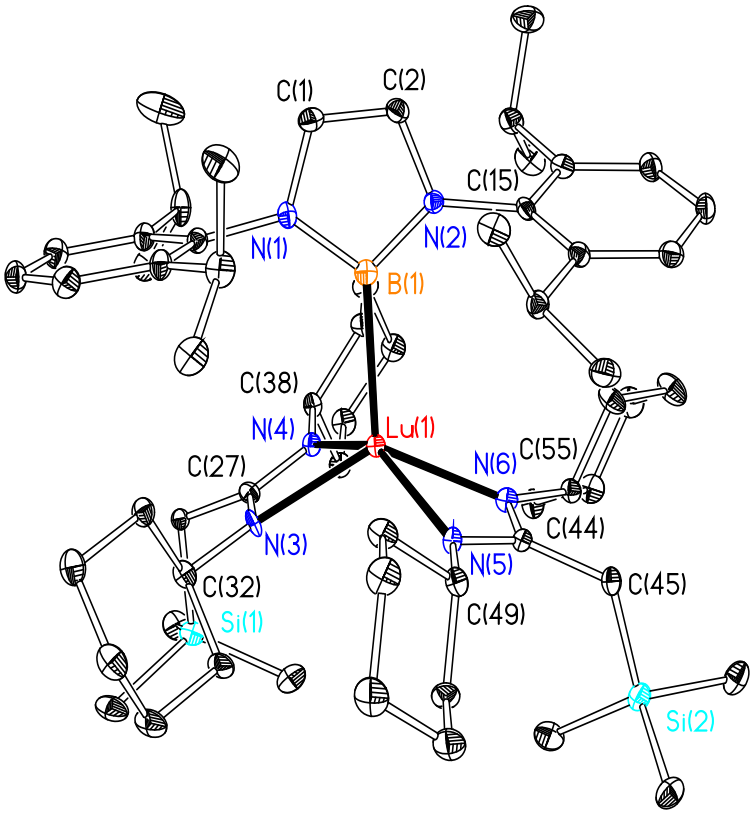

Figure 4.9. Displacement ellipsoid plot (20 % probability) of Lu{$(Me_3SiCH_2)C(NCy)_2$}$_2${$B(NArCH)_2$} (**24**). H atoms and pentane of crystallisation omitted for clarity.

Table 4.6. Selected distances (Å) and angles (°) for **24**.

Lu(1)-B(1)	2.620(5)	B(1)-N(1)	1.486(7)
Lu(1)-N(3)	2.267(3)	B(1)-N(2)	1.448(6)
Lu(1)-N(4)	2.307(4)	N(1)-C(1)	1.396(6)
Lu(1)-N(5)	2.337(4)	N(2)-C(2)	1.423(6)
Lu(1)-N(6)	2.279(4)	C(1)-C(2)	1.326(7)
N(1)-B(1)-N(2)	101.2(4)	N(5)-Lu(1)-N(6)	58.68(13)
N(3)-Lu(1)-N(4)	58.95(13)		

Figure 4.10 shows a plot of B–N bond distances against the N–B–N bond angle for all compounds featuring an unsupported metal-boron bond, with the source of boron coming from the boryl anion. There is a clear relationship where the bond distances become progressively shorter as the bond angles become progressively more obtuse,

and they do so as the metals bound to the heterocycle form progressively more covalent bonds, with some examples highlighted.

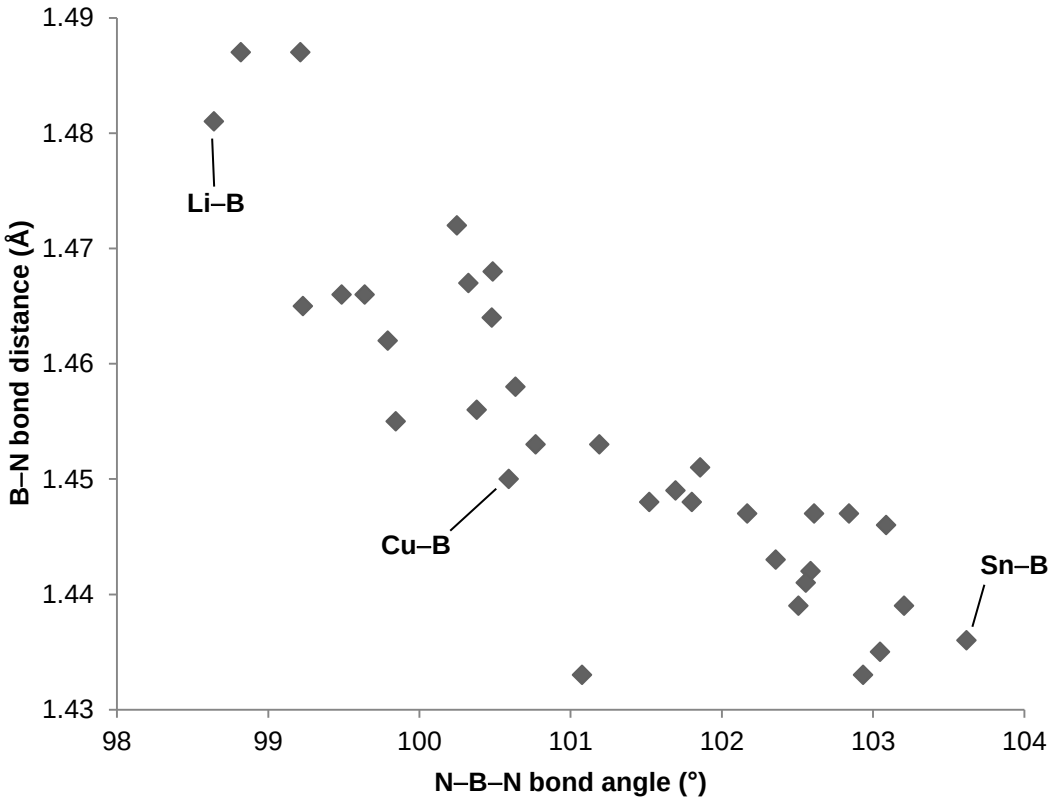

Figure 4.10. B–N bond distance *vs* N–B–N bond angle for compounds with M–B(NArCH)$_2$ bonds.

As with the rare earth metal gallyl compounds, carbodiimides were chosen to investigate the reactivity of the Ln–B bond. Addition of one equivalent of RNCNR (R = ^{i}Pr or Cy) to **22** in C_6D_6 at ambient temperature led to no reaction, with warming to 60 °C also resulting in no reaction. Changing the solvent to THF-d_8 and repeating the reaction under the same conditions also led to no products being formed.

4.4.4 Sc–B *vs* Sc–Ga: Structural Comparison

The lack of reactivity at the Sc–B bond of **22** compared to that of the Sc–Ga bond of **14** may be attributed to the structures of **14** and **22** differing significantly despite the identical supporting ligand sets. Compound **22** does not coordinate THF despite the reaction being performed in THF. Conversely, **14** retains a molecule of coordinated THF from the starting reagent **6-BPh$_4$** even after reaction in toluene and extraction with pentane. The requirement of THF to saturate the coordination sphere in **14** is a

result of the significant difference in Sc–E bond lengths. Compound **22** has a Sc–B bond length of 2.4981(9) Å, whilst **14** has a Sc–Ga bond length of 3.0365(3) Å, a difference of 0.5384 Å. This difference can be rationalised by considering the covalent radii for the larger gallium (1.22(3) Å) *vs* the smaller boron (0.84(3) Å),[23] and the less nucleophilic nature of the gallyl anion compared to the boryl anion.[24] These contribute to a more crowded scandium metal centre for **22**. Based upon existing studies,[25] insertion of carbodiimides into the Ln–E bond would be expected to follow the path outlined in Scheme 4.11, whereby coordination of the carbodiimide to the metal centre occurs prior to insertion. The lack of available coordination sites on **22** contributes to the observed lack of reactivity.

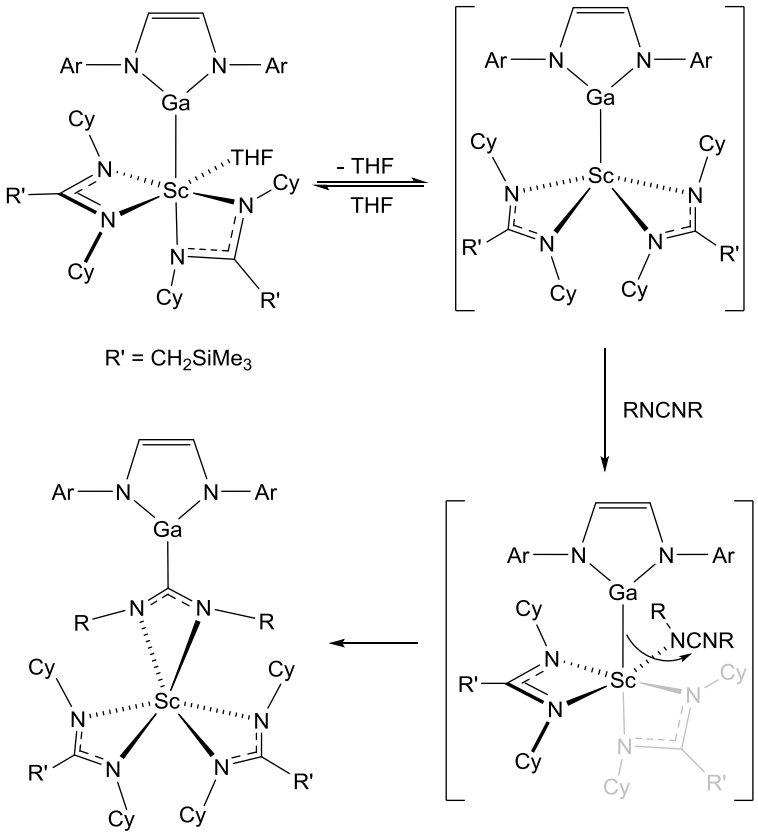

Scheme 4.11. Proposed insertion reaction pathway.

As mentioned in Chapter 3, there is a small but significant *trans* influence affecting the bond lengths in **14**. This influence can have a 'structural effect', *i.e.* affect the bond length of the *trans* substituent, or a 'kinetic effect', *i.e.* affect the lability of the *trans* substituent.[26] The structural effect can be seen in **14**, where the amidinate Sc–N bond *trans* to THF is significantly shorter than those of the other amidinate Sc–N

bonds, as expected for substituents *trans* to neutral donor ligands, but the kinetic effect is less clear.

The rapid nature of the carbodiimide insertion reaction suggests that there may be a labilising effect for both the Sc–O bond of the coordinated THF and the Sc–Ga bond, both of which are *trans* to anionic Sc–N bonds. A labile THF would allow for facile displacement and coordination of the carbodiimide, whilst a relatively labile Sc–Ga bond would accelerate insertion. Whilst no significant difference was observed in the amidinate Sc–N bond distance *trans* to the gallyl ligand of the experimentally derived molecular structure when compared to Sc–N bonds *trans* to nitrogen, the very same bond in the computationally derived geometry optimised structure of **14**, **14C**, was slightly shorter than those found *trans* to nitrogen. This could suggest that the *trans* influence of amidinate nitrogen is greater than that of the gallyl, and may be labilising the Sc–Ga bond.

4.5 DFT Computational Analysis

DFT computational analysis was sought to elucidate the bonding and structural features of the bis(amidinate) compounds. There will first be a discussion of the structural features of the boryl compounds **22**–**24** and how they relate to the corresponding gallyl compounds **14**–**16**. Hypothetical compounds will be calculated to help aid the discussion. A discussion of the electronic structure and bonding features of these systems will then follow. This section will conclude with a discussion of the energetics of the insertion reactions that produced compounds **17**–**21**.

4.5.1 Geometry Optimised Structures

4.5.1.1 Five-coordinate Ln–B Structures

Scalar relativistic, gradient corrected density functional theory using the PBE functional was carried out in collaboration with Ms Abigail Mountain and Prof. Nikolas Kaltsoyannis at University College London. The geometry optimised structures for Ln{(Me_3SiCH_2)C($NCy)_2$}$_2${$B(NArCH)_2$} (Ln = Sc (**22C**), Y (**23C**) or Lu (**24C**), Figure 4.11) were calculated with dispersion corrections applied, as are all subsequent models. Selected results are presented in Table 4.7. The calculated structures show excellent agreement with those found experimentally, with the

unusual distorted SBP geometry being adopted in all three cases and exhibiting the expected periodic trend Sc–B < Y–B > Lu–B in Ln–B bond length.

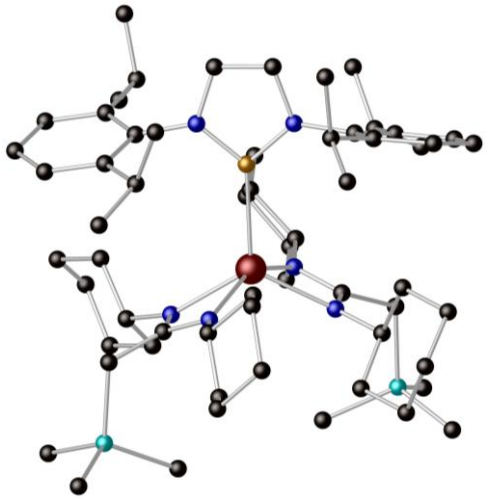

Figure 4.11. Ball and stick plot (arbitrary radius) of the calculated structure of $Sc\{(Me_3SiCH_2)C(NCy)_2\}_2\{B(NArCH)_2\}$ (**22C**). H atoms omitted for clarity.

The calculated structures **22C**–**24C** accurately recreate the trends seen in the experimentally derived molecular structures with regards to the amidinate ligands. The two Ln–N bond distances found on the same amidinate ligand do not match, with one being approximately 0.07 Å longer than the other in all cases (*ca.* 0.05 Å for **22**–**24**). As with the real structures **22**–**24**, the C–N bond distances for the amidinate are virtually equal for **22C**–**24C** indicating that the π-electrons are delocalised evenly across the N–C–N backbone. This again suggests that steric effects are most likely the source of this difference in bond lengths, as the amidinate ligands twist out of their preferred positions to accommodate their bulky *N*- and *C*-bound substituents.

Table 4.7. Selected DFT computational results for Ln{$(Me_3SiCH_2)C(NCy)_2\}_2${$E(NArCH)_2$} (Ln = Sc, E = Ga (**14C$_{-THF}$**) or B (**22C**); Y, E = Ga (**15C$_{-THF}$**) or B (**23C**); Lu, E = Ga (**16C$_{-THF}$**) or B (**24C**)), and **Ge–Ga**.[a]

	14C$_{-THF}$	**15C$_{-THF}$**	**16C$_{-THF}$**	**22C**	**23C**	**24C**	**Ge–Ga**
r(Ln–E) or r(Ge-Ga)(Å)	2.726	2.890	2.825	2.473	2.638	2.574	2.416
N–E–N angle (°)	83.9	83.6	83.9	99.9	99.8	99.9	86.7
Ln–E interaction energy	*b*	*b*	*b*	-555.2	-556.1	-620.6	-377.83
Pre-relaxation ("steric") energy	*b*	*b*	*b*	498.5	559.9	625.6	549.06
orbital energy	*b*	*b*	*b*	-688.9	-795.6	-873.5	-895.86
Δq (Ln–E(NArCH)) (Hirshfeld Charge Difference)	0.73	0.88	0.87	0.70	0.84	0.84	0.37
ρ (electron density)	0.044	0.039	0.044	0.058	0.051	0.057	0.077
$\nabla^2\rho$ (electron density Laplacian)	0.026	0.029	0.026	0.028	0.033	0.035	-0.044
H (energy density)	-0.010	-0.008	-0.012	-0.014	-0.012	-0.016	-0.033
Normalised Ln/E & Ge/Ga Mulliken contributions to the highest occupied localized orbital (HOLO) (%)	22/78	19/81	26/74	28/72	26/74	31/69	45/55
Delocalisation index	0.463	0.447	0.481	0.516	0.495	0.518	0.792

a. All energies in kJ mol^{-1}. AIM data (atomic units) obtained at the Ln–E or Ge–Ga bond critical point.
b. Values could not be obtained.

In order to further investigate this and to elucidate the electronically preferred geometric structure, model structures of **22C**–**24C**, Ln{MeC(NMe)$_2$}$_2${B(NXylCH)$_2$} (Ln = Sc (**22SC**), Y (**23SC**) or Lu (**24SC**), Figure 4.12), were calculated, with the cyclohexyl and trimethylsilyl groups on the amidinate being replaced with methyl groups, and the di-*iso*-propylphenyl groups on the boryl replaced with *ortho*-xylyl groups. Removal of these sterically demanding groups and geometry optimisation of the resultant structure lead to a less distorted SBP structure, where the Ln–N bond distances are now virtually equal.

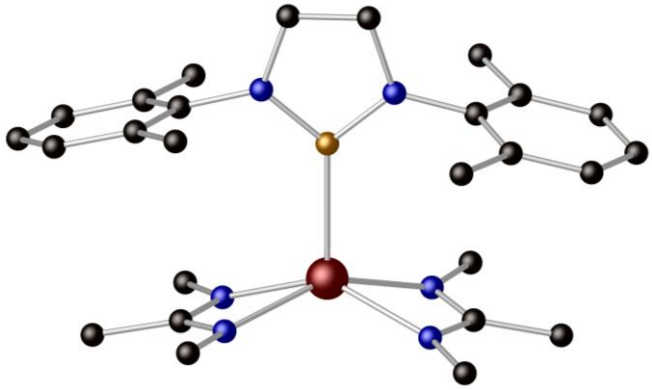

Figure 4.12. Ball and stick plot (arbitrary radius) of the calculated structure of Sc{MeC(NMe)$_2$}$_2${B(NXylCH)$_2$} (**22SC**). H atoms omitted for clarity.

The calculated compound **22SC** (Figure 4.12) has a self-consistent field (SCF) energy associated with its geometry optimised form. To elucidate the energy associated with the adoption of a TBP geometry, the ligands were fixed such that the ligands in the equatorial plane maintain B–Sc–N and N–Sc–N angles of 116 °, whilst the N–Sc–N axial angle is fixed at 148 ° to accommodate this. With these angles fixed, the structure was then optimised, and it was found that the TBP form is disfavoured by +16.5 kJ mol^{-1} relative to the SBP form. This might suggest that the electronically preferred geometry for five-coordinate rare earth metal boryl compounds is SBP. However, the constrained nature of the amidinate ligands may be imposing adoption of a SBP geometry. In order to eliminate both steric bulk and any ligand imposed constraints, another model system was calculated, Sc(H)$_2${B(NArCH)$_2$}(OMe$_2$)$_2$ (**1C$_H$**, Figure 4.13). This MX$_3$L$_2$ arrangement closely resembles that of the five-coordinate boryl compounds Ln(CH$_2$SiMe$_3$)$_2${B(NArCH)$_2$)}(THF)$_2$ (Ln = Lu (**3**), Gd (**2.57**) or Er (**2.58**)), reported earlier in this Thesis and by Hou and co-workers[19] (see Chapter 2), with the highlighted metals adopting SBP geometries. The di-*iso*-

propylphenyl groups of the boryl are replaced with *ortho*-xylyl groups, the alkyl groups with hydrides and THF with dimethyl ether.

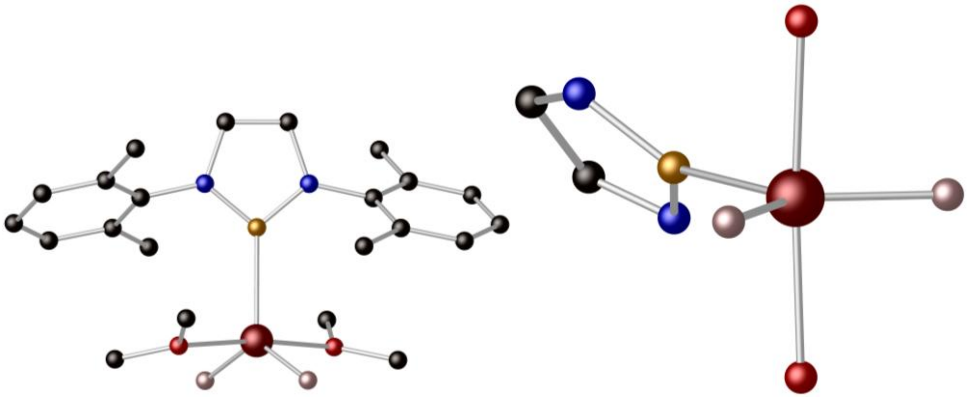

Figure 4.13. Ball and stick plots (arbitrary radius) of the calculated structure of $Sc(H)_2\{B(NArCH)_2\}(OMe_2)_2$, $\mathbf{1C_H}$. View on right, Ar and Me groups omitted for clarity.

After optimisation $\mathbf{1C_H}$ adopts a TBP geometry with both neutral ligands occupying the *trans* coordination sites, as expected for five-coordinate small to mid-size rare earth metal compounds of the type MX_3L_2. The O–Sc–O angle is 173.7 °, with both H–Sc–B (117 °) angles and the H–Sc–H (126 °) angle all close to ideal for TBP. With the results observed in the model systems **22SC** and $\mathbf{1C_H}$, the earlier suggestion can now be modified. It is more accurate to say that the electronically preferred geometry for five-coordinate rare earth metal boryl compounds featuring non-constrained ligands (such as **3**) is TBP, but due to steric considerations adopt SBP geometries. The electronically preferred geometry for five-coordinate rare earth metal boryl compounds featuring bis(amidinate) ligands is SBP, with some distortion of that geometry dependent upon the steric demands of the *N*- and *C*-bound substituents and the bite angle of the amidinate. These observations also preclude the notion that the strong *trans* influence of the boryl has a decisive effect on the geometry adopted by these systems.

4.5.1.2 Hypothetical Six-coordinate Ln–B Structures

The boryl compounds **22**–**24** are isolated as five-coordinate, THF-free compounds. In an effort to elucidate the underlying reasons for this, and to provide a more direct comparison with the gallyl compound, $Sc\{(Me_3SiCH_2)C(NCy)_2\}_2\{Ga(NArCH)_2\}(THF)$ (**14**), hypothetical six-coordinate versions of **22C**–**24C** featuring an extra molecule of coordinated THF, $Ln\{(Me_3SiCH_2)C(NCy)_2\}_2\{B(NArCH)_2\}(THF)$ (Ln = Sc (**22C$_{THF}$**), Y (**23C$_{THF}$**) and Lu (**24C$_{THF}$**)), were calculated, with selected results presented in Table 4.8. The geometry optimised structures of **22C$_{THF}$**–**24C$_{THF}$** (*e.g.* **22C$_{THF}$**, Figure 4.14) resemble those of the calculated structures of **14C**–**16C**, forming six-coordinate distorted octahedral structures. The increase in coordination number from five in **22C**–**24C** to six in **22C$_{THF}$**–**24C$_{THF}$** is reflected in longer Ln–B bond distances for all three metals in **22C$_{THF}$**–**24C$_{THF}$**, with the Ln–B bond distances for **22C$_{THF}$**–**24C$_{THF}$** being *ca.* 0.1 Å longer than for those found in **22C**–**24C**. Of note is a slight decrease (*ca.* 1 °) of the N–B–N angle in **22C$_{THF}$**–**24C$_{THF}$**, indicating a slightly more ionic Ln–B interaction for all three rare earth metal-boryl bonds. The amidinate ligands occupy three equatorial sites and one axial site, with the four amidinate nitrogens arranged such that one amidinate nitrogen is found *trans* to THF, one is found *trans* to the boryl ligand, and the remaining two *trans* to each other. One of the more striking structural features of the scandium gallyl compound **14** are the bond distances that are affected by a small, but significant *trans* influence. This unusual detail was also observed in the geometry optimised calculated structure **14C** (see Chapter 3 for complete discussion). This provides confidence that any unusual structural features found in **22C$_{THF}$**–**24C$_{THF}$** would also be observed, if isolable, in an experimentally derived structure.

Table 4.8. Selected DFT computational results for Ln{$(Me_3SiCH_2)C(NCy)_2$}$_2${$E(NArCH)_2$}(THF) (Ln = Sc, E= Ga (**14C**) or B (**22C$_{THF}$**); Y, E= Ga (**15C**) or B (**23C$_{THF}$**); Lu, E= Ga (**16C**) or B (**24C$_{THF}$**)).[a]

	14C	**15C**	**16C**	**22C$_{THF}$**	**23C$_{THF}$**	**24C$_{THF}$**
r(Ln–E) (Å)	2.886	3.036	2.974	2.589	2.745	2.672
Ln–N *trans* to THF (Å)	2.153	2.311	2.268	2.171	2.335	2.292
Ln–N *trans* to E (Å)	2.189	2.340	2.296	2.281	2.434	2.388
Ln–N *trans* to N (mean (Å))	2.201	2.365	2.322	2.239	2.386	2.345
N–E–N angle (°)	82.8	82.8	83.0	99.1	99.1	99.4
Ln–E interaction energy	-479.7	-492.1	-505.2	-552.4	-554.6	-574.4
Pre-relaxation (“steric”) energy	332.2	421.0	487.8	450.9	534.9	634.4
orbital energy	-688.9	-795.6	-873.5	-865.9	-963.8	-1077.7
Δq (Ln–E(NArCH)) (Hirshfeld Charge Difference)	1.27	1.42	1.42	1.23	1.38	1.37
ρ (electron density)	0.033	0.030	0.034	0.048	0.043	0.048
$\nabla^2\rho$ (electron density Laplacian)	0.027	0.031	0.028	0.026	0.034	0.037
H (energy density)	-0.006	-0.005	-0.007	-0.010	-0.008	-0.012
Normalised Ln/E Mulliken contributions to the highest occupied localised orbital (HOLO) (%)	19/81	11/89	19/81	26/74	23/77	28/72
Delocalisation Index	0.334	0.326	0.345	0.440	0.411	0.432

a. All energies in kJ mol^{-1}. AIM data (atomic units) obtained at the Ln–E bond critical point.

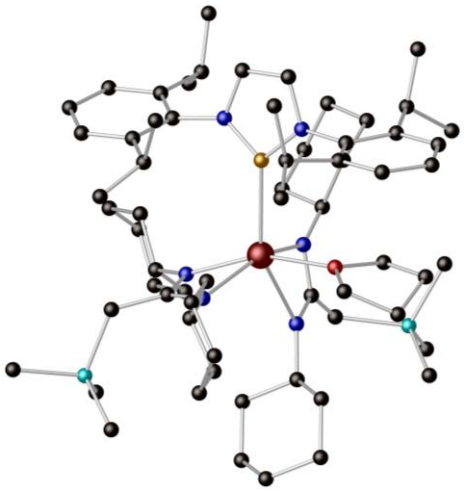

Figure 4.14. Ball and stick plot (arbitrary radius) of the calculated structure of $Sc\{Me_3SiCH_2)C(NCy)_2\}_2\{B(NArCH)_2\}(THF)$ (**22C$_{THF}$**). H atoms omitted for clarity.

Indeed, a *trans* influence is observed affecting bond distances in the structures of **22C$_{THF}$**–**24C$_{THF}$**, with the Ln–N bond *trans* to THF up to 0.08 Å shorter than the Ln–N bonds *trans* to an amidinate nitrogen. More interestingly, whereas the Sc–N bond *trans* to the gallyl ligand in **14C** was found to be shorter than the Sc–N bonds *trans* to an amidinate nitrogen (see Table 3.3, page 94), in the case of **22C$_{THF}$** the Sc–N bond *trans* to the boryl is longer than that of the Sc–N bonds *trans* to an amidinate nitrogen. This confirms the strength of the boryl *trans* influence, and that it exceeds that of the corresponding gallyl and that of the amidinate, a conclusion that is in line with that found in literature.[27] This result is replicated for **23C$_{THF}$** and **24C$_{THF}$**, where the Ln–N bond *trans* to the boryl is *ca.* 0.04 Å longer than the Ln–N bonds *trans* to nitrogen.

As mentioned, the Ln–B bond distances in **22C**–**24C** increase by *ca.* 0.1 Å upon coordination of THF to produce **22C$_{THF}$**–**24C$_{THF}$**. The scandium (2.589 Å), yttrium (2.745 Å) and lutetium (2.672 Å) bond distances come above (Sc = 2.54(10) Å), at (Y = 2.74(10) Å) or just below (Lu = 2.71(11) Å) the sum of their respective covalent radii. All of the Ln–B bond distances for the compounds featuring this bond described in this Thesis, and those reported by Hou and co-workers, come comfortably under the sum of their respective covalent radii. The Ln–Ga bond distance in **14** is different, with the larger, less nucleophilic gallyl anion forming a bond with the rare earth metal that exceeds the sum of their respective covalent radii (see Chapter 3) and yet are still isolable, a trend replicated in the literature for early transition, rare earth and alkaline

earth metal gallyl compounds.[28] The boryl anion also forms a more covalent bond than the gallyl anion, as evidenced by larger N–E–N angles (see Bent's rule discussion, page 89) and increased metal contributions to the Ln–E bond when E = B (see Chapter 2, Table 2.4) compared to E = Ga (see Chapter 3, Table 3.3). Taking into account the precedent set by those reported boryl compounds, the Ln–B bond distances in **22C$_{THF}$**–**24C$_{THF}$** can be considered outliers. Addition of THF may have a destabilising effect on the compound by forcing the Ln–B bond to lengthen, which would be more unfavourable than for the Ln–Ga bond (see section 4.5.4 *vide infra*).

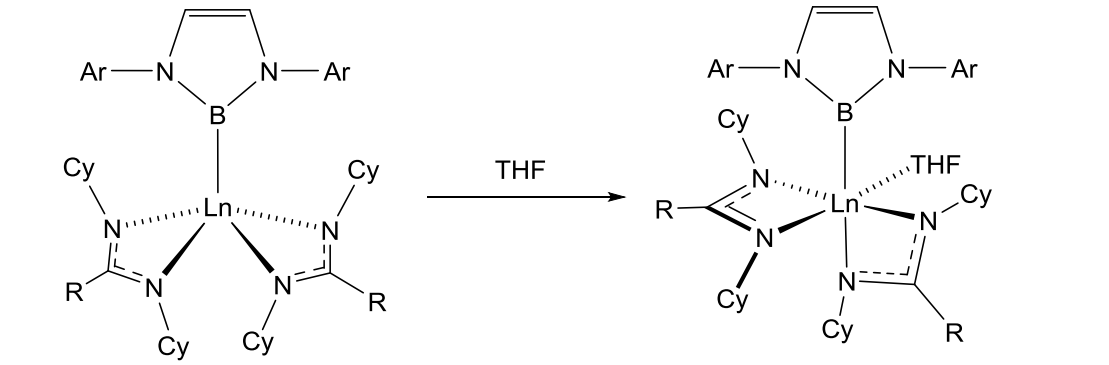

Ln = Sc (**22C**), Y (**23C**) or Lu (**24C**)

Ln = Sc (**22C$_{THF}$**), Y (**23C$_{THF}$**) or Lu (**24C$_{THF}$**)

R = CH_2SiMe_3

Equation 4.3

To help quantify this, a study was initiated to assess computationally the reaction of THF and **22C**–**24C** to form the hypothetical compounds **22C$_{THF}$**–**24C$_{THF}$** (Equation 4.3), with the results summarised in Table 4.9. In all cases, the calculated $\Delta_r H$ values indicate that formation of **22C$_{THF}$**–**24C$_{THF}$** is favourable, with coordination of THF becoming more favourable as the size of the metal covalent radius increases. However, the $T\Delta_r S$ values are significant, and result in positive values for $\Delta_r G$ to make the addition of THF in all cases unfavourable, with the formation of **22C$_{THF}$**–**24C$_{THF}$** becoming more unfavourable as the size of the metal covalent radius decreases. The results of this study are in agreement with the observed structural features in **22C$_{THF}$**–**24C$_{THF}$** and the experimental findings described in section 4.4.3.2, that **22C$_{THF}$**–**24C$_{THF}$** are not isolable compounds.

Table 4.9. Calculated values for the reaction of THF and **22C**–**24C**.[a]

Ln	$\Delta_r H$	$T\Delta_r S$ [b]	$\Delta_r G$
Sc (**22C$_{THF}$**)	-16.00	-42.28	26.27
Y (**23C$_{THF}$**)	-44.62	-56.33	11.72
Lu (**24C$_{THF}$**)	-34.73	-49.64	14.91

a. All values in kJ mol^{-1}; *b*. T = 298.15 K

Structural analysis of the hypothetical compounds **22C$_{THF}$**–**24C$_{THF}$** has provided an insight into how the boryl ligand affects the structure of the bis(amidinate) framework in a six-coordinate system, and has allowed easy comparison with the calculated models of the isolable six-coordinate gallyl systems **14C**–**16C**. Certain structural features, such as bond distances affected by *trans* influence, are similar, but the individual properties of the boryl and gallyl ligands, such as difference in strength of *trans* influence and trends in Ln–E bond distance, can still be identified.

4.5.1.3 Hypothetical Five-coordinate Ln–Ga Structures

Thus far, the computational study has provided insight into six-coordinate rare earth metal boryl and gallyl systems. The same insight was required for five-coordinate rare earth metal boryl and gallyl systems, and so would require computational studies on hypothetical THF-free versions of **14C**–**16C**, Ln{Me_3SiCH_2)C($NCy)_2$}$_2${$Ga(NArCH)_2$} (Ln = Sc (**14C$_{–THF}$**), Y (**15C$_{–THF}$**) or Lu (**16C$_{–THF}$**)), so as to facilitate a comparison with the isolable five-coordinate Ln–B compounds **22C**–**24C**.

The calculated, geometry optimised structures of **14C$_{–THF}$**–**16C$_{–THF}$** (*e.g.* **14C$_{–THF}$**, Figure 4.15) resemble those of the calculated structures of **22**–**24**, **22C**–**24C**, forming five-coordinate distorted SBP structures, with the amidinate ligands forming the base of the pyramid and the gallyl coordinated in the apical position.

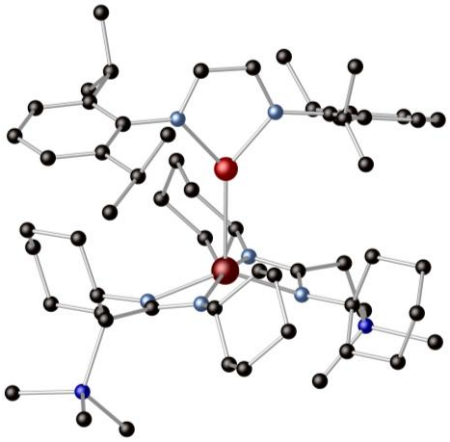

Figure 4.15. Ball and stick plot (arbitrary radius) of the calculated structure of $Sc\{Me_3SiCH_2)C(NCy)_2\}_2\{Ga(NArCH)_2\}$ (**14C$_{-THF}$**). H atoms omitted for clarity.

The calculated structures **14C$_{-THF}$**–**16C$_{-THF}$** match the trends observed in the computationally derived molecular structures of **22C**–**24C** with regards to the amidinate ligands. The two Ln–N bond distances found on the same amidinate ligand do not match, with one being *ca.* 0.04 Å longer than the other in all cases (*cf.* 0.07 Å for **22C**–**24C)**. The C–N bond distances for the amidinate are virtually equal for **14C$_{-THF}$**–**16C$_{-THF}$**, indicating that the π-electrons are delocalised evenly across the N–C–N backbone. This compares well with the observed bond distances in the N–C–N backbone for **22C**–**24C**, suggesting that steric effects are again the source of the difference in bond lengths.

However, whilst the decrease in coordination number from six in **14C**–**16C** to five in **14C$_{-THF}$**–**16C$_{-THF}$** is reflected in shorter Ln–Ga bond distances for all three metals in **14C$_{-THF}$**–**16C$_{-THF}$** (*ca.* 0.15 Å shorter than for those found in **14C**–**16C**), the larger, less nucleophilic gallyl forms a longer Ln–E bond than its boryl counterpart in **22C**–**24C**. This longer bond opens up the coordination sphere around the metal, providing more room for the bulky amidinate ligands to coordinate in such a way as to equalise the Ln–N bond distances, and results in a smaller difference in bond distances for the amidinate ligands in **14C$_{-THF}$**–**16C$_{-THF}$** compared to **22C**–**24C**. The aforementioned shortening of the Ln–Ga bond in **14C$_{-THF}$**–**16C$_{-THF}$** is accompanied by a small increase (*ca.* 1 °) of the N–Ga–N angle, indicating a slightly more covalent Ln–Ga interaction for all three rare earth metal-gallyl bonds. There is a pleasing symmetry in this observation, as it is almost exactly the opposite observed for the

changes in Ln–B bond distance and N–B–N angle in **22C$_{THF}$**–**24C$_{THF}$**. As mentioned in section 4.5.1.2, the hypothetical six-coordinate boryl compounds are not isolable species due in part to this resulting in an unfavourable lengthening of the Ln–B bond. The hypothetical five-coordinate gallyl compounds are also not isolable species, but in their case the larger, less nucleophilic gallyl cannot form an Ln–Ga bond that is short enough to form a stable five-coordinate compound.

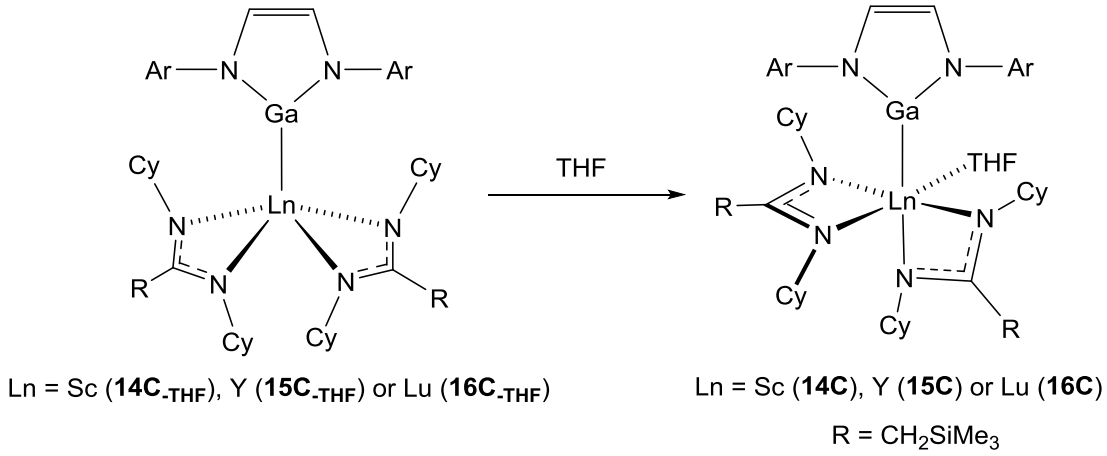

Ln = Sc (**14C$_{-THF}$**), Y (**15C$_{-THF}$**) or Lu (**16C$_{-THF}$**)

Ln = Sc (**14C**), Y (**15C**) or Lu (**16C**)

R = CH_2SiMe_3

Equation 4.4

The addition of THF to the boryl analogues **22C**–**24C** to form the hypothetical compounds **22C$_{THF}$**–**24C$_{THF}$** was probed computationally and revealed that in spite of favourable $\Delta_r H$ values, the large $T\Delta_r S$ values made the THF addition reaction unfavourable (Table 4.9). The same computational assessment of that reaction for the gallyl systems (Equation 4.4) could provide an insight into why **14C$_{–THF}$**–**16C$_{–THF}$** are not isolable, even with the reaction and work-up being performed in the absence of THF.

The results of the computational assessment of the reaction of THF and **14C$_{–THF}$**–**16C$_{–THF}$** are presented in Table 4.10. As with the boryl examples, in all cases the calculated $\Delta_r H$ values indicate that formation of **14C**–**16C** is favourable, with coordination of THF becoming more favourable as the size of the metal covalent radius increases. In addition, the $\Delta_r H$ values for the gallyl examples are 2–5 times larger than those of the corresponding boryl examples, whilst the $T\Delta_r S$ values remain roughly the same, indicating little difference in reaction entropy change going from the boryl systems to the gallyl systems. This large difference in the $\Delta_r H$ values leads to favourable $\Delta_r G$ values, making the addition of THF in all cases favourable, with the

formation of **14C**–**16C** becoming more favourable as the size of the metal covalent radius increases. The results of this study are in agreement with the experimental findings described in section 3.4.1 (Chapter 3, page 84), where **14**–**16** are isolable compounds.

Table 4.10. Calculated values for the reaction of THF and $\mathbf{14C_{–THF}}$–$\mathbf{16C_{–THF}}$.[a]

Ln	$\Delta_r H$	$T\Delta_r S$ [b]	$\Delta_r G$
Sc (**14C**)	-87.18	-41.39	-45.78
Y (**15C**)	-104.69	-44.87	-59.81
Lu (**16C**)	-103.30	-50.97	-52.33

a. All values in kJ mol^{-1}; *b*. T = 298.15 K

4.5.1.4 Summary

The geometry optimised structures of five and six-coordinate boryl and gallyl compounds featuring bis(amidinate) supporting ligand sets have been discussed. Hypothetical five-coordinate gallyl ($\mathbf{14C_{–THF}}$–$\mathbf{16C_{–THF}}$) and six-coordinate boryl ($\mathbf{22C_{THF}}$–$\mathbf{24C_{THF}}$) systems were calculated to facilitate comparisons with the isolable five-coordinate boryl (**22C**–**24C**) and six-coordinate gallyl (**14C**–**16C**) systems. The higher coordination number for the gallyl systems results in a more ionic Ln–Ga interaction, whilst the lower coordination number for the boryl systems results in a more covalent Ln–B interaction. The THF addition reactions to produce the hypothetical six-coordinate boryl and isolable six-coordinate gallyl compounds were computationally assessed. It was found that the $\Delta_r H$ values for the both the boryl and gallyl systems suggested a favourable reaction, but while the $T\Delta_r S$ values disfavour the reaction for the boryl systems, the significantly larger $\Delta_r H$ values favour the reaction for the gallyl systems by overcoming the $T\Delta_r S$ values.

4.5.2 Ln–E Electronic Structures

4.5.2.1 Comparison of Six-coordinate Ln–B and Ln–Ga

The electronic structure of the six-coordinate gallyl compounds **14C**–**16C** were discussed in detail in Chapter 3. Here, the electronic structure of the hypothetical six-

coordinate boryl compounds **22C$_{THF}$**–**24C$_{THF}$** will be presented and compared to **14C**–**16C**.

The Hirshfeld charge differences between the metals and the boryl fragment Δ*q*(Ln–Boryl) in **22C$_{THF}$**–**24C$_{THF}$** were calculated and the results presented in Table 4.8 (p. 129). In all cases, the charge differences are large, indicating that all of the Ln–B bonds are predominantly ionic. The charge differences are slightly lower than those found for **14C**–**16C**, as expected for the less ionic Ln–B interaction. The scandium example, **22C$_{THF}$**, possesses the smallest charge difference, continuing the trend observed that the scandium-element bond is the least ionic of the three rare earth metal-element bonds. Compounds **23C$_{THF}$** and **24C$_{THF}$** have significantly larger charge differences than **22C$_{THF}$**, as observed for the other reported Y–E and Lu–E bonds. To probe the nature of the bonding in **22C$_{THF}$**–**24C$_{THF}$**, the canonical Kohn-Sham molecular orbitals were analysed. However, as with **14C**–**16C**, this method could not clearly identify the Ln–B σ-bonding orbital due to significant delocalization, and so the Boys-Foster localized orbitals (LO), which are found by unitary transformations of the canonical functions in order to minimize the spatial extent of the resultant orbitals, were calculated. With this method, the Ln–B bonding orbital was identified as the highest occupied localized orbital (HOLO), as visualised in Figure 4.16 for **22C$_{THF}$**, and is a predominantly σ-orbital.

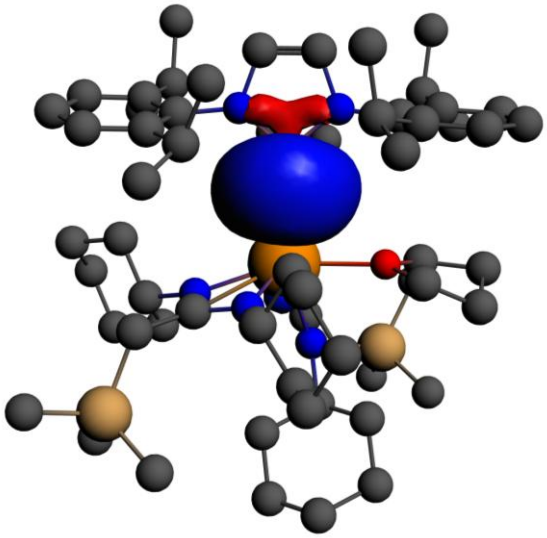

Figure 4.16. Three-dimensional representation of the HOLO of the calculated structure of Sc{Me$_3$SiCH$_2$)C(NCy)$_2$}$_2${B(NArCH)$_2$}(THF) (**22C$_{THF}$**). H atoms omitted for clarity.

The normalised contributions to the σ-bonding HOLO were calculated, with the results shown in Table 4.8. As with all Ln–E examples, the boryl anion is found to be the major contributor in all cases, indicating predominantly ionic bonds, but the boryl anion contributes less to the Ln–E bond than the corresponding gallyl. The Lu–B HOLO showed the largest degree of mixing between the two atoms, followed closely by the Sc–B HOLO, whilst the Y–B HOLO showed the lowest degree of mixing. This compares favourably with the relative degrees of mixing seen in the HOLOs of **14C**–**16C**, where Y < Sc = Lu. Taking into account the conclusion reached with the Hirshfeld charge difference analysis, the Sc–B bond can be considered the least ionic of the three, whilst the Y–B bond is the most ionic. Atoms-in-Molecules (AIM) analysis was carried out and generated values for the electron density (ρ), the energy density (H) and the electron density Laplacian ($\nabla^2\rho$) at the Ln–B bond critical point for **22C$_{THF}$**–**24C$_{THF}$**. The small values for ρ and H, coupled with the small, positive $\nabla^2\rho$ reinforce the conclusions reached from analysis of the Hirshfeld charge differences and the Boys-Foster Localized orbitals, that the Ln–B bond is predominantly ionic. The Lu–B bond has marginally the largest H value, whilst the Sc–B bond has marginally the largest ρ value, whereas for the gallyl examples **14C**–**16C** the Lu–Ga bond had marginally larger values for both. Overall, these small margins, as well as the marginal difference observed for the degree of mixing in the Sc–B and Lu–B HOLOs suggest that these are equally the least ionic of the three Ln–B bonds. In contrast, the AIM, HOLO composition and Hirshfeld data are in agreement in suggesting that the Y–B bond is the most ionic, as observed for the Y–B bond for **2C** and the Y–Ga bond of **15C**.

4.5.2.2 Comparison of Five-coordinate Ln–B and Ln–Ga

The Hirshfeld charge differences between the metals and the gallyl fragment Δq(Ln–Boryl) were calculated and the results presented in Table 4.7 (p. 126). In all cases, the charge differences were large, indicating that all of the Ln–B bonds are predominantly ionic. Compound **22C** possesses the smallest charge difference, indicating that the Sc–B bond is the least ionic of the three rare earth metal-boron bonds, whilst **23C** and **24C** had significantly larger charge differences. To further probe the nature of the bonding, another attempt was made to analyse the canonical

Kohn-Sham molecular orbitals, but significant delocalization again obscured any information about the Ln-B σ-bond, and so the Boys-Foster localized orbitals (LO) were again calculated. With this method, the Ln–B bonding orbital was identified as the highest occupied localized orbital (HOLO), as visualised in Figure 4.17 for **22C**, and is a predominantly σ-orbital.

The normalised contributions to the σ-bonding HOLO were calculated, with the results shown in Table 4.7. In all cases, the boryl anion is found to be the major contributor, indicating predominantly ionic bonds. The Lu–B HOLO showed the largest degree of mixing between the two atoms, followed by the Sc–B HOLO, whilst the Y–B HOLO showed the lowest degree of mixing. Taking into account the conclusion reached with the Hirshfeld charge difference analysis, the Sc–B bond can be considered the least ionic of the three, whilst the Y–B bond is the most ionic.

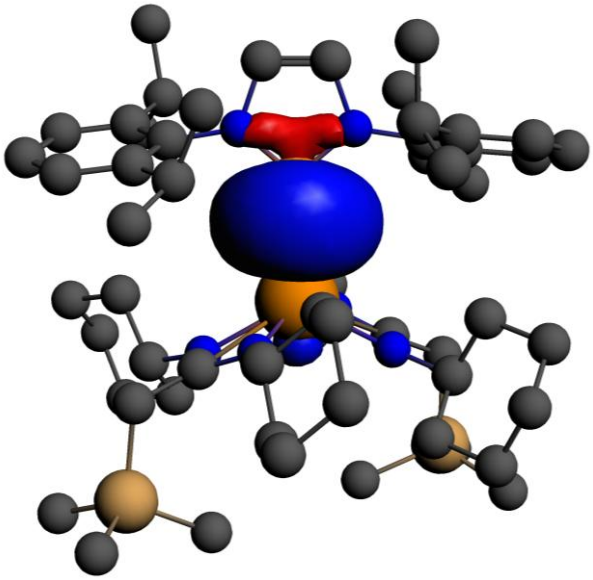

Figure 4.17. Three-dimensional representation of the HOLO of the calculated structure of $Sc\{Me_3SiCH_2)C(NCy)_2\}_2\{B(NArCH)_2\}$ (**22C**). H atoms omitted for clarity.

AIM analysis was carried out and generated values for the electron density (ρ), the energy density (H) and the electron density Laplacian ($\nabla^2\rho$) at the Ln–B bond critical point. The small values for ρ and H, coupled with the small, positive $\nabla^2\rho$ reinforce the conclusions reached from analysis of the Hirshfeld charge differences and the Boys-Foster localized orbitals, that the Ln–B bond is predominantly ionic. The Lu–B bond

has marginally the largest *H* value, whilst the Sc–B bond has marginally the largest ρ value. Overall, these small margins, as well as the marginal difference observed for the degree of mixing in the Sc–B and Lu–B HOLOs suggest that these are equally the least ionic of the three Ln–B bonds. In contrast, the AIM, HOLO composition and Hirshfeld data are in agreement in suggesting that the Y–B bond is the most ionic, as observed for the Y–B bond for **2C** and **23C$_{THF}$**, and the Y–Ga bond of **15C**.

The Hirshfeld charge differences between the metals and the gallyl fragment Δq(Ln–Gallyl) in **14C$_{-THF}$**–**16C$_{-THF}$** were calculated and the results presented in Table 4.7. As expected, the charge differences were large in all cases, indicating that all of the Ln–Ga bonds are predominantly ionic. The charge differences are slightly greater than those found for **22C**–**24C**, as seen for the six-coordinate Ln–E interactions. The scandium example, **14C$_{-THF}$**, possesses the smallest charge difference, with **15C$_{-THF}$** and **16C$_{-THF}$** having significantly larger charge differences than **14C$_{-THF}$**, as observed for the other reported Ln–E bonds. To probe the nature of the bonding in **14C$_{-THF}$**–**16C$_{-THF}$**, the Boys-Foster localized orbitals (LO) were calculated. With this method, the Ln–Ga bonding orbital was identified as the highest occupied localized orbital (HOLO), as visualised in Figure 4.18 for **14C$_{-THF}$**, and is a predominantly σ-orbital.

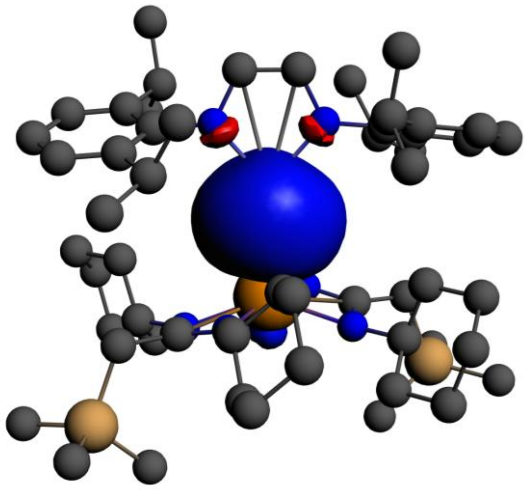

Figure 4.18. Three-dimensional representation of the HOLO of the calculated structure of Sc{Me_3SiCH_2)C$(NCy)_2$}$_2${$Ga(NArCH)_2$} (**14C$_{-THF}$**). H atoms omitted for clarity.

The normalised contributions to the σ-bonding HOLO were calculated, with the results shown in Table 4.7. As with all Ln–E examples, the gallyl anion is found to be the major contributor in all cases, indicating predominantly ionic bonds. The gallyl anion contribution to the Ln–E bond is greater than the corresponding boryl, continuing the observed trend. The Lu–Ga HOLO showed the largest degree of mixing between the two atoms, followed by the Sc–Ga HOLO, whilst the Y–Ga HOLO showed the lowest degree of mixing. This compares well with the relative degrees of mixing seen in the HOLOs of **22C**–**24C**, where Y < Sc < Lu. Taking into account the conclusion reached with the Hirshfeld charge difference analysis, the Sc–Ga bond can be considered the least ionic of the three, whilst the Y–Ga bond is the most ionic. AIM analysis was carried out and generated values for the electron density (ρ), the energy density (H) and the electron density Laplacian ($\nabla^2\rho$) at the Ln–Ga bond critical point for **14C$_{-THF}$**–**16C$_{-THF}$**. The small values for ρ and H, coupled with the small, positive $\nabla^2\rho$ reinforce the conclusions reached from analysis of the Hirshfeld charge differences and the Boys-Foster localized orbitals, that the Ln–Ga bond is predominantly ionic. The Lu–Ga bond has marginally the largest H and ρ values, whereas for the boryl examples **22C**–**24C** the Lu–B bond had marginally larger values for H only. This suggests that, according to the HOLO data, the Lu–Ga bond is the least ionic of the three Ln–Ga bonds, which disagrees with the Hirshfeld Δq data. In contrast, the AIM, HOLO composition and Hirshfeld data are in agreement in suggesting that the Y–Ga bond is the most ionic, as observed for the Y–B bond for **2C** and **23C**.

In general, increasing the coordination number of bis(amidinate) Ln–E compounds from five to six leads to more ionic Ln–E interactions for both boryl and gallyl examples, with significant increases in Hirshfeld charge differences, and lower degrees of mixing in the HOLOs. Whilst there is a difference in the degree of mixing in the HOLO between five-coordinate Sc–Ga and Lu–Ga, upon increase in coordination number that difference disappears, with the degree of mixing in the HOLO now equal for both scandium and lutetium. For the boryl examples, the degree of mixing is always greatest for lutetium. The AIM data at the Ln–E bond critical point for both the five and six-coordinate gallyl examples produce values for the energy density (H) and the electron density (ρ) that suggest that the Lu–Ga bond is

the least ionic, whereas the AIM data for the five and six-coordinate boryl examples are less clear, with values for *H* indicating Lu–B as least ionic and the values for ρ suggesting Sc–B. However, the AIM data suggest that the yttrium examples for both five and six-coordinate bis(amidinate) boryl and gallyl examples are the most ionic in all cases. The AIM calculations also produce a value for the delocalisation index, which is a measure of the bond order in the Ln–E interaction. The more ionic Ln–Ga interactions produce smaller values than the more covalent Ln–B interaction.

4.5.2.3 Ln–E Bond Ionicity

It has been established that the Ln–E interaction is predominantly ionic in character. In order to provide context to the nature of the Ln–E bond, calculations on a system that would be expected to produce a less ionic (or more covalent) M–E (M = metal) interaction was sought. Therefore, DFT computational studies were carried out on the model compound, $GeMe_3\{Ga(NArCH)_2\}$ (**Ge–Ga**, Figure 4.19), and the results of these calculations are presented in Table 4.7.

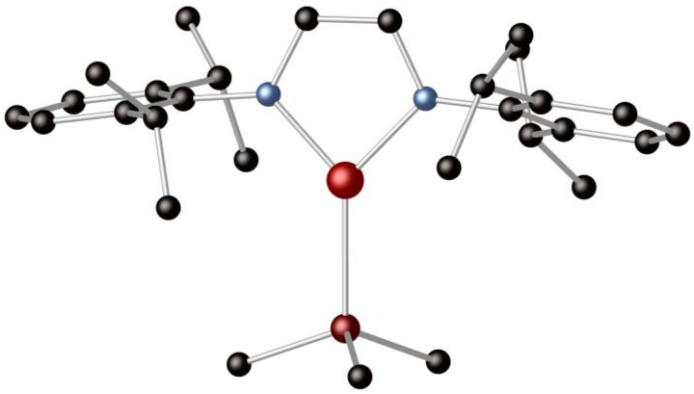

Figure 4.19. Ball and stick plot (arbitrary radius) of the calculated structure of $GeMe_3\{Ga(NArCH)_2\}$ (**Ge–Ga**). H atoms omitted for clarity.

As previously discussed, certain structural features of the main group heterocycle can provide information as to the nature of the M–E bond. For **Ge–Ga**, the N–Ga–N angle of the heterocycle is found to be 86.7 °, considerably more obtuse than the corresponding angle for **14C**–**16C** (82.8 ° (mean)) and indicates a less ionic (or more covalent) M–E interaction for **Ge–Ga** than for **14C**–**16C**. The calculated M–E bond distance in **Ge–Ga** (2.416 Å) is shorter than those calculated for both the five-

coordinate (**14C$_{-THF}$**, 2.726 Å) and six-coordinate (**14C**, 2.886 Å) scandium gallyl compounds, but compares favourably with the M–E bond distance in the four-coordinate scandium boryl compound, $Sc(CH_2SiMe_3)_2\{B(NArCH)_2\}(THF)$ (**1C**), which has a calculated bond distance of 2.458 Å.

For comparison of electronic structures with the compounds discussed in this Chapter and Chapter 3, the Boys-Foster localized orbitals (LO) for **Ge–Ga** were calculated, and identified the M–E bond of **Ge–Ga** as the highest occupied localized orbital (HOLO). The degree of mixing in the M–E HOLO is significantly higher for **Ge–Ga** than for those found for **14C**–**16C**, with the non-gallium metal contribution rising sharply from 19 % in **14C**, to 45 % for **Ge–Ga**. This result is in agreement with the structurally observed evidence for a less ionic M–E bond, and demonstrates the utility of studying changes in the structure of the main group heterocycle to gain information on the ionicity (or covalency) of the M–E bond. The greater covalency of the Ge–Ga interaction is also reflected in a much larger value for the delocalisation index than that found for the more ionic Ln–E interaction (0.792 *vs.* (*e.g.*) 0.334 for **14C**).

4.5.2.4 Ln–E Bond Energy

The bond dissociation energy (BDE) of the Ln–E bond was calculated for **22C**–**24C**, **22C$_{THF}$**–**24C$_{THF}$** and **14C**–**16C**, with the results presented in Table 4.11. The results show that the Ln–Ga bond has a lower BDE than that of the Ln–B bond, which correlates with the interaction energies obtained for these compounds (see Tables 4.7 and 4.8). Upon change in coordination number for the boryl examples from five (**22C**–**24C**) to six (**22C$_{THF}$**–**24C$_{THF}$**), the lengthening of the Ln-B bond results in a lower BDE for the **22C$_{THF}$**–**24C$_{THF}$**.

Table 4.11. Bond dissociation energies (BDEs) for **22C**–**24C**, **22C$_{THF}$**–**24C$_{THF}$** and **14C**–**16C**.[a]

Ln	Bond	BDE
Sc (**22C**)	Sc–B	499.5
Y (**23C**)	Y–B	513.4
Lu (**24C**)	Lu–B	536.0
Sc (**22C$_{THF}$**)	Sc–B	433.2
Y (**23C$_{THF}$**)	Y–B	477.1
Lu (**24C$_{THF}$**)	Lu–B	487.3
Sc (**14C**)	Sc–Ga	411.0
Y (**15C**)	Y–Ga	432.0
Lu (**16C**)	Lu–Ga	442.2

a. All values in kJ mol^{-1}

4.5.3 E–N Bonding

Thus far, the geometry optimised structures of five and six-coordinate compounds containing Ln–E bonds and the composition of those bonds have been discussed, and related to changes observed in the main group heterocycle. A discussion of the composition of the E–N bonds, which are critical to the structural features observed in the heterocycle, follows.

Section 4.5.2 discussed the calculation of the Boys-Foster localized orbitals (LO) for **14C$_{-THF}$**–**16C$_{-THF}$**, whilst the LOs of **14C**–**16C** were calculated in Chapter 3 (see p. 94). In addition to identifying the Ln–Ga HOLO, four gallyl-based LOs were identified for each of the compounds in **14C$_{-THF}$**–**16C$_{-THF}$** and **14C**–**16C**. The *s* and *p*-orbital contributions to the Ga–N bond are of interest, as it is their relative contributions that dictate the structural features of the heterocycle. To compare how the orbital composition of the Ga–N bond relates to the orbital composition of the Ln–Ga bonds, and how this composition changes upon increasing the coordination number, the *s* and *p*-orbital contributions to the Ln–Ga bond were also determined.

Table 4.12 presents the results of the calculations for **14C$_{-THF}$**–**16C$_{-THF}$** and **14C**–**16C**. It was observed structurally that increasing the coordination number from five (**14C$_{-THF}$**–**16C$_{-THF}$**) to six (**14C**–**16C**) results in longer Ga–N bonds and a more acute N–Ga–N angle. The normalised gallium-centred *s* and *p* contributions to the Ga–N bond can provide further information. For example, the gallium in the Ga–N bonds in **14C$_{-THF}$** contributes 26.1% *s*-character, whilst the same atom in the Ga–N bonds in **14C** contributes 22.2 % *s*-character. This decrease leads to the lengthening of the Ga–N bonds observed in **14C**–**16C**.

The Boys-Foster LO calculations were also carried out on the germanium system, $GeMe_3\{Ga(NArCH)_2\}$ (**Ge–Ga**), with the results of the calculations presented in Table 4.12. The more covalent Ge–Ga bond (see section 4.5.2.3) has a gallyl heterocycle with shorter Ga–N bonds and a more obtuse N–Ga–N angle than those found for both five coordinate (**14C$_{-THF}$**–**16C$_{-THF}$**) and six coordinate (**14C**–**16C**) rare earth metal gallyl compounds. It was expected that the gallium-centred *s*-contribution to the Ga–N bonds would be larger than with the rare earth examples. Indeed, the gallium contribution in the Ga–N bonds of the heterocycle in **Ge–Ga** was found to be 31 % *s*-character, a 5–12 % increase in *s*-character compared to the gallium contribution in the rare earth metal gallyl compounds.

Finally, the Boys-Foster LO calculations were then extended to the boryl heterocycles in **22C**–**24C** and **22C$_{THF}$**–**24C$_{THF}$**, with the results of the calculations presented in Table 4.13. Four boryl-based LOs were identified for each of the compounds in **22C**–**24C** and **22C$_{THF}$**–**24C$_{THF}$**. The boron *s*-contribution in the B–N bond is larger than that of the corresponding gallyl, with the smaller boron atom producing shorter E–N bonds that produce a more obtuse N–E–N angle. It was observed structurally that increasing the coordination number from five (**22C**–**24C**) to six (**22C$_{THF}$**–**24C$_{THF}$**) results in longer B–N bonds and a more acute N–B–N angle. The normalised boron-centred *s* and *p* contributions to the B–N bond can provide further information. For example, the boron in the B–N bonds in **22C** contributes 28.0 % *s*-character, whilst the same atom in the B–N bonds of **22C$_{THF}$** contributes 26.7 % *s*-character. This decrease leads to the lengthening of the B–N bonds observed in **22C$_{THF}$**–**24C$_{THF}$**.

Table 4.12. Selected DFT computational results for Ln{$(Me_3SiCH_2)C(NCy)_2$}$_2${$Ga(NArCH)_2$}$(THF)_n$ (Ln = Sc, n = 0 (**14C$_{–THF}$**), n = 1 (**14C**); Y, n = 0 (**15C$_{–THF}$**), n = 1 (**15C**); Lu, n = 0 (**16C$_{–THF}$**), n = 1 (**16C**) and $GeMe_3${$Ga(NArCH)_2$} (**Ge–Ga**).

	14C$_{–THF}$	**15C$_{–THF}$**	**16C$_{–THF}$**	**14C**	**15C**	**16C**	**Ge–Ga**
r(M–Ga) (Å)	2.726	2.890	2.825	2.886	3.036	2.974	2.416
r(Ga–N) (mean (Å))	1.935	1.929	1.926	1.979	1.968	1.968	1.881
N–Ga–N angle (°)	83.9	83.6	83.9	82.8	82.8	82.9	86.7
Normalised M/Ga Mulliken contributions to the highest occupied localized orbital (HOLO) (%)	22/78	19/81	26/74	19/81	11/89	19/81	45/55
Normalised Gallyl *s*/*p* contributions to the M–Ga highest occupied localized orbital (HOLO) (%)	73/27	73/27	74/26	77/23	76/24	77/23	67/33
Normalised Gallyl *s*/*p* contributions to the Ga–N localized orbital (LO) (%)	26/74	24/76	25/75	22/78	19/81	21/79	31/69
Net Hirshfeld Charge at Gallyl	0.23	0.19	0.20	0.21	0.19	0.19	0.35

Table 4.13. Selected DFT computational results for Ln{$(Me_3SiCH_2)C(NCy)_2$}$_2${$B(NArCH)_2$}$(THF)_n$ (Ln = Sc, n = 0 (**22C**), n = 1 (**22C$_{THF}$**); Y, n = 0 (**23C**), n = 1 (**23C$_{THF}$**); Lu, n = 0 (**23C**), n = 1 (**23C$_{THF}$**).

	22C	**23C**	**24C**	**22C$_{THF}$**	**23C$_{THF}$**	**24C$_{THF}$**
r(Ln–B) (Å)	2.473	2.638	2.574	2.589	2.745	2.672
r(B–N) (mean (Å))	1.477	1.471	1.471	1.496	1.487	1.488
N–B–N angle (°)	99.9	99.8	99.9	99.1	99.1	99.4
Normalised Ln/B Mulliken contributions to the highest occupied localized orbital (HOLO) (%)	28/72	26/74	31/69	26/74	23/77	28/72
Normalised Boryl *s*/*p* contributions to the Ln–B highest occupied localized orbital (HOLO) (%)	56/44	57/43	57/43	59/41	59/41	60/40
Normalised Boryl *s*/*p* contributions to the B–N localized orbital (LO) (%)	28/72	27/73	29/71	27/73	24/76	29/71
Net Hirshfeld Charge at Boryl	-0.05	-0.07	-0.06	-0.05	-0.07	-0.07

4.5.4 Ln–E Potential Energy Surfaces

The potential energy surface of the Ln–B bonds were probed by incrementally varying the Ln–B bond distances of **22C**–**24C** about their equilibrium values and optimising all other geometric parameters. However, as with the gallyl examples **14C**–**16C**, unfavourable steric interactions between the aryl rings of the boryl heterocycle and the amidinate cyclohexyl and trimethylsilyl groups had a disproportionately large effect on the overall geometry and energy of the system such that information about the Ln–B interaction was masked. Calculations were repeated on models of **22C**–**24C**, Ln{MeC(NMe)$_2$}$_2${B(NXylCH)$_2$} (Ln = Sc (**22SC**), Y (**23SC**) or Lu (**24SC**), Figure 4.12) featured in Section 4.5.1.1. The results show that, as with previous examples of Ln–E bonds, the Ln–B bonds have very shallow potential energy surfaces, with small shifts in bond length inducing only a small energy change. For example, the scandium-boron bond in **22SC** requires approximately 4.5 kJ mol^{-1} for a ±0.1 Å change about the equilibrium distance.

This compares well with the boryl and gallyl compounds introduced in the preceding Chapters. Whilst the potential energy surfaces remain shallow for both the boryl and gallyl examples, a comparison of the potential energy surfaces of the boryl (**22SC** and **24SC**) and gallyl (**14SC** and **16SC**) compounds, as highlighted in Figure 4.20, shows the boryl examples require more energy overall to lengthen the bond past the equilibrium distance.

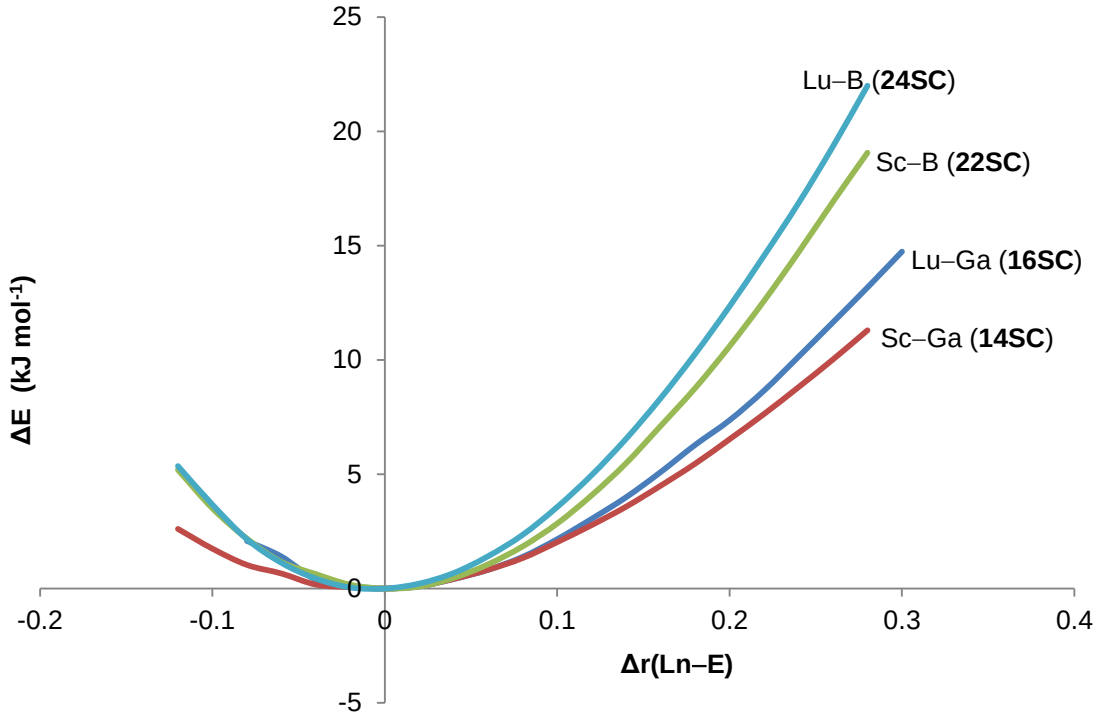

Figure 4.20. Relative changes in energy with respect to changes in Ln–E bond distance from their optimised values in Ln{MeC(NMe)$_2$}$_2${Ga(NXylCH)$_2$}(THF) (**14SC** and **16SC**) or Ln{MeC(NMe)$_2$}$_2${B(NXylCH)$_2$} (**22SC** and **24SC**).

4.5.5 Computational Assessment of Carbodiimide Insertion into the Ln–E Bond

The addition of one equivalent of the carbodiimide CyNCNCy to the rare earth metal bis(amidinate) gallyl compounds Ln{(Me$_3$SiCH$_2$)C(NCy)$_2$}$_2${Ga(NArCH)$_2$}(THF) (Ln = Sc (**14**), Y (**15**) or Lu (**16**)) resulted in the products of insertion into the metal-gallium bond, Ln{(Me$_3$SiCH$_2$)C(NCy)$_2$}$_2${(Ga(NArCH)$_2$)C(NCy)$_2$} (Ln = Sc (**17**), Y (**20**) or Lu (**21**)). On the NMR tube scale in C_6D_6, these reactions were quantitative and virtually instantaneous. The corresponding reaction with the rare earth metal bis(amidinate) boryl compounds Ln{(Me$_3$SiCH$_2$)C(NCy)$_2$}$_2${B(NArCH)$_2$} (Ln = Sc (**22**), Y (**23**) or Lu (**24**)) resulted in no reaction. This difference in reactivity is attributed to the steric saturation of the rare earth metal centre in the boryl compounds **22**–**24** that hinders pre-coordination of the carbodiimide, and the higher bond dissociation energy (BDE) of the Ln–B bond compared to the Ln–Ga bond.

In order to further probe the reaction and to quantify the observed results, a study was initiated to assess computationally the carbodiimide insertion reaction into the Ln–Ga bond of the bis(amidinate) gallyls **14C**–**16C** and the hypothetical insertion reaction

into the Ln–B bond of the bis(amidinate) boryls **22C**–**24C**. For a more authentic comparison to the reaction involving **14C**–**16C**, the assessment also included the hypothetical six-coordinate bis(amidinate) boryls $\mathbf{22C}_{THF}$–$\mathbf{24C}_{THF}$.

4.5.5.1 Reactions involving Ln–Ga (14C-16C) and Ln–B (22C-24C)

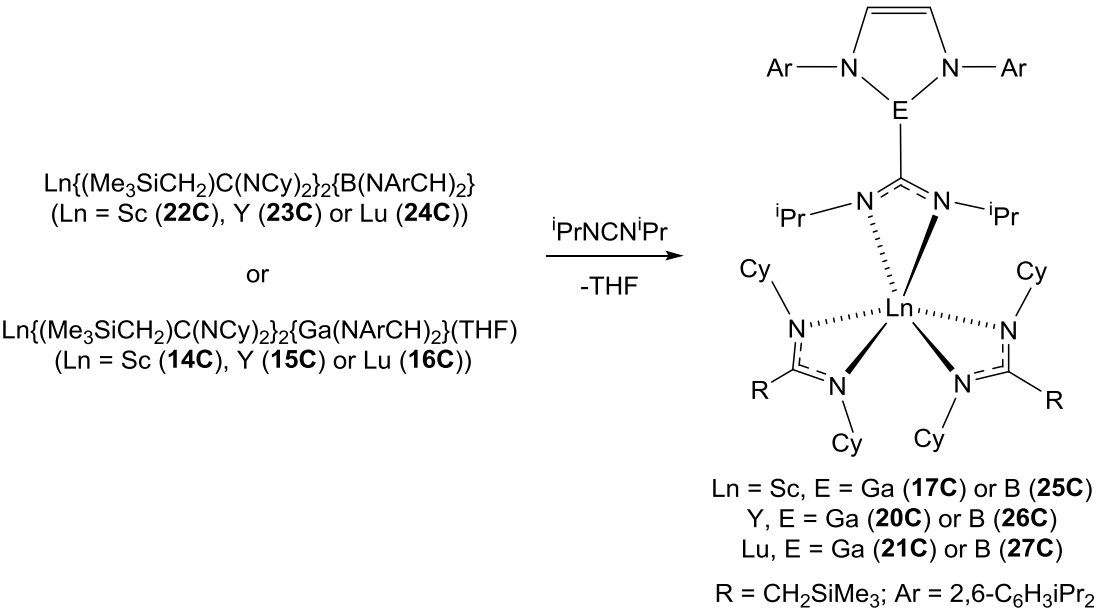

Figure 4.21. Representative carbodiimide insertion reactions.

The reaction outlined in Figure 4.21 was assessed and produced results that are presented in Table 4.14. The $\Delta_r H$ values for the reaction involving the six-coordinate gallyl model systems **14C**–**16C** are approximately 2.5 times lower than those involving the boryl model systems **22C**–**24C**. The origin of the relatively low change in reaction enthalpy for the gallyl examples may be attributed to the loss of THF, a requirement for the reaction to proceed, being disfavoured for the gallyl compounds (see Section 4.5.1.3). The lack of coordinated THF in **22C**–**24C** results in the reaction of carbodiimide and **22C**–**24C** producing only one product from two reactants, which results in more negative $\Delta_r S$ values than for the corresponding reaction of carbodiimide with **14C**–**16C**. Whilst the change in reaction entropy may be more unfavourable for the reactions involving **22C**–**24C**, the large and favourable change in reaction enthalpy overcomes the $T\Delta_r S$ term to produce values for $\Delta_r G$ that favour the insertion into the Ln–B bond to form the hypothetical products of insertion **25C**–**27C**, and suggests that this reaction is more favourable than the insertion into the Ln-Ga bond of **14C**–**16C**. Since experiment shows no reaction involving

compounds **22**–**24**, the large negative values for $\Delta_r H$ and $\Delta_r G$ in the hypothetical reactions involving **22C**–**24C** must have a different origin. It was postulated that, rather than insertion into the Ln–B bond, formation of a B–C bond was the driving force for the reactions.

The expected outcome would see the B–C BDE being greater than that of the Ga–C bond, as the orbital overlap and energy difference between the respective orbitals will decrease down the group. This is supported by experimentally derived BDEs for both X_2B–C (376 kJ mol^{-1}) and X_2Ga–C (245 kJ mol^{-1}).[29] However, the data available are derived from E–C(sp^3) bonds, whilst the carbodiimide insertion reactions form products featuring E–C(sp^2) bonds. Calculations were therefore carried out on model systems {Ga(NArcH)$_2$}Ph (**Ga$_{Ph}$**) and {B(NArcH)$_2$}Ph (**B$_{Ph}$**) to assess the relative strengths of the E–C bonds. Phenyl groups that form E–C(sp^2) bonds in the model systems would provide a more accurate estimation for the E–C(sp^2) bond strength in the full systems. The B–C bond distance in the geometry optimised structure of **B$_{Ph}$** (1.558 Å) closely matched that of the molecular structure of {B(NArcH)$_2$}Ph (1.579 Å, see compound **1.20**, Chapter 1) as reported by Yamashita and Nozaki,[21] whilst the Ga–C bond distance in the geometry optimised structure of **Ga$_{Ph}$** (1.910 Å) closely matches that reported for the molecular structure of {Ga(NArcH)$_2$}(2,4,6-$C_6H_2{}^iPr$) (1.936(3) Å) by Jones and co-workers.[17] These results provide confidence in the quality of the calculated structures of **Ga$_{Ph}$** and **B$_{Ph}$**.

The BDEs were calculated for the geometry optimised structures of **Ga$_{Ph}$** and **B$_{Ph}$**, producing values of 377 kJ mol^{-1} and 666 kJ mol^{-1} respectively. Whilst the higher BDE for B–C(sp^2) bonds compared to Ga–C(sp^2) bonds matches the expected trend for bonds featuring these elements, the BDEs for the E–C(sp^2) are higher in energy than those obtained experimentally for the corresponding E–C(sp^3) bonds.

Table 4.14. Calculated values for the reaction of Ln{$(Me_3SiCH_2)C(NCy)_2\}_2${$E(NArCH)_2$}(THF) (Ln = Sc, E= Ga (**14C**) or B (**22C$_{THF}$**); Y, E= Ga (**15C**) or B (**23C$_{THF}$**); Lu, E= Ga (**16C**) or B (**24C$_{THF}$**)) or Ln{$(Me_3SiCH_2)C(NCy)_2\}_2${$B(NArCH)_2$} (Ln = Sc (**22C**), Y (**23C**) and Lu (**24C**)) with ^{i}PrNCN^{i}Pr.[a]

	14C	**15C**	**16C**	**22C**	**23C**	**24C**	**22C$_{THF}$**	**23C$_{THF}$**	**24C$_{THF}$**
$\Delta_r H$	-137.43	-125.56	-130.97	-307.21	-320.08	-308.17	-291.20	-275.46	-276.42
$\Delta_r S$	-0.039	-0.044	-0.017	-0.175	-0.203	-0.155	-0.033	-0.014	-0.018
$\Delta_r G$	-125.75	-112.45	-126.04	-255.06	-259.48	-261.98	-281.34	-271.20	-271.07

a. All values in kJ mol^{-1}

4.5.5.2 Reactions involving Ln–Ga (14C–16C) and Ln–B ($22C_{THF}$–$24C_{THF}$)

As mentioned, whilst the computational study of the insertion reactions involving the calculated five-coordinate boryl compounds **22C**–**24C** gave additional information into the behaviour of the real compounds **22**–**24**, a more useful comparison would involve the calculated hypothetical six-coordinate boryl compounds **$22C_{THF}$**–**$24C_{THF}$**. The results of the computational assessment are presented in Table 4.14.

As with the five-coordinate boryl examples, the change in reaction enthalpy for **$22C_{THF}$**–**$24C_{THF}$** is much larger than that found for **14C**–**16C**, but now the presence of THF creates an additional barrier not present before. Loss of THF is still unfavourable (see Section 4.5.1.2), but far less so than that for the gallyl examples **14C**–**16C**. This results in a small increase in $\Delta_r H$ for **$22C_{THF}$**–**$24C_{THF}$** compared to **22C**–**24C**.

The values for $\Delta_r S$ for **$22C_{THF}$**–**$24C_{THF}$** are now roughly equal to those found for **14C**–**16C**, with both systems now involved in a two reactant-two product process. The less negative $\Delta_r S$ values for **$22C_{THF}$**–**$24C_{THF}$** result in a smaller $T\Delta_r S$ term, which compensates for the higher $\Delta_r H$ values to produce $\Delta_r G$ values that are lower than those found for the reactions involving **22C**–**24C**, but still higher than the values found for **14C**–**16C**, as B–C(sp^2) bonds are formed.

4.6 Conclusions

In this Chapter, the reactivity of metal-boryl, metal-gallyl and metal-metal bonds was introduced. The reactivity studies of the rare earth metal gallyl compounds Ln{$(Me_3SiCH_2)C(NCy)_2$}$_2${$Ga(NArCH)_2$}(THF) (Ln = Sc (**14**), Y (**15**) or Lu (**16**)) introduced in Chapter 3 towards carbodiimides were presented. Insertion of carbodiimide (RNCNR, where R = Cy, ^{i}Pr or Tol) into the Ln–Ga bond afforded Sc{$(Me_3SiCH_2)C(NCy)_2$}$_2${$(Ga(NArCH)_2)C(NR)_2$} (R = Cy (**17**), ^{i}Pr (**18**) or Tol (**19**)) and Ln{$(Me_3SiCH_2)C(NCy)_2$}$_2${$(Ga(NArCH)_2)C(NCy)_2$} (Ln = Y (**20**), Lu (**21**)). These results constitute the first insertion reactions with Ln–Ga bonded compounds and unsaturated substrates, and indeed the first successful reactions of any type at an unsupported metal-gallium bond. The rare earth metal boryl compounds Ln{$(Me_3SiCH_2)C(NCy)_2$}$_2${$B(NArCH)_2$} (Ln = Sc (**22**), Y (**23**) or Lu (**24**)) were then synthesised to allow for comparative reactivity studies. It was found, however, that

compounds **22–24** would not react with carbodiimides in the manner observed with **14**–**16**.

DFT computational analysis was sought to elucidate the bonding and structural features of the bis(amidinate) compounds, and to probe the energetics of the insertion reactions that produced compounds **17**–**21**. A comprehensive computational study, carried out in collaboration with Ms. Abigail Mountain and Prof. Nikolas Kaltsoyannis (UCL), was presented. It was found that steric hindrance around the Ln–B bond was the origin of the lack of reactivity for the boryl compounds **22–24**, whilst sterics and the constrained nature of the *N*,*N'*-disubstituted amidinate ligand was the origin of the unusual square-based pyramidal geometry adopted by **22–24**. The insertion reactions into the Ln–Ga bond were computationally assessed, and compared with the hypothetical insertion reactions into the Ln–B bond. Although insertion into the Ln–B bond of **22–24** was not possible experimentally, the computational assessment of the reaction suggested that it should be more favourable than the corresponding reaction with **14–16**. This result was attributed to the fact that insertion in the Ln–B bond would form a B–C(sp^2) bond, which was found to be a considerably stronger bond than a Ga–C(sp^2) bond.

4.7 References

1 J. F. Hartwig, *Accounts Chem. Res.*, 2012, **45**, 864.

2 (a) G. J. Irvine, M. J. G. Lesley, T. B. Marder, N. C. Norman, C. R. Rice, E. G. Robins, W. R. Roper, G. R. Whittell and L. J. Wright, *Chem. Rev.*, 1998, **98**, 2685; (b) S. Aldridge and D. L. Coombs, *Coord. Chem. Rev.*, 2004, **248**, 535; (c) H. Braunschweig, R. D. Dewhurst and A. Schneider, *Chem. Rev.*, 2010, **110**, 3924; (d) I. A. I. Mkhalid, J. H. Barnard, T. B. Marder, J. M. Murphy and J. F. Hartwig, *Chem. Rev.*, 2010, **110**, 890.

3 (a) H. Kono, K. Ito and Y. Nagai, *Chemistry Letters*, 1975, 1095; (b) D. Mannig and H. Noth, *Angew. Chem. Int. Ed.*, 1985, **24**, 878.

4 G. Lesley, P. Nguyen, N. J. Taylor, T. B. Marder, A. J. Scott, W. Clegg and N. C. Norman, *Organometallics*, 1996, **15**, 5137.

5 M. Satoh, Y. Nomoto, N. Miyaura and A. Suzuki, *Tetrahedron Lett.*, 1989, **30**, 3789.

6 I. D. Gridnev, N. Miyaura and A. Suzuki, *Organometallics*, 1993, **12**, 589.

7 H. Braunschweig and M. Colling, *Coord. Chem. Rev.*, 2001, **223**, 1.

8 D. Adhikari, J. C. Huffman and D. J. Mindiola, *Chem. Commun.*, 2007, 4489.

9 T. Sagawa, Y. Asano and F. Ozawa, *Organometallics*, 2002, **21**, 5879.

10 D. S. Laitar, P. Muller and J. P. Sadighi, *J. Am. Chem. Soc.*, 2005, **127**, 17196.

11 (a) D. S. Laitar, E. Y. Tsui and J. P. Sadighi, *J. Am. Chem. Soc.*, 2006, **128**, 11036; (b) *Organometallics*, 2006, **25**, 2405.

12 (a) C. Jones, D. P. Mills, R. P. Rose and A. Stasch, *Dalton Trans.*, 2008, 4395; (b) C. Jones, D. P. Mills, R. P. Rose, A. Stasch and W. D. Woodul, *J. Organomet. Chem.*, 2010, **695**, 2410.

13 S. P. Green, C. Jones and A. Stasch, *Science*, 2007, **318**, 1754.

14 B. D. Rekken, T. M. Brown, J. C. Fettinger, H. M. Tuononen and P. P. Power, *J. Am. Chem. Soc.*, 2012, **134**, 6504.

15 H. Braunschweig, A. Damme, R. D. Dewhurst and A. Vargas, *Nat. Chem.*, 2013, **5**, 115.

16 M. Pasquali, S. Gambarotta, C. Floriani, A. Chiesivilla and C. Guastini, *Inorg. Chem.*, 1981, **20**, 165.

17 S. P. Green, C. Jones, K. A. Lippert, D. P. Mills and A. Stasch, *Inorg. Chem.*, 2006, **45**, 7242.

18 D. A. Fletcher, R. F. McMeeking and D. Parkin, *J. Chem. Inf. Comput. Sci.*, 1996, **36**, 746 (The U.K. Chemical Database Service: CSD versions 5.34 and 5.35, updated May 2013 and November 2013 respectively).

19 S. H. Li, J. H. Cheng, Y. H. Chen, M. Nishiura and Z. M. Hou, *Angew. Chem. Int. Ed.*, 2011, **50**, 6360.

20 (a) J. Lee, M. Brewer, M. Berardini and J. G. Brennan, *Inorg. Chem.*, 1995, **34**, 3215; (b) K. Norton, G. A. Kumar, J. L. Dilks, T. J. Emge, R. E. Riman, M. G. Brik and J. G. Brennan, *Inorg. Chem.*, 2009, **48**, 3573; (c) K. Krogh-Jespersen, M. D. Romanelli, J. H. Melman, T. J. Emge and J. G. Brennan, *Inorg. Chem.*, 2010, **49**, 552.

21 Y. Segawa, Y. Suzuki, M. Yamashita and K. Nozaki, *J. Am. Chem. Soc.*, 2008, **130**, 16069.

22 H. A. Bent, *Chem. Rev.*, 1961, **61**, 275.

23 B. Cordero, V. Gomez, A. E. Platero-Prats, M. Reves, J. Echeverria, E. Cremades, F. Barragan and S. Alvarez, *Dalton Trans.*, 2008, 2832.

24 A. V. Protchenko, L. M. A. Saleh, D. Vidovic, D. Dange, C. Jones, P. Mountford and S. Aldridge, *Chem. Commun.*, 2010, **46**, 8546.

25 G. A. Pierce, S. Aldridge, C. Jones, T. Gans-Eichler, A. Stasch, N. D. Coombs and D. J. Willock, *Angew. Chem. Int. Ed.*, 2007, **46**, 2043.

26 B. J. Coe and S. J. Glenwright, *Coord. Chem. Rev.*, 2000, **203**, 5.

27 S. P. Green, C. Jones, D. P. Mills and A. Stasch, *Organometallics*, 2007, **26**, 3424.

28 M. Asay, C. Jones and M. Driess, *Chem. Rev.*, 2011, **111**, 354.

29 A. J. Downs and H.-J. Himmel, *The Group 13 Metals Aluminium, Gallium, Indium and Thallium: Chemical Patterns and Peculiarities* Wiley, 2011.

Chapter Five

Experimental Details and Characterising Data

5.1 General Methods and Instrumentation

All manipulations were carried out using standard Schlenk line or dry-box techniques under an atmosphere of argon or dinitrogen. Solvents were degassed by sparging with dinitrogen and dried by passing through a column of the appropriate drying agent.[1] Toluene, THF and Et_2O were pre-dried over activated 4 Å molecular sieves, refluxed over potassium or sodium/potassium alloy (Et_2O) respectively and distilled. NMR spectra were recorded in C_6D_6 or CD_2Cl_2 which were dried over potassium or P_2O_5 respectively, distilled under reduced pressure and stored under dinitrogen in Teflon valve ampoules. NMR samples were prepared under dinitrogen in 5 mm Wilmad 507-PP tubes fitted with J. Young Teflon valves. ^{1}H, $^{13}C\{^{1}H\}$, and $^{11}B\{^{1}H\}$ NMR spectra were recorded on Varian Mercury-VX 300 MHz spectrometer, Bruker Avance III HD Nanobay 400 MHz or Bruker Avance III 500 MHz spectrometers at ambient temperature unless stated otherwise and referenced internally to residual protio-solvent (^{1}H) or solvent (^{13}C) resonances and are reported relative to tetramethylsilane (δ = 0 ppm). ^{11}B NMR spectra were referenced to $Et_2O{\cdot}BF_3$. Assignments were confirmed using two dimensional ^{1}H–^{1}H and ^{13}C–^{1}H NMR correlation experiments. Chemical shifts are quoted in δ (ppm) and coupling constants in Hz. IR spectra were recorded on Nicolet Magna 560 E.S.P. or Thermo Scientific Nicolet iS5 FT-IR spectrometers. Samples were prepared in a dry-box as Nujol mulls between NaCl plates, and the data are quoted in wavenumbers (cm^{-1}). Elemental analyses were carried out by Mr. Stephen Boyer of the Elemental Analysis Service at London Metropolitan University or Elemental Analysis Ltd, Devon.

5.2 Literature Preparations

Unless stated, starting materials were purchased from Sigma Aldrich, Strem Chemicals or Alfa Aesar and used without further purification. $[Et_3NH][BPh_4]$ was prepared from the reaction of $NaBPh_4$ and $[Et_3NH]Cl$ in water. After reacting for 3 h, the resultant precipitate was filtered, washed with hot (80 °C) water, washed three times with diethyl ether and dried *in vacuo* overnight. $Ln(CH_2SiMe_3)_3(THF)_2$ (Ln = Sc, Y or Lu),[2] $[Ln(CH_2SiMe_3)_2(THF)_n][BPh_4]$ (Ln = Sc, Lu (n = 3) or Y (n = 3 or 4)),[3] $[K\{Ga(NArCH)_2\}(Et_2O)]_2$ and $Li\{B(NArCH)_2\}(THF)_2$ were synthesised according to published procedures.[4] N,N'-diisopropylcarbodiimide was purchased from Alfa Aesar, N,N'-dicyclohexylcarbodiimide and 1,3-di-*p*-tolylcarbodiimide were

purchased from Sigma Aldrich and either sparged with argon (^{i}PrNCN^{i}Pr), sublimed prior to use (CyNCNCy) or used without further purification (TolNCNTol).

5.3 X-ray Data Collection and Processing Parameters

Crystals were mounted on glass fibres using perfluoropolyether oil and cooled rapidly in a stream of cold N_2 using an Oxford Cryosystems Cryostream unit. Diffraction data were measured using either an Enraf-Nonius KappaCCD or Agilent Technologies Supernova diffractometer using Mo–K_α or Cu–K_α radiation, respectively. As appropriate, absorption and decay corrections were applied to the data and equivalent reflections merged.[5] The structures were solved with SIR92[6] or Superflip[7] and further refinements and all other crystallographic calculations were performed using the CRYSTALS program suite.[8] Other details of the structure solution and refinements are given in the CD Appendix.

5.4 DFT Computational Details

DFT computational studies were carried out by Dr Krishna H. Birjkumar (Chapter 2) and Ms Abigail R. E. Mountain (Chapters 3 and 4) under the supervision of Prof. Nikolas Kaltsoyannis at University College London. Scalar relativistic, gradient-corrected density functional theory calculations were carried out using the Grimme D3 dispersion correction[9] with the PBE functional,[10] as implemented in Amsterdam Density Functional 2009.01 and 2013.01 Rev. C (ADF)[11] and the Gaussian 09 Rev. A02 and Rev. D.01 (G09)[12] quantum chemistry codes. Atoms-in-molecules analyses were performed using the AIMALL programme, using formatted G09 checkpoint files as input.[13]

Geometry optimisations were carried out in ADF, using the Zeroth Order Regular Approximation (ZORA) Hamiltonian. Slater Type Orbital basis sets of triple zeta plus double polarization function quality (TZ2P) ZORA basis sets were used for Sc, Y, Lu and Ga, and the double zeta plus polarization (DZP) ZORA basis set was used for the rest of the atoms. The frozen core approximation was incorporated for all atoms; Sc(2p), Si(2p), Ga(3p), Y(3d), Lu(4d), and 1s for all the other atoms bar H. The default SCF convergence criteria were used together with an integration grid of 4.5 and a geometry convergence energy gradient of 0.001 Hartree Å^{-1}. Hirshfeld charge,[14] Boys-Foster Localised Orbitals[15] and Ziegler-Rauk bond energy decomposition[16] analyses were carried out. Bond energy decomposition data for **14C$_{-THF}$**–**16C$_{-THF}$**

could not be obtained owing to difficulties converging the gallyl fragments with Aufbau orbital populations.

Grimme D3 dispersion corrected PBE single point calculations on optimized ADF structures were carried out in G09, to produce formatted checkpoint files for use in AIMALL. A segmented all-electron relativistically contracted basis set, of TZVP quality for Lu,[17] and relativistically recontracted variants of the Karlsruhe def2 TZVP basis sets were used for all other atoms. Due to DIIS convergence difficulties, the SCF for **1** was converged using the XQC setting. The Douglas-Kroll-Hess second order Hamiltonian (DKH2) was employed in all G09 calculations.

5.5 Experimental Details and Characterising Data for Chapter 2

$Sc(CH_2SiMe_3)_2\{B(NArCH)_2\}(THF)$ (1). To a stirred solution of $[Sc(CH_2SiMe_3)_2(THF)_3][BPh_4]$ (280 mg, 0.371 mmol) in THF (15 mL) at -40 °C was added a solution of $Li\{B(NArCH)_2\}(THF)_2$ (200 mg, 0.371 mmol) in THF (15 mL) at -40 °C. The resulting light yellow solution was stirred for 16 h at -40 °C and then allowed to warm to RT. Volatiles were removed under reduced pressure and the resulting solid was extracted into pentane (2 x 10 mL) and filtered. Removal of the volatiles under reduced pressure yielded the title compound as a light brown solid which was dried *in vacuo*. Yield: 162 mg (64 %). Diffraction-quality crystals were grown from a concentrated pentane solution cooled to -30 °C.

^{1}H NMR (C_6D_6, 299.9 MHz, 293 K): δ 7.26 - 7.19 (6 H, overlapping 2 x m, *m*- and *p*-$C_6\underline{H}_3{}^i Pr_2$), 6.24 (2 H, s, NCH), 3.52 (4 H, sept, ^3J = 6.9 Hz, C$\underline{H}$Me$_2$), 3.48 (4 H, br. m, OCH_2), 1.41 (12 H, d, ^3J = 6.9 Hz, CH$\underline{Me}_2$), 1.24 (12 H, d, ^3J = 6.9 Hz, CH$\underline{Me}_2$), 1.15 (4 H, br. m, $OCH_2C\underline{H}_2$), 0.12 (18 H, s, $SiMe_3$), 0.10 (4 H, s, $C\underline{H}_2SiMe_3$). $^{13}C\{^1H\}$ NMR (C_6D_6, 75.4 MHz, 293 K): δ 146.8 (*i*-$\underline{C}_6H_3{}^i Pr_2$), 143.9 (*o*-$\underline{C}_6H_3{}^i Pr_2$), 126.9 (*p*-$\underline{C}_6H_3{}^i Pr_2$), 123.4 (*m*-$\underline{C}_6H_3{}^i Pr_2$), 118.7 (ArN$\underline{C}$H), 69.8 ($OCH_2$), 60.4 ($\underline{C}H_2SiMe_3$), 28.6 ($\underline{C}HMe_2$), 25.8 (CH$\underline{Me}_2$), 25.0 ($OCH_2\underline{C}H_2$), 24.2 (CH$\underline{Me}_2$), 3.7 ($SiMe_3$). $^{11}B\{^1H\}$ (C_6D_6, 96.2 MHz, 293 K): δ 38 (br). IR (NaCl plates, Nujol mull, cm^{-1}): 1404 (m), 1361 (s), 1325 (m), 1250 (s), 1237 (s), 1217 (w), 1109 (w), 1058 (w), 1000 (w), 934 (w), 851 (s), 804 (s), 758 (s), 714 (m), 688 (s), 623 (w), 487 (s). Anal. found (calcd. for $C_{38}H_{66}BSc\,N_2OSi_2$): C, 67.45 (67.23); H, 9.36 (9.80); N, 4.37 (4.13) %.

$Y(CH_2SiMe_3)_2\{B(NArCH)_2\}(THF)_2$ (2). To a stirred solution of $[Y(CH_2SiMe_3)_2(THF)_4][BPh_4]$ (323 mg, 0.371 mmol) in THF (15 mL) at -40 °C was

added a solution of Li{B(NArCH)$_2$}(THF)$_2$ (200 mg, 0.371 mmol) in THF (20 mL) at -40 °C. The resulting light yellow solution was stirred for 16 h at -40 °C and then allowed to warm to RT. Volatiles were removed under reduced pressure and the resulting solid was extracted into hexane (2 x 10 mL) and filtered. Removal of the volatiles under reduced pressure yielded the title compound as a pale yellow microcrystalline powder which was dried *in vacuo*. Yield: 204 mg (69 %). Diffraction-quality crystals were grown from a concentrated hexane solution cooled to -30 °C.

^{1}H NMR (C_6D_6, 299.9 MHz, 293 K): δ 7.25 - 7.16 (6 H, overlapping 2 x m, *m*- and *p*-$C_6\underline{H}_3{}^i\mathrm{Pr}_2$), 6.26 (2 H, s, NCH), 3.66 (8 H, br. m, OCH_2), 3.60 (4 H, sept, ^3J = 6.9 Hz, $C\underline{H}Me_2$), 1.37 (12 H, d, ^3J = 6.9 Hz, $CH\underline{Me}_2$), 1.34 (8 H, br. m, $OCH_2C\underline{H}_2$), 1.23 (12 H, d, ^3J = 6.9 Hz, $CH\underline{Me}_2$), 0.18 (18 H, s, $SiMe_3$), -0.88 (4 H, d, $^2J_{YH}$ = 2.5 Hz, $C\underline{H}_2SiMe_3$). ^{13}C{^{1}H} NMR (C_6D_6, 75.4 MHz, 293 K): δ 146.8 (*i*-$\underline{C}_6H_3{}^i\mathrm{Pr}_2$), 146.2 (o-$\underline{C}_6H_3{}^i\mathrm{Pr}_2$), 126.5 (p-$\underline{C}_6H_3{}^i\mathrm{Pr}_2$), 124.2 (m-$\underline{C}_6H_3{}^i\mathrm{Pr}_2$), 120.3 (ArN$\underline{C}$H), 70.0 ($OCH_2$), 33.7 (d, $^1J_{YC}$ = 35 Hz, $\underline{C}H_2SiMe_3$), 28.7 ($\underline{C}HMe_2$), 25.7 ($CH\underline{Me}_2$), 25.4 ($OCH_2\underline{C}H_2$), 23.9 ($CH\underline{Me}_2$), 4.79 ($SiMe_3$). ^{11}B{^{1}H} (C_6D_6, 96.2 MHz, 293 K): δ 45 (br). IR (NaCl plates, Nujol mull, cm^{-1}): 1933 (w), 1867 (w), 1581 (m), 1564 (m), 1361 (s), 1325 (s), 1296 (w), 1265 (s), 1236 (s), 1207 (m), 1175 (m), 1109 (m), 1056 (m), 1015 (m), 933 (m), 847 (s), 762 (s), 747 (s), 637 (w), 617 (w), 482 (s) . Anal. found (calcd. for $C_{42}H_{74}BN_2O_2Si_2Y$): C, 61.52 (63.46); H, 8.95 (9.38); N, 3.62 (3.52) %. The lower than expected %C is attributed to incomplete combustion as seen elsewhere for related compounds.[18]

Lu(CH$_2$SiMe$_3$)$_2${B(NArCH)$_2$}(THF)$_2$ (3). To a stirred solution of [Lu(CH$_2$SiMe$_3$)$_2$(THF)$_3$][BPh$_4$] (328 mg, 0.371 mmol) in THF (15 mL) at -40 °C was added a solution of Li{B(NArCH)$_2$}(THF)$_2$ (200 mg, 0.371 mmol) in THF (15 mL) at -40 °C. The resulting light yellow solution was stirred for 16 h at -40 °C and then allowed to warm to RT. Volatiles were removed under reduced pressure and the resulting solid was extracted into pentane (2 x 10 mL) and filtered. Removal of the volatiles under reduced pressure yielded the title compound as a light yellow microcrystalline powder which was dried *in vacuo*. Yield: 229 mg (70 %). Diffraction-quality crystals were grown from a concentrated hexane solution cooled to -80 °C.

^{1}H NMR (C_6D_6, 299.9 MHz, 293 K): δ 7.24- 7.18 (6 H, overlapping 2 x m, *m*- and *p*-$C_6\underline{H}_3{}^{i}Pr_2$), 6.33 (2 H, s, NCH), 3.64 (8 H, m, OCH_2), 3.56 (4 H, sept, ^{3}J = 6.9 Hz, $C\underline{H}Me_2$), 1.35 (12 H, d, ^{3}J = 6.9 Hz, $CH\underline{Me}_2$), 1.32 (8 H, m, $OCH_2C\underline{H}_2$), 1.22 (12 H, d, ^{3}J = 6.9 Hz, $CH\underline{Me}_2$), 0.15 (18 H, s, $SiMe_3$), -1.08 (4 H, s, $C\underline{H}_2SiMe_3$). ^{13}C{^{1}H} NMR (C_6D_6, 75.4 MHz, 293 K): δ 146.6 (*i*-$\underline{C}_6H_3{}^{i}Pr_2$), 144.8 (*o*-$\underline{C}_6H_3{}^{i}Pr_2$), 126.6 (*p*-$\underline{C}_6H_3{}^{i}Pr_2$), 123.4 (*m*-$\underline{C}_6H_3{}^{i}Pr_2$), 120.4 (ArN$\underline{C}$H), 69.8 ($OCH_2$), 53.4 ($\underline{C}H_2SiMe_3$), 28.6 ($\underline{C}HMe_2$), 25.9 ($CH\underline{Me}_2$), 25.3 ($OCH_2\underline{C}H_2$), 23.9 ($CH\underline{Me}_2$), 4.8 ($SiMe_3$). ^{11}B{^{1}H} ($C_6D_6$, 96.2 MHz, 293 K): δ 62 (br). IR (NaCl plates, Nujol mull, cm^{-1}): 1404 (m), 1362 (s), 1326 (m), 1261 (s), 1237 (s), 1209 (w), 1177 (w), 1104 (s), 1016 (s), 853 (s), 805 (s), 762 (s), 747 (w), 690 (m), 670 (m), 495 (s). Anal. found (calcd. for $C_{42}H_{74}BLuN_2O_2Si_2$): C, 53.04 (57.26); H, 7.46 (8.47); N, 3.41 (3.18) %. The lower than expected %C and %H is attributed to incomplete combustion as seen elsewhere for related compounds.[18]

Isolation of $SnCl_2\{B(NArCH)_2\}_2$ (4). To a solution of UCl_4 (20 mg, 52.6 μmol) in THF-d_8 (0.25 mL) was added a solution of $Sn\{B(NArCH)_2\}_2$ (47 mg, 52.6 μmol) in THF-d_8 (0.25 mL), producing a pale green solution that was allowed to react overnight. All the volatiles were removed under reduced pressure leaving a yellow-green residue which was extracted into hexane and filtered. Slow evaporation of the hexane solution produced yellow crystals, which were determined by an X-ray diffraction study to be $SnCl_2\{B(NArCH)_2\}_2$.

5.6 Experimental Details and Characterising Data for Chapter 3

$[Sc\{(Me_3SiCH_2)C(N^{i}Pr)_2\}_2(THF)_2][BPh_4]$ (5-BPh_4). To a stirred solution of $[Sc(CH_2SiMe_3)_2(THF)_3][BPh_4]$ (500 mg, 0.66 mmol) in THF (15 mL) was added ^{i}PrNCN^{i}Pr (205 μL, 167 mg, 1.32 mmol). The resulting solution was allowed to stir for 1h at room temperature, following which the volatiles were removed under reduced pressure and the resulting white solid was washed with diethyl ether (2 x 15 mL) and pentane (2 x 15 mL) and dried *in vacuo* to afford the title compound as a white powder. Yield: 504 mg (76 %).

^{1}H NMR (CD_2Cl_2, 299.9 MHz, 293 K): δ 7.31 (8 H, br. m, *o*-$C_6\underline{H}_5$), 7.03 (8 H, m, *m*-$C_6\underline{H}_5$), 6.88 (4 H, t, ^{3}J = 7.2 Hz, *p*-$C_6\underline{H}_5$), 4.03 (8 H, br. m, OCH_2), 3.46 (4 H, sept, ^{3}J = 6.4 Hz, N($C\underline{H}Me_2$)), 2.03 (4 H, s, $C\underline{H}_2SiMe_3$), 1.98 (8 H, br. m, $OCH_2C\underline{H}_2$), 1.13 (24 H, d, ^{3}J = 6.4 Hz, N($CH\underline{Me}_2$)), 0.17 (18 H, s, $CH_2Si\underline{Me}_3$). ^{13}C{^{1}H} NMR (CD_2Cl_2,

75.4 MHz, 293 K) δ 179.8 (^{i}PrNCN^{i}Pr), 164.4 (q, $^{1}J_{BC}$ = 49.3 Hz, *i*-C_6H_5), 136.2 (*o*-C_6H_5), 125.9 (*m*-C_6H_5), 122.1 (*p*-C_6H_5), 72.7 (OCH_2), 48.0 ($\underline{C}HMe_2$), 25.8 ($CH\underline{Me}_2$), 25.1 ($OCH_2\underline{C}H_2$), 18.3 ($\underline{C}H_2SiMe_3$), 0.1 ($CH_2Si\underline{Me}_3$). $^{11}B\{^{1}H\}$ NMR (CD_2Cl_2, 96.2 MHz, 293 K) δ -5.97. IR (NaCl plates, Nujol mull, cm^{-1}): 1579 (w), 1252 (w), 1209 (w), 1175 (w), 1141 (w), 1101 (w), 1013 (w), 848 (m), 731 (w), 703 (w). Anal. Found (calcd. for $C_{58}H_{86}BN_4O_2ScSi_2$) C 64.45 (70.85); H 9.05 (8.82); N 5.56 (5.70) %. The lower than expected %C is attributed to incomplete combustion as seen elsewhere for related compounds.[18] The NMR spectrum shown in Figure 5.1 supports the bulk purity of the compound.

[Sc{(Me$_3$SiCH$_2$)C(NCy)$_2$}$_2$(THF)$_2$][BPh$_4$] (6-BPh$_4$). To a solid mixture of $Sc(CH_2SiMe_3)_3(THF)_2$ (500 mg, 1.11 mmol) and $[Et_3NH][BPh_4]$ (467 mg, 1.11 mmol) at -78 °C was added THF (50 mL). The resulting suspension was allowed to warm to room temperature and react overnight. To the now clear and colourless solution was added a solution of CyNCNCy (457 mg, 2.22 mmol) in THF (10 mL). The resulting solution was allowed to stir for 1 h at room temperature, after which the volatiles were removed under reduced pressure. The resulting white solid was washed with diethyl ether (2 x 15 mL) and pentane (2 x 15 mL) and dried *in vacuo* to afford the title compound as a white powder. Yield: 1060 mg (87 %).

^{1}H NMR (CD_2Cl_2, 499.9 MHz, 293 K): δ 7.34 (8 H, br. m, *o*-$C_6\underline{H}_5$), 7.04 (8 H, m, *m*-$C_6\underline{H}_5$), 6.89 (4 H, t, ^{3}J = 7.2 Hz, *p*-$C_6\underline{H}_5$), 4.01 (8 H, br. m, OCH_2), 3.01 (4 H, br. m, NCH (Cy)), 2.03 (4 H, s, $C\underline{H}_2SiMe_3$), 1.95 (8 H, br. m, OCH_2CH_2), 1.79, 1.69, 1.30, 1.12 (40 H, br. m, N$\underline{C}$y), 0.20 (18 H, s, CH_2SiMe_3). $^{13}C\{^{1}H\}$ NMR (CD_2Cl_2, 125.7 MHz, 293 K): δ 179.9 (CyN$\underline{C}$NCy), 164.6 (q, $^{1}J_{BC}$ = 49.3 Hz, *i*-C_6H_5), 136.4 (*o*-C_6H_5), 126.1 (*m*-C_6H_5), 122.2 (*p*-C_6H_5), 72.9 (OCH_2), 56.9 (CH of $CH_2C(N\underline{C}y)_2$)), 36.5 (NCy), 26.2 (NCy), 26.0 (NCy), 25.3 ($OCH_2\underline{C}H_2$), 18.7 ($\underline{C}H_2SiMe_3$), 0.2 ($CH_2Si\underline{Me}_3$). $^{11}B\{^{1}H\}$ NMR (CD_2Cl_2, 160.4 MHz, 293 K): δ -6.55. IR (NaCl plates, Nujol mull, cm^{-1}): 1579 (m), 1396 (w), 1363 (m), 1348 (w), 1259 (m), 1199 (m), 1185 (m), 1139 (m), 1123 (s), 1014 (m), 997 (w), 850 (s), 806 (w), 779 (w), 743 (w), 731 (s), 702 (s), 638 (w), 612 (m). Anal. Found (calcd. for $C_{66}H_{102}BN_4O_2ScSi_2$): C 72.28 (72.36); H 9.20 (9.38); N 5.02 (5.11) %.

[Sc{(Me$_3$SiCH$_2$)C(NTol)$_2$}$_2$(THF)$_2$][BPh$_4$] (7-BPh$_4$). To a stirred solution of $[Sc(CH_2SiMe_3)_2(THF)_3][BPh_4]$ (500 mg, 0.66 mmol) in THF (15 mL) was added TolNCNTol (295 mg, 1.32 mmol). The resulting solution was allowed to stir for 1h at

room temperature, following which the solution was filtered. The volatiles were removed from the filtrate under reduced pressure and the resulting white solid was washed with diethyl ether (2 x 15 mL) and pentane (2 x 15 mL) and dried *in vacuo* to afford the title compound as a white powder. Yield: 575 mg (77 %).

^{1}H NMR (CD_2Cl_2, 299.9 MHz, 293 K): δ 7.33 (8 H, br. m, *o*-$C_6\underline{H}_5$), 7.14 (8 H, d, o-$C_6\underline{H}_4Me$) 7.04 (8 H, m, *m*-$C_6\underline{H}_5$), 6.88 (4 H, t, ^{3}J = 7.2 Hz, *p*-$C_6\underline{H}_5$), 6.70 (8 H, d, m-$C_6\underline{H}_4Me$), 3.86 (8 H, br. m, OCH_2), 2.35 (12 H, s, $C_6H_4\underline{Me}$), 2.26 (4 H, s, $C\underline{H}_2SiMe_3$), 1.77 (8 H, br. m, OCH_2CH_2), -0.27 (18 H, s, $CH_2Si\underline{Me}_3$). ^{13}C{^{1}H} NMR (CD_2Cl_2, 75.4 MHz, 293 K) δ 182.1 (TolN$\underline{C}$NTol), 164.4 (q, $^{1}J_{BC}$ = 49.3 Hz, *i*-C_6H_5), 143.8 (*i*-C_6H_4Me), 136.3 (o-C_6H_5) 134.6 (*p*-C_6H_4Me), 130.3 (o-C_6H_4Me), 126.0 (m-C_6H_5), 125.1 (*m*-C_6H_4Me), 122.1 (p-C_6H_5), 72.7 (OCH_2), 25.6 ($OCH_2\underline{C}H_2$), 20.9 ($C_6H_4\underline{Me}$), 18.9 ($\underline{C}H_2SiMe_3$), -0.35 ($CH_2Si\underline{Me}_3$). ^{11}B{^{1}H} NMR (CD_2Cl_2, 128.4 MHz, 298 K) δ -6.58. IR (NaCl plates, Nujol mull, cm^{-1}): 1599 (m), 1579 (m), 1557 (m), 1505 (s), 1455 (s), 1377 (m), 1251 (s), 1226 (s), 1140 (m), 1099 (m), 1005 (m), 845 (s), 812 (m), 732 (s), 703 (s), 612 (m). Anal. Found (calcd. for $C_{70}H_{86}BN_4O_2ScSi_2$) C 74.36 (74.57); H 7.56 (7.69); N 5.06 (4.97) %.

[Y{(Me$_3$SiCH$_2$)C(N^{i}Pr)$_2$}$_2$(THF)$_3$][BPh$_4$] (8-BPh$_4$). To a stirred solution of [Y(CH_2SiMe_3)$_2$(THF)$_4$][BPh_4] (500 mg, 0.57 mmol) in THF (15 mL) was added ^{i}PrNCN^{i}Pr (177 μL, 144 mg, 1.15 mmol). The resulting solution was allowed to stir for 1h at room temperature, following which the volatiles were removed under reduced pressure and the resulting white solid was washed with pentane (2 x 15 mL) and dried *in vacuo* to afford the title compound a white powder. Yield: 366 mg (61 %).

^{1}H NMR (CD_2Cl_2, 299.9 MHz, 293 K): δ 7.33 (8 H, br. m, *o*-$C_6\underline{H}_5$), 7.04 (8 H, m, *m*-$C_6\underline{H}_5$), 6.89 (4 H, t, ^{3}J = 7.2 Hz, *p*-$C_6\underline{H}_5$), 4.04 (6 H, br. m, OCH_2), 3.83 (6 H, br. m, OCH_2), 3.43 (4 H, overlapping 2 x sept, ^{3}J = 6.3 Hz, N($C\underline{H}Me_2$)), 2.03 (4 H, s, $C\underline{H}_2SiMe_3$), 1.96 (12 H, br. m, $OCH_2C\underline{H}_2$), 1.10 (24 H, d, ^{3}J = 6.3 Hz, N($CH\underline{Me}_2$)), 0.16 (18 H, s, $CH_2Si\underline{Me}_3$). ^{13}C{^{1}H} NMR (CD_2Cl_2, 75.4 MHz, 293 K) δ 179.3 (^{i}PrN$\underline{C}$N^{i}Pr), 164.4 (q, $^{1}J_{BC}$ = 49.3 Hz, *i*-C_6H_5), 136.3 (*o*-C_6H_5), 126.1 (*m*-C_6H_5), 122.2 (*p*-C_6H_5), 72.3 (OCH_2), 47.4 ($\underline{C}HMe_2$), 26.7 ($CH\underline{Me}_2$), 25.6 ($OCH_2\underline{C}H_2$), 18.2 ($\underline{C}H_2SiMe_3$), 0.1 ($CH_2Si\underline{Me}_3$). ^{11}B{^{1}H} NMR (CD_2Cl_2, 160.4 MHz, 293 K) δ -6.58. IR (NaCl plates, Nujol mull, cm^{-1}): 1599 (m), 1579 (m), 1557 (m), 1505 (s), 1455 (s), 1377 (m), 1251 (m), 1226 (m), 1140 (m), 1099 (m), 1005 (m), 845 (s), 812 (m), 732

(s), 703 (s), 612 (m). Anal. Found (calcd. for $C_{58}H_{94}BN_4O_3Si_2Y$): C, 66.09 (66.26); H, 8.95 (9.01); N, 5.25 (5.33) %.

[Y{(Me$_3$SiCH$_2$)C(NCy)$_2$}$_2$(THF)$_2$][BPh$_4$] (9-BPh$_4$). To a solid mixture of $Y(CH_2SiMe_3)_3(THF)_2$ (500 mg, 1.01 mmol) and $[Et_3NH][BPh_4]$ (426 mg, 1.01 mmol) at -78 °C was added THF (50 mL). The resulting suspension was allowed to warm to room temperature and react for 2 h. To the now clear and colourless solution was added a solution of CyNCNCy (417 mg, 2.02 mmol) in THF (10 mL). The resulting solution was allowed to stir for 1 h at room temperature, after which the volatiles were removed under reduced pressure. The resulting white solid was washed with pentane (2 x 15 mL) and dried *in vacuo* to afford the title compound as a white powder. Yield: 979 mg (85 %). Crystals suitable for X-ray diffraction were grown from a concentrated THF solution cooled to -30 °C.

^{1}H NMR (CD_2Cl_2, 299.9 MHz, 293 K): δ 7.35 (8 H, br. m, *o*-$C_6\underline{H}_5$), 7.06 (8 H, m, *m*-$C_6\underline{H}_5$), 6.90 (4 H, t, ^3J = 7.2 Hz, *p*-$C_6\underline{H}_5$), 4.03 (8 H, br. m, OCH_2), 2.95 (4 H, br. m, NCH (Cy)), 2.01 (4 H, s, $C\underline{H}_2SiMe_3$), 1.97 (8 H, br. m, OCH_2CH_2), 1.77, 1.30, 1.11 (40 H, br. m, N$\underline{C}$y), 0.18 (18 H, s, CH_2SiMe_3). $^{13}C\{^1H\}$ NMR (CD_2Cl_2, 75.4 MHz, 293 K): δ 178.8 (CyN$\underline{C}$NCy), 164.3 (q, $^1J_{BC}$ = 49.3 Hz, *i*-C_6H_5), 136.2 (*o*-C_6H_5), 125.9 (*m*-C_6H_5), 122.1 (*p*-C_6H_5), 72.2 (OCH_2), 56.0 (CH of $CH_2C(N\underline{C}y)_2$)), 37.6 (NCy), 26.1 (NCy), 26.0 (NCy), 25.3 ($OCH_2\underline{C}H_2$), 18.2 ($\underline{C}H_2SiMe_3$), -0.12 ($CH_2Si\underline{Me}_3$). $^{11}B\{^1H\}$ NMR (CD_2Cl_2, 160.4 MHz, 293 K): δ -6.59. IR (NaCl plates, Nujol mull, cm^{-1}): 1579 (w), 1456 (s), 1377 (s), 1339 (m), 1318 (w), 1250 (m), 1206 (m), 1173 (m), 1138 (m), 1097 (m), 1032 (w), 1007 (m), 849 (s), 732 (s), 703 (s), 644 (w), 612 (m). (Anal. Found (calcd. for $C_{66}H_{102}BN_4O_2Si_2Y$): C 69.23 (69.57); H 8.85 (9.02); N 4.71 (4.92) %.

[Y{(Me$_3$SiCH$_2$)C(NTol)$_2$}$_2$(THF)$_2$][BPh$_4$] (10-BPh$_4$). To a stirred solution of $[Y(CH_2SiMe_3)_2(THF)_4][BPh_4]$ (500 mg, 0.57 mmol) in THF (15 mL) was added a solution of TolNCNTol (255 mg, 1.15 mmol) in THF (5 mL). The resulting solution was allowed to stir for 1h at room temperature, following which the solution was filtered. The volatiles were removed from the filtrate under reduced pressure and the resulting white solid was washed with diethyl ether (2 x 15 mL) and pentane (2 x 15 mL) and dried *in vacuo* to afford the title compound as a pale yellow powder. Yield: 475 mg (67 %).

^{1}H NMR (CD_2Cl_2, 299.9 MHz, 293 K): δ 7.32 (8 H, br. m, *o*-$C_6\underline{H}_5$), 7.03 (8 H, m, *m*-$C_6\underline{H}_5$), 6.88 (4 H, t, ^{3}J = 7.2 Hz, *p*-$C_6\underline{H}_5$), 6.87 (8 H, d, o-$C_6\underline{H}_4Me$), 6.42 (8 H, d, m-$C_6\underline{H}_4Me$), 3.88 (8 H, br. m, OCH_2), 2.27 (12 H, s, $C_6H_4\underline{Me}$), 2.08 (4 H, s, $C\underline{H}_2SiMe_3$), 1.81 (8 H, br. m, $OCH_2C\underline{H}_2$), -0.38 (18 H, s, $CH_2Si\underline{Me}_3$). ^{13}C{^{1}H} NMR (CD_2Cl_2, 75.4 MHz, 293 K) δ 180.3 (TolN$\underline{C}$NTol), 164.4 (q, $^{1}J_{BC}$ = 49.3 Hz, *i*-C_6H_5), 145.6 (*i*-$\underline{C}_6H_4Me$), 136.2 (o-C_6H_5) 132.8 (*p*-$\underline{C}_6H_4Me$), 129.7 (o-$\underline{C}_6H_4Me$), 126.0 (m-C_6H_5), 125.2 (*m*-$\underline{C}_6H_4Me$), 122.1 (p-C_6H_5), 71.4 (OCH_2), 25.7 ($OCH_2\underline{C}H_2$), 20.8 ($C_6H_4\underline{Me}$), 18.9 ($\underline{C}H_2SiMe_3$), -0.15 ($CH_2Si\underline{Me}_3$). ^{11}B{^{1}H} NMR (CD_2Cl_2, 160.4 MHz, 293 K) δ -6.56. IR (NaCl plates, Nujol mull, cm^{-1}): 1580 (m), 1505 (s), 1456 (s), 1377 (m), 1250 (m), 1228 (m), 1149 (w), 1105 (m), 1032 (w), 1014 (m), 968 (w), 844 (s), 808 (w), 732 (m), 637 (w), 624 (w), 612 (m). Anal. Found (calcd. for $C_{70}H_{86}BN_4O_2Si_2Y$): C 71.54 (71.78); H 7.51 (7.40); N 4.54 (4.78) %.

[Lu{(Me$_3$SiCH$_2$)C(N^{i}Pr)$_2$}$_2$(THF)$_3$][BPh$_4$] (11-BPh$_4$). To a stirred solution of [Lu(CH_2SiMe_3)$_2$(THF)$_3$][BPh_4] (500 mg, 0.24 mmol) in THF (15 mL) was added ^{i}PrNCN^{i}Pr (175 μL, 60 mg, 0.47 mmol). The resulting solution was allowed to stir for 1h at room temperature, following which the volatiles were removed under reduced pressure and the resulting white solid was washed with diethyl ether (2 x 15 mL) and pentane (2 x 15 mL) and dried *in vacuo* to afford the title compound as a white powder. Yield: 405 mg (59 %).

^{1}H NMR (CD_2Cl_2, 299.9 MHz, 293 K): δ 7.34 (8 H, br. m, *o*-$C_6\underline{H}_5$), 7.05 (8 H, m, *m*-$C_6\underline{H}_5$), 6.90 (4 H, t, ^{3}J = 7.2 Hz, *p*-$C_6\underline{H}_5$), 4.06 (6 H, br. m, OCH_2), 3.93 (6 H, br. m, OCH_2), 3.59 (4 H, sept, ^{3}J = 6.3 Hz, N($C\underline{H}Me_2$)), 2.06 (4 H, s, $C\underline{H}_2SiMe_3$), 1.99 (12 H, br. m, $OCH_2C\underline{H}_2$), 1.11 (24 H, d, ^{3}J = 6.3 Hz, N($CH\underline{Me}_2$)), 0.18 (18 H, s, $CH_2Si\underline{Me}_3$). ^{13}C{^{1}H} NMR (CD_2Cl_2, 75.4 MHz, 293 K) δ 178.7 (^{i}PrN$\underline{C}$N^{i}Pr), 164.3 (q, $^{1}J_{BC}$ = 49.3 Hz, *i*-C_6H_5), 136.2 (*o*-C_6H_5), 125.9 (*m*-C_6H_5), 122.1 (*p*-C_6H_5), 72.5 (OCH_2), 71.39 (OCH_2) 47.3 ($\underline{C}HMe_2$), 26.3 ($CH\underline{Me}_2$), 25.7 ($OCH_2\underline{C}H_2$), 25.3 ($OCH_2\underline{C}H_2$), 18.6 ($\underline{C}H_2SiMe_3$), 0.0 ($CH_2Si\underline{Me}_3$). ^{11}B{^{1}H} NMR (CD_2Cl_2, 96.2 MHz, 293 K) δ -6.59. IR (NaCl plates, Nujol mull, cm^{-1}): 1880 (w), 1818 (w), 1640 (s), 1579 (s), 1340 (w), 1260 (m), 1210 (w), 1174 (w), 1097 (w), 1013 (w), 914 (w), 800 (w), 731 (m), 702 (m), 645 (w), 624 (w), 611 (m). Anal. Found (calcd. for $C_{58}H_{94}BLuN_4O_3Si_2$): C 53.77 (61.25); H 7.05 (8.33); N 3.86 (4.93) %. This compound was found to be particularly air and moisture sensitive, and did not provide

satisfactory combustion data. The reported data are an average of six samples tested. The NMR spectrum shown in Figure 5.2 supports the bulk purity of the compound.

[Lu{(Me$_3$SiCH$_2$)C(NCy)$_2$}$_2$(THF)$_2$][BPh$_4$] (12-BPh$_4$). To a solid mixture of Lu(CH$_2$SiMe$_3$)$_3$(THF)$_2$ (500 mg, 0.86 mmol) and [Et$_3$NH][BPh$_4$] (363 mg, 0.86 mmol) at -78 °C was added THF (50 mL). The resulting suspension was allowed to warm to room temperature and react for 2 h. To the now clear and colourless solution was added CyNCNCy (355 mg, 1.72 mmol) in THF (10 mL). The resulting solution was allowed to stir for 1 h at room temperature, after which the volatiles were removed under reduced pressure. The resulting white solid was washed with diethyl ether (2 x 15 mL) and pentane (2 x 15 mL) and dried *in vacuo* to afford the title compound as a white powder. Yield: 880 mg (83 %).

^{1}H NMR (CD$_2$Cl$_2$, 299.9 MHz, 293 K): δ 7.34 (8 H, br. m, *o*-C$_6$H$_5$), 7.05 (8 H, m, *m*-C$_6$H$_5$), 6.90 (4 H, t, ^3J = 7.2 Hz, *p*-C$_6$H$_5$), 4.03 (8 H, br. m, OCH$_2$), 3.10 (4 H, br. m, NCH (Cy)), 2.03 (4 H, s, CH$_2$SiMe$_3$), 1.98 (8 H, br. m, OCH$_2$CH$_2$), 1.76, 1.70, 1.29, 1.10 (40 H, br. m, NCy), 0.18 (18 H, s, CH$_2$SiMe$_3$). ^{13}C{^{1}H} NMR (CD$_2$Cl$_2$, 75.4 MHz, 293 K): δ 179.8 (CyNCNCy), 164.3 (q, $^1J_{BC}$ = 49.3 Hz, *i*-C$_6$H$_5$), 136.2 (*o*-C$_6$H$_5$), 126.1 (*m*-C$_6$H$_5$), 122.1 (*p*-C$_6$H$_5$), 72.5 (OCH$_2$), 55.9 (CH of CH$_2$C(NCy)$_2$)), 26.3-25.6 (NCy), 25.2 (OCH$_2$CH$_2$), 18.7 (CH$_2$SiMe$_3$), -0.09 (CH$_2$SiMe$_3$). ^{11}B{^{1}H} NMR (CD$_2$Cl$_2$, 160.4 MHz, 293 K): δ-6.58. IR (NaCl plates, Nujol mull, cm^{-1}): 1578 (s), 1362 (w), 1347 (w), 1311 (w), 1258 (s), 1200 (s), 1184 (m), 1140 (w), 1122 (s), 1063 (w), 1033 (w), 1008 (s), 958 (w), 890 (w), 849 (s), 805 (w), 778 (w), 743 (m), 731 (m), 700 (s), 636 (m), 612 (m), 582 (w). Anal. Found (calcd. for C$_{66}$H$_{102}$BLuN$_4$O$_2$Si$_2$): C 59.44 (64.68); H 8.37 (8.39); N 4.51 (4.57) %. The lower than expected %C is attributed to incomplete combustion as seen elsewhere for related compounds.[18] The NMR spectrum shown in Figure 5.3 supports the bulk purity of the compound.

[Lu{(Me$_3$SiCH$_2$)C(NTol)$_2$}$_2$(THF)$_2$][BPh$_4$] (13-BPh$_4$). To a solid mixture of Lu(CH$_2$SiMe$_3$)$_3$(THF)$_2$ (500 mg, 0.86 mmol) and [Et$_3$NH][BPh$_4$] (363 mg, 0.86 mmol) at -78 °C was added THF (50 mL). The resulting suspension was allowed to warm to room temperature and react for 2 h. To the now clear and colourless solution was added TolNCNTol (383 mg, 1.72 mmol) in THF (10 mL). The resulting solution was allowed to stir for 1h at room temperature, following which the solution was filtered. The volatiles were removed from the filtrate under reduced pressure and the

resulting white solid was washed with diethyl ether (2 x 15 mL) and pentane (2 x 15 mL) and dried *in vacuo* to afford the title compound as a pale yellow powder. Yield: 920 mg (85 %).

^{1}H NMR (CD_2Cl_2, 499.9 MHz, 293 K): δ 7.36 (8 H, br. m, *o*-$C_6\underline{H}_5$), 7.05 (8 H, m, *m*-$C_6\underline{H}_5$), 6.91 (4 H, t, (coupling could not be determined due to overlap with tolyl doublet, *p*-$C_6\underline{H}_5$), 6.89 (8 H, d, *o*-$C_6\underline{H}_4Me$), 6.47 (8 H, d, *m*-$C_6\underline{H}_4Me$), 4.02 (8 H, br. m, OCH_2), 2.30 (12 H, s, $C_6H_4\underline{Me}$), 2.13 (4 H, s, $C\underline{H}_2SiMe_3$), 1.84 (8 H, br. m, $OCH_2C\underline{H}_2$), -0.35 (18 H, s, $CH_2Si\underline{Me}_3$). ^{13}C{^{1}H} NMR (CD_2Cl_2, 125.7 MHz, 293 K) δ 180.4 (TolN$\underline{C}$NTol), 164.6 (q, $^{1}J_{BC}$ = 49.3 Hz, *i*-C_6H_5), 145.7 (*i*-$\underline{C}_6H_4Me$), 136.4 (*o*-C_6H_5) 132.8 (*p*-$\underline{C}_6H_4Me$), 129.9 (*o*-$\underline{C}_6H_4Me$), 126.2 (*m*-C_6H_5), 125.6 (*m*-$\underline{C}_6H_4Me$), 122.3 (*p*-C_6H_5), 72.1 (OCH_2), 25.9 ($OCH_2\underline{C}H_2$), 21.0 ($C_6H_4\underline{Me}$), 19.5 ($\underline{C}H_2SiMe_3$), -0.09 ($CH_2Si\underline{Me}_3$). ^{11}B{^{1}H} NMR (CD_2Cl_2, 160.4 MHz, 293 K) δ -6.55. IR (NaCl plates, Nujol mull, cm^{-1}): 1942 (w), 1888 (w), 1812 (w), 1598 (w), 1580 (w), 1306 (w), 1259 (s), 1174 (w), 1106 (m), 1066 (w), 1018 (m), 970 (w), 916 (w), 843 (s), 731 (m), 702 (m), 637 (w), 624 (w), 612 (m). Anal. Found (calcd. for $C_{70}H_{86}BLuN_4O_2Si_2$): C 61.98 (66.86); H 6.87 (6.89); N 4.58 (4.46) %. The lower than expected %C is attributed to incomplete combustion as seen elsewhere for related compounds.[18] The NMR spectrum shown in Figure 5.4 supports the bulk purity of the compound.

Sc{(Me$_3$SiCH$_2$)C(NCy)$_2$}$_2${Ga(NArCH)$_2$}(THF) (14). A solid mixture of [Sc{(Me$_3$SiCH$_2$)C(NCy)$_2$}$_2$(THF)$_2$][BPh$_4$] (392 mg, 0.35 mmol) and [KGa(NArCH)$_2$(Et$_2$O)]$_2$ (200 mg, 0.35 mmol) was cooled to -78 °C. To this cooled mixture was added, with stirring, toluene (20 mL). The resulting suspension was allowed to warm to room temperature and react for 2 h. The reaction mixture was filtered and the all the volatiles were removed from the filtrate. The resulting orange solid was extracted into pentane, filtered, and all the volatiles removed from the filtrate, resulting in a bright orange powder which was dried *in vacuo* to afford the title compound. Yield: 274 mg (71 %). Crystals suitable for X-ray diffraction were grown from slow evaporation of a hexane solution.

^{1}H NMR (C_6D_6, 299.9 MHz, 293 K): δ 7.30 - 7.28 (4 H, overlapping 2 x m, *m*-$C_6\underline{H}_3{}^{i}Pr_2$), 7.22 - 7.19 (2 H, overlapping 2 x m, *p*-$C_6\underline{H}_3{}^{i}Pr_2$), 6.27 (2 H, s, NCH), 3.97 (4 H, br. m, OCH_2), 3.91 (4 H, br. m, $C\underline{H}Me_2$), 2.88 (4 H, br. m, NCH (Cy)), 1.86 (4 H, br. s, $C\underline{H}_2SiMe_3$), 1.86, 1.82, 1.65, 1.38, 1.21 (40 H, br. m, N$\underline{C}$y), 1.47 (12 H, d, ^{3}J

= 6.9 Hz, CH$\underline{Me}_2$), 1.46 (12 H, d, ^3J = 6.9 Hz, CH$\underline{Me}_2$), 1.24 (4 H, br. m, OCH$_2\underline{CH}_2$), 0.08 (18 H, s, CH$_2$Si$\underline{Me}_3$). $^{13}C\{^1H\}$ NMR (C_6D_6, 75.4 MHz, 293 K): δ 176.1 ($C(NCy)_2$), 152.8 (*i*-$\underline{C}_6H_3{}^iPr_2$), 145.9 (*o*-$\underline{C}_6H_3{}^iPr_2$), 123.6 (*p*-$\underline{C}_6H_3{}^iPr_2$), 122.9 (*m*-$\underline{C}_6H_3{}^iPr_2$), 122.9 (ArN$\underline{C}$H), 72.6 (OCH$_2$), 57.1 (CH of CH$_2$C(N$\underline{Cy}$)$_2$)), 28.8 ($\underline{C}HMe_2$), 27.1-26.3 (br. m, overlapping resonances for NCy), 26.0 (CH$\underline{Me}_2$), 25.1 (OCH$_2\underline{C}$H$_2$), 24.4 (CH$\underline{Me}_2$), 17.8 ($\underline{C}$H$_2$SiMe$_3$), 0.05 (SiMe$_3$). IR (NaCl plates, Nujol mull, cm^{-1}): 1624 (w), 1586 (w), 1397 (s), 1377 (w), 1362 (s), 1253 (s), 1200 (m), 1183 (w), 1122 (m), 1022 (w), 997 (w), 888 (w), 852 (s), 802 (w), 777 (m), 758 (m), 694 (m), 636 (m). Anal. Found (calcd. for $C_{64}H_{110}GaN_6OScSi_2$): C 66.66 (66.82); H 9.55 (9.64); N 7.41 (7.30) %.

Y{(Me$_3$SiCH$_2$)C(NCy)$_2$}$_2${Ga(NArCH)$_2$}(THF) (15). A solid mixture of [Y{(Me$_3$SiCH$_2$)C(NCy)$_2$}$_2$(THF)$_2$][BPh$_4$] (407 mg, 0.35 mmol) and [KGa(NArCH)$_2$(Et$_2$O)]$_2$ (200 mg, 0.35 mmol) was cooled to -78 °C. To this cooled mixture was added, with stirring, toluene (20 mL). The resulting suspension was allowed to warm to room temperature and react for 2 h. The reaction mixture was filtered and all the volatiles were removed from the filtrate. The resulting orange solid was extracted into pentane, filtered, and all the volatiles removed from the filtrate, resulting in a bright orange powder which was dried *in vacuo* to afford the title compound. Yield: 184 mg (43 %).

^1H NMR (C_6D_6, 400.1 MHz, 300 K): δ 7.28 - 7.26 (4 H, overlapping 2 x m, *m*-$\underline{C}_6\underline{H}_3{}^iPr_2$), 7.20 - 7.18 (2 H, overlapping 2 x m, *p*-$\underline{C}_6\underline{H}_3{}^iPr_2$), 6.33 (2 H, s, NCH), 3.98 (4 H, br. m, C$\underline{H}$Me$_2$), 3.83 (4 H, br. m, OCH$_2$), 2.85 (4 H, br. m, NCH (Cy)), 1.87 (4 H, br. s, C$\underline{H}_2$SiMe$_3$), 1.86, 1.80, 1.65, 1.35 (40 H, br. m, N$\underline{Cy}$), 1.45 (24 H, d, ^3J = 6.9 Hz, CH$\underline{Me}_2$), 1.46 (12 H, d, ^3J = 6.9 Hz, CH$\underline{Me}_2$), 1.24 (4 H, br. m, OCH$_2\underline{CH}_2$), 0.08 (18 H, s, CH$_2$Si$\underline{Me}_3$). $^{13}C\{^1H\}$ NMR (C_6D_6, 100.6 MHz, 300 K): δ 176.1 ($C(NCy)_2$), 152.8 (*i*-$\underline{C}_6H_3{}^iPr_2$), 146.0 (*o*-$\underline{C}_6H_3{}^iPr_2$), 123.4 (*p*-$\underline{C}_6H_3{}^iPr_2$), 122.9 (*m*-$\underline{C}_6H_3{}^iPr_2$), 122.9 (ArN$\underline{C}$H), 71.8 (OCH$_2$), 56.6 (CH of CH$_2$C(N$\underline{Cy}$)$_2$)), 28.8 ($\underline{C}HMe_2$), 26.7, 26.4, 26.3, 26.1 (NCy), 26.4 (CH$\underline{Me}_2$), 24.1 (OCH$_2\underline{C}$H$_2$), 24.6 (CH$\underline{Me}_2$), 17.5 ($\underline{C}$H$_2$SiMe$_3$), 0.17 (SiMe$_3$). IR (NaCl plates, Nujol mull, cm^{-1}): 1588(w), 1543 (w), 1463 (s), 1377 (m), 1361 (m), 1254 (m), 1196 (w), 1181 (w), 1119 (m), 852 (s), 801 (w), 758 (w). Anal. Found (calcd. for $C_{64}H_{110}GaN_6OSi_2Y$): C 64.20 (64.36); H 9.18 (9.28); N 6.96 (7.04) %.

Lu{(Me$_3$SiCH$_2$)C(NCy)$_2$}$_2${Ga(NArCH)$_2$}(THF) (16). A solid mixture of [Lu{(Me$_3$SiCH$_2$)C(NCy)$_2$}$_2$(THF)$_2$][BPh$_4$] (438 mg, 0.35 mmol) and [KGa(NArCH)$_2$(Et$_2$O)]$_2$ (200 mg, 0.35 mmol) was cooled to -78 °C. To this cooled mixture was added, with stirring, toluene (20 mL). The resulting suspension was allowed to warm to room temperature and react for 2 h. The reaction mixture was filtered and the volatiles were removed from the filtrate. The resulting orange solid was extracted into pentane, filtered, and all the volatiles removed from the filtrate, resulting in a bright orange powder which was dried *in vacuo* to afford the title compound. Yield: 272 mg (59 %).

^{1}H NMR (C$_6$D$_6$, 299.9 MHz, 293 K): δ 7.29 - 7.26 (4 H, overlapping 2 x m, *m*-C$_6$H$_3$^{i}Pr$_2$), 7.20 - 7.18 (2 H, overlapping 2 x m, *p*-C$_6$H$_3$^{i}Pr$_2$), 6.34 (2 H, s, NCH), 3.97 (4 H, br. m, OCH$_2$), 3.83 (4 H, br. m, CHMe$_2$), 2.90 (4 H, br. m, NCH (Cy)), 1.90 (4 H, br. s, CH$_2$SiMe$_3$), 2.00-1.51, 1.38-1.15 (40 H, br. m, NCy), 1.45 (24 H, d, ^3J = 6.9 Hz, CHMe$_2$), 1.46 (12 H, d, ^3J = 3.5 Hz, CHMe$_2$), 1.31 (4 H, br. m, OCH$_2$CH$_2$), 0.08 (18 H, s, CH$_2$SiMe$_3$). ^{13}C{^{1}H} NMR (C$_6$D$_6$, 75.4 MHz, 293 K): δ 174.4 (C(NCy)$_2$), 152.2 (*i*-C$_6$H$_3$^{i}Pr$_2$), 145.9 (*o*-C$_6$H$_3$^{i}Pr$_2$), 123.8 (*p*-C$_6$H$_3$^{i}Pr$_2$), 123.2 (*m*-C$_6$H$_3$^{i}Pr$_2$), 123.2 (ArNCH), 72.2 (OCH$_2$), 56.4 (CH of CH$_2$C(NCy)$_2$)), 28.6 (CHMe$_2$), 26.9, 26.7, 26.4, 26.1 (NCy), 26.7 (OCH$_2$CH$_2$, br. overlapping with NCy), 26.0 (CHMe$_2$), 24.5 (CHMe$_2$), 17.5 (CH$_2$SiMe$_3$), -0.03 (SiMe$_3$). IR (NaCl plates, Nujol mull, cm^{-1}): 1586 (w), 1548 (w), 1463 (s), 1396 (w), 1360 (m), 1321 (w), 1256 (s), 1199 (m), 1183 (w), 1121 (s), 1020 (w), 933 (w), 888 (w), 852 (s), 802 (m), 759 (m), 695 (w), 636 (w). Anal. Found (calcd. for C$_{64}$H$_{110}$GaLuN$_6$OSi$_2$): C 59.85 (60.03); H 8.55 (8.66); N 6.60 (6.56) %.

5.7 Experimental Details and Characterising Data for Chapter 4

Sc{(Me$_3$SiCH$_2$)C(NCy)$_2$}$_2${(Ga(NArCH)$_2$)C(NCy)$_2$} (17). To a stirred solution of Sc{(Me$_3$SiCH$_2$)C(NCy)$_2$}$_2${Ga(NArCH)$_2$}(THF) (152 mg, 0.13 mmol) in hexane (2.5 mL) at room temperature was added a solution of CyNCNCy (27 mg, 0.13 mmol) in hexane (2.5 mL). After 5 minutes, a yellow precipitate formed. The supernatant was filtered away, and the remaining yellow solid was dried *in vacuo* to afford the title compound. Yield: 102 mg (60 %).

^{1}H NMR (C$_6$D$_6$, 299.9 MHz, 293 K): δ 7.30 – 7.20 (6 H, overlapping 2 x m, *m*- and *p*-C$_6$H$_3$^{i}Pr$_2$), 6.13 (2 H, s, NCH), 3.61 (4 H, sept, ^3J = 6.9 Hz, CHMe$_2$), 2.98 (6 H, br. m,

(CH of $CH_2C(N\underline{C}y)_2$)), 2.07 (4 H, br. s, $C\underline{H}_2SiMe_3$), 2.04, 1.85 1.63, 1.32 (60 H, br. m, N$\underline{C}$y), 1.46 (12 H, dd, ^3J = 6.9 Hz, CH$\underline{Me}_2$), 1.37 (12 H, dd, ^3J = 6.9 Hz, CH$\underline{Me}_2$), 0.08 (18 H, s, $CH_2Si\underline{Me}_3$). $^{13}C\{^1H\}$ NMR (C_6D_6, 75.4 MHz, 293 K): δ 178.2 (Ga($\underline{C}$(NCy)$_2$), 175.9 ($\underline{C}$(NCy)$_2$), 146.7 (*i*-$\underline{C}_6H_3{}^iPr_2$), 145.7, 145.16 (*o*-$\underline{C}_6H_3{}^iPr_2$), 125.9 (*p*-$\underline{C}_6H_3{}^iPr_2$), 123.9, 123.5 (*m*-$\underline{C}_6H_3{}^iPr_2$), 122.5 (ArN$\underline{C}$H), 67.2 (CH of GaC(N$\underline{C}$y)$_2$)), 57.2, 56.8 (CH of $CH_2C(N\underline{C}y)_2$)), 29.5, 28.9 ($\underline{C}$HMe$_2$), 26.8, 26.7, 26.6, 26.5 (NCy), 24.2, 23.3 (CH$\underline{Me}_2$), 17.2 ($\underline{C}H_2SiMe_3$), 0.07 ($SiMe_3$). IR (NaCl plates, Nujol mull, cm^{-1}): 2121 (m), 1641 (w), 1552 (w), 1401 (w), 1362 (m), 1316 (w), 1253 (m), 1197 (m), 1184 (w), 1166 (w), 1122 (m), 1075 (w), 996 (w), 887 (w), 852 (s), 797 (w), 753 (w), 697 (w), 634 (m). Anal. Found (calcd. for $C_{73}H_{124}GaN_8OScSi_2$): C 68.03 (68.25); H 9.67 (9.73); N 8.84 (8.72) %

Sc{(Me$_3$SiCH$_2$)C(NCy)$_2$}$_2${(Ga(NArCH)$_2$)C(N^{i}Pr)$_2$} (18). To a stirred solution of Sc{(Me$_3$SiCH$_2$)C(NCy)$_2$}$_2${Ga(NArCH)$_2$}(THF) (100 mg, 87 μmol) in hexane (2.5 mL) at room temperature was added a solution of ^{i}PrNCN^{i}Pr (11 mg, 87 μmol) in hexane (2.5 mL). The red-orange solution immediately turned a dark yellow-brown, indicating formation of the product. The volatiles were removed under reduced pressure and the resulting yellow-brown powder was dried *in vacuo* to afford the title compound. Yield: 65 mg (62 %). Crystals suitable for X-ray diffraction were grown from slow evaporation of a concentrated hexane solution.

^1H NMR (C_6D_6, 400.1 MHz, 300 K): δ 7.23 - 7.18 (6 H, overlapping 2 x m, *m*- and *p*-$C_6\underline{H}_3{}^iPr_2$), 6.23 (2 H, s, NCH), 3.61 (4 H, br. m, C$\underline{H}$Me$_2$) 3.61 (4 H, sept, ^3J = 6.4 Hz, C$\underline{H}$Me$_2$), 3.30 (2 H, sept, ^3J = 6.4 Hz, C$\underline{H}$Me$_2$), 2.92 (4 H, br. m, NCH (Cy)), 1.94 (4 H, br. s, $C\underline{H}_2SiMe_3$), 2.01, 1.93, 1.81, 1.64, 1.57 (60 H, br. m, N$\underline{C}$y), 1.40 (12 H, dd, ^3J = 6.4 Hz, CH$\underline{Me}_2$), 1.33 (12 H, dd, ^3J = 6.4 Hz, CH$\underline{Me}_2$), 0.13 (18 H, s, $CH_2Si\underline{Me}_3$). $^{13}C\{^1H\}$ NMR (C_6D_6, 100.6 MHz, 300 K): δ 179.4 (Ga($\underline{C}$(N^{i}Pr)$_2$), 175.9 ($\underline{C}$(NCy)$_2$), 145.9 (*i*-$\underline{C}_6H_3{}^iPr_2$), 145.7 (*o*-$\underline{C}_6H_3{}^iPr_2$), 126.1 (*p*-$\underline{C}_6H_3{}^iPr_2$), 123.4 (*m*-$\underline{C}_6H_3{}^iPr_2$), 121.9 (ArN$\underline{C}$H), 67.2 (CH of GaC(N$\underline{C}$y)$_2$)), 56.7 (CH of $CH_2C(N\underline{C}y)_2$)), 28.9 ($\underline{C}$HMe$_2$), 26.8, 23.8 (CH$\underline{Me}_2$), 26.4, 26.2, 26.0, 25.8 (NCy), 17.2 ($\underline{C}H_2SiMe_3$), 0.13 ($SiMe_3$). IR (NaCl plates, Nujol mull, cm^{-1}): 1651 (s), 1563 (m), 1450 (s), 1382 (m), 1363 (m), 1241 (s), 1156 (w), 994 (w), 890 (w), 832 (s), 748 (m). Anal. Found (calcd. for $C_{67}H_{116}GaN_8OScSi_2$): C 66.67 (66.81); H 9.73 (9.71); N 9.26 (9.30) %

Sc{(Me$_3$SiCH$_2$)C(NCy)$_2$}$_2${(Ga(NArCH)$_2$)C(NTol)$_2$} (19). To a stirred solution of Sc{(Me$_3$SiCH$_2$)C(NCy)$_2$}$_2${Ga(NArCH)$_2$}(THF) (100 mg, 87 μmol) in hexane (2.5

mL) at room temperature was added a solution of TolNCNTol (19 mg, 87 μmol) in C_6H_6 (2.5 mL). The red-orange solution immediately turned a dark yellow-brown, indicating formation of the product. The volatiles were removed under reduced pressure and the resulting yellow-brown residue was dissolved in hexane (2 mL). The volatiles were removed under reduced pressure and the resulting yellow-brown powder was dried *in vacuo* to afford the title compound. Yield: 69 mg (61 %). Crystals suitable for x-ray diffraction were grown from slow evaporation of a concentrated hexane solution.

^{1}H NMR (C_6D_6, 299.9 MHz, 293 K): δ 7.34 (4 H, br. m, *o*-$C_6\underline{H}_4Me$), 7.32 – 7.28 (6 H, overlapping 2 x m, *m*- and *p*-$C_6\underline{H}_3{}^iPr_2$), 7.27 (4 H, br. m, *m*-$C_6\underline{H}_4Me$), 6.12 (2 H, s, NCH), 3.65 (4 H, sept, ^3J = 6.9 Hz, C$\underline{H}Me_2$), 2.60 (4 H, br. m, NCH (Cy)), 2.22 (6 H, s, $C_6H_4\underline{Me}$), 2.01 (4 H, br. s, C$\underline{H}_2SiMe_3$), 1.97, 1.86 1.61, 1.16, 1.04, 0.97 (60 H, br. m, N$\underline{Cy}$), 1.36 (12 H, br. dd, CH$\underline{Me}_2$), 1.23 (12 H, br. dd, CH$\underline{Me}_2$), 0.14 (18 H, s, $CH_2Si\underline{Me}_3$). ^{13}C{^{1}H} NMR (C_6D_6, 75.4 MHz, 293 K): δ 179.2 (Ga($\underline{C}$(NTol)$_2$), 176.4 ($\underline{C}$(NCy)$_2$), 147.9 (*i*-$\underline{C}_6H_4Me$), 146.3 (*i*-$\underline{C}_6H_3{}^iPr_2$), 145.6, 145.3 (*o*-$\underline{C}_6H_3{}^iPr_2$), 132.6 (*p*-$\underline{C}_6H_4Me$), 130.8 (*m*-$\underline{C}_6H_4Me$), 125.6 (*p*-$\underline{C}_6H_3{}^iPr_2$), 124.7, 123.1 (*m*-$\underline{C}_6H_3{}^iPr_2$), 121.3 (ArN$\underline{C}$H), 120.7 (*o*-$\underline{C}_6H_4Me$), 57.1, 56.4 (CH of $CH_2C(N\underline{Cy})_2$)), 28.1 ($\underline{C}HMe_2$), 37.4, 36.8, 36.5, 36.1 (NCy), 29.8 (N-$\underline{C}$H), 26.2, 25.6, 25.3, 23.0 (NCy), 27.2, 24.2 (CH$\underline{Me}_2$), 21.2 ($C_6H_4\underline{Me}$), 17.1 ($\underline{C}H_2SiMe_3$), -0.1 ($SiMe_3$). IR (NaCl plates, Nujol mull, cm^{-1}): 1641 (w), 1621 (w), 1596 (w), 1558 (w), 1505 (m), 1464 (m)m, 1379 (w), 1362 (m), 1253 (m), 1202 (m), 1183 (w), 1141 (w), 1121 (m), 1043 (w), 996 (w), 888 (w), 851 (s), 811 (w), 757 (m), 701 (m), 637 (m). Anal. Found (calcd. for $C_{75}H_{116}GaN_8OScSi_2$): C 69.15 (69.26); H 9.14 (8.99); N 8.50 (8.62) %

Y{(Me$_3$SiCH$_2$)C(NCy)$_2$}$_2${(Ga(NArCH)$_2$)C(NCy)$_2$} (20). To a stirred solution of Y{(Me$_3$SiCH$_2$)C(NCy)$_2$}$_2${Ga(NArCH)$_2$}(THF) (100 mg, 0.84 μmol) in hexane (2.5 mL) at room temperature was added a solution of CyNCNCy (17 mg, 0.84 μmol) in hexane (2.5 mL). The red-orange solution immediately turned yellow, indicating formation of the product. All the volatiles were removed under reduced pressure and the resulting yellow-brown powder was dried *in vacuo* to afford the title compound. Yield: 73 mg (65 %) Crystals suitable for X-ray diffraction were grown from a concentrated hexane solution cooled to -30 °C.

^{1}H NMR (C_6D_6, 299.9 MHz, 293 K): δ 7.28 – 7.18 (6 H, overlapping 2 x m, *m*- and *p*-$C_6\underline{H}_3{}^iPr_2$), 6.18 (2 H, s, NCH), 3.61 (4 H, sept, ^3J = 6.9 Hz, C$\underline{H}Me_2$), 2.92 (6 H, br. m,

NCH (Cy)), 1.99, 1.82, 1.62, 1.30 (60 H, br. m, NCy), 1.96 (4 H, br. s, CH_2SiMe_3), 1.46 (12 H, dd, ^3J = 6.9 Hz, $CHMe_2$), 1.35 (12 H, dd, ^3J = 6.9 Hz, $CHMe_2$), 0.14 (18 H, s, CH_2SiMe_3). $^{13}C\{^1H\}$ NMR (C_6D_6, 75.4 MHz, 293 K): δ 177.6 (Ga(C(NCy)$_2$), 175.5 (C(NCy)$_2$), 146.2 (*i*-$C_6H_3{}^iPr_2$), 145.6, 145.2 (*o*-$C_6H_3{}^iPr_2$), 125.8 (*p*-$C_6H_3{}^iPr_2$), 124.0, 123.4 (*m*-$C_6H_3{}^iPr_2$), 122.2 (ArNCH), 67.2 (CH of GaC(NCy)$_2$)), 57.2, 56.8 (CH of CH_2C(NCy)$_2$)), 29.3, 28.7 ($CHMe_2$), 26.5, 26.2, 25.8, 25.6 (NCy), 24.2, 23.5 ($CHMe_2$), 17.0 (CH_2SiMe_3), -0.07 ($SiMe_3$). IR (NaCl plates, Nujol mull, cm^{-1}): 2121 (s), 1643 (w), 1557 (w), 1361 (w), 1253 (m), 1194 (w), 1182 (w), 1165 (w), 1148 (w), 1118 (m), 995 (m), 888 (m), 852 (s), 800 (m), 757 (m), 700 (m), 634 (m). Anal. Found (calcd. for $C_{73}H_{124}GaN_8OSi_2Y$): C 65.88 (65.99); H 9.55 (9.41); N 8.37 (8.43) %.

Lu{(Me$_3$SiCH$_2$)C(NCy)$_2$}$_2${(Ga(NArCH)$_2$)C(NCy)$_2$} (21). To a stirred solution of Lu{(Me$_3$SiCH$_2$)C(NCy)$_2$}$_2${Ga(NArCH)$_2$}(THF) (100 mg, 78 μmol) in hexane (2.5 mL) at room temperature was added a solution of CyNCNCy (16 mg, 78 μmol) in hexane (2.5 mL). The red-orange solution immediately turned a dark yellow-brown, indicating formation of the product. The volatiles were removed under reduced pressure and the resulting yellow-brown powder was dried *in vacuo* to afford the title compound. Yield: 80 mg (72 %).

^1H NMR (C_6D_6, 299.9 MHz, 293 K): δ 7.26 – 7.18 (6 H, overlapping 2 x m, *m*- and *p*-$C_6H_3{}^iPr_2$), 6.16 (2 H, s, NCH), 3.60 (4 H, sept, ^3J = 6.9 Hz, $CHMe_2$), 3.07 (6 H, br. m, NCH (Cy)), 2.02 (4 H, br. s, CH_2SiMe_3), 1.97, 1.82, 1.63, 1.29 (60 H, br. m, NCy), 1.45 (12 H, dd, ^3J = 6.9 Hz, $CHMe_2$), 1.35 (12 H, dd, ^3J = 6.9 Hz, $CHMe_2$), 0.08 (18 H, s, CH_2SiMe_3). $^{13}C\{^1H\}$ NMR (C_6D_6, 75.4 MHz, 293 K): δ 177.6 (Ga(C(NCy)$_2$), 175.1 (C(NCy)$_2$), 146.7 (*i*-$C_6H_3{}^iPr_2$), 145.7, 145.2 (*o*-$C_6H_3{}^iPr_2$), 125.9 (*p*-$C_6H_3{}^iPr_2$), 123.8, 123.4 (*m*-$C_6H_3{}^iPr_2$), 122.3 (ArNCH), 66.7 (CH of GaC(NCy)$_2$)), 56.6, 56.3 (CH of CH_2C(NCy)$_2$)), 29.5, 28.9 ($CHMe_2$), 26.5, 25.8, 25.7 (NCy), 24.2, 23.5 ($CHMe_2$), 17.5 (CH_2SiMe_3), -0.04 ($SiMe_3$). IR (NaCl plates, Nujol mull, cm^{-1}): 1642 (m), 1558 (w), 1467 (s), 1378 (w), 1361 (m), 1252 (m), 1198 (w), 1183 (w), 1168 (w), 1150 (w), 1121 (m), 1078 (w), 995 (w), 852 (s), 797 (w), 753 (w), 698 (w), 633 (w). Anal. Found (calcd. for $C_{73}H_{124}GaLuN_8OSi_2$): C 61.80 (61.98); H 8.92 (8.83); N 7.85 (7.92) %.

Sc{(Me$_3$SiCH$_2$)C(NCy)$_2$}$_2${B(NArCH)$_2$} (22). To a cold (-30 °C) solution of Sc(CH_2SiMe_3)$_2${B(NArCH)$_2$}(THF) (280 mg, 0.414 mmol) in THF (2 mL) was added

a solution of CyNCNCy (171 mg, 0.827 mmol) in THF (1 mL). The resulting yellow solution was warmed to room temperature and stirred for 30 mins. The volatiles were then removed under reduced pressure leaving a light brown solid. The solid was redissolved in pentane (5 mL), and placed in a freezer at -30 °C overnight, whereupon an off-white, microcrystalline solid had formed. The supernatant was filtered away, and the solid washed with cold (-30 °C) pentane, filtered and dried *in vacuo* to afford the title compound as an off-white solid. Yield: 176 mg (42 %). Crystals suitable for X-ray diffraction were grown from slow evaporation of a concentrated hexane solution.

^{1}H NMR (C_6D_6, 400.1 MHz, 298 K): δ 7.27 (6 H, overlapping 2 x m, *m*- and *p*-$C_6\underline{H}_3{}^{i}Pr_2$), 6.17 (2 H, s, ArNC$\underline{H}$), 3.70 (4 H, br. m, C$\underline{H}Me_2$), 2.93 (4 H, br. m, NCH (Cy)), 1.92 (4 H, br. s, C$\underline{H}_2SiMe_3$), 1.80, 1.76, 1.68, 1.61 (40 H, br. m, N$\underline{C}y$), 1.49 (12 H, d, ^{3}J = 6.9 Hz, CH$\underline{Me}_2$), 1.27 (12 H, d, ^{3}J = 6.9 Hz, CH$\underline{Me}_2$), 0.05 (18 H, s, $CH_2Si\underline{Me}_3$). ^{13}C{^{1}H} NMR (C_6D_6, 100.6 MHz, 298 K): δ 177.8 ($\underline{C}(NCy)_2$), 146.4 (*o*-$\underline{C}_6H_3{}^{i}Pr_2$), 146.2 (*i*-$\underline{C}_6H_3{}^{i}Pr_2$), 126.1 (*p*-$\underline{C}_6H_3{}^{i}Pr_2$), 123.3 (*m*-$\underline{C}_6H_3{}^{i}Pr_2$), 120.5 (ArN$\underline{C}$H), 57.3 (CH of $CH_2C(N\underline{C}y)_2$)), 36.0, 27.0, 26.4, 26.1 (NCy), 29.1 ($\underline{C}HMe_2$), 26.4 (CH$\underline{Me}_2$), 24.0 (CH$\underline{Me}_2$), 16.9 ($\underline{C}H_2SiMe_3$), 0.20 ($SiMe_3$). ^{11}B{^{1}H} NMR (C_6D_6, 128.4 MHz, 293 K): δ 38 (br). IR (NaCl plates, Nujol mull, cm^{-1}): 1581(w), 1454 (s), 1393 (w), 1378 (w), 1360 (m), 1338 (w), 1323 (w), 1301 (w), 1252 (s), 1200 (m), 1180 (m), 1153 (w), 1143 (w), 1113 (s), 1049 (w), 995 (w), 886 (w), 843 (s), 804 (w), 799 (w), 775 (w), 753 (m), 707 (m), 695 (w), 687 (w). Anal. Found (calcd. for $C_{60}H_{102}BN_6ScSi_2$): C 70.61 (70.69); H 10.21 (10.09); N 8.14 (8.24) %

Y{(Me$_3$SiCH$_2$)C(NCy)$_2$}$_2${B(NArCH)$_2$} (23). To a cold (-30 °C) solution of $Y(CH_2SiMe_3)_2\{B(NArCH)_2\}(THF)_2$ (200 mg, 0.25 mmol) in THF (2 mL) was added a cold (-30 °C) solution of CyNCNCy (104 mg, 0.50 mmol) in THF (1 mL). The resulting yellow solution was warmed to room temperature and stirred for 15 mins. The volatiles were then removed under reduced pressure leaving a light yellow/brown solid. The solid was redissolved in pentane (5 mL), and placed in a freezer at -30 °C overnight, whereupon a white, microcrystalline solid had formed. The supernatant was filtered away, and the solid washed with cold (-30 °C) pentane, filtered and dried *in vacuo* to afford the title compound as a white solid. Yield: 110 mg (41 %). Crystals suitable for X-ray diffraction were grown from slow evaporation of a concentrated hexane solution.

^{1}H NMR (C_6D_6, 400.1 MHz, 298 K): δ 7.25 (6 H, overlapping 2 x m, *m*- and *p*-$C_6\underline{H}_3{}^{i}Pr_2$), 6.22 (2 H, s, NCH), 3.75 (4 H, sept, ^{3}J = 6.9 Hz, C$\underline{H}$Me$_2$), 2.87 (4 H, br. m, NCH (Cy)), 1.88 (4 H, br. s, C$\underline{H}_2$SiMe$_3$), 1.88, 1.76, 1.68, 1.61 (40 H, br. m, N$\underline{Cy}$), 1.44 (12 H, d, ^{3}J = 6.9 Hz, CH$\underline{Me}_2$), 1.28 (12 H, d, ^{3}J = 6.9 Hz, CH$\underline{Me}_2$), 0.06 (18 H, s, CH$_2$Si$\underline{Me}_3$). ^{13}C{^{1}H} NMR (C_6D_6, 100.6 MHz, 298 K): δ 176.7 ($\underline{C}$(NCy)$_2$), 146.4 (*o*-$\underline{C}_6H_3{}^{i}Pr_2$), 145.7 (*i*-$\underline{C}_6H_3{}^{i}Pr_2$), 126.2 (*p*-$\underline{C}_6H_3{}^{i}Pr_2$), 123.3 (*m*-$\underline{C}_6H_3{}^{i}Pr_2$), 120.5 (ArN$\underline{C}$H), 56.9 (CH of CH$_2$C(N$\underline{Cy}$)$_2$)), 36.8, 26.8, 26.3, 26.0 (NCy), 29.1 ($\underline{C}$HMe$_2$), 26.2 (CH$\underline{Me}_2$), 23.8 (CH$\underline{Me}_2$), 16.6 ($\underline{C}$H$_2$SiMe$_3$), 0.2 (SiMe$_3$). ^{11}B{^{1}H} NMR (C_6D_6, 128.4 MHz, 293 K): δ 44. IR (NaCl plates, Nujol mull, cm^{-1}): 1568 (w), 1464 (s), 1403 (w), 1377 (m), 1363 (m), 1346 (w), 1329 (w), 1308 (w), 1259 (m), 1114 (w), 1090 (w), 851 (w), 802 (m), 757 (m), 720 (w), 686 (w), 668 (w). Anal. Found (calcd. for $C_{60}H_{102}BN_6Si_2Y$): C 67.91 (67.77); H 9.82 (9.67); N 8.05 (7.90) %

Lu{(Me$_3$SiCH$_2$)C(NCy)$_2$}$_2${B(NArCH)$_2$} (24). To a cold (-30 °C) solution of Lu(CH$_2$SiMe$_3$)$_2${B(NArCH)$_2$}(THF)$_2$ (100 mg, 0.11 mmol) in THF (2 mL) was added a cold (-30 °C) solution of CyNCNCy (47 mg, 0.22 mmol) in hexane (1 mL). The resulting yellow solution was warmed to room temperature and stirred for 15 mins. The volatiles were then removed under reduced pressure leaving a light yellow/brown solid. The solid was redissolved in pentane (5 mL), and placed in a freezer at -30 °C overnight, whereupon a white, microcrystalline solid had formed. The supernatant was filtered away, and the solid washed with cold (-30 °C) pentane, filtered and dried *in vacuo* to afford the title compound as an off-white solid. Yield: 55 mg (42 %). Crystals suitable for X-ray diffraction were grown from a concentrated pentane solution cooled to -30 °C.

^{1}H NMR (C_6D_6, 499.9 MHz, 298 K): δ 7.25 (6 H, overlapping 2 x m, *m*- and *p*-$C_6\underline{H}_3{}^{i}Pr_2$), 6.28 (2 H, s, NCH), 3.75 (4 H, sept, ^{3}J = 6.9 Hz, C$\underline{H}$Me$_2$), 3.02 (4 H, br. m, NCH (Cy)), 1.89 (4 H, br. s, C$\underline{H}_2$SiMe$_3$), 1.87, 1.76, 1.67, 1.61 (40 H, br. m, N$\underline{Cy}$), 1.44 (12 H, d, ^{3}J = 6.9 Hz, CH$\underline{Me}_2$), 1.28 (12 H, d, ^{3}J = 6.9 Hz, CH$\underline{Me}_2$), 0.06 (18 H, s, CH$_2$Si$\underline{Me}_3$). ^{13}C{^{1}H} NMR (C_6D_6, 125.7 MHz, 298 K): δ 176.3 (C(NCy)$_2$), 146.4 (*o*-$\underline{C}_6H_3{}^{i}Pr_2$), 145.8 (*i*-$\underline{C}_6H_3{}^{i}Pr_2$), 126.2 (*p*-$\underline{C}_6H_3{}^{i}Pr_2$), 123.3 (*m*-$\underline{C}_6H_3{}^{i}Pr_2$), 121.4 (ArN$\underline{C}$H), 57.1 (CH of CH$_2$C(N$\underline{Cy}$)$_2$)), 36.5, 26.9, 26.3, 26.0 (NCy), 29.1 ($\underline{C}$HMe$_2$), 26.4 (CH$\underline{Me}_2$), 23.8 (CH$\underline{Me}_2$), 17.2 ($\underline{C}$H$_2$SiMe$_3$), 0.20 (SiMe$_3$). ^{11}B{^{1}H} NMR (C_6D_6, 160.4 MHz, 293 K): δ 61. IR (NaCl plates, Nujol mull, cm^{-1}): 1642 (w), 1581 (w), 1566 (w), 1555 (w), 1465 (s), 1392 (w), 1378 (w), 1360 (s), 1324 (w), 1260 (s), 1254

(s), 1200 (m), 1181 (m), 1152 (m), 1143 (m), 1114 (s), 1049 (w), 1028 (w), 995 (w), 958 (w), 934 (w), 920 (w), 843 (s), 803 (m), 753 (m), 702 (m), 688 (w), 634 (w). Anal. Found (calcd. for $C_{60}H_{102}BLuN_6Si_2$): C 62.52 (62.70); H 8.87 (8.94); N 7.20 (7.31) %

5.8 Supplementary Figures and Tables

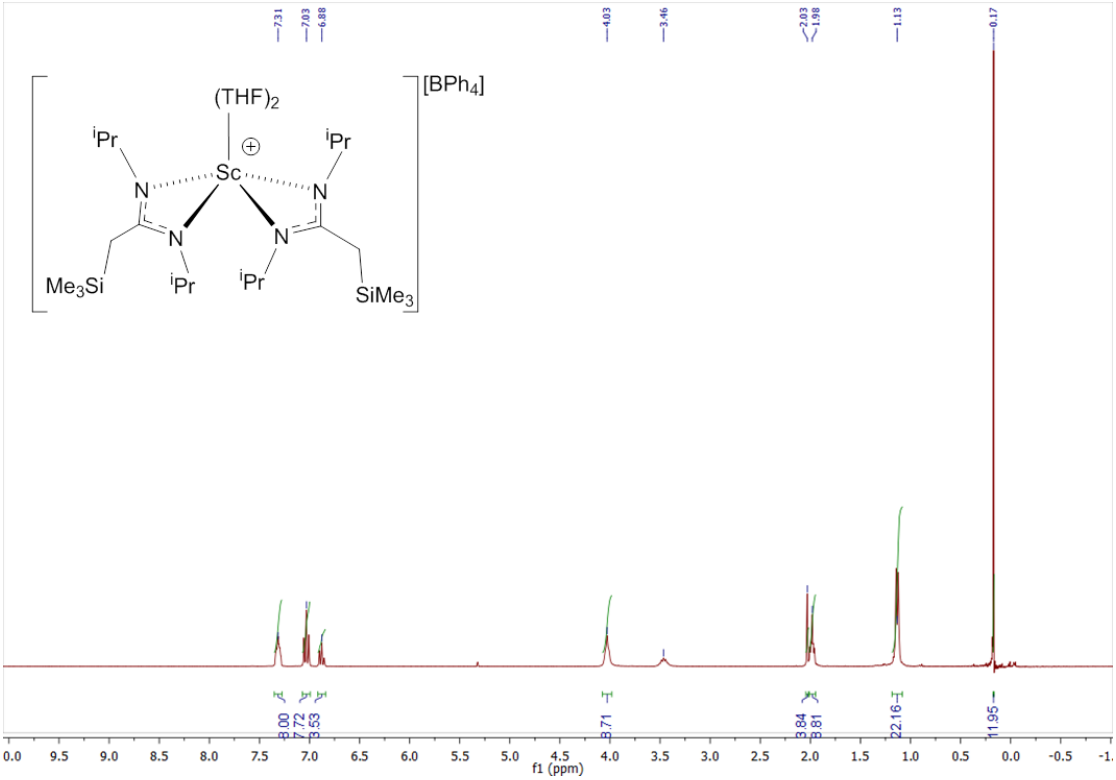

Figure 5.1. ^{1}H NMR spectrum (CD_2Cl_2, 299.9 MHz, 293 K) of **[Sc{(Me$_3$SiCH$_2$)C(N^{i}Pr)$_2$}$_2$(THF)$_2$][BPh$_4$] (5-BPh$_4$)**

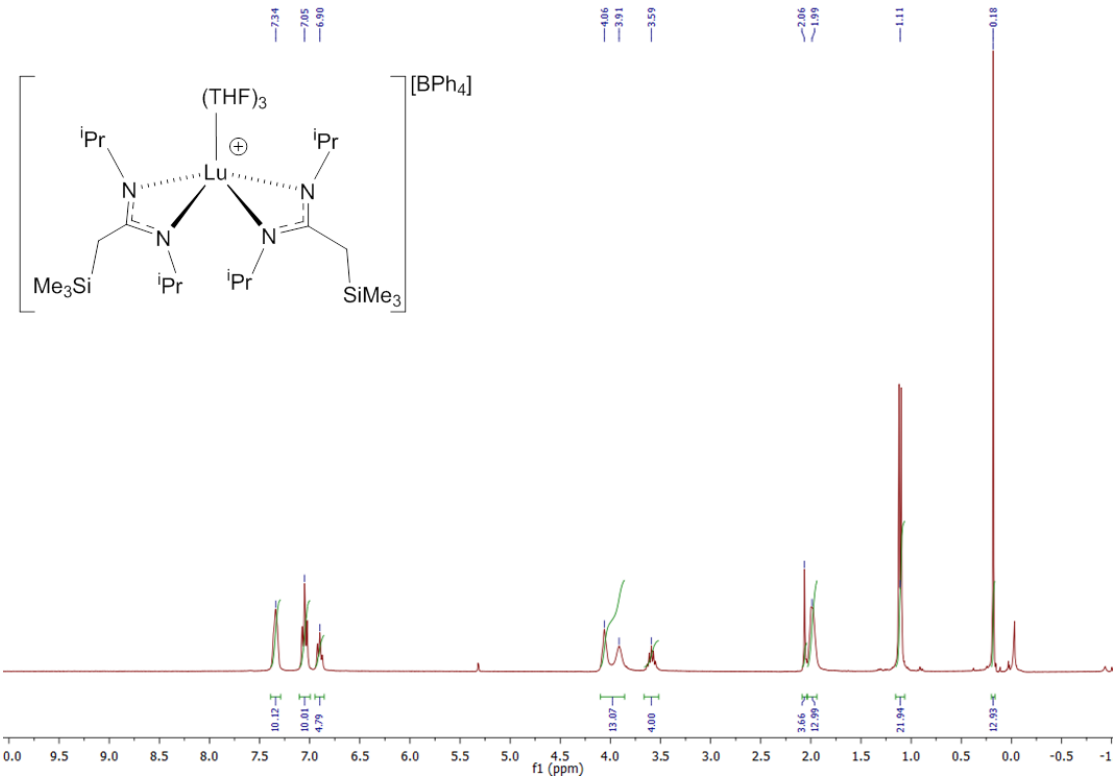

Figure 5.2. ^{1}H NMR spectrum (CD_2Cl_2, 299.9 MHz, 293 K) of **[Lu{(Me$_3$SiCH$_2$)C(N^{i}Pr)$_2$}$_2$(THF)$_3$][BPh$_4$] (11-BPh$_4$)**

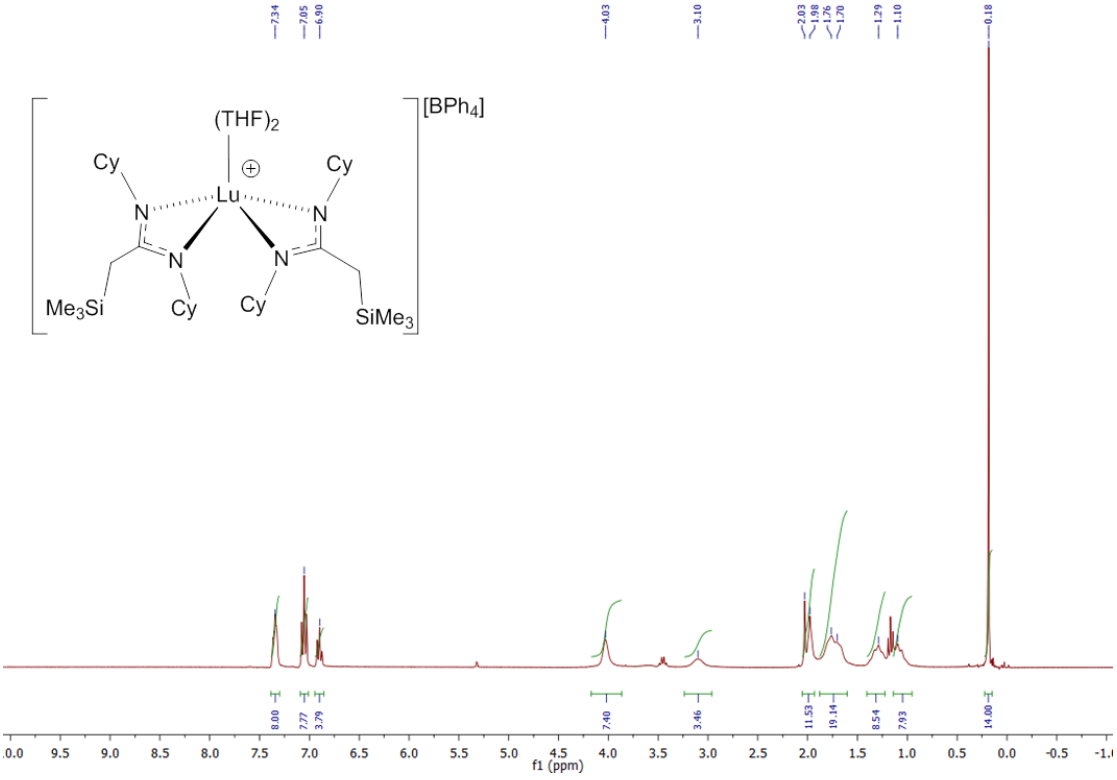

Figure 5.3. ^{1}H NMR spectrum (CD_2Cl_2, 299.9 MHz, 293 K) of **[Lu{(Me$_3$SiCH$_2$)C(NCy)$_2$}$_2$(THF)$_2$][BPh$_4$] (12-BPh$_4$)**

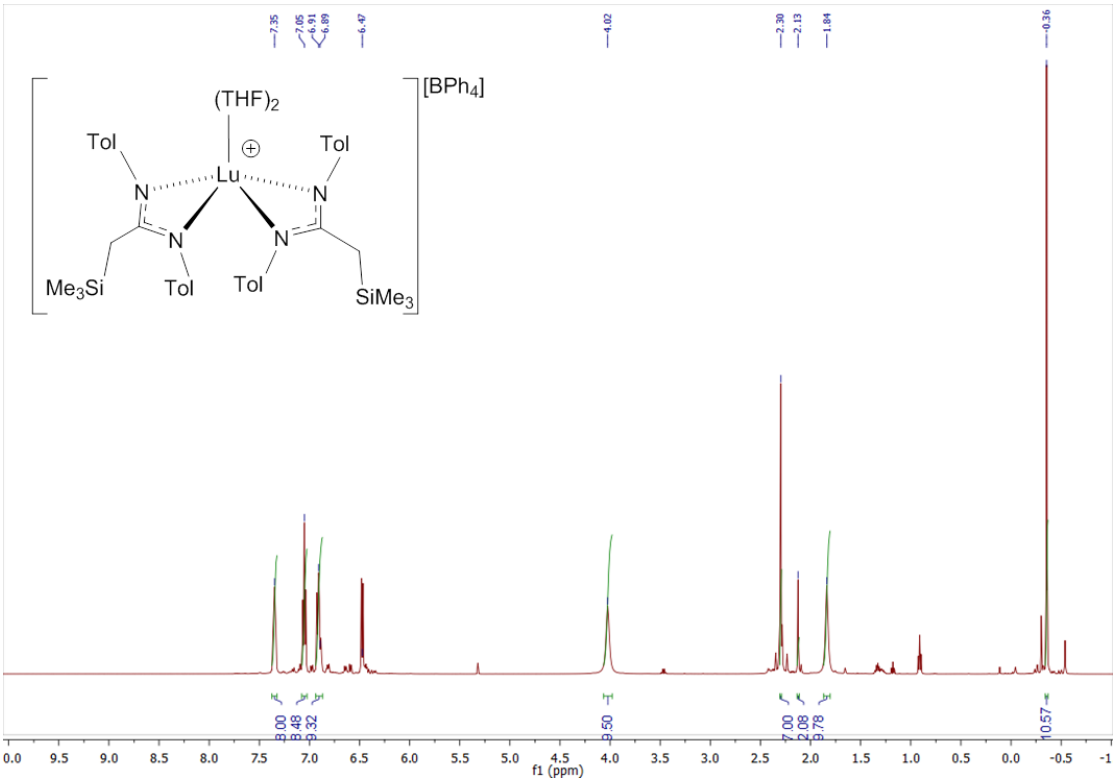

Figure 5.4. ^{1}H NMR spectrum (CD_2Cl_2, 499.9 MHz, 293 K) of **[Lu{(Me_3SiCH_2)C(NTol)$_2$}$_2$(THF)$_2$][BPh_4] (13-BPh_4)**

Table 5.1. X-ray data collection and processing parameters for $Ln(CH_2SiMe_3)_2\{B(NArCH)_2\}(THF)_n$ (Ln = Sc (**1**, n = 1), Y (**2**, n = 2) or Lu (**3**, n = 2)) and $SnCl_2\{B(NArCH)_2\}$ (**4**) (*a*. $R_1 = \Sigma||F_o|-|F_c|| / \Sigma|F_o|$; $R_w = \sqrt{\{\Sigma w(|F_o|-|F_c|)^2 / \Sigma w|F_o|^2\}}$ for data with $I > 3\sigma(I)$).

compound	**1**	**2**	**3**	**4**
empirical formula	$C_{38}H_{66}B_1N_2O_1Sc_1Si_2$	$C_{42}H_{74}B_1N_2O_2Si_2Y_1$	$C_{42}H_{74}B_1Lu_1N_2O_2Si_2$	$C_{52}H_{72}B_2Cl_2N_4Sn_1$
fw	678.89	794.95	881.01	964.39
temp / K	293	150	150	150
wavelength / Å	0.71073	0.71073	1.54184	0.71073
space group	*P* n	*P* 2_1/n	*P* 2_1	*P* $2_12_12_1$
a / Å	11.4076(2)	21.3465(3)	10.3787(3)	11.36740(10)
b / Å	15.0050(2)	10.3553(2)	18.8034(4)	18.77150(10)
c / Å	12.8787(2)	23.5353(4)	12.3583(3)	24.6570(2)
α / deg	90	90	90	90
β / deg	102.091(2)	113.890(1)	102.152(2)	90
γ / deg	90	90	90	90
V / $Å^3$	2155.55(7)	4756.7(1)	2357.74(10)	5261.39(7)
Z	2	4	2	4
d (calcd) / $Mg·m^{-3}$	1.046	1.110	1.241	1.217
abs coeff / mm^{-1}	0.254	1.308	4.730	0.623
R indices: R_1 =	0.0714[a]	0.0835[a]	0.0563[a]	0.0328[a]
R_w =	0.0625[a]	0.0781[a]	0.0662[a]	0.0340[a]

Table 5.2. X-ray data collection and processing parameters for [Y{(Me_3SiCH_2)C($NCy)_2$}$_2$($THF)_2$][BPh_4] (**9-BPh_4**), Sc{(Me_3SiCH_2)C($NCy)_2$}$_2${Ga($NArCH)_2$}(THF) (**14**), Sc{(Me_3SiCH_2)C($NCy)_2$}$_2${(Ga($NArCH)_2$)C($N^iPr)_2$} (**18**) and Sc{(Me_3SiCH_2)C($NCy)_2$}$_2${(Ga($NArCH)_2$)C($NTol)_2$} (**19**) (*a*. $R_1 = \Sigma||F_o|-|F_c|| / \Sigma|F_o|$; $R_w = \sqrt{\{\Sigma w(|F_o|-|F_c|)^2 / \Sigma w|F_o|^2\}}$ for data with I > 3σ(I)).

compound	**9-BPh_4**	**14**	**18**	**19**
empirical formula	$C_{66}H_{102}B_1N_4O_2Si_2Y_1$	$C_{70}H_{122}Ga_1N_6O_1Sc_1Si_2$	$C_{67}H_{116}Ga_1N_8Sc_1Si_2$	$C_{75}H_{116}Ga_1N_8Sc_1Si_2$
fw	1139.45	1234.63	1204.53	1300.66
temp / K	150	150	150	150
wavelength / Å	1.54180	1.54180	1.54184	1.54184
space group	C c c a	*P* 2_1/n	*P* c c n	*P* $\bar{1}$
a / Å	17.260(4)	13.18630(10)	13.8794(2)	15.1147(2)
b / Å	40.837(8)	23.2023(2)	17.5587(3)	16.8868(3)
c / Å	21.530(4)	24.3738(3)	29.2962(7)	29.5114(4)
α / deg	90	90	90	87.2141(12)
β / deg	90	99.2856(9)	90	87.5152(12)
γ / deg	90	90	90	89.0047(14)
V / $Å^3$	15176(5)	7359.51(13)	7139.6(2)	7515.6(2)
Z	8	4	4	4
d (calcd) / $Mg·m^{-3}$	0.997	1.114	1.121	1.149
abs coeff / mm^{-1}	1.665	1.867	1.911	1.854
R indices: R_1 =	0.0491[a]	0.0399[a]	0.0557[a]	0.0355[a]
R_w =	0.0563[a]	0.0517[a]	0.0166[a]	0.0200[a]

Table 5.3. X-ray data collection and processing parameters for Y{(Me_3SiCH_2)C($NCy)_2$}$_2${(Ga($NArCH)_2$)C($NCy)_2$} (**20**) and Ln{(Me_3SiCH_2)C($NCy)_2$}$_2${B($NArCH)_2$} (Ln = Sc (**22**), Y (**23**) or Lu (**24**)) (*a*. $R_1 = \Sigma||F_o|-|F_c|| / \Sigma|F_o|$; $R_w = \sqrt{\{\Sigma w(|F_o|-|F_c|)^2 / \Sigma w|F_o|^2\}}$ for data with I > 3σ(I)).

compound	**20**	**22**	**23**	**24**
empirical formula	$C_{73}H_{124}Ga_1N_8Si_2Y_1$	$C_{60}H_{102}B_1N_6Sc_1Si_2$	$C_{60}H_{102}B_1N_6Si_2Y_1$	$C_{60}H_{102}B_1Lu_1N_6Si_2$
fw	1328.65	1019.45	1063.40	1221.61
temp / K	150	150	150	150
wavelength / Å	1.54184	1.54184	1.54184	1.54184
space group	$P\bar{1}$	$P\bar{1}$	$P\bar{1}$	$P\bar{1}$
a / Å	17.4044(6)	12.8550(5)	12.9008(4)	12.9210(4)
b / Å	21.7307(9)	13.3992(4)	13.4345(3)	13.5834(4)
c / Å	22.5363(9)	19.9902(8)	20.2583(6)	21.1203(9)
α / deg	78.814(3)	87.800(3)	87.105(2)	91.194(3)
β / deg	67.479(3)	81.227(3)	82.129(3)	92.334(3)
γ / deg	77.248(6)	66.092(3)	65.964(3)	113.409(3)
V / $Å^3$	7622.4(6)	3109.9(2)	3176.37(17)	3396.2(2)
Z	4	2	2	2
d (calcd) / $Mg·m^{-3}$	1.158	1.089	1.112	1.195
abs coeff / mm^{-1}	2.071	1.671	1.938	3.412
R indices: R_1 =	0.0651[a]	0.0304[a]	0.0301[a]	0.0610[a]
R_w =	0.0624[a]	0.0401[a]	0.0395[a]	0.0443[a]

5.9 References

1 A. B. Pangborn, M. A. Giardello, R. H. Grubbs, R. K. Rosen and F. J. Timmers, *Organometallics*, 1996, **15**, 1518.

2 M. F. Lappert and R. Pearce, *Journal of the Chemical Society, Chemical Communications*, 1973, 126.

3 B. R. Elvidge, S. Arndt, P. M. Zeimentz, T. P. Spaniol and J. Okuda, *Inorg. Chem.*, 2005, **44**, 6777.

4 (a) R. J. Baker, R. D. Farley, C. Jones, M. Kloth and D. M. Murphy, *Journal of the Chemical Society, Dalton Transactions*, 2002, 3844; (b) Y. Segawa, Y. Suzuki, M. Yamashita and K. Nozaki, *J. Am. Chem. Soc.*, 2008, **130**, 16069.

5 (a) Z. Otwinowski and W. Minor, *Processing of X-ray Diffraction Data Collected in Oscillation Mode*, Academic Press, New York, 1997; (b) Agilent Technologies, Oxford, 2011.

6 A. Altomare, G. Cascarano, C. Giacovazzo and A. Guagliardi, *J. Appl. Crystallogr.*, 1993, **26**, 343.

7 L. Palatinus and G. Chapuis, *J. Appl. Crystallogr.*, 2007, **40**, 786.

8 P. W. Betteridge, J. R. Carruthers, R. I. Cooper, K. Prout and D. J. Watkin, *J. Appl. Crystallogr.*, 2003, **36**, 1487.

9 S. Grimme, J. Antony, S. Ehrlich and H. Krieg, *J. Chem. Phys.*, 2010, **132**, 19.

10 (a) J. P. Perdew, K. Burke and M. Ernzerhof, *Phys. Rev. Lett.*, 1996, **77**, 3865; (b) *Phys. Rev. Lett.*, 1997, **78**, 1396.

11 (a) C. F. Guerra, J. G. Snijders, G. te Velde and E. J. Baerends, *Theo. Chem. Acc.*, 1998, **99**, 391; (b) G. T. Velde, F. M. Bickelhaupt, E. J. Baerends, C. F. Guerra, S. J. A. Van Gisbergen, J. G. Snijders and T. Ziegler, *J. Comput. Chem.*, 2001, **22**, 931.

12 Gaussian 09, Rev. A02 and Rev. D01, M. J. Frisch, G. W. Trucks, H. B. Schlegel, G. E. Scuseria, M. A. Robb, J. R. Cheeseman, G. Scalmani, V. Barone, B. Mennucci, G. A. Petersson, H. Nakatsuji, M. Caricato, X. Li, H. P. Hratchian, A. F. Izmaylov, J. Bloino, G. Zheng, J. L. Sonnenberg, M. Hada, M. Ehara, K. Toyota, R. Fukuda, J. Hasegawa, M. Ishida, T. Nakajima, Y. Honda, O. Kitao, H. Nakai, T. Vreven, J. Montgomery, J. A., J. E. Peralta, F. Ogliaro, M. Bearpark, J. J. Heyd, E. Brothers, K. N. Kudin, V. N. Staroverov, R. Kobayashi, J. Normand, K. Raghavachari, A. Rendell, J. C. Burant, S. S.

Iyengar, J. Tomasi, M. Cossi, M. Rega, N. J. Millam, M. Klene, J. E. Knox, J. B. Cross, V. Bakken, C. Adamo, J. Jaramillo, R. E. Gomperts, O. Stratmann, A. J. Yazyev, R. Austin, C. Cammi, J. W. Pomelli, R. Ochterski, R. L. Martin, K. Morokuma, V. G. Zakrzewski, G. A. Voth, P. Salvador, J. J. Dannenberg, S. Dapprich, A. D. Daniels, O. Farkas, J. B. Foresman, J. V. Ortiz, J. Cioslowski and D. J. Fox, Gaussian, Inc., Wallingford, CT, 2009.

13 (a) AIMALL, version 10.12.13, T. A. Keith, 2010; (b) version 13.11.04, T. A. Keith, 2013.

14 F. L. Hirshfeld, *Theo. Chim. Acta*, 1977, **44**, 129.

15 (a) C. Edmiston and K. Ruedenberg, *Rev. Mod. Phys.*, 1963, **35**, 457; (b) J. M. Foster and S. F. Boys, *Rev. Mod. Phys.*, 1960, **32**, 300; (c) W. von Niessen, *J. Chem. Phys.*, 1972, **56**, 4290.

16 (a) T. Ziegler and A. Rauk, *Inorg. Chem.*, 1979, **18**, 1755; (b) *Inorg. Chem.*, 1979, **18**, 1558.

17 D. A. Pantazis and F. Neese, *J. Chem. Theory Comput.*, 2009, **5**, 2229.

18 C. S. Tredget, S. C. Lawrence, B. D. Ward, R. G. Howe, A. R. Cowley and P. Mountford, *Organometallics*, 2005, **24**, 3136.